THE UNIVERSITY *of* EDINBURGH

Estimation of Uncertainty in the Hydro-morphodynamic Characteristics of the Meghna Estuary, Bangladesh

Sifat Sarwar

Doctor of Philosophy

The University of Edinburgh

2020

Acknowledgements

First, and foremost, I would like to acknowledge the tremendous support I received from my primary supervisor Prof. Alistair Borthwick. His knowledge, humility, punctuality, guidance, and care made this 4-year long journey of Ph.D. very smooth and memorable. He is one of the kindest humans I have ever met. I am honoured to be one of his students.

I would like to thank Dr. Vengatesan Venuopal, who became my principal supervisor when Alistair retired. He was very kind to guide an additional student till the end. His valuable support was crucial.

My Ph.D. was fully funded by Schlumberger Founder Faculty for the Future fellowship program. I am grateful for their support and co-operation.

I also thank Prof. Alexander Horner-Devine, Dr. Nirnimesh Kumar, Jacob, Wuming and all the staff I met at the University of Washington, The USA. I was a visiting Ph.D. student for one year and I thank them for making me a part of their research group. They made my stay in Seattle very pleasant. I am also grateful to Vest Scholarships for selecting me for the award and for funding this one-year program.

I am grateful to all my colleagues- Monika, Ross, Ignacio, Mbayer, Joe, Will, Obinna, John, Desen, for their support and encouragement. Edinburgh became my second home because of them. I am grateful to Dr. Shaheen, who became more like a family member rather than a landlady. She was an awesome support during the COVID-19 pandemic.

And last, but not the least, I want to acknowledge the support from every one of my family – my father, who incepted the dream of pursuing Ph.D. in my mind; my mother, who passed away but left me with courage and patience; my husband, who missed me but supported my decision all along; and my brothers, who grew up so fast and bore all the responsibilities at home in my absence.

Abstract

The coastal zone of Bangladesh is a part of the Ganga–Brahmaputra–Meghna basin, and is home to about 38.5 million people. This coastal community is particularly vulnerable to natural disasters, such as catastrophic floods from extreme river flows, cyclones, land erosion, and sea level rise. Although advances in computational hydraulics facilitate the numerical simulation of extreme events in the coastal zone, informing risk assessment, the numerical models themselves propagate uncertainty from input to output parameters. This thesis presents a numerical derived distribution approach for uncertainty propagation through a computational model of tidal and fluvial processes in Meghna estuary of Bangladesh. The approach involves discretization of an estimated probability distribution function of a key input variable, the computation of a response function linking a single input parameter to a single output variable of interest, and the use of conservation of probability to determine the probability distribution of the output variable. The method requires only a few simulations to be conducted, and so it is very efficient to implement. In the thesis, Delft3D, a well-established computational tool, is verified for a series of standard tests. Then, Delft3D model is set up for the Meghna estuary and Bay of Bengal. Uncertainty propagation is then examined by studying the effect of uncertain bed roughness on the estimate of maximum water level, the effect of uncertain sea level rise on the maximum water level, and the effect of uncertain floc size on the sediment deposition rate at selected sites around the Meghna estuary of Bangladesh. It is found that with a 50% increase of mean Manning's *n*, the maximum water level can increase from 24% to 80% at various locations. For several IPCC scenarios of sea level rise, the standard deviation of maximum water level increases about 33-40% at the same locations. For a mean floc size of 227 micron and standard deviation of 171 micron, the coefficient of variation of cohesive sediment deposition rate is estimated to range from 19.8% to 37.6% at three locations in the Meghna estuary.

Lay Summary

Numerical model is very useful tool to investigate a problem in the coastal environment, but some uncertainties can arise from model assumptions and data unavailability. In statistics, uncertainty is estimated as the deviation of a parameter from its expected value and its estimation is very important for risk analysis. This thesis successfully applies a new approach to investigate the uncertainties in some chosen parameters relevant to coastal flooding and fine sediment movement. This approach is efficient with fewer calculation, and it is time saving.

A numerical model using Delft3D simulation engine is developed for Meghna estuary of Bangladesh to obtain the tidal elevation and sediment deposition rate at various locations. The uncertainty evolved in the highest tidal elevation around Meghna estuary due to the uncertainties in bed roughness and sea level rise varies in a wide range, giving a clear indication of flood risk. The policy makers, engineers, planners, or any relevant authority can use this information for flood mitigation planning. Also, the uncertainty incorporated in the fine sediment deposition rate due to the uncertainty in the size of sediment floc is of considerable amount. This shows the necessity of paying attention to the bed condition change while planning the land use and land development in this region.

Declaration

I certify:

(a) that the thesis, research project or dissertation has been composed by me, and

(b) either that the work is my own, or, where I have been a member of a research group, that I have made a substantial contribution to the work, such contribution being clearly indicated, and

(c) that the work has not been submitted for any other degree or professional qualification except as specified, and

(d) that any included publications are my own work, except where indicated throughout the thesis and summarised and clearly identified on the declarations page of the thesis.

_____

Sifat Sarwar

Contents

List of Figures

List of Tables

List of Abbreviations

ADI	Alternating Direction Implicit
BIWTA	Bangladesh Inland Water Transport Authority
BWDB	Bangladesh Water Development Board
BTM	Bangladesh Transverse Mercator
CDF	Cumulative Distribution Function
GDP	Gross Domestic Product
IPCC	Intergovernmental Panel for Climate Change
PDF	Probability Density Function
PMF	Probability Mass Function
RCP	Representative Concentration Pathway
SLR	Sea Level Rise
SRTM	Shuttle Radar Topography Mission
UTM	Universal Transverse Mercator
USGS	United States Geological Survey

Notation List

α	Shape factor for gravitational force
β	Shape factor for drag force
ν	Kinematic viscosity of water
μ	Mean
σ	Standard deviation
κ	von Kármán constant
τ_0	Bed shear stress
τ_e	Critical shear stress for erosion
ρ_s	Density of solid sediment
ρ_w	Density of water
d_p	Particle diameter
d_f	Floc diameter
d_{50}	Median grain size
f	Probability density function
g	Acceleration due to gravity
h	Water depth
k_s	Nikuradse roughness
n	Manning's roughness parameter
n_f	A constant related to R_e
p	Probability mass function
u_*	Friction velocity
$\bar{u}$	Depth-averaged velocity
z_0	Bed roughness length
C	Chézy coefficient
C_D	Drag coefficient
C_M	Dry density
D	Deposition rate
E	Expected value
E_1, E_2	Site-specific dimensional coefficients

F	Cumulative distribution function
$Kurt$	Kurtosis
$Kurt_n$	Non-dimensional kurtosis
Pr	Probability
R	Hydraulic radius
R_e	Reynolds number
R_{ef}	Floc Reynolds number
$Skew$	Skewness
$Skew_n$	Non-dimensional skewness
x, X	Input variable
y, Y	Output variable
Z	Maximum water level

Chapter 1

Introduction and Literature Review

1.1. Background

The coastal zone of Bangladesh is a densely populated area. The coastline of Bangladesh is 710 km long; its coastal and island communities comprise about 38.5 million people, nearly one-third of the total population of Bangladesh (*Bangladesh Planning Commission, 2018*). The coastal zone, depicted in figure 1.1, covers approximately 47,211 sq. km land area, and consists of natural sandy beaches on the eastern side, an estuary at the confluence of three major rivers in the middle, and a muddy coast with mangrove forest called the Sundarbans on the western part (*Bahauddin et al., 2016*). The Ganges, Brahmaputra and Meghna rivers flow through the Meghna estuary to the Bay of Bengal.

The coastal population of Bangladesh is highly vulnerable to natural disasters. Bangladesh Planning Commission (*2018*) reported seven prominent risks in the coastal zone in a baseline study for Delta plan 2100- coastal floods, cyclone and storm surges, riverbank erosion and vulnerability of islands, sea level rise, salinity intrusion, water logging, and coastal erosion. Furthermore, land scarcity exposes the coastal community to a much higher level of risk, and so policy makers are striving to develop an efficient coastal zone management plan. Among the seven coastal hazards, this thesis considers flood, sea level rise, and coastal erosion-accretion in Bangladesh.

Bangladesh and its dynamic coast have been a region of interest for many researchers and organizations. Delta Plan 2100 began in 2014 to establish a long-term holistic and integrated plan for the delta. Scientists, engineers, planners and other experts urgently need to consider the possibility of coastal-related natural disasters in Bangladesh. Numerical modelling is an efficient tool for simulation of complicated environmental processes which could be extremely useful for complex geographical regions, such as the Meghna estuary and Bay of Bengal. But unavailability of field observation data in terms of quality and quantity, makes it very difficult. In this circumstance, uncertainty analysis can be highly beneficial for scientists and policy makers to understand the physical processes occurring in the region, and also to estimate the underlying risks. This thesis provides an introduction to natural disasters affecting the coastal zone of Bangladesh, selects a suitable method for uncertainty analysis of parameters underlying coastal flood risk and fine sediment deposition. The motivation behind this thesis is to help make progress towards an overall coastal risk management model for Bangladesh by developing a fast, effective methodology for uncertainty propagation.

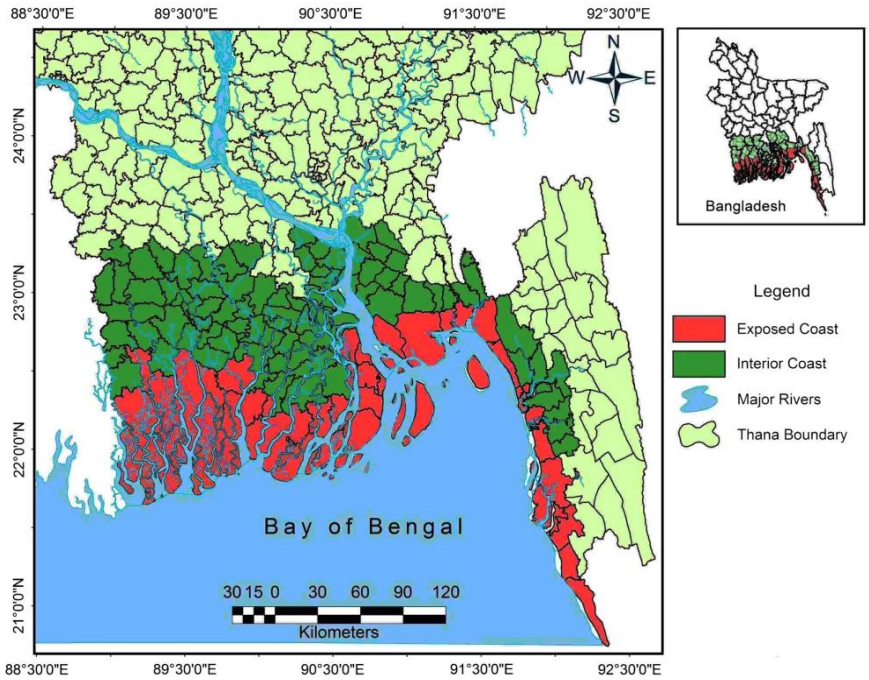

Figure 1.1: The coastal zone of Bangladesh (Bahauddin et al., 2016).

1.2. Aim and Objectives of this research

The aim of this PhD study is to use numerical simulation to estimate the effect of uncertainty in selected input parameters on the physical processes that govern the coastal flooding and sediment dynamics in the Meghna estuary including erosion and deposition. The numerical modelling is carried out in Delft3D-FLOW simulation tool. The probability distribution of the parameter of interest is either assumed or obtained from data available in literature. The functional relation between the output and input parameter is obtained from the numerical simulation. Then the uncertainty in the output parameter is calculated using numerical probability transfer method.

The objectives are listed below:

i. To find and use a suitable method for uncertainty analysis using a few model outputs.
ii. To create a detailed computational grid for the Meghna estuary.
iii. To determine the effect of uncertainty in bed roughness parameter on the maximum water level at different locations around the Meghna estuary for present tidal and river forcings.
iv. To determine the impact of uncertainty in sea level rise on the maximum water level at different locations around the Meghna estuary.
v. To estimate the effect of uncertainty in floc size of suspended cohesive sediment on the sediment deposition rate at critical locations around the Meghna estuary.

1.3. Synopsis

This thesis contains 9 chapters in total. Chapter 1 outlines the background of the study, and describes existing problems of land erosion, flood inundation, and sea level rise affecting the coast of Bangladesh. Chapter 2 provides a literature review of uncertainty propagation methods, paying particular

attention to their different merits and drawbacks. Chapter 3 describes the numerical probability transfer method at the heart of the thesis, supplemented with mathematical examples. Chapter 4 describes the Delft3D-FLOW model, including the governing equations, solver, and verification tests. Chapter 5 discusses the model set up and results where the effect of uncertainty in bed roughness on the uncertainty of maximum water level is discussed. Chapter 6 investigates the influence of uncertainty in sea level rise on uncertainty in maximum water level. Chapter 7 examines the effect of uncertainty in floc size on the uncertainty in sediment deposition rate. Chapter 8 provides a discussion of the implications of the numerical analogy of derived distribution approach and results for coastal flood risk assessment in Bangladesh. Chapter 9 lists the main conclusions and makes several recommendations for future research.

1.4. Natural Calamities in the Coastal region of Bangladesh

1.4.1. Flood

The Ganges–Brahmaputra–Meghna basin is dominated by the Asian monsoon system. The complex and differentiated circulation mechanisms of the Asian monsoon system result in distinct precipitation patterns in the overall Himalayan region. Maximum rainfall is recorded from June to September and minimum precipitation from November to March. The average annual rainfall in the catchment area of the Ganges is 1,400 mm, the Brahmaputra/Jamuna 2,100 mm and the Meghna 4,000 mm (*Ahmad 1989*).

Throughout the basin, the river systems have tremendous importance. They provide water for irrigation, for hydro-power production, and for groundwater recharge, as well as for daily economic and social life. The systems contribute significantly to annual flooding (both beneficial and damaging) and to soil fertility. Interlinked rivers, ponds, groundwater tables and the sea have strong

influence on the rising and recession phases of a flood event (*Hofer and Messerli, 2006*).

The Ganges–Brahmaputra–Meghna basin has an important political dimension: the Ganges, the Brahmaputra and the Meghna are international and transboundary river systems. 7–8 per cent of the total catchment area is located within Bangladesh, 62 per cent in India, 18 per cent in China, 8 per cent in Nepal and 4 per cent in Bhutan (*Hughes et al. 1994*). Five countries manage and share the water resources of the Ganga–Brahmaputra–Meghna basin. Bangladesh is the lowest downstream riparian country and is influenced by the adverse effects of interventions and activities higher up the river system. Management of water resources often results in difficult international negotiations or even political tensions, particularly regarding the sharing of the dry season flow.

Hossain et al. (*1987*), Miah (*1988*), Ahmad (*1989*) and Brammer et al. (*1993*) classified four basic flood types in Bangladesh:

- Monsoon floods of major rivers (water level slowly rises and falls)
- Flash floods (hydrographs rise and fall sharply)
- Floods owing to excessive rainfall, and
- Tidal floods (because of cyclones and storm surges).

Hussain (*2017*) identified some cropping systems and cropping patterns based on saline that are suitable for saline, drought, and flood prone areas of Bangladesh. He investigated the flood prone areas (figure 1.2) and considered similar types of floods for his research. The flood dimension varies in each year. In 1994, only 419 km^2 of flood-affected area (0.28 per cent of the country) was reported, whereas in 1998 the area under floodwater exceeded 100,000 km^2 (68 percent of the country) (*Hofer and Messerli, 2006*).

In terms of the impacts of floods on people affected, the depth of inundation is an important parameter. Winsemius et al. (*2013*) produced an inundation map for Bangladesh after downscaling from global datasets for the year 1961-1990 as shown in figure 1.3(a). They proposed a framework for flood risk

assessment in terms of annual flood damage and annual affected GDP. They found the inundation depth to be less than 5 m in severely affected areas.

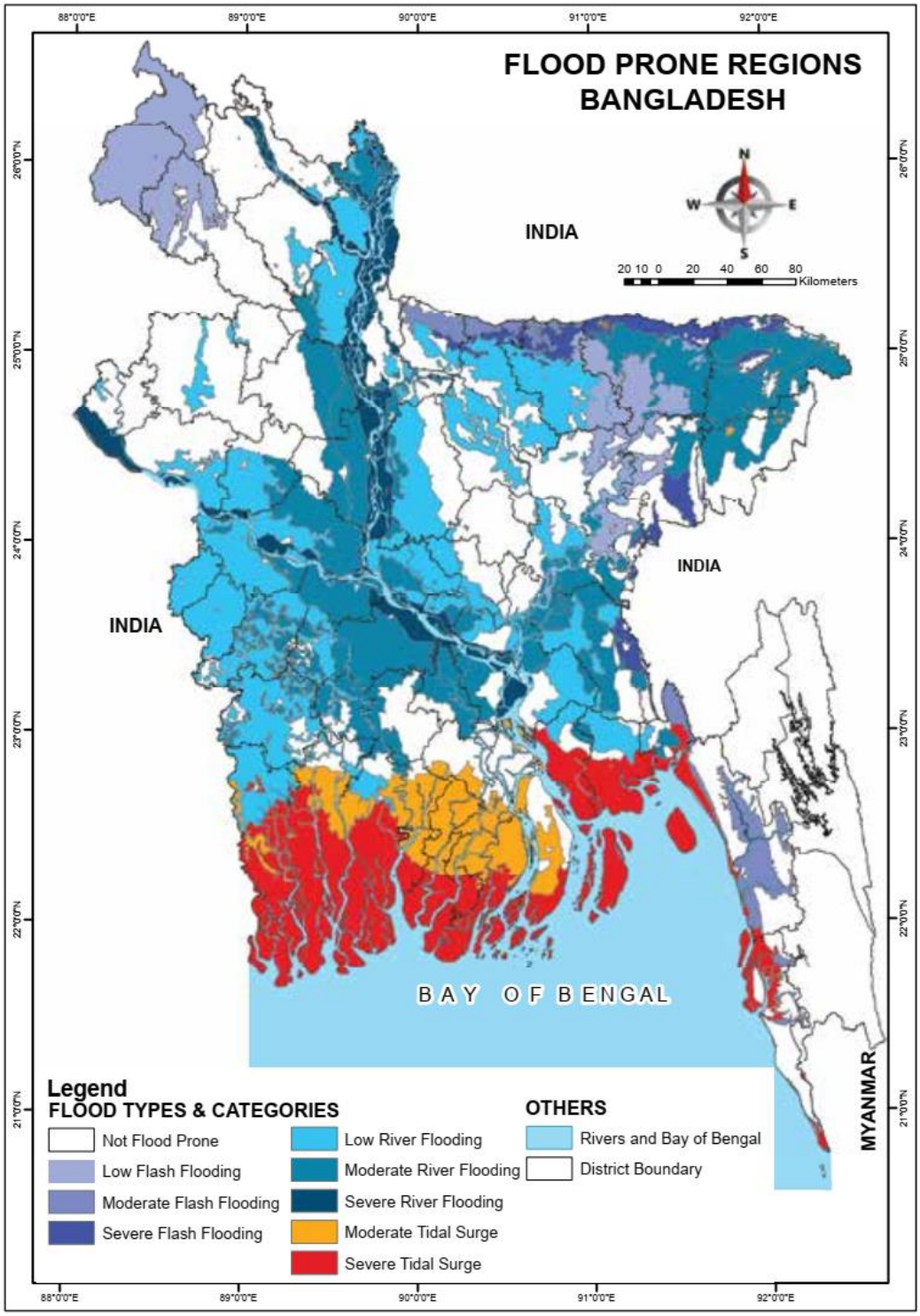

Figure 1.2: Flood types and flood prone regions in Bangladesh (Hussain, 2017).

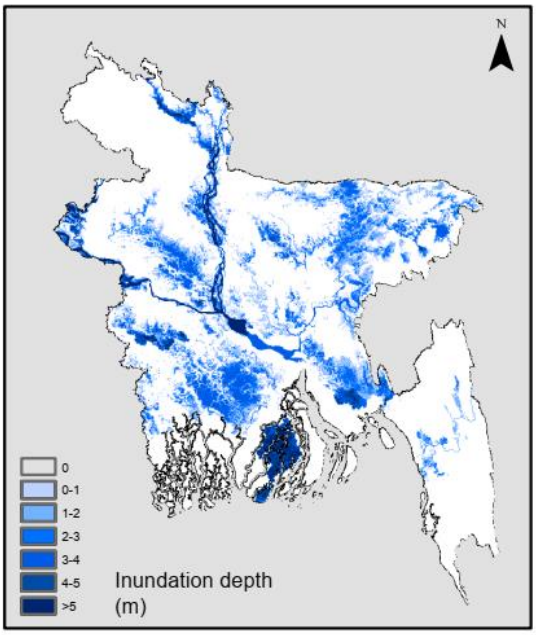

(a)

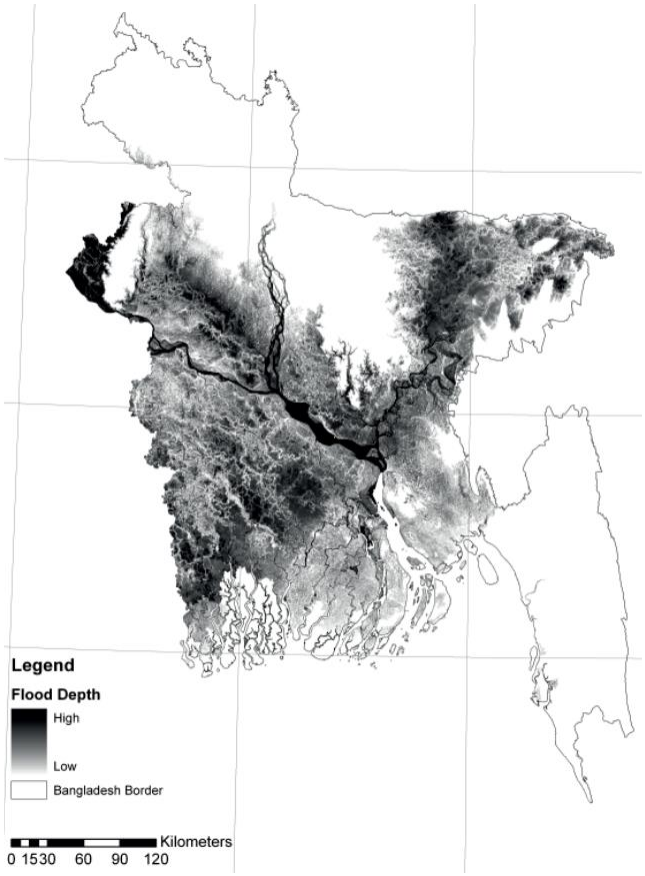

(b)

Figure 1.3: (a) Inundation depth map for the flood events in 1961-1990 in Bangladesh (Winsemius et al., 2013). (b) Identification of floodplain using flood inundation modelling for 2000-2010 (Baldassarre et al., 2014).

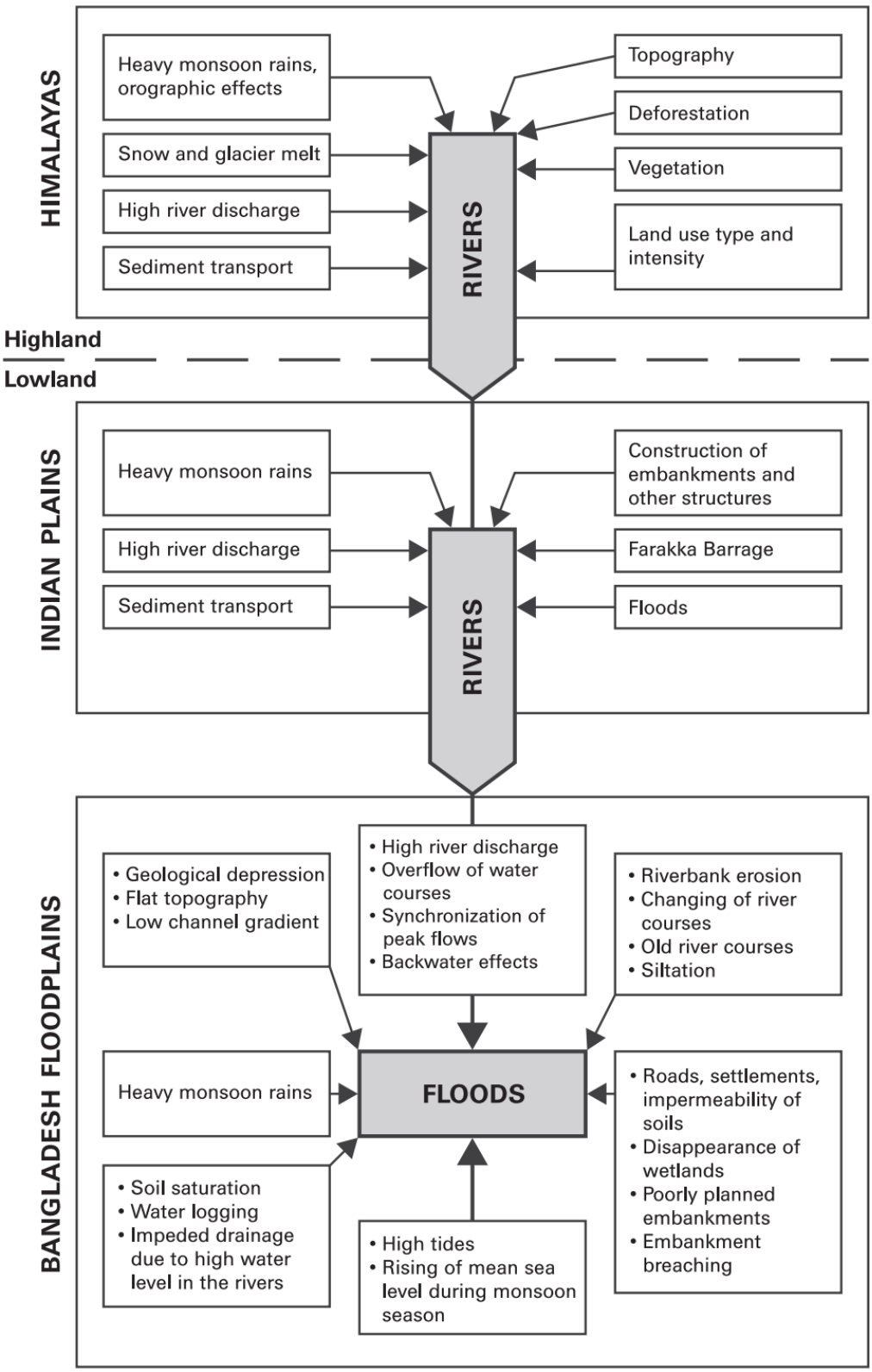

Figure 1.4: The causes of floods in Bangladesh Compiled by Hofer and Messerli (2006).

Baldassare et al. (*2014*) used flood inundation modelling technique to recreate the floodplain using the information for the year 2000-2010 as shown in figure 1.3(b). They claimed to be in satisfactory agreement with Winsemius et al. (*2013*).

There are numerous causes of floods in Bangladesh. Bangladesh Water Development Board's (BWDB) flood report for 1991 (*BWDB 1991a*) compared specific aspects of the 1984, 1987, 1988, and 1991 floods, and found that a standardization of floods is difficult because each flood event occurs under specific conditions. Hofer and Messerli (*2006*) summarized all the causes they found from the literature in the form of a flow chart (figure 1.4).

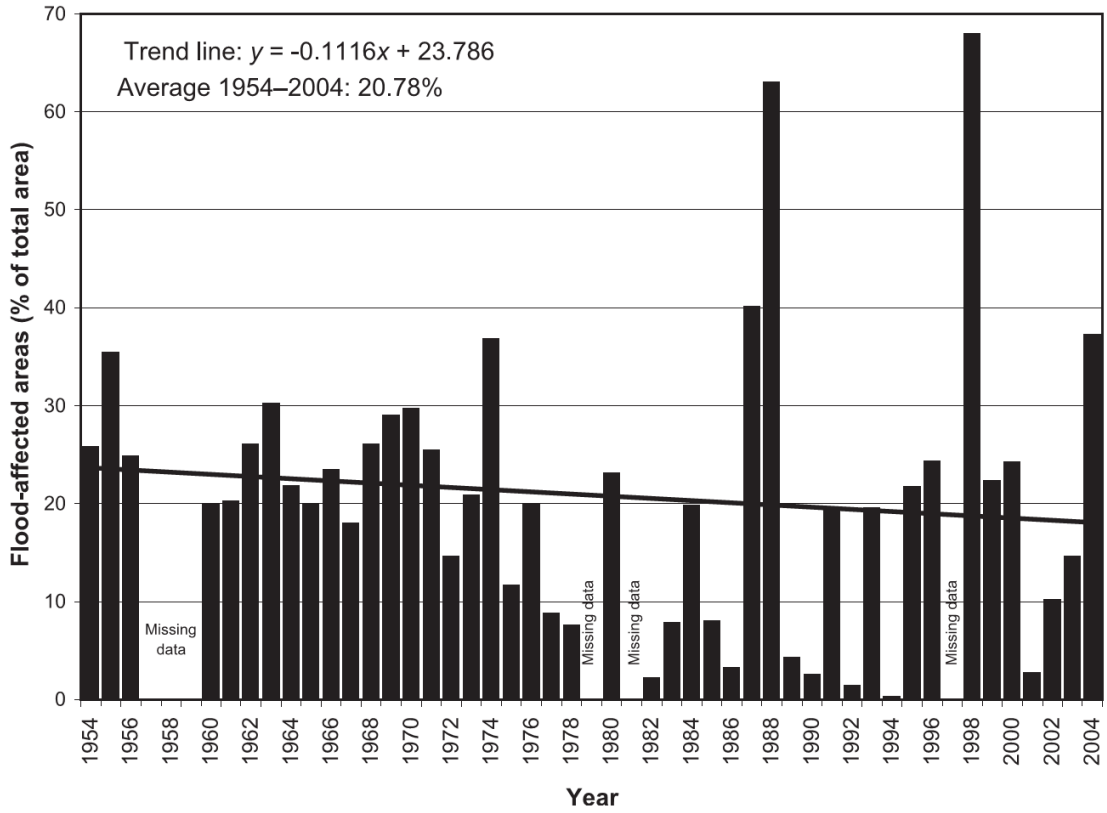

Figure 1.5: Extent of flood-affected areas in Bangladesh, 1954-2004 (Hofer and Messerli, 2006)

Figure 1.5 shows the extent of flood affected areas and it can be seen that two of the worst floods in the history of flooding in Bangladesh occurred in 1988 and 1998. The 1998-flood was the longest lasting (mid-July to the end

of September) and most devastating in 100 years, flooding 67.93% area of the country (*Hofer and Messerli, 2006*). The extent of damage was huge. Dhaka, the capital city, was significantly damaged, affecting its then population of 9 million (*Hofer and Messerli, 2006*). Different sources reported the number of human fatalities varied from 783-1500 (table 1.1).

Table 1.1: Extent of damage and deaths during the flood of 1998, compiled by Hofer and Messerli (*2006*)

Item	**Damage**
No. of districts affected	53 (out of 64)
No. of people affected (different sources)	30,000,000; 31,648,746
No. of human deaths from flood-related causes (different sources)	783; 1,050; 1,414; >1500
No. of people facing malnutrition and disease	25 million
Estimated damage in agricultural sector: rice damaged cultivated area damaged crops washed away	 2.2 million tonnes 1,565,390 hectares on 100,000 hectares
Estimated losses in forestry sector	US$52 million
Estimated losses in fisheries sector	US$73.9 billion
Estimated losses in livestock sector	US$500 million
Roads and highway damaged (partially or completely)	15,000 km
Embankments damaged (partially of completely)	about 4500 km
No. of bridges and culverts damaged	20,500
No. of houses damaged (different sources)	550,000; 894,015
No. of educational damaged	24,000
No. of industrial units damaged	11,000

The combined effect of different factors resulted in a huge flood in 1998 in Bangladesh. Hofer and Messerli (*2006*) summarized the causes listed in previous literature. 1997 and 1998 were El Niño/La Niña years. During the monsoon period, the rainfall intensity was 40% more than usual. The three major rivers reached their peaks simultaneously between 7 and 11

September. There was a simultaneous combination of flash flood, river flood, and tidal flood. Haque and Nicholls (*2018*) reported that the three major rivers usually have different timings of peak flood, but because of other natural phenomena (rainfall intensity and timing, drainage capacity, storage capacity, infiltration rate, etc.), synchronization of the peaks occurred in both the 1998 and 1988 flood events. In 1988, about 63.01% of the total area of Bangladesh was flooded. Before recession of the first flood wave, heavy rainfall occurring in the northern and north-eastern part of Bangladesh prolonged the flood creating a nationwide flood event (*Hofer and Messerli, 2006*).

In recent years, Philip et al. (*2019*) used hydrological models to study the August 2017 flood event. It was a major flood event which was considered as an event that occurs from once in 30 years to once in 100 years. Extreme rainfall caused this severe flood event and over 30 districts were affected. This flood affected 6.9 million people, damaged 2292 schools, caused 13,035 cases of waterborne illness, made 2,97,250 people displaced, destroyed approximately 5,93,250 houses and caused 114 deaths (*Philip et al., 2019).*

1.4.2. Sea Level Rise

Bangladesh is under threat of climate change impact. Sea level rise (SLR) will encourage penetration of oceanic water into the river system, and the resulting salt intrusion will adversely affect freshwater resources and food production (*Kusche et al., 2016*). The rising sea level is expected to affect the flow-sediment regime, which in turn will also change flood inundation patterns and local sediment balances (*Akter et al., 2016*). SLR can increase drainage blocking, river flooding, and cause more frequent storm surge inundation (*Karim and Mimura, 2008*). Sea level rise can even threaten the sustainability of mangrove forests, coral reefs, and salt marshes (*Lovelock et al., 2015*)

Over the past 11,000 years, there has been a steady increase in the Earth's surface temperature which resulted in a more than 50 m rise in ocean level worldwide. During this period, the mean global rate of sea level rise was about 2 mm/yr (*Mikhailov and Dotsenko, 2007*). Analysis of data from the northern

Indian Ocean obtained over a period of more than 40 years up to 2004 has shown the local rate of sea level rise off the Indian sub-continent was 1.06-1.75 mm/year during that period (*Brammer, 2014*). With a probability of 50%, global mean sea level rise is expected to reach 0.75 m for 1.5º rise in temperature and 0.80 m for 2º C rise in temperature by 2100 with respect to 2000 (*Schaeffer et al., 2012*).

In its 5th Assessment Report, The Intergovernmental Panel for Climate Change (IPCC) examined the following contributory factors used in forecasting sea level change scenarios: glaciers, ice sheet surface mass balance, ice sheet dynamics, groundwater and reservoirs, gravity and solid Earth effects, thermal expansion, density and circulation changes, waves and storm surges (*Church et al., 2013*). IPCC considered four "Representative Concentration Pathway" (RCP) scenarios which are combinations of the contributory factors with different value ranges. Figure 1.6 displays the sea level rise projections obtained from the process-based model given by IPCC (*Church et al., 2013*).

In addition to sea level rise, tectonic sinking is occurring in the Bengal basin. The exact rate of subsidence has yet to be determined. Umitsu (*1993*) reported that the Bengal delta is sinking at a rate of 3 mm/yr, whereas Syvitski et al. (*2009*) suggested the rate is up to 18 mm/yr at some places. Sarker et al. (*2012*) estimated the subsidence rate to be up to 2.5 mm/yr, based on the plinth level of several historical buildings, and suggested that the buildings would have been 2.4 to 7.5 m below the tidal plain if the subsidence had occurred at the rate reported by Syvitski et al (*2009*).

IPCC projections (*Church et al., 2013*) are adopted by Lovelock et al. (*2015*) to investigate the vulnerability of Indo-pacific mangrove forests due to sea level rise. Kay et al. (*2016*) also considered the IPCC scenarios together with land subsidence rates in the range -2.5 to +2.5 mm/yr to project the Sundarbans mangrove forest area in 2100. Kay et al. found that the Sundarbans, which is at 2 m above mean sea level, appears resilient to sea level rise (but this is strongly dependent on the land subsidence rate).

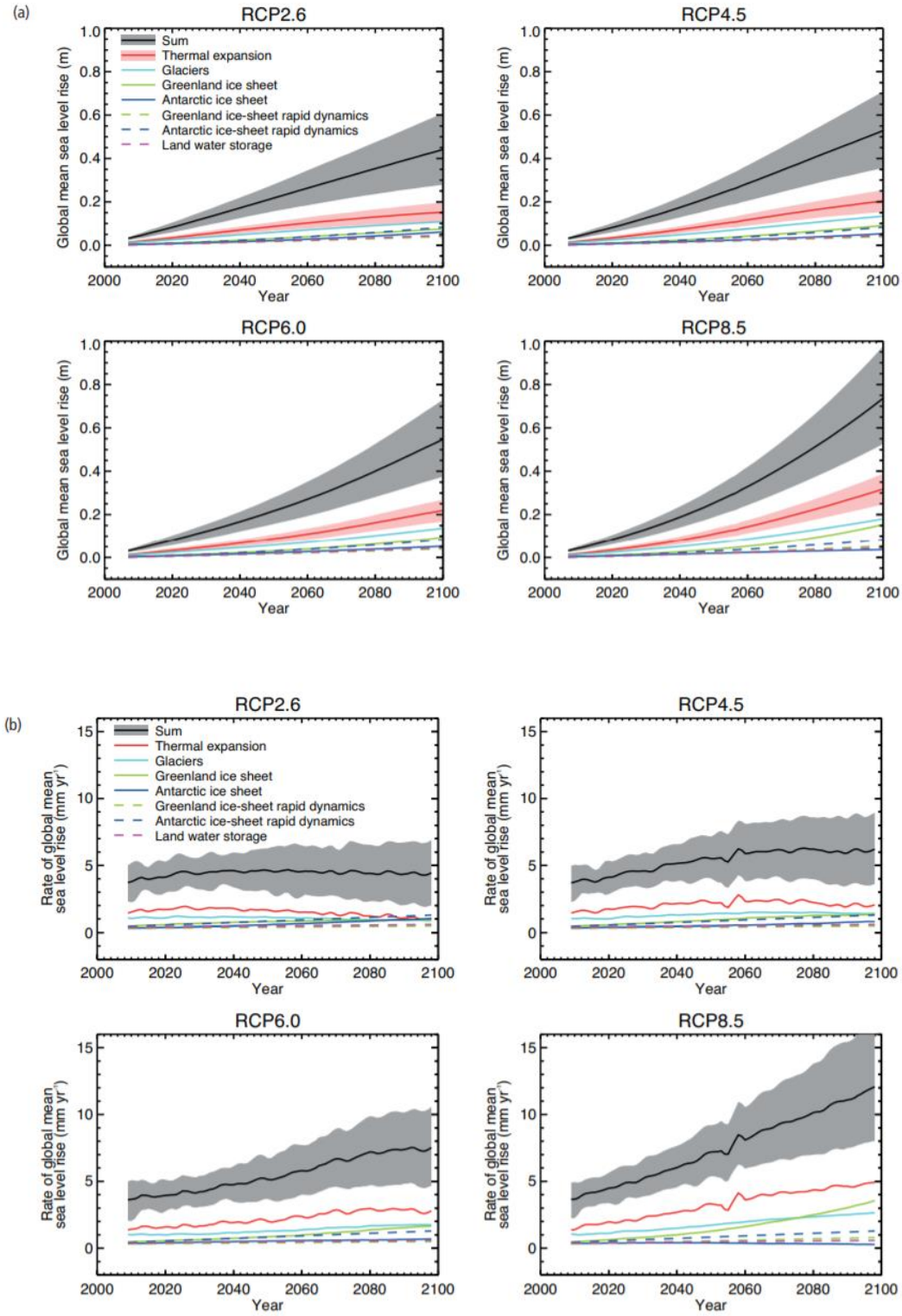

Figure 1.6 : Projections from the process based model by IPCC: (a) global mean sea level rise relative to 1986-2005; and (b) the rate of global mean sea level rise and its contributions (Church et al., 2013).

Kay et al. (*2015*) investigated how the combined effect of sea level rise and changes in other environmental conditions under climate change may alter the frequency of extreme sea level events for the period 1971 to 2099. They adopted the value of sea level rise as 0.63-0.88 m by the year 2090. This estimate considers a rate of land subsidence of 2.5 mm/yr. However, Kay et al. (*2015*) mentioned a further 0.5 m rise can be added if the melting of West Atlantic sheet is included. Although there are different opinions about the rate of subsidence, it is clear that the south-central and south-western part of Bangladesh is subsiding, which, together with sea level rise, has a significant impact in delta formation, sustainability of ecosystems and inundation.

1.4.3. Coastal Erosion

Bangladesh's distinct monsoon and dry seasons cause different magnitudes of rainfall, river flow, and sediment yield. During the monsoon season, the rainfall is very intense and consequently the river flow is greatly increased. The heavy rainfall in the Himalaya region increases the sediment yield of its constituent rivers. The combined effect of flow and sediment dominates the characteristics of the rivers, and hence the character of the Meghna estuary, where very complex interactions also take place between river and tide (*Akter et al., 2016*). Erosion and deposition of the sediment depends on local currents in the river and estuary; in fast currents there is sufficient shear to erode the bed with sediment particles transported predominantly in suspension (*Brammer, 2014*). The banks and bed level of the Meghna estuary have changed almost continuously over the centuries, with extensive erosion and deposition occurring near the islands. River erosion is a perennial problem in Bangladesh, which contains a network of about 230 rivers. The scarcity of land exposes residents living in the high-risk zone to natural calamities.

Figure 1.7 shows the map overlay of shoreline position from the Lloyd survey in 1840 and the LANDSAT image in 1984, given by Allison (*1998)* and cited by Mikhailov and Dotsenko (*2007*), showing land erosion and accretion

phenomena occurring around the mouth of the Meghna Estuary. Allison (1998) calculated the volume of eroded and accreted land at various locations from different maps over several time periods and found that there is a trend of net sediment accumulation at the delta front.

In 1960s, embankment construction commenced in the coastal area of Bangladesh. The works both provided flood protection by decreasing the submergence of land and prohibited sediment from reaching the delta front by decreasing sediment input to the delta. The dikes substantially altered the hydro-morphodynamic characteristics of the delta by raising water levels in the diked channels and reducing sediment input which in turn enhanced changes to the local erosion-accretion pattern in the channels (*Mikhalov and Dotsenko, 2007*).

Figure 1.7: Changes in the delta coastline of the Ganges and Brahmaputra rivers over the period of 1840 – 1984 (Mikhailov and Dotsenko, 2007 adopted from Alison, 1998): 1. Accretion, 2. Erosion. The numbers represent different islands and passes: 1. Sandwip pass, 2. Hatia pass, 3. Shahbazpur pass, 4. Tetulia pass, 5. Haringhata branch mouth, 6. Hoogly branch mouth, 7. Sandwip island, 8. Hatia island, 9. Bhola island, 10. Sagar island.

Erosion and accretion have been occurring in the vicinity of Bhola Island. Barua (*1997*) reported that the erosion rate, particularly at the northeast bank-line of Bhola, had an average value of about 150 m per year in the period between 1940 and 1963. Brammer (*2014*) provided a comparison between the land boundaries of 1943 and 2003, finding that about 40% of the eastern side of Sandwip island was eroded, though there was a net accretion of land

(figure 1.8). There is also considerable amount of erosion occurring at the North of Hatia island.

With the help of satellite images, Mahmood et al. (2020) produced a shoreline movement map for recent years (figure 1.9). It is evident from the map that the whole mouth of Meghna estuary is geographically very dynamic.

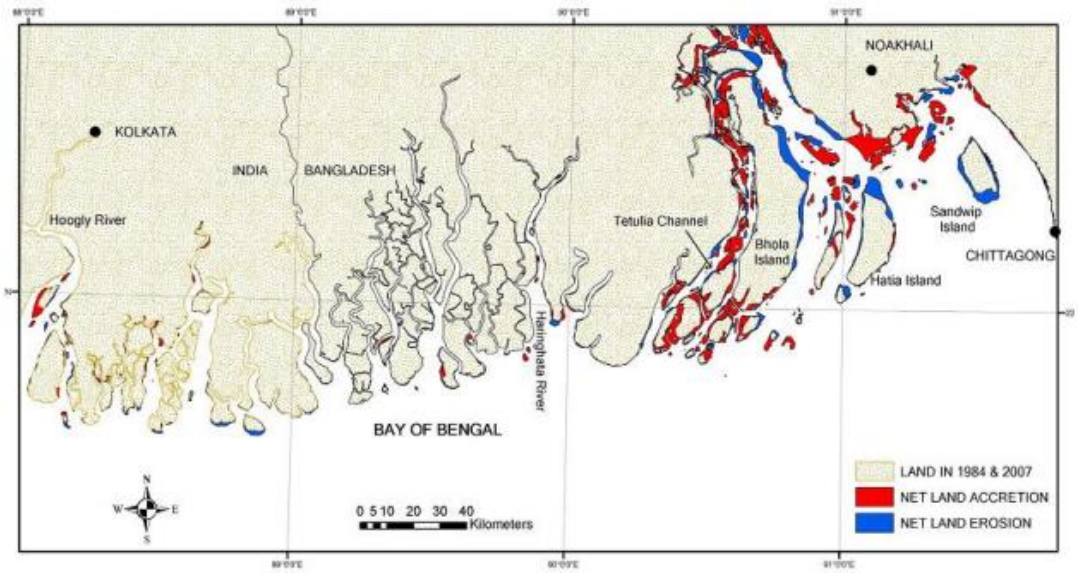

Figure 1.8: Changes in delta coastline in Bangladesh over the period 1984-2007 (Brammer, 2014).

In the Integrated Coastal Zone Management Program of the Government of Bangladesh, the prime concern is the safety of coastal communities. During 1995-2001, the Meghna Estuary Studies prepared a master plan for the area that projected deposition and accretion processes over a period of 25 years and determined a list of priority projects and possible interventions (*Ministry of Water Resources, 2001*). The Ministry of Water Resources of Bangladesh (*1999*) identified several areas as being prone to erosion. A study of historical maps was undertaken, and a projected coastline estimated for 2025. However, the solutions to control erosion, proposed by the Ministry of Water Resources of Bangladesh (*1999*), were very expensive and the conventional methods of erosion control had been shown not to be economically viable at that stage of development in Bangladesh.

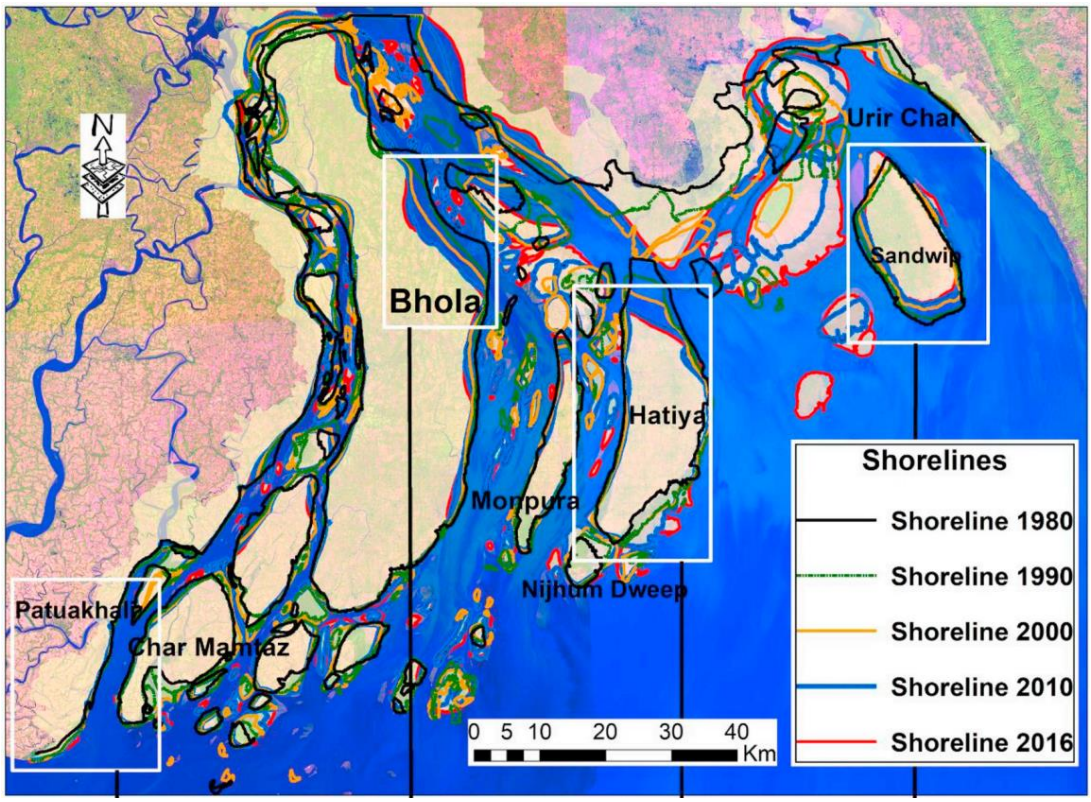

Figure 1.9: Shoreline movement in Bangladesh in the period of 1980-2016 (Mahmood et al., 2020).

In 2007, an Estuary Development Plan was prepared by the Ministry of Water Resources in Bangladesh. The plan focused mainly on land reclamation and proposed the construction of 19 cross-dams at several locations in accretion zones of the estuary (*Ministry of Water Resources, 2007)*.

Formulation of the Bangladesh Delta Plan 2100 started in 2014 in order to establish a long-term holistic and integrated plan for the delta. The Bangladesh Government's policy was to integrate climate change adaptation in a strategic way with a knowledge-based approach to make efficient use of the limited natural resources in Bangladesh. The problems under consideration included flood vulnerability, water security, food security, and siltation constraints, related to the mighty rivers and coastal area of Bangladesh. This thesis studies the flood inundation, sea level rise and suspended cohesive sediment deposition at different location around Meghna

estuary with the help of a Delft3D model in order to have an insight through a proper scientific approach (chapter 5, 6, and 7). The hydro-morphodynamic characteristics of this estuary are described in section 1.5.

1.5. Meghna Estuary and its Hydro-morhodynamic Characteristics

The Bengal Basin (also known as Ganges-Brahmaputra-Meghna Basin) consists of Bangladesh and parts of three eastern states of India (West Bengal, Assam and Tripura). According to Siddiqie-E-Akbar et al. (*2011*), more than 90% of the river flow passing through Bangladesh originates in upstream countries such as India and Nepal, whereas Bangladesh occupies only 7% of the total Ganges-Brahmaputra-Meghna basin area. The riverine discharge through the Meghna estuary is the fourth largest in the world (*Milliman and Meade, 1983; Mukherjee et al., 2009*) and the sediment discharge rate of $\sim 1\times10^{9}$ t/yr is the highest (*Goodbred and Kuehl, 2000; Mukherjee et al., 2009*).

Meghna estuary covers the zone of transformation of the Meghna River as it flows to the Bay of Bengal over a shallow shelf to a deeper basin. Several channels have formed in the estuary and they carry the river discharge to the bay. Large islands like Bhola, Hatia, and Sandwip are located at the mouth of the estuary. According to Jacobsen et al. (*2002*), Meghna Estuary is a 'Coastal Plain' estuary, which means that the estuary is very sensitive to driving forces. Fischer et al. (*1979*) mention that such estuaries are very sensitive to tidal conditions, river discharge, and wind speed. The morphology of the Meghna estuary is greatly influenced by the local hydrodynamic conditions. Sediment transport by the river to the estuary, grain size distribution, sediment concentration, bed composition, etc., are dominated by the hydrodynamic flow conditions in the estuary. Figure 1.10 shows the elevation of the Bengal basin where it can be found that it is a flat land with altitude around 5-10 m above mean sea level.

Several large and small rivers flow to the Bay of Bengal through the Meghna Estuary; however, the Lower Meghna surpasses all other rivers by its enormous volume. Two major rivers, the Ganges and Jamuna (nowadays, the mainstream of the Brahmaputra), combine to form the river Padma which in turn enters the Meghna at Chandpur, Bangladesh which eventually flows into the Bay of Bengal. The Lower Meghna, which commences at Chandpur, has two distinct seasonal flows which can vary from 10,000 m^3/s in the dry season to 100,000 m^3/s in the monsoon season. Figure 1.11 depicts the seasonal variation of water and sediment discharge the Ganges–Brahmaputra–Meghna River system.

Field data obtained from MorphoFlood project at IHE Delft in the Netherlands at two hydrological stations in Padma and Upper Meghna show that the discharge of the Padma River is roughly 5 times higher than that of the Meghna River in monsoon (figure 1.12). In the dry season, the flow in both rivers is low, with the Padma having higher discharge than the Meghna.

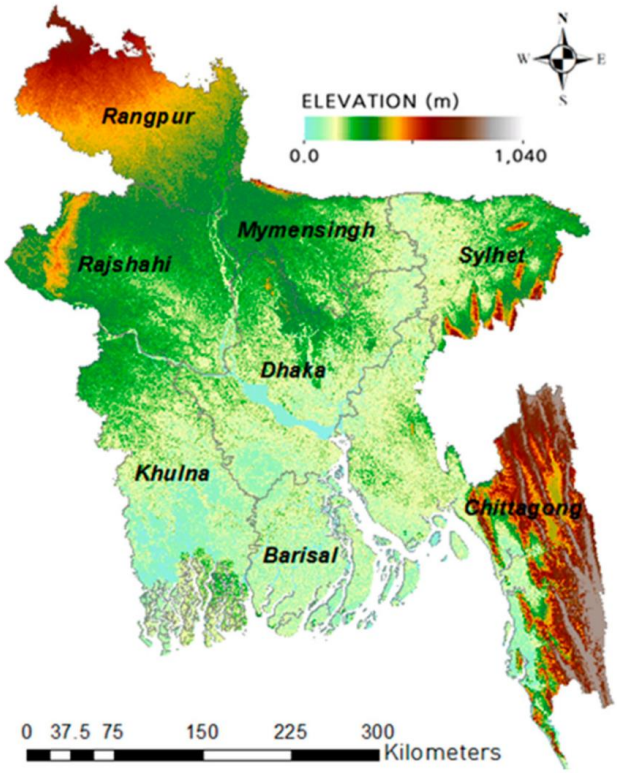

Figure 1.10: *Land elevation map of Bangladesh* (*Kamruzzaman et al., 2019)*

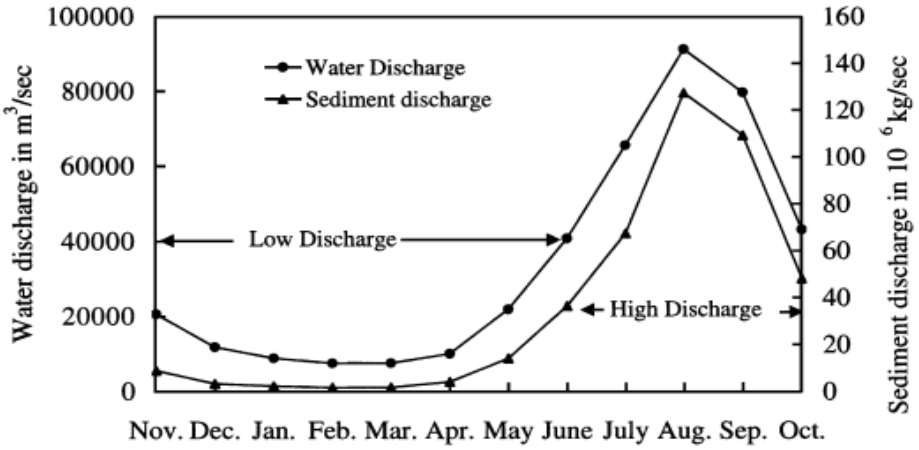

Figure 1.11: Average monthly variations in water discharge and suspended sediment discharge of the combined Ganges–Brahmaputra–Meghna River system (Source: Islam et al, 2002)

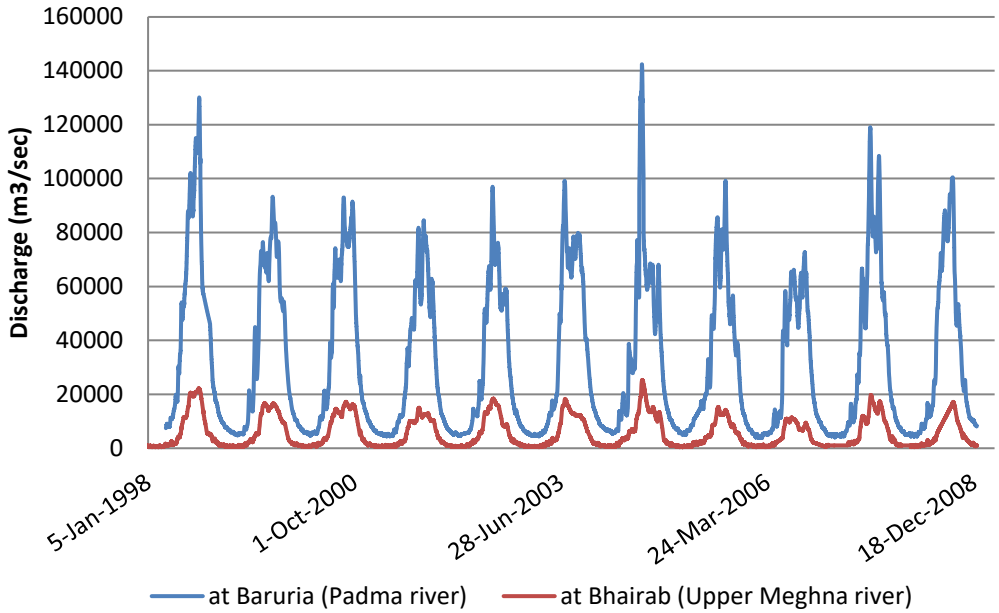

Figure 1.12: Observed daily discharge time histories in Padma (i.e., Ganges and Brahmaputra combined) and Meghna rivers, 1998-2008 (Source: MorphoFlood project, UNESCO-IHE Institute for Water Education, Delft, The Netherlands)

During Meghna Estuary Study I and II, [*Ministry of Water Resources, (1999,2001*)] found that the tidal waves in the coastal region of Bangladesh is affected by Coriolis acceleration, the coastal geometry (e.g., the funnelling shape of coastline around north of Sandwip island), the width of transitional continental shelf and the friction due to fresh water flow and bottom

topography. These are the factors that cause amplification and deformation of the waves. The reports also mentioned that M_2 and S_2 tide components are dominant in the estuary and the tidal range throughout the estuary varies from 2-4 m.

Wave conditions in the Bay of Bengal are mild. Patra and Bhaskaran (*2016*) gave an overview of annual fluctuation of wave and wind. They found that in the Bay of Bengal, the significant wave height is around 0.5-1 m and hardly goes above 2m. The wind speed is in the range of 2-6 m/s (*Patra and Bhaskaran, 2016*).

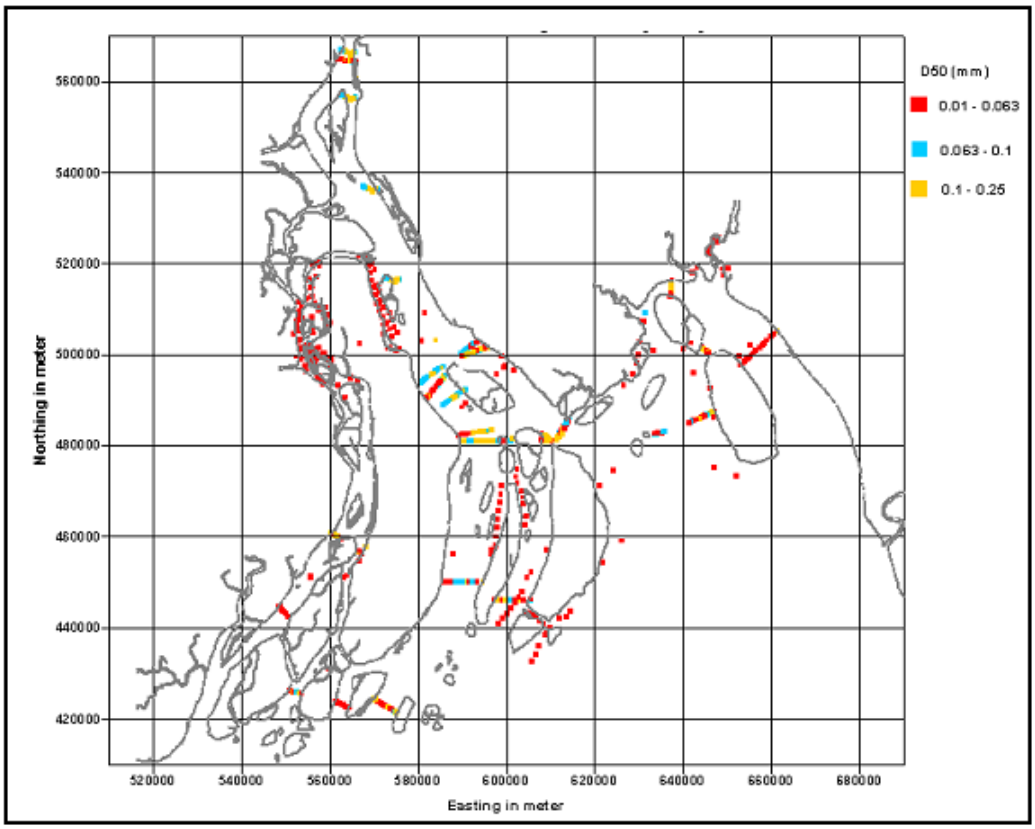

Figure 1.13: Spatial distribution of D_{50} in the Meghna Estuary (Source: Ministry of Water Resources, 2001).

In almost all rivers, there is a tendency for sediment size to decrease from the river upstream to the estuary as the larger particles settle before the smaller, and the river bed slope becomes increasingly mild. During the Meghna

Estuary Study-II (*Ministry of Water Resources, 2001*), several samples were collected from different locations, and the analyses showed that the bed consisted of fine sand with silt. The silt content varied from 20% to 50%. The median bed material grain size varied from 16-250 μm (figure 1.13).

The Bangladesh Ministry of Water Resources (*2001*) found the distribution of grain size was almost invariably uniform, and that the composition of bed material altered in both the stream-wise and transverse directions at the river sections considered. Suspended sediment in the Meghna Estuary consists mostly of very fine sand and silt. The suspended sediment particles move back and forth near the tidal inlets. In general, coarser particles are moved by near-bed transport processes. Mud and silt are predominantly transported as suspended material by the current.

The Bangladesh Ministry of Water Resources, (*2001*) also reported that the sediment concentration is slightly higher near the bed than the surface, which indicates that the estuary is vertically well mixed. More than 70% of the suspended sediment in the upstream rivers has particle diameter smaller than 63 μm. Kuehl et al. (*1989*) observed that the sediment in the estuary mainly comprised fine materials. Barua (*1990*) reported that the turbidity maximum was generally located at or near the head of the salt intrusion where salinity is 1-5 ppt, and that its location fluctuated seasonally throughout the estuary. In the monsoon season, almost the entire estuary is filled with fresh water and saline water tends to exit the estuary. Salinity was found to be 1-2 ppt in the monsoon season, and only near the Sandwip channel a higher salinity recorded (*Barua, 1990*).

In recent years, researchers found a higher concentration of salt in the west side of Bangladesh coastline than the eastern side of it. Dasgupta et al. (*2014*) investigated salinity at 34 locations in the coastal region, where the western sites had salinities higher than 30 ppt and the eastern sites had less than 2 ppt. The reason is that the east side of the coast accommodates all the river and tributaries with freshwater discharge, and the west side consists of tidal creeks with no freshwater input. Jahan et al. (*2015*) gave a detailed picture of

the spatial variation of salinity with 334 samples collected during February 2014 to May 2014 and found a prominent gradient in salinity from northwest to southwest. Lower Meghna river contained near freshwater with salinity less than 0.5 ppt, and the higher salinity was found at the southwest of the coast with salinity higher than 34 ppt. The same pattern of salinity distribution was found by Akter et al. (*2019*) from the data collected in 2010 and 2011.

1.6. Uncertainty analysis and its significance in Bangladesh context

One of the biggest challenges in working on hydro-morpdynamic behaviour of the riverine and coastal system of Bangladesh is the unavailability of field data. Bricheno et al. (*2016*) mentioned Bangladesh as "notoriously data-poor" and found that validation of a hydrodynamic model for this region is very difficult. Moreover, the quality of the collected data is not good. For example, Bangladesh Inland Water Transport Authority (BIWTA) and BWDB collect daily high and low water level in the rivers, but generally, water level data are collected at 6 a.m. and 6 p.m. every day (*Bricheno et al., 2016*). To calibrate and validate a hydrodynamic model, these two data are not sufficient and more frequent data are required. Because, from these two values it is not possible to produce a semidiurnal tide signal. In a semidiurnal tidal cycle, there are two peaks and two troughs daily. In addition, not all the tidal components have exactly 12 hours or 24 hours cycle. Depending on the interaction among the sun, the moon and the earth, the tidal components have various tidal periods. So, the collection times (6 a.m. and 6 p.m.) do not necessarily represent the daily high and low water level. Visual Tide Staff is used to collect water level data, which is not a very reliable approach (*Bricheno et al., 2016).* Visual Tide Staff is a graduated pole which stands upright in the water and the reading of the level of the water is collected manually. Its installation cost is low, and operation is easy. But the collected data is more prone to human errors and thus, data accuracy is less. During bad weather, it is often impossible to collect data using Visual Tide Staff.

Sediment data are scarcer and more random. While collecting suspended sediment data from BWDB for this thesis, data for only 5 random days were obtained in year 2007. Sediment transport itself is a chaotic process. It depends on many complicated and associated processes which are either unexplored or imprecisely understood. Even the best methods can calculate the sediment transport rates with an accuracy of a factor of 2 in only 70% cases of river engineering, and may not achieve the accuracy of a factor of 5 in 70% of the cases in the coastal engineering (*Soulsby, 1997*).

Now, uncertainty analysis can be effectively used in researches for the locations where field data are not easily available. Uncertainty, as a measure of data variability, was first described by Karl Pearson in the late 1800s (*Sulsbarg, 2002*). Back then, the scientists considered the incorporated variability in measurement as the error. Pearson introduced the idea of uncertainty, acknowledging the variability occurring in nature. He was a disciple of the English scientist Sir Francis Galton who is known as the "discoverer" of fingerprints. But Galton is also the person who first discovered the phenomenon of "regression to the mean" and the mathematical measure of it as "the coefficient of correlation". Galton established a biometric laboratory in London and collected various biological data of the people. Later, it was Pearson who discovered that the measurements themselves are scattered after analysing the accumulated biological data. He found that the measurements do not have exact values, rather they have a range of values and that range can be quantified as uncertainty (*Sulsbarg, 2002*).

Pearson discovered a set of probability distribution to describe the scatter of the data and four parameters were introduced to describe the characteristics of those distributions. These parameters are:

i. Mean – the central value around which the data are distributed
ii. Standard deviation –how far most of the data are scattered from the mean
iii. Skewness – to which degree the data are accumulated on one side of the mean, and

iv. Kurtosis – how far the rare measurements are scattered from the mean.

Apart from the field data, another source of uncertainty in numerical modelling is the assumptions made in the model itself. Numerical modelling is a useful tool to study a complex natural system where several driving forces act simultaneously. During the numerical simulation of an estuarine system, uncertainty can arise from different sources and these sources can be categorized as follows (*Kreitmair et al., 2019*):

i. Lack of field data – river discharge, tidal elevation, velocity, etc.
ii. Insufficient information about physical parameters – bed roughness, bathymetry, boundary condition, initial condition, etc.
iii. Inappropriate numerical parameters – grid resolution, time step, etc., and
iv. Model assumptions.

There have been numerous studies on the rising sea level in the Bay of Bengal, some of them are discussed in section 1.2.2. These studies gave the range of the predicted sea level rise by next 50 or 100 years which is obtained from different process-based models for different scenarios. So, the rate of rise has underlying uncertainty within itself. Bed roughness is a calibration parameter in hydro-morphodynamic modelling, which is a source of uncertainty as the spatial distribution of roughness parameter in a region is not exactly known or measured. Similarly, there is very little information available about the cohesive sediment size and floc size around the Meghna Estuary, though it is evident that the coastal region of Bangladesh is dominated by mud.

It is clear from the discussion that the physical parameters and field data in the estuarine and coastal region of Bangladesh have considerable amount of uncertainties. These uncertainties have significant impact on the model outputs. It is very important to quantify these uncertainties and to understand

how it affects the related output parameters such as maximum water level, which is an indicator of flooding.

Chapter 2

Review of Uncertainty Propagation Analysis Techniques

2.1 Preamble

Shallow flow solvers used for flood prediction are usually based on mass and momentum equations. Unknowns in physical parameters (i.e. parameter uncertainty), incomplete idealisation of the physical processes, and model limitations (convergence, accuracy, and round-off errors) all contribute to uncertainty propagation. Initial and boundary conditions are routes by which uncertainty reach the equation system. Examples include uncertainty in specification of the bed friction roughness, sediment grain size, eddy diffusion coefficient, and other empirical closure parameters. The accuracy of outputs from a shallow flow water-sediment solver is therefore highly dependent on the accuracy of the input data. As indicated by Xiu (*2009*) it is important that uncertainty is taken seriously from the beginning of numerical model simulations in order to assess the reliability and possible variability of model outputs, which of course provide insight into the water-sediment processes.

2.2. Uncertainty Propagation Techniques

Over the past twenty or so years, considerable effort has been directed towards developing techniques for quantifying uncertainty propagation through partial differential equations. These techniques can be broadly

classified as sensitivity analysis, stochastic models based on perturbation methods, Monte Carlo simulation, response surface methods, differential sensitivity, and polynomial chaos expansions. This chapter will consider each of these approaches in turn, where possible in the context of shallow water-sediment-morphology simulation, before summarising the merits and demerits of each approach, and thus providing a rationale for the uncertainty propagation methods proposed in the present thesis.

2.2.1 Sensitivity analysis

Perhaps the earliest and simplest technique involves sensitivity analysis whereby an input parameter is varied by ± per cent, and assessment made of the impact on an output variable. A typical example is the use of sensitivity analysis by Qin et al. (*2002*) to examine the effect of uncertainty in assigned weights and grades on the priority order of three options for post-reclamation coastline at Deep Bay, South China. Ni et al. (*2002*) used the assigned weights suggested by Qin et al. (*2002*) to determine an optimal reclaimed coastline from several options. Ni et al. used numerical models to predict changes to local hydrodynamics, etc., identified factors of influence and issues of concern, before assigning weights and using the analytic hierarchy process to rank the options, thus aiding decision makers in making their choice.

2.2.2 Stochastic models based on Perturbation Methods

Stochastic modelling has been used for uncertainty quantification for more than a decade. Stochastic models estimate uncertainty propagation throughout the simulation and are not limited to calculating errors and bounds by post-processing the output (Lin et al*., 2007*). Horritt (*2002)* used first- and second-order perturbation methods to develop a stochastic model of shallow flow hydrodynamics, and thence to study the influence of uncertain bed topography. The stochastic model gave results in good agreement with Monte Carlo simulations. Later, Horritt (*2006*) used a linear perturbation expansion

to develop a simplified relationship between the uncertain input parameters and the output, and tested the model for a meandering channel, floodplain, and full channel-floodplain flows with uncertain input values of Manning's roughness coefficient. Horritt obtained a computational speed up of more than 50 compared to the Monte Carlo method.

Flandoli and Pappalettera (*2020*) used a stochastic model to identify the noise required to reduce the complexity of interaction between different scales. Flandoli and Pappalettera identified both the large-scale and small-scale components of the deterministic equations of geophysical fluid dynamics for cases where the small-scale components were stochastically modelled.

2.2.3 Monte Carlo Simulation

The Monte Carlo method (*Mazhdrakov et al., 2018*) owes its name to Stansilaw Ulam, John von Neumann, and Nicholas Metropolis, all of whom worked at the Los Alamos National Laboratory in the 1940s. Ulam suggested the technique as a way of solving a solitaire problem to von Neumann, who applied the method in nuclear fission calculations. Metropolis proposed the name Monte Carlo after the casino in Monaco.

Monte Carlo simulation (and associated techniques) are routinely used to assess how the probability distribution of an input variable X translates into a probability distribution of an output variable Y (*Hofer, 2018*). The method works as follows. First, let the output variable be $Y = f(\alpha_1, \alpha_2, \dots\dots\dots \alpha_m)$ such that Y is the output function of input parameters $\alpha_1, \alpha_2, \dots\dots\dots \alpha_m$. If the input parameters have known probability distributions and they are statically independent, then it is possible to obtain the probability distribution of Y. In the Monte Carlo method, direct simulation is used to obtain the probability distribution of Y. First, $\alpha_1, \alpha_2, \dots\dots\dots \alpha_m$ are assumed numerical constants representing a joint probability distribution to the input. Then a large number of independent samples $\alpha_1^{(i)}, \alpha_2^{(i)} \dots\dots\dots \alpha_m^{(i)}$, where $i = 1, 2, \dots\dots\dots N$, are used to calculate the outputs $Y^{(i)}$, $i = 1, 2, \dots\dots\dots N$, from the assigned joint probability. From this output, summary statistics are calculated, and

confidence intervals evaluated as required. The major advantage of the Monte Carlo method is its general applicability. There is no restriction on the joint probability distribution and the relationship between the input and output. Confidence intervals are easy to determine.

Monte Carlo simulation is extremely useful, and can be readily extended to multiple input variable probability distributions. It does however suffer from a major shortcoming in that huge numbers (often > 10^5 or 10^6) of simulations are required as part of its repetitive resampling. This incurs an enormous computational overhead, rendering Monte Carlo unsuitable at present for application to complicated systems of nonlinear partial differential equations, such as the shallow water-sediment-morphodynamic equations considered in this thesis, given current computer technology. Moreover, it is difficult to assess the sensitivity of the results to the assumed input distributions, because a single change to an input distribution then requires re-running of the entire set of simulations. For the same reason, it is difficult to determine which input parameter has the greatest influence on output uncertainty using Monte Carlo simulation.

Monte Carlo methods have been applied to uncertain flood prediction based on input parameter uncertainty using a simplified parameterization by Aronica et al. (*1998*) and Bates et al. (*2004*) and a distributed parameterization of a simplified model by Romanowicz and Beven (*1998*). Also, Andrade *et al*. (2001) used a Bayesian statistical model based on Monte Carlo Markov Chain algorithms and a maximum likelihood method to improve estimates of the additional storage volume required by a reservoir for flood control.

Monte Carlo simulation is often used as a tool for risk assessment. Lin et al. (*2017*) developed an integrated framework for risk assessment of cyclone induced flooding which considered storm climatology change, sea level rise and coastal development. Lin et al. used the Monte Carlo method to estimate risk metrics and the probability distribution of the present value of future losses. Wang and Wang (*2019*) created a high-resolution projection for Texas and produced a Markov chain Monte Carlo-based hydrologic forecast for the

Guadalupe river basin. Xu et al. (*2014*) applied an integrated hydrodynamic model and Monte Carlo model to predict extreme water levels in Colombo, Sri Lanka. In this case, a Monte Carlo stochastic model was used to simulate the meteorological driving forces of cyclone storm surges.

Monte Carlo simulation has also been used in sediment sourcing and tracking. For example, it was used to track the source distribution of organic carbon and to evaluate sedimentary organic carbon cycling from the lower Pearl river to the South China Sea (*Li et al., 2017*). Recently, Monte Carlo simulation formed part of a sediment fingerprinting framework to estimate the contribution of terrestrial sources of fine sediment to coastal deposits in Southern Iran (*Gholami et al., 2019*).

2.2.4 Response Surface Methods

Response surface methods have been devised to overcome the computational limitations of Monte Carlo simulation (*Cox and Baybutt, 1981*). In these approaches, the complicated output function $Y = f(\alpha_1, \alpha_2, \dots \dots \dots \alpha_m)$ is replaced by an analytic approximation, $\tilde{Y} = R(\alpha_1, \alpha_2, \dots \dots \dots \alpha_m)$, called a response surface, where R is a linear combination of simple functions and the coefficients are derived from least square fitting. Once a response surface has been fitted, then Monte Carlo simulation can be used to establish the output probability distribution. The major advantage of this method is its computational economy. A reduced number of simulations is needed after fitting a response curve. However, it is difficult to obtain the desired accuracy in approximating the original output using a response curve.

The Derived Distribution method is an example of a response surface method. For about fifty years, an analytic version of the derived distribution approach has been applied to problems involving parameter uncertainty, where the functional dependence of the output parameter on the input parameter is known. Ang and Tang (*1975*) demonstrated that the approach directly mapped the probability density function of an uncertain input parameter onto that of an output parameter. By relating the uncertainty to the variance of the

input parameter around its mean value, it is then possible to estimate the propagated uncertainty from the variance of the output parameter. The method extends to all higher moment statistics, such as skewness, kurtosis, etc., and so provides a very useful way of examining the overall effect of parameter uncertainty on the system. A nice explanation of the analytical technique is given by Ramírez (*2005*) who illustrates the application of the technique to the function of a single variable, and compares its application to the derivation of effective discharge when discharge is a random variable whose probability is governed by a log-normal distribution against results obtained by Soar and Thorne (*2001*). The derived distribution approach assumes that the dependent (output) variable is either monotonically increasing or monotonically decreasing function of a single, continuous, independent (input) variable so that there is a unique inverse relationship between the output and input. This limitation is discussed later in the thesis.

The derived distribution approach is summarized (very briefly) as follows. First, an analytical expression is specified for the probability density function of the input parameter, with the variance representing uncertainty. Then, the cumulative distribution function of the input parameter is determined by integration, from which the cumulative distribution function of the output parameter is then evaluated through conservation of probability noting the functional relationship between the input and output. In the derived distribution approach, conservation of probability is expressed as "the likelihood that Y takes on a value on an interval of width $\mathrm{d}y$ centred on the value y is equal to the likelihood that X takes on a value in an interval centred on the corresponding value $x = g^{-1}(y)$ but of width $\mathrm{d}x = \mathrm{d}g^{-1}(y)$" (*Benjamin and Cornell, 1970).* After changing the variable of integration, the resulting cumulative distribution function of the output variable is differentiated to provide its probability density function.

Being direct, this method offers fast assessment of uncertainty propagation through model equations that are sufficiently simple and monotonic in relating input to output. The method has been quite widely applied by hydrologists

and water resources engineers. In a seminal paper, Eagleson (*1972*) derived the peak streamflow probability distribution for a kinematic flood routing model from input catchment and climate parameter PDF distributions, and found that the model gave results in good agreement with field observations from catchments in Connecticut, USA. Using a first-order approximation of annual precipitation yield, Eagleson (*1978*) used the derived distribution approach to determine the cumulative distribution function of annual yield from the cumulative distribution function of precipitation, and applied the approach to cases involving an arid climate (Santa Paula, California, USA) and a subhumid climate (Clinton, Massachusetts, USA). Later, Hebson and Wood (*1982*) obtained satisfactory agreement between derived and observed flood frequency distributions for two catchments in the Appalachian Mountains, USA. Díaz-Granados et al. (*1983, 1984*) obtained derived flood frequency distributions based on input distributions related to excess rainfall density, etc., for the Davisdon, Santa Paula Creek, and Nashua River catchments in the USA. Kurothe et al. (1997) extended the method to account for negative correlation between rainfall intensity and duration (previously assumed independent of each other) and demonstrated the method gave satisfactory results for the Davidson catchment, USA. Ramírez and Senarath (*2000*) used the derived distribution method to determine an expression for the probability density function of interception capacity that accounted for sub-grid scale variabilities in rainfall intensity and precipitation depth. The derived distribution approach was applied to flood prediction in a basin in Italy comprising 16 poorly gauged watersheds (*Brocchiola and Rosso, 2009*). Gottschalk and Weingertner (*1998*) used a similar approach to derive a peak flow distribution from the distribution of rainfall volume and runoff coefficient, and using a unit hydrograph. Chen and Adams (2007) used the derived distribution approach to develop an analytical stormwater quality model. Recently, Perona *et al*. (*2013*) obtained analytical expressions for probability distribution functions of optimally allocated river flows to human activity and the environment, using the derived distribution approach. Meier et al. *(2016*) estimated the probability distribution function of annual rainfall from short-term records and showed that

the derived distribution approach can be used for a such a dataset where information is missing for certain years.

Kreitmair (*2019*) and Kreitmair et al. (*2020*) proposed a numerical analogue of the derived distribution approach, which involved discretizing the cumulative probability distribution. They successfully applied the approach to the effect of uncertainty in bed roughness (expressed by the Manning coefficient) on tidal power estimates for idealized cases and the Pentland Firth.

2.2.5 Differential Sensitivity

The differential sensitivity method can be summarized as follows. Provided the input parameters $(\alpha_1, \alpha_2, \dots\dots\dots \alpha_m)$ are numerical constants, then sensitivity functions of the output function $Y = (x_1, x_2, \dots\dots\dots x_n;\ \alpha_1, \alpha_2, \dots\dots\dots \alpha_m)$ can be determined from the partial derivatives $\frac{\partial Y}{\partial \alpha_i}$, where $i = 1,2, \dots\dots m$ and $(x_1, x_2, \dots\dots\dots x_n)$ are the phase-space functions on which the sensitivity functions depend. These functions are calculated from associated linear equations, and the coefficients depend on the original function. Once the sensitivity functions are determined, they are combined with the input uncertainty to calculate the output uncertainty. However, this method is based on the relationship between output and input parameters, which may be unavailable in practical cases. The disadvantage of this method is that the calculation of sensitivity functions becomes computationally very expensive when the number of input parameters becomes large.

Fiorini et al. (*2020*) applied the differential sensitivity method to the Navier-Stokes equations and proposed an efficient way of determining the variance of the velocity field when input parameters are uncertain. Fiorini *et al*. derived sensitivity equations and used sensitivity as a proxy to variance. They compared their results with Monte Carlo simulation and found their proposed approach to be significantly more computationally efficient. Singler (*2005*) also

considered the Navier-Stokes equations, and found that sensitivity to a small disturbance could provide a predictive indicator of transition to turbulence.

2.2.6 Polynomial Chaos

Polynomial chaos methods greatly reduce or even remove the requirement of repetitive sampling that limits statistical sampling techniques like Monte Carlo simulation (see e.g. *Li et al.,, 2009*). Polynomial chaos methods were first introduced in the early 2000s (see e.g. *Ghanem and Spanos, 2003*; and *Xiu and Hesthaven, 2005*), and are very well documented in the literature, such as the book by Xiu (2010). The method can cope with a wide variety of stochastic variables, which represent the probability distribution function (*Lacor and Savin, 2018*).

The polynomial chaos method was established as a spectral representation of the uncertainty of random polynomials, denoted here as ξ with values in a set Γ. If u is a random variable related to a spatial variable x and time $t \geq 0$, then the polynomial chaos expansion is

$$u(x,t,\xi) = \sum_{i=0}^{P-1} c_i(x,t)\, \emptyset_i(\xi) \tag{2.1}$$

where c_i denotes the deterministic expansion coefficients, $\emptyset_i$ are N-variate polynomials and are functions of $\xi = (\xi_1, \xi_2, \ldots\ldots\ldots \xi_N)$ in which ξ_j represents a random variable with values in a set Γ_j, N is the number of input uncertainties (also known as the number of random dimensions) and P is the number of expansion factors. (*Lacor and Savin, 2019)*

The first step in the solution process is to choose polynomials $\emptyset_n$ that are orthogonal to the probability density function. The next step is to estimate the expansion coefficients c_n. Finally, statistical parameters are obtained directly from the polynomial chaos expansion. (*Yang et al., 2017)*

Polynomial chaos expansions have been applied in practical engineering problems, reducing the cost of computation in uncertainty quantification.

However, the computational cost is still high when polynomial chaos is used for design optimization. Also, when information about the input probability distribution is incomplete, then the polynomial chaos expansion method may no longer be suitable.

Polynomial chaos methods may be sub-classified as either non-intrusive or intrusive. Non-intrusive methods, as proposed by Xiu and Hesthaven (*2005*) and Mishra *et al*. (*2012*), involve repeated runs of a deterministic model using different input values, and then constructing a stochastic solution from the outputs using interpolation and quadrature. Intrusive stochastic Galerkin methods have lower computational cost in that they determine the stochastic moments of the numerical solution through a single simulation of deterministic equations derived in stochastic space using a Galerkin projection, as has been shown by Elman *et al*. (2011).

Generalized polynomial chaos stochastic Galerkin methods have been widely applied in computational fluid dynamics. Examples include uncertainty propagation in shallow water flows by Ge at al. (*2008*) and Shaw and Kesserwani (*2020*), who achieved spectral convergence for cases involving a sufficiently smooth solution. Other applications include gas dynamics (*Hu and Jin, 2016*; *Shu et al. 2017*), disperse two-phase flow (*Jin and Shu, 2017*), and diffusion (*Xiu and Shen, 2009*). It should however be noted that Després et al. (*2013*) showed that generalized polynomial chaos stochastic Galerkin methods can involve complex eigenvalues that lead to loss of hyperbolicity when applied to nonlinear hyperbolic systems of conservation laws (such as can be the case in shallow flow models). Even so, the technique is appropriate to hyperbolic systems that are linear or involve scalar laws (*Xu, 2010*) or are symmetric (*Hu et al., 2015*). Poëtte et al. (*2009*) overcame this drawback by applying a global polynomial chaos approximation for entropic variables that are introduced alongside the conservative variables, but at considerable computational cost owing to the requirement to solve local minimization problems throughout the mesh at each time increment. Pettersson et al. (*2014*) also addressed the drawback, this time for Riemann solvers based on

Roe variables, again at increased computational burden (originating from having to solve a nonlinear equation system when switching between the Roe and conserved variables at each mesh interface at each time step).

Chertock et al. (*2015a,b*) have proposed operator-splitting versions of the stochastic Galerkin method which they applied to uncertainty propagation through the one-dimensional Euler equations for compressible flow and the one-dimensional Saint-Venant equations for shallow flow in the absence of bed roughness. The method involved separating the overall hyperbolic system into a linear system (solved using a generalized polynomial chaos stochastic Galerkin method) with adjunct nonlinear equations. Chertock et al.'s approach enables uncertainty propagation for the full range of flow conditions from subcritical to supercritical.

2.2.7 Stochastic Differential Equations

A stochastic differential equation is essentially a differential equation whose coefficients are either random numbers or random functions of independent variables (*Van Kampen, 2007*). Stochastic differential equations are appropriate for describing systems subject to external noise, and form the basis of modern modelling tools applied in many different areas, including telecommunications, economics, finance, biology, and quantum theory (*Russo, 2006*).

A common example of a stochastic differential equation arises from modelling an underlying asset price with geometric Brownian motion. Let $W(t)$ be Brownian motion and the asset price $S(t)$ be a stochastic process. Then the stochastic differential equation for the process $S(t)$ is

$$\frac{\mathrm{d}S(t)}{S(t)} = \mu \mathrm{d}t + \sigma \mathrm{d}W(t); \qquad S(t_0) = S_0 \tag{2.2}$$

where *t* is time, μ is a term related to drift, σ relates to volatility, t_0 is the initial time, and S_0 is the initial asset price. Most stochastic differential equations do not have closed-form solutions; instead, they are solved numerically using the

finite difference method, Monte Carlo Simulation, or the Tree method for specified initial condition (*Hull, 2018*).

Jiang (*1998*) used an Ito stochastic differential flood routing equation with random input term to estimate the uncertain reservoir level hydrograph and hence evaluate the risk of dam overtopping failure. Dai *et al*. (2018) applied the stochastic differential equation method to flood risk analysis. First, they calculated uncertainties in the inflow forecast, the reservoir discharge capacity curve, and the reservoir storage curve. Then, they evaluated the mean and variance of the water level at each time step. Finally, they estimated the flood risk and determined the impact of parameter uncertainty on flood-control reservoir operation. Chen *et al*. (2020a) used a stochastic differential equation for flood routing. They also calculated flood risk, and proposed an improved risk-assessment model for reservoir flood-control operation.

2.3 Discussion

The foregoing sections have described different types of uncertainty analysis methods, and examined how and where they have been applied (mainly in the context of hydraulic and hydrological engineering). The method selected by researchers has depended on the actual problem, the goal of the research, and the type of data available. Monte Carlo simulation appears to be the most widely used in uncertainty estimation because of its ease of application and general robustness; nevertheless, Monte Carlo simulation involves huge number of computations. Several of the other methods mentioned here (response surface, stochastic differential equations, and differential sensitivity) attempt to use Monte Carlo simulation more efficiently. Table 2.1 summarizes the advantages and disadvantages of the different methods.

Present day models used to simulate environmental processes, such as flow and sediment dynamics, are inherently robust. Large sets of non-linear partial differential equations are solved with these models. Depending on the size of domain, the number of vertical layers (if applicable) and the numerical solution technique, such tools can be very time-consuming even with the modern

computer technology. Thus, even though Monte Carlo simulation looks an appealing method for assessing uncertainty propagation through a coastal flood model for Bangladesh, its enormous computational overhead makes Monte Carlo simulation unfeasible for direct application in the present thesis. Instead, the response surface method, notably the derived distribution approach, offers a suitable option to reduce the computation time for uncertainty analysis, given that the relationship curve can be generated from the output of the physical process model. With only a few simulations, the probability distribution of the output parameter can be generated.

2.4 Concluding Remarks

From the foregoing, a numerical version of the derived distribution approach is selected for application to uncertainty propagation from several key input parameters to extreme water levels and sediment transport processes along the coast of Bangladesh. This is because of the relative ease of application, computational efficiency, and accuracy (as assessed for its analytical version) of the numerical version of the derived distribution approach. To the author's knowledge, this is the first time the derived distribution technique has been applied to parameter uncertainty propagation through the shallow water-sediment-morphodynamic equations in the context of Bangladesh.

Table 2.1: Comparison between different uncertainty propagation techniques

Method	Advantages	Disadvantages
Sensitivity Analysis	Straightforward technique (input parameter varying $\pm$ percent),	May not be efficient for complicated systems with a set of non-linear or stochastic equations
Stochastic models based on perturbation methods	Speedier calculation than Monte Carlo method	Complexity of analysis
Monte Carlo simulation	Applicable for all kind of risk assessment, no prerequisite of any relationship between the input and output parameters.	Huge number of simulations required, repetitive resampling requires running all the simulations from the beginning, extremely time-consuming, difficult to assess the influence of a single input parameter on the output parameter
Response surface	Computationally more efficient than Monte Carlo method, reduced number of simulations	Achieving desired may be difficult with the response curve for the output parameter
Differential sensitivity	Widely applicable, and computationally more efficient than Monte Carlo method	Large model and extensive process of code development

Polynomial chaos	Reduced time for computation.	Requires complete information of the input parameter, can be computationally expensive if repetitive sampling is needed (e.g. for design optimization)
Stochastic differential equations	Suitable for a system with external noise	Computationally expensive when numerically solved (using finite difference method, Monte Carlo simulation, etc.)

Chapter 3

Probability Distribution Transfer Methodology for Uncertainty Propagation Analysis

3.1. Introduction

In models of complex natural systems, the values of all independent, input variables are not always known with certainty. In such cases, uncertainty propagates from independent input variables to dependent output variables. If the functional dependence is known, or can be assumed to reasonable accuracy, then a probabilistic approach called the derived distribution approach can be used to determine the probability distribution of a dependent variable from that of an independent variable *(Ang and Tang, 1975).* This analytical approach has been effectively used by many researchers as mentioned in chapter 2, e.g. for flood frequency estimation (*Loukas, 2002*), flood prediction in a poorly gauged basin in Italy (*Brocchiola and Rosso, 2009*), stormwater quality modelling (*Chen and Adams, 2007b*), and variability in annual precipitation (*Meier et al., 2016*).

This thesis adopts an analogous approach to the Derived Distribution Approach, whereby probability distributions of independent and dependent variables are considered in discrete, rather than continuous, form. A similar discrete approach was adopted by Kreitmair et al. (*2019*) to estimate uncertainty propagation in tidal stream power assessment. To the author's

knowledge, this is the first time that the numerical analogue of the Derived Distribution Approach has been applied to maximum tidal elevations, flood inundation, sediment transport, and bed morphological change in the context of an actual large-scale bay subject to sea level rise.

3.2. Derived probability distribution

The following derivation is a summary of the original description of the derived probability distribution given by Ang and Tang (*1975).* Let us consider a function of a single random variable $Y = g(X)$. By definition, when $Y = y$ and $X = x$, then $x = g^{-1}(y)$ where g^{-1} is the inverse function of g. We assume that $g(x)$ has a unique inverse function $g^{-1}(y)$.

Let us assume that $g(x)$ has a unique inverse function $g^{-1}(y)$, and $g(x)$ is a monotonically increasing function. The probability distribution of a random variable is defined by its cumulative distribution function (CDF). Thus

$$F_Y(y) = Pr[Y \leq y] = Pr[X \leq g^{-1}(y)] = F_X[g^{-1}(y)] = F_X(x) \quad . \tag{3.1}$$

Now, if X is a discrete random variable, then its probability distribution is obtained from its probability mass function (PMF).

Hence,

$$p_Y(y) = p_X[g^{-1}(y)] \quad . \tag{3.2}$$

Thus,

$$F_Y(y) = \sum_{all\ x_i \leq g^{-1}(y)} p_X(x_i) \quad . \tag{3.3}$$

For continuous X, equation (3.1) leads to

$$F_Y(y) = \int_{x \leq g^{-1}(y)} f_X(x)\, \mathrm{d}x = \int_{-\infty}^{g^{-1}(y)} f_X(x)\, \mathrm{d}x \ . \tag{3.4}$$

Differentiating $x = g^{-1}(y)$ with respect to y, we get

$$\frac{\mathrm{d}x}{\mathrm{d}y} = \frac{\mathrm{d}g^{-1}}{\mathrm{d}y} \qquad [\because \mathrm{d}g^{-1} = \mathrm{d}g^{-1}(y)] \ .$$

Thus,

$$\mathrm{d}x = \frac{\mathrm{d}g^{-1}}{\mathrm{d}y}\mathrm{d}y \quad . \tag{3.5}$$

As $x \to -\infty,\ y \to -\infty$; and when $x = g^{-1}(y),\ y = g\left(g^{-1}(y)\right) = y$.

Replacing x and $\mathrm{d}x$ in equation (3.4),

$$F_Y(y) = \int_{-\infty}^{y} f_X(g^{-1}) \frac{\mathrm{d}g^{-1}}{\mathrm{d}y}\mathrm{d}y \quad . \tag{3.6}$$

Therefore, the Probability Density Function (PDF) of Y is

$$f_Y(y) = \frac{\mathrm{d}F_Y(y)}{\mathrm{d}y} = f_X(g^{-1}) \frac{\mathrm{d}g^{-1}}{\mathrm{d}y} \quad . \tag{3.7}$$

Now, let $g(x)$ be a monotonically decreasing function. If $y = -g(x)$, then $x = -g^{-1}(y)$. Thus equation 3.4 becomes

$$F_Y(y) = \int_{-\infty}^{-g^{-1}(y)} f_X(x)\,\mathrm{d}x \quad . \tag{3.8}$$

Substituting $x = -g^{-1}(y)$, we get

$$\frac{\mathrm{d}x}{\mathrm{d}y} = -\frac{\mathrm{d}g^{-1}}{\mathrm{d}y} \qquad [\because \mathrm{d}g^{-1} = \mathrm{d}g^{-1}(y)] \ .$$

Thus,

$$\mathrm{d}x = -\frac{\mathrm{d}g^{-1}}{\mathrm{d}y}\mathrm{d}y \quad . \tag{3.9}$$

As $x \to -\infty,\ y \to \infty$; and when $x = -g^{-1}(y),\ y = -g\left(-g^{-1}(y)\right) = y.$

Replacing x and dx in equation (3.8),

$$F_Y(y) = -\int_{\infty}^{y} f_X(g^{-1}) \frac{\mathrm{d}g^{-1}}{\mathrm{d}y}\mathrm{d}y = \int_{y}^{\infty} f_X(g^{-1}) \frac{\mathrm{d}g^{-1}}{\mathrm{d}y}\mathrm{d}y \quad . \tag{3.10}$$

Since the total probability is 1, we can write

$$\int_{y}^{\infty} f_X(g^{-1}) \frac{\mathrm{d}g^{-1}}{\mathrm{d}y}\mathrm{d}y = 1 - \int_{-\infty}^{y} f_X(g^{-1}) \frac{\mathrm{d}g^{-1}}{\mathrm{d}y}\mathrm{d}y \quad . \tag{3.11}$$

Hence,

$$F_Y(y) = 1 - F_X(g^{-1}) \quad , \tag{3.12}$$

and

$$f_Y(y) = \frac{\mathrm{d}F_Y(y)}{\mathrm{d}y} = -f_X(g^{-1}) \frac{\mathrm{d}g^{-1}}{\mathrm{d}y} \quad . \tag{3.13}$$

In equation (3.13), $\frac{\mathrm{d}g^{-1}}{\mathrm{d}y}$ is negative. So, the derived probability density function is

$$f_Y(y) = f_X[g^{-1}(y)] \left|\frac{\mathrm{d}g^{-1}(y)}{\mathrm{d}y}\right| = f_X(x) \left|\frac{\mathrm{d}x}{\mathrm{d}y}\right| \quad . \tag{3.14}$$

In general,

$$f_Y(y)|\mathrm{d}y| = f_X(x)|\mathrm{d}x| \quad . \tag{3.15}$$

So the probability of Y having a value within an interval of $|\mathrm{d}y|$ is equal to the probability of X having a value within an interval of $|\mathrm{d}x|$. Thus, if the PDF of X is known and a monotonic functional relationship between Y and X is available, then the PDF of Y can be determined with the help of equation (3.14).

3.3. Numerical probability transfer model

This thesis adopts the method of numerical transfer of probability density function (PDF) developed by Kreitmar (*2019*) who examined the influence of uncertainty in bed roughness co-efficient on estimates of hydro-kinetic power in a one-dimensional open channel. Kreitmar compared results from the numerical PDF transfer method with those from an analytic PDF transfer method and a Taylor expansion method. The results were in near perfect

agreement with each other (when the grid was sufficiently fine) for uncertainty propagation from bed roughness to power for turbines in an idealized strait. This method is highly advantageous in situations where the functional dependence of the output parameter on the input parameter is not known.

The numerical PDF transfer method is developed for cases where the probability distribution of the independent variable is described by discrete probability values within a truncated region, N.

The present thesis considers three distinct studies on uncertainty: i) the effect of underlying uncertainty in Manning's roughness parameter *n* on estimates of maximum water level, ii) the effect of uncertainty in floc size of cohesive sediment on statistics of bed morphology change rate, and iii) the influence of uncertainty in sea level rise on flood inundation. In these cases, the independent variables are Manning's roughness parameter, the floc size of cohesive sediment, and sea level elevation above a fixed datum. The forgoing parameters were used to provide input data to an established numerical model, Delft3D. Output from the numerical simulation was then used to establish the functional relationship between the independent and dependent variables.

Let us consider the first case. Here, Manning's roughness parameter *n* is assumed to be normally distributed with mean μ_n and standard deviation σ_n, such that.

$$f(n|\,\mu_n, \sigma_n^2) = \frac{1}{\sqrt{2\pi\sigma_n^2}} e^{\frac{(n-\mu_n)^2}{2\sigma_n^2}} \quad . \tag{3.16}$$

The corresponding cumulative distribution function is

$$F(n|\,\mu_n, \sigma_n^2) = \frac{1}{\sqrt{2\pi\sigma_n^2}} \int_{-\infty}^{n_0} e^{\frac{(n'-\mu_n)^2}{2\sigma_n^2}} \, \mathrm{d}n'$$

$$= \frac{1}{2}\left[1 + \mathrm{erf}\left(\frac{n_0-\mu_n}{\sigma_n\sqrt{2}}\right)\right] . \tag{3.17}$$

The probability that the value of a realization of random variable n falls between n_A and n_B, where $n_A < n_B$, is

$$\Pr(n_A < n < n_B) = \int_{n_A}^{n_B} f(n|\,\mu_n, \sigma_n^2)\,\mathrm{d}n$$

$$= F(n_B) - F(n_A)$$

$$= \frac{1}{2}\left[\mathrm{erf}\left(\frac{n_B-\mu_n}{\sigma_n\sqrt{2}}\right) - \mathrm{erf}\left(\frac{n_A-\mu_n}{\sigma_n\sqrt{2}}\right)\right] . \qquad (3.18)$$

If the values of n are sufficiently finely spaced, then the likelihood of a value n_i being realised can be defined as the probability of n falling within the interval bounded by $n_{i-\frac{1}{2}}$ and $n_{i+\frac{1}{2}}$, such that

$$\Pr(n = n_i) = \Pr\left(n_{i-\frac{1}{2}} \leq n < n_{i+\frac{1}{2}}\right)$$

$$= \Pr\left(\frac{1}{2}\left(n_{i-\frac{1}{2}} + n_i\right) \leq n < \frac{1}{2}\left(n_i + n_{i+\frac{1}{2}}\right)\right)$$

$$= \frac{1}{2}\left[\mathrm{erf}\left(\frac{n_{i+\frac{1}{2}}-\mu_n}{\sigma_n\sqrt{2}}\right) - \mathrm{erf}\left(\frac{n_{i-\frac{1}{2}}-\mu_n}{\sigma_n\sqrt{2}}\right)\right] . \qquad (3.19)$$

By analogy with the derived probability distribution, the above equation also describes the associated probability of maximum water level Z, given that Z is a function of n. The expected value of Z can be calculated as

$$E[Z] = \sum_i Z_i(n = n_i)\Pr(n = n_i) \quad , \qquad (3.20)$$

and the variance is

$$\sigma_Z^2 = \sum_i (Z_i(n = n_i) - E[Z])^2 \Pr(n = n_i) . \qquad (3.21)$$

The higher order (m^{th} order) statistical moments are given by

$$\mu_m = \sum_i (Z_i(n = n_i) - E[Z])^m \Pr(n = n_i) , \qquad (3.22)$$

where $m = 3$ provides the skewness of the distribution (indicates asymmetry) and $m = 4$ gives the kurtosis (indicates tailed-ness or peakedness).

Similar procedures are used for the sea level rise and floc size cases in this thesis in chapter 6 and 7.

Importantly, the foregoing approach is applicable to any kind of probability distribution of an independent variable. In the absence of field data, we have chosen a truncated normal distribution for the Manning roughness parameter (that is commonly used as a calibration parameter in hydro-morphodynamic models of rivers, estuaries, and coastal waters). For other cases, where available, relevant data are extracted from literature and a best-fit distribution determined for the independent variable. In short, the Delft3D model is run for an input parameter with known or assumed probability distribution, the model output is collected, and then the PDF of the output parameter is determined using the above-mentioned approach. However, the output uncertainty is not fed back to the system. The thesis is aimed to estimate the PDF of an output parameter from a specific input PDF, and thus no feedback process is necessary. The output uncertainty can be fed back for further research where the impact of this output uncertainty on some other parameter is to be calculated.

The detailed procedure is as follows:

i. Carry out numerical simulations and tabulate results for input parameter x against output parameter *y*. Use a cubic spline to obtain interpolated values. Plot *y* against x.
ii. Select mean μ_x and standard deviation σ_x of the input parameter data.
iii. Select a standard probability distribution (e.g. normal distribution) and plot:

    - Probability density function, PDF $p(x)$
    - Cumulative density function, CDF $c(x)$.

iv. Check the results by calculating the expected value $E[x]{\sim}x$ and variance, $Var[x]{\sim}\sigma_x^2$.

v. Divide the PDF and CDF into a prescribed number i_{max} of bins, ensuring that the probabilities are always positive-valued.

vi. For each bin from $i = 1,2\ldots, i_{max}$ determine the middle value x_i. Use the relationship between *y* and x to determine corresponding y_i

vii. Determine CDF values $c(x)_{i-1/2}$ and $c(x)_{i+1/2}$ at either end of the bin, and hence determine the probability $Pr_i = c(x)_{i+1/2} - c(x)_{i-1/2}$.

viii. Calculate expected value of the output parameter from $E[y] = \sum_{i=1}^{i_{max}} Pr_i\, y_i$.

ix. Calculate variance in output parameter from $Var[y] = \sum_{i=1}^{i_{max}} Pr_i(y_i - E[y])^2$.

x. Calculate skewness from $Skew[y] = \sum_{i=1}^{i_{max}} Pr_i(y_i - E[y])^3$.

xi. Calculate kurtosis from $Kurt[y] = \sum_{i=1}^{i_{max}} Pr_i(y_i - E[y])^4$

xii. Determine output values at either end of each bin, $y_{i-1/2}$ and $y_{i+1/2}$, for $c(x)_{i-1/2}$ and $c(x)_{i+1/2}$ using the relationship between y and x. Hence determine bin widths, $\Delta y_i = y_{i+1/2} - y_{i-1/2}$.

xiii. Determine PDF for y as $p(y)_i = \frac{Pr_i}{\Delta y_i}$ and plot $p(y)_i$ against y_i for $i = 1,2\ldots, i_{max}$ (figure 3.1).

xiv. Hence determine CDF of y by numerical integration, $(y)_i = \sum_{i=1}^{i_{max}} p(y)_i\, \Delta y_i$, and plot $c(y)_i$ against y_i for $i = 1,2\ldots, i_{max}$. Whereas the bin widths Δx_i may each have the same value, the bin widths Δy_i will be different to each other if there is a non-linear relationship between y and x.

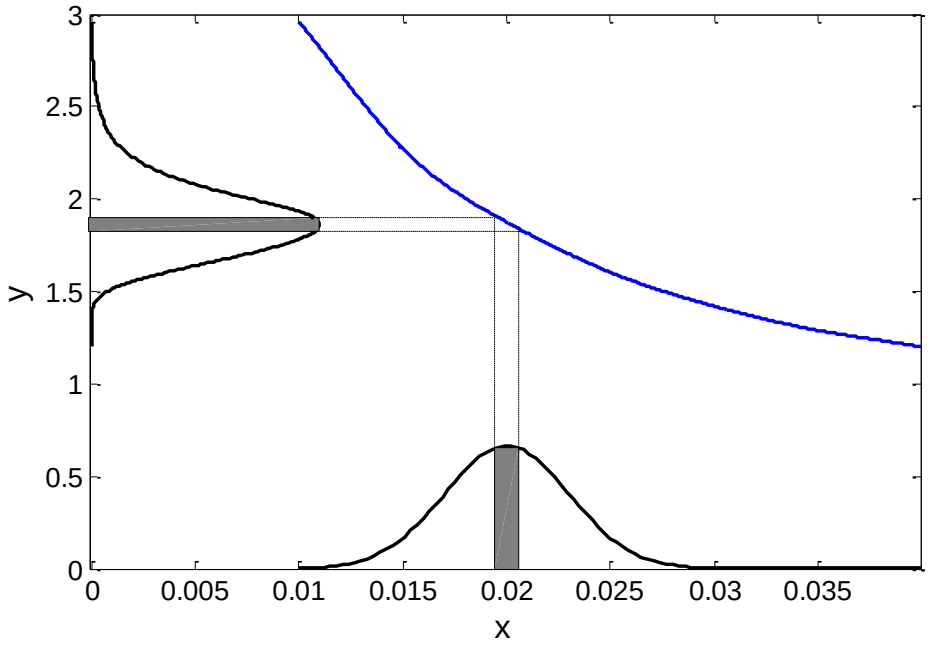

Figure 3.1: Probability density transfer from a PDF of x to a PDF of y through a function y = g(x).

3.4. Example

Let us consider a function $y(x)$ as follows:

$$y = ae^{-cx}, \quad x \geq 0 \ . \tag{3.23}$$

Here, the independent variable x is a realization of a random variable X.

Also, let the PDF of X be

$$f_X(x) = \alpha e^{-\alpha x}, \quad x \geq 0 \ . \tag{3.24}$$

Now, the CDF of Y can be expressed as

$$F_Y(y) = \int_{-\left(\frac{1}{c}\right)\ln\left(\frac{y}{a}\right)}^{\infty} \alpha e^{-\alpha x}\,\mathrm{d}x = \left(\frac{y}{a}\right)^{\alpha/c}, \quad 0 \leq y \leq a \ . \tag{3.25}$$

Then the PDF of Y can be derived as

$$f_Y(y) = \frac{\alpha}{ac}\left(\frac{y}{a}\right)^{\frac{\alpha}{c}-1}, \quad 0 \leq y \leq a, \quad \alpha, a, c \geq 0 \ . \tag{3.26}$$

Now, consider the case when $a = 5, \alpha = 2, c = 3$ and $0 \leq x \leq 1$. Figure 3.2 shows the resulting functional relation between x and y.

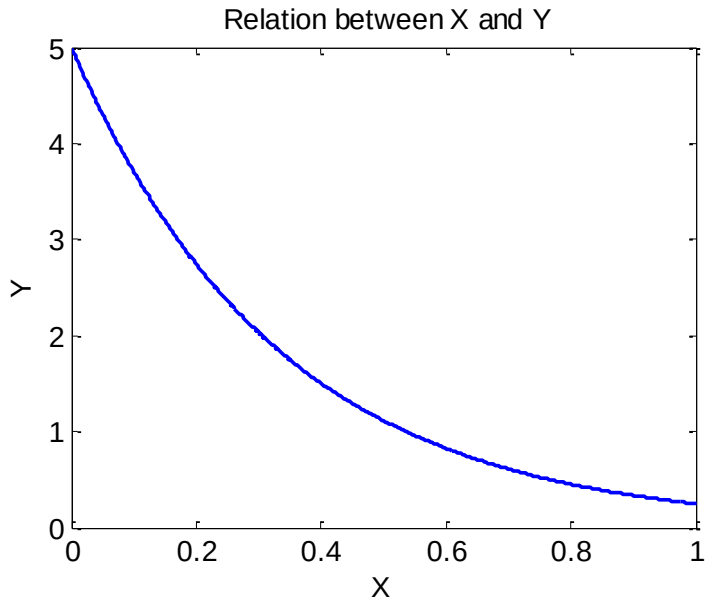

Figure 3.2: Example case: representation of the functional relationship between x and y, where $y = \alpha e^{-cx},\ x \geq 0, \alpha = 2,\ c = 3.$

Figure 3.3 displays the corresponding PDF of X.

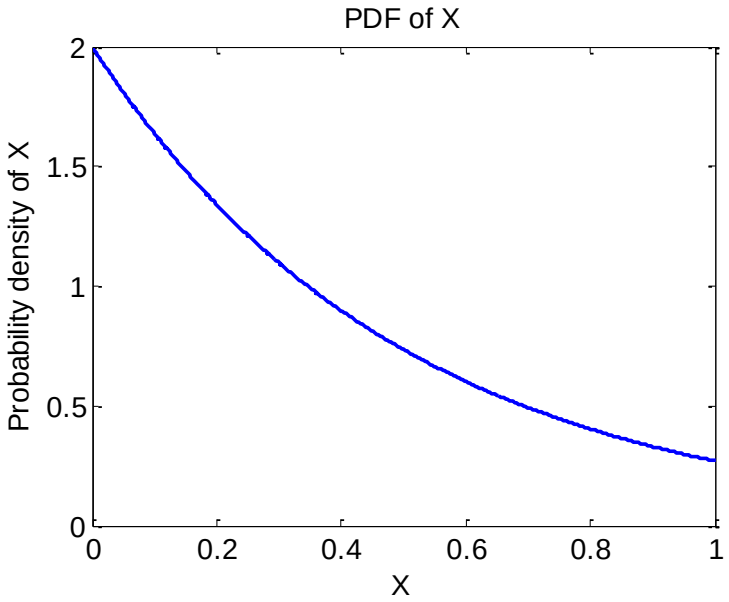

Figure 3.3: Example case: probability density function of X.

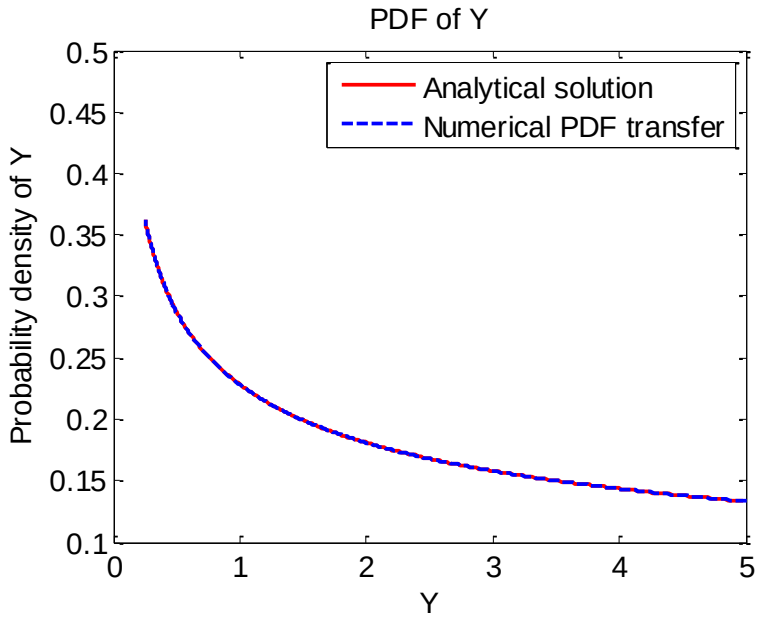

(a)

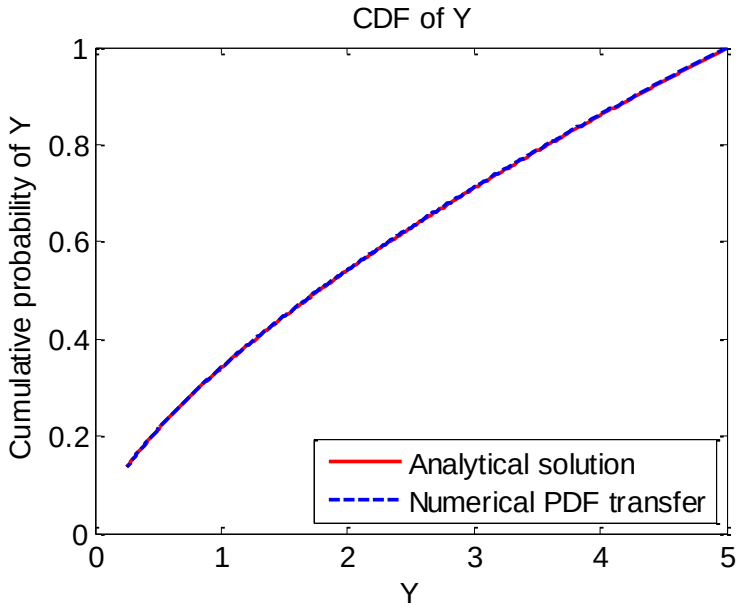

(b)

Figure 3.4: Example case: probability density function (PDF) and cumulative distribution function (CDF) of y.

Figure 3.4 superimposes the analytical solution for PDF of Y obtained using the derived distribution approach on the solution from the numerical transfer approach. For the numerical transfer approach, the PDF of X has been divided into 501 bins (a sufficiently large number to ensure convergence) and the PDF

and CDF of Y obtained using the procedure listed in Section 3.3. It can readily be seen that both solutions are in complete agreement with each other.

3.5. Concluding Remarks

The discrete derived distribution approach offers two major advantages. First it is very straightforward to apply in practice. Second, whereas Monte Carlo simulation requires a huge amount of computations, of the order O(10^5) or O(10^6) runs of a given code, the discrete derived distribution approach is computationally far more efficient requiring only a few runs of a process-based model provided a probability distribution is available for the independent (input) variable. By ensuring a sufficient number of bins are used during the discretization of the input probability distribution, the discrete derived distribution method has been shown in this chapter to generate an identical result to that from the analytical derived distribution method for a benchmark case. Using the discrete derived distribution approach, risk analysis can be conveniently undertaken for output parameters from deterministic models because establishing the functional between output and input parameters requires very few simulations, and can be refined easily using cubic spline interpolation. The derived distribution method is invariably successful for monotonically decreasing or increasing (continuous or discrete) functions, where $\left|\frac{\mathrm{d}x}{\mathrm{d}y}\right| > 0$ according to equation 3.14. However, the derived distribution approach does have significant drawbacks, as follows. First, from equation 3.14, it can be seen that as $\mathrm{d}y \to 0$, then $f_Y(y)$ becomes singular. Second, although the discrete derived distribution approach can be very efficient to apply in practice, it can be very complicated to obtain a derived probability distribution from distributions of multiple independent variables, particularly for high order non-linear systems.

Chapter 4

Conceptual Description of Delft3D-FLOW and Verification Tests

4.1. Introduction

Delft3D is a numerical model of free surface flows that is based on the finite-difference discretisation of the sigma-transformed mass and momentum equations. This computer software suite can carry out simulations of river and tidal flows, sediment transport, waves, water quality and changes to bed morphology *(Deltares, 2014)*. Of the available modules, Delft3D-FLOW lies at the heart of the three-dimensional simulation program. Lesser et al. (*2004*) described the following advantages of this module: *a)* non-equilibrium sediment concentration profiles are incorporated in the suspended sediment calculations, *b)* the density effects of sediment in suspension are included in the hydrodynamic calculations, and *c)* changes in bathymetry immediately feed back to the hydrodynamic calculations. The major disadvantages are: *a)* the first order upwinding scheme used to update the bathymetry which makes the bed changes inherently diffusive, *b)* the curvilinear co-ordinate system which creates difficulties in regenerating the bends and curves of the rivers and coastlines accurately in the model domain. A major consideration is that Delft3D is open-source software, and is accessible to users in developing countries which do not have the financial resources to purchase licenses for alternative commercial software.

4.2. Model formulation

4.2.1. Hydrodynamics

Delft3D-FLOW module solves the continuity and Navier-Stokes momentum equations for an incompressible fluid, with shallow water and Boussinesq assumptions. Vertical acceleration is neglected in the vertical momentum equation which is why the equation becomes the hydrostatic pressure equation. The vertical velocities are computed from the continuity equation. A set of partial differential equations is solved on a finite-difference grid in combination with an appropriate set of initial and boundary conditions *(Deltares, 2014).*

Delft3D-FLOW uses orthogonal curvilinear co-ordinates in the horizontal plane. Velocity components are normal to the cell faces of the curvilinear grid. The curvature terms are used in the equations of motion while grid transformation. In the vertical direction Delft3D-FLOW offers two different vertical grid systems: the *σ* co-ordinate system (*σ*-model) and the Cartesian *Z* co-ordinate system (*Z*-model). The hydrodynamic equations are valid for both systems *(Deltares, 2014).*

4.2.2. σ- co-ordinate system

The *σ* co-ordinate system is defined as:

$$\sigma = \frac{z-\zeta}{d+\zeta} = \frac{z-\zeta}{H} \tag{4.1}$$

Here, z is the vertical co-ordinate above a fixed datum in physical space, ζ is the free surface elevation above the reference plane (at z = 0), d is the depth below the reference plane, and H is the total water depth ($d+\zeta$) as shown in figure 4.1 *(Deltares, 2014).*

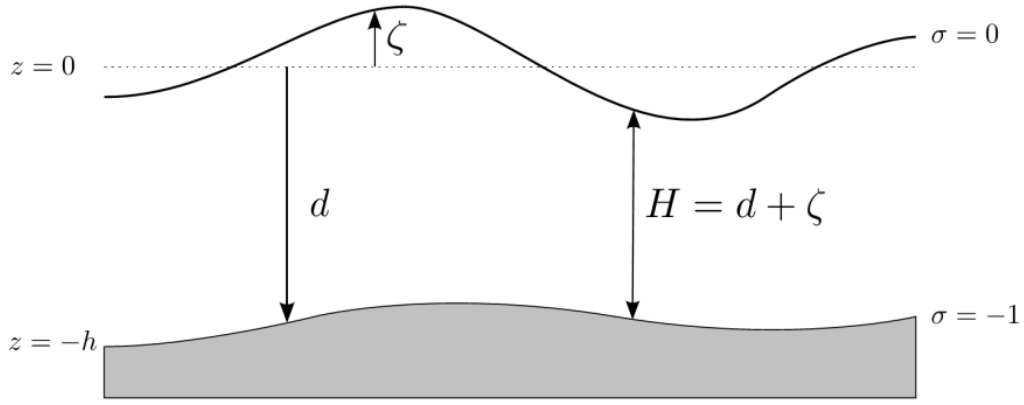

Figure 4.1: Definition of water level (ξ), depth (h) and total depth (H) (Deltares, 2014).

The σ grid is fitted so that is lies exactly between the bottom and the free surface. At the bottom σ = -1 and at the free surface σ = 0 (figure 4.2). It is assumed that the mapping is unique between the bed and free surface in the vertical direction (e.g.. there is no overturning of the free surface). The number of layers over the domain is constant and each layer is not strictly horizontal (owing to the mapping). The distribution of the layer thickness is non-uniform and allows more resolution near the boundary layers in the zones of interest. Thus it is possible to obtain a smooth representation of the topography.

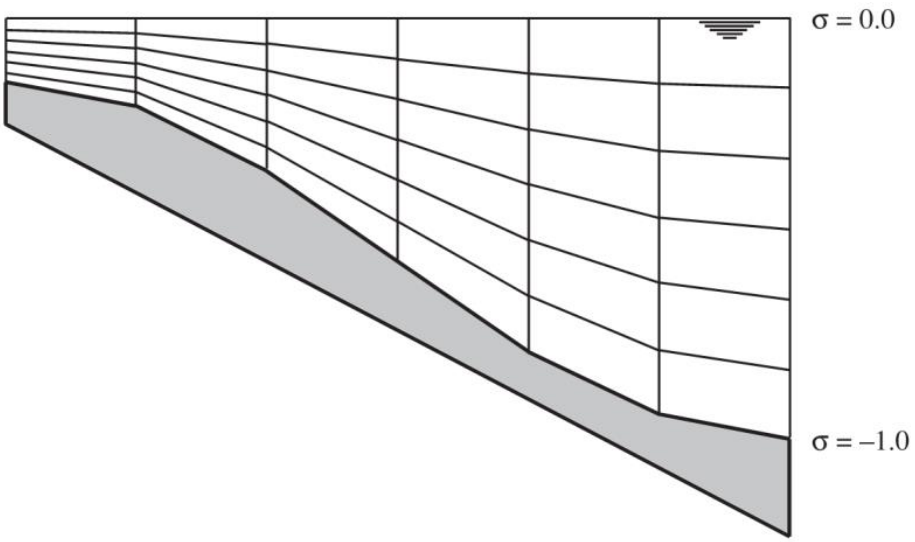

Figure 4.2: Example of σ grid (Deltares, 2014).

4.2.3. Cartesian co-ordinate system (vertical Z-model)

The *σ* grid is boundary fitted, but the *Z*-grid is not. The *Z*-grid is like a staircase (zig-zag boundary) where the free surface and the bottom surface are not considered as co-ordinate lines (figure 4.3). The co-ordinate lines of the *σ* grid intersect density interfaces which can cause significant errors in approximation of density gradients of stratified flow which are common in coastal seas, estuaries and lakes. The *σ* grid may not have enough resolution around the pycnocline, but the *Z*-grid has horizontal co-ordinate layers which are nearly parallel to density interfaces (which are particularly important in regions with steep bottom slopes). The use of *Z*-grid reduces the artificial mixing of scalar constituents such as salinity and temperature *(Deltares, 2014).*

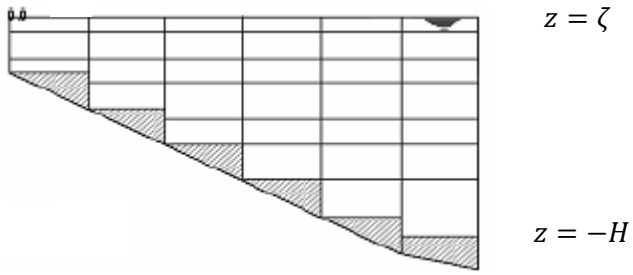

Figure 4.3: Example of Z-grid (Deltares, 2014).

4.2.4. Continuity equation

The continuity equation (depth-averaged) is obtained by integrating the continuity equation for an incompressible fluid ($\nabla \cdot \vec{u} = 0$) over the total depth, while accounting for the kinematic boundary conditions at water surface and bed level. The resulting equation is given by:

$$\frac{\partial \zeta}{\partial t} + \frac{1}{\sqrt{G_{\xi\xi}}\sqrt{G_{\eta\eta}}} \frac{\partial((d+\zeta)U\sqrt{G_{\eta\eta}})}{\partial \xi} + \frac{1}{\sqrt{G_{\xi\xi}}\sqrt{G_{\eta\eta}}} \frac{\partial((d+\zeta)V\sqrt{G_{\xi\xi}})}{\partial \eta} = (d+\zeta)Q. \quad (4.2)$$

Here, $\sqrt{G_{\xi\xi}}$ and $\sqrt{G_{\eta\eta}}$ are the Jacobian coefficients used to transform curvilinear to rectangular co-ordinates for ξ and η direction respectively, *U* and *V* are the depth-averaged velocities

$$U = \frac{1}{d+\zeta} \int_d^\zeta u \, dz = \int_{-1}^0 u \, d\sigma \quad . \tag{4.3}$$

$$V = \frac{1}{d+\zeta} \int_d^\zeta v \, dz = \int_{-1}^0 v \, d\sigma \, . \tag{4.4}$$

and *Q* is the contributions per unit area due to the discharge or withdrawal of water, precipitation and evaporation

$$Q = \int_{-1}^0 (q_{in} - q_{out}) \, d\sigma + P - E \, , \tag{4.5}$$

with q_{in} and q_{out} being the local sources and sinks of water per unit of volume [1/s] respectively, *P* being the non-local source term of precipitation and *E* being non-local sink term due to evaporation (*Deltares, 2014*).

4.2.5. Horizontal momentum equations

The momentum equations in ξ and η direction are given by:

$$\frac{\partial u}{\partial t} + \frac{u}{\sqrt{G_{\xi\xi}}} \frac{\partial u}{\partial \xi} + \frac{v}{\sqrt{G_{\eta\eta}}} \frac{\partial u}{\partial \eta} + \frac{w}{d+\zeta} \frac{\partial u}{\partial \sigma} - \frac{v^2}{\sqrt{G_{\xi\xi}}\sqrt{G_{\eta\eta}}} \frac{\partial \sqrt{G_{\eta\eta}}}{\partial \xi} + \frac{uv}{\sqrt{G_{\xi\xi}}\sqrt{G_{\eta\eta}}} \frac{\partial \sqrt{G_{\xi\xi}}}{\partial \eta} - fv =$$
$$- \frac{1}{\rho_0 \sqrt{G_{\xi\xi}}} P_\xi + + F_\xi + \frac{1}{(d+\zeta)^2} \frac{\partial}{\partial \sigma} \left(v_V \frac{\partial u}{\partial \sigma} \right) + M_\xi \quad . \tag{4.6}$$

and

$$\frac{\partial v}{\partial t} + \frac{u}{\sqrt{G_{\xi\xi}}} \frac{\partial v}{\partial \xi} + \frac{v}{\sqrt{G_{\eta\eta}}} \frac{\partial v}{\partial \eta} + \frac{w}{d+\zeta} \frac{\partial v}{\partial \sigma} - \frac{u^2}{\sqrt{G_{\xi\xi}}\sqrt{G_{\eta\eta}}} \frac{\partial \sqrt{G_{\xi\xi}}}{\partial \eta} + \frac{uv}{\sqrt{G_{\xi\xi}}\sqrt{G_{\eta\eta}}} \frac{\partial \sqrt{G_{\eta\eta}}}{\partial \xi} - fu =$$
$$- \frac{1}{\rho_0 \sqrt{G_{\eta\eta}}} P_\eta + + F_\eta + \frac{1}{(d+\zeta)^2} \frac{\partial}{\partial \sigma} \left(v_V \frac{\partial v}{\partial \sigma} \right) + M_\eta \quad . \tag{4.7}$$

Here, v_V is the vertical eddy viscosity coefficient, P_ξ and P_η are the pressure gradients, the forces F_ξ and F_η are the imbalance of horizontal Reynolds stresses, M_ξ and M_η are the contributions due to external sources and sinks of momentum *(Deltares, 2014).*

4.2.6. Hydrostatic pressure assumption

The hydrostatic pressure equation is obtained by assuming the vertical acceleration very small compared to the gravitational acceleration, i.e. when the buoyancy effects and sudden variations in the bottom topography are not taken into account. According to Deltares (*2014*), the expression is:

$$\frac{\partial P}{\partial \sigma} = -\rho g h \quad . \tag{4.8}$$

4.2.7. Transport equation

In Delft3D-FLOW module, advection diffusion equation is used to calculate the transport of dissolved substances and heat where source and sink terms are included to simulate discharges and withdrawals. A first-order decay process corresponding to an exponentially decreasing numerical solution is adopted.

The transport equation is as follows:

$$\frac{\partial (d+\zeta)c}{\partial t} + \frac{1}{\sqrt{G_{\xi\xi}}\sqrt{G_{\eta\eta}}}\left\{\frac{\partial\left[\sqrt{G_{\eta\eta}}(d+\zeta)uc\right]}{\partial \xi} + \frac{\partial\left[\sqrt{G_{\xi\xi}}(d+\zeta)vc\right]}{\partial \eta}\right\} + \frac{\partial \omega c}{\partial \sigma} =$$

$$\frac{d+\zeta}{\sqrt{G_{\xi\xi}}\sqrt{G_{\eta\eta}}}\left\{\frac{\partial}{\partial \xi}\left(D_H \frac{\sqrt{G_{\eta\eta}}}{\sqrt{G_{\xi\xi}}}\frac{\partial c}{\partial \xi}\right) + \frac{\partial}{\partial \eta}\left(D_H \frac{\sqrt{G_{\xi\xi}}}{\sqrt{G_{\eta\eta}}}\frac{\partial c}{\partial \eta}\right)\right\} + \frac{1}{d+\zeta}\frac{\partial}{\partial \sigma}\left(D_V \frac{\partial c}{\partial \sigma}\right) -$$

$$\lambda_d (d+\zeta)c + S. \tag{4.9}$$

with D_H the horizontal diffusion coefficient, D_V the horizontal diffusion coefficient, λ_d the first order decay process and S the source and sink terms per unit area (*Deltares, 2014*).

$$S = (d+\zeta)(q_{in}c_{in} - q_{out}c) + Q_{tot} \quad . \tag{4.10}$$

where, q_{in} is the discharge of water , q_{out} is the withdrawal of water and Q_{tot} is the exchange of heat through the free surface. The total horizontal diffusion coefficient D_H is defined by

$$D_H = D_{SGS} + D_V + D_H^{back} \quad . \tag{4.11}$$

Here, D_{SGS} is the diffusion due to the sub-grid scale turbulence model and D_H^{back} is a user-defined diffusion coefficient for the horizontal diffusion. This user-defined coefficient can be used for calibration and it is independent of the horizontal eddy viscosity (*Deltares, 2014*).

The vertical diffusion coefficient D_V is defined by

$$D_V = \frac{\nu_{mol}}{\sigma_{mol}} + \max\left(D_{3D}, D_V^{back}\right). \quad (4.12)$$

Here, D_{3D} is the diffusion due to turbulence model in vertical direction, ν_{mol} is the kinematic viscosity of water and σ_{mol} is either the (molecular) Prandtl number for heat diffusion or the Schmidt number for diffusion of dissolved matter (*Deltares, 2014*).

4.2.8. Boundary conditions

A set of initial and boundary conditions for water level and velocity is mandatory to get a mathematical problem with a unique solution using Delft3D-FLOW. The model domain needs to be enclosed by means of two types of boundary – closed and open. Open boundaries are introduced in a computational model to obtain a limited computational area so that the computational effort can reduced to an appropriate level. Moreover, the open boundaries are situated far away from the area of interest to avoid any unphysical flows across such boundaries arising from linear interpolation, disturbance caused by reflection of outgoing waves, etc. Velocity normal to closed boundary is set to zero (*Deltares, 2014*).

An open boundary can be set with water level, velocity or discharge data. Discharge and velocity directions are considered to be normal to the open boundary. The boundary conditions can be prescribed in one of three ways: a uniform profile, a logarithmic profile, and a 3D profile (i.e. each σ-layer specified) (*Deltares, 2014*).

Another way suggested by Roelvink and Walstra (*2004*) is to let the model predict the correct boundary condition by providing the water level gradient in

the alongshore direction. This type of boundary condition is called a Neumann boundary condition. Neumann boundaries can only be applied in cross-shore boundaries with an offshore water level boundary.

Noting that ω is the vertical velocity relative to the σ–plane, the impermeability of the free surface (σ = 0, or $z = \zeta$) and the bottom surface (σ = -1, or $z = -d$) is prescribed by the following kinematic conditions:

$$\omega|_{\sigma=-1} = 0 \text{ and } \omega|_{\sigma=0} = 0; \quad [\sigma \text{ co-ordinate system}]$$

$$\omega|_{z=-1} = 0 \text{ and } \omega|_{z=\zeta} = 0\ . \quad [Z \text{ co-ordinate system}]$$

The boundary conditions for the momentum equations at the sea-bed are:

$$\frac{\nu_V}{H}\frac{\partial u}{\partial \sigma}\Big|_{\sigma=-1} = \frac{1}{\rho_0}\tau_{b\xi}\ ; \tag{4.13}$$

$$\frac{\nu_V}{H}\frac{\partial v}{\partial \sigma}\Big|_{\sigma=-1} = \frac{1}{\rho_0}\tau_{b\eta}\ . \tag{4.14}$$

where, $\tau_{b\xi}$ and $\tau_{b\eta}$ are the components of the bed shear stress in the ξ and η directions respectively (*Deltares, 2014*).

In a similar manner, the free surface boundary conditions for the momentum equations are determined as:

$$\frac{\nu_V}{H}\frac{\partial u}{\partial \sigma}\Big|_{\sigma=-1} = \frac{1}{\rho_0}\,|\vec{\tau}_s|\cos\theta\ ; \tag{4.15}$$

$$\frac{\nu_V}{H}\frac{\partial u}{\partial \sigma}\Big|_{\sigma=-1} = \frac{1}{\rho_0}\,|\vec{\tau}_s|\sin\theta\ . \tag{4.16}$$

where θ is the angle between the wind stress vector and the local direction of the gridline η, and $|\vec{\tau}_s|$ is the magnitude of the wind-shear stress (*Deltares, 2014*).

For transport boundary conditions, it is assumed that the transport of dissolved matter is advection dominated. Therefore, it is necessary to specify the inflow transport boundary condition, and the outflow boundary condition should be

free. It is possible to use different sediment fractions with the transport boundary specified in each σ-layer (*Deltares, 2014*).

4.3. Sediment transport

4.3.1. Suspended sediment transport

3D transport of suspended sediment is calculated as follows:

$$\frac{\partial c^{(l)}}{\partial t} + \frac{\partial uc^{(l)}}{\partial x} + \frac{\partial vc^{(l)}}{\partial y} + \frac{\partial\left(w - w_s^{(l)}\right)c^{(l)}}{\partial z} - \frac{\partial}{\partial x}\left(\varepsilon_{s,x}^{(l)}\frac{\partial c^{(l)}}{\partial x}\right) - \frac{\partial}{\partial y}\left(\varepsilon_{s,y}^{(l)}\frac{\partial c^{(l)}}{\partial y}\right) - \frac{\partial}{\partial z}\left(\varepsilon_{s,z}^{(l)}\frac{\partial c^{(l)}}{\partial z}\right) = 0\ . \quad (4.17)$$

where, $\partial c^{(l)}$ is the mass concentration of sediment fraction (l) [kg/m^3]; u, v and w are the flow velocity components [m/s]; $\varepsilon_{s,x}^{(l)}$, $\varepsilon_{s,y}^{(l)}$ and $\varepsilon_{s,z}^{(l)}$ are the eddy diffusivities of sediment fraction (l) [m^2/s]; and $w_s^{(l)}$ is the (hindered) sediment settling velocity of sediment fraction (l) [m/s] (*Deltares, 2014*).

Although the computation of suspended sediment transport is similar to that of salinity and heat, there are some distinct characteristics of sediment such as the exchange of sediment between the bed and flow, the settling velocity of sediment under the action of gravity, the effect of sediment on local mixture density, etc. The formulations of these processes are different for sand and mud (*Deltares, 2014*).

The following equation given by Eckart (1958) is used to adjust the density of water with varying salinity, temperature and sediment concentration:

$$\rho = \rho_w \sum_{l=1}^{lsed} c_{vol}^{(l)}\left(\rho_s^{(l)} - \rho_w\right) \quad (4.18)$$

Here, ρ_w is the density of the water including salinity and temperature effects, $c_{vol}^{(l)}$ is the volumetric concentration of sediment fraction l, $\rho_s^{(l)}$ is the density of

solid particles for sediment fraction l, and $lsed$ is the total number of sediment fractions.

In salt water, the cohesive material flocculates and the flocs tend to settle at a higher rate than individual particles. The settling velocity of the sediment flocs is calculated as follows:

$$w_{s,0}^{(l)} = \begin{cases} \frac{w_{s,max}^{(l)}}{2}\left(1 - cos\left(\frac{\pi S}{S_{max}}\right)\right) + \frac{w_{s,f}^{(l)}}{2}\left(1 + cos\left(\frac{\pi S}{S_{max}}\right)\right), & \text{when } S \leq S_{max} \\ w_{s,max,}^{(l)} & \text{when } S > S_{max} \end{cases}$$

(4.19)

where, $w_{s,0}^{(l)}$ = the (non-hindered) settling velocity of sediment fraction(l), $w_{s,max}^{(l)}$ = WSM, settling velocity of sediment fraction(l) at salinity concentration S_{max}, $w_{s,f}^{(l)}$ = WS0, fresh water settling velocity of sediment fraction(l), S = salinity, S_{max} = maximal salinity at which WSM is specified (*Deltares, 2014*).

The settling velocity of non-cohesive material is computed following the method of Van Rijn (*1993*):

$$w_{s,0}^{(l)} = \begin{cases} \frac{(s^{(l)}-1)gD_s^{(l)2}}{18\nu}, & 65\ \mu\text{m} < D_s \leq 100\ \mu\text{m} \\ \frac{10\nu}{D_s}\left(\sqrt{1 + \frac{0.01(s^{(l)}-1)gD_s^{(l)3}}{\nu^2}} - 1\right), & 100\ \mu\text{m} < D_s \leq 1000\ \mu\text{m} \\ 1.1\sqrt{(s^{(l)}-1)gD_s^{(l)}}, & 1000\ \mu\text{m} < D_s \end{cases}$$

(4.20)

where, $s^{(l)}$is the relative density $\frac{\rho_s^{(l)}}{\rho_w}$ of sediment fraction(l), $D_s^{(l)}$ is the representative diameter of sediment fraction(l), ν is the kinematic viscosity coefficient of water [m^2/s] (*Deltares, 2014*).

Sediment exchange between the bed and the flow is calculated considering that the sediment source and sink are situated at the near-bottom layer completely above a reference height. This layer is referred to as kmx-layer. At each half time step, the quantity of sediment dropping out due to settling and the quantity sediment entering the flow due to vertical diffusion are computed (*Deltares, 2014*).

For non-cohesive sediment, Van Rijn (*1993*) suggested the following formula for reference height, a:

$$a = \min\left[max\left\{(AKSFAC)\, k_s, \frac{\Delta_r}{2}, 0.01h\right\}, 0.20h\right] \tag{4.21}$$

where, a is Van Rijn's reference height, $AKSFAC$ is a user-defined proportionality factor, k_s is a user-defined current-related effective roughness height, Δ_r is the wave-induced ripple height, and h is the water depth. Van Rijn's reference height, a is limited to a maximum of 20% of the water depth and it comes into effect in very shallow areas. The sediment transported below the reference height is considered as bedload transport and that transported above that height is treated as the suspended sediment transport.

The reference concentration is calculated either by the sediment transport formula or derived from the suspended sediment concentration rate. The default formula for reference concentration calculation is the van Rijn (1993):

$$c_a^{(l)} = 0.015\, \rho_s^{(l)}\, \frac{D_{50}^{(l)} \left(T_a^{(l)}\right)^{1.5}}{a \left(D_*^{(l)}\right)^{0.3}} \tag{4.22}$$

where, $c_a^{(l)}$ is the mass concentration at reference height a, $D_*^{(l)}$ is a non-dimensional parameter, $T_a^{(l)}$ is the non-dimensional bed-shear stress, $\rho_s^{(l)}$ is the specific density of sediment fraction (l) [kg/m^3]. The non-dimensional parameter $D_*^{(l)}$ is defined as

$$D_*^{(l)} = D_{50}^{(l)} \left[\frac{\left(s^{(l)}-1\right)g}{\nu^2}\right]. \tag{4.23}$$

The notations have their usual meanings mentioned in equation (4.23). The non-dimensional bed-shear stress is expressed by

$$T_a^{(l)} = \frac{\left(\mu_c^{(l)}\tau_{b,cw} + \mu_w^{(l)}\tau_{b,w}\right) - \mu_{cr}^{(l)}}{\mu_{cr}^{(l)}}. \tag{4.24}$$

Here, $\mu_c^{(l)}$ is efficiency factor for current, $\tau_{b,cw}$ is the bed shear stress due to current, $\mu_w^{(l)}$ is efficiency factor for waves, $\tau_{b,w}$ is the bed-shear stress due to waves, and $\mu_{cr}^{(l)}$ is the critical bed shear stress (*Deltares, 2014*).

The layer lying close to the bottom layer being completely above the van Rijn's reference height is mentioned as the *kmx*-layer in Delft3D-FLOW User Manual. Figure 4.4 shows the location of the *kmx*-layer. Sediment exchange between the bed and the flow of the water is calculated on the basis of source and sink terms in this layer. The sediment concentration below the *kmx*-layer is rapidly adjusted to the same concentration of the *kmx*-layer (*Deltares, 2014*).

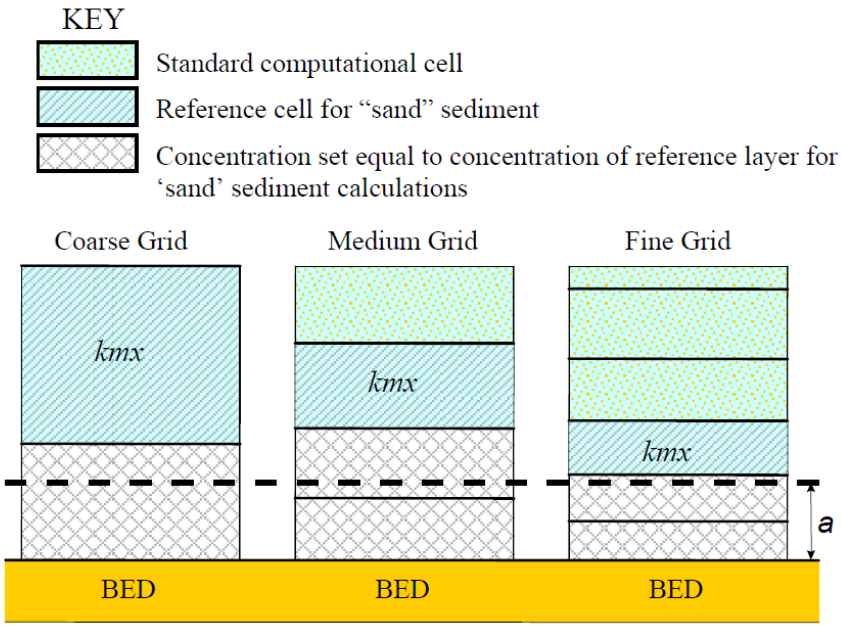

Figure 4.4: Location of the kmx-layer; a is Van Rijn's reference height (*Deltares, 2014*).

4.3.2. Bedload transport

In Delft3D-FLOW module, bedload transport is calculated for non-cohesive sediment of different sediment fractions. A selection of different formulae is provided for bedload transport computation. Of these, the Van Rijn (1993) formula is set as default. First, the magnitude and direction of bedload transport at the cell centre (water level points) are computed, then the transport rates at all the cell faces (velocity points) are determined using an upwind computational scheme, and finally the transport rates are corrected for the bed slope effect (figure 4.5) (*Deltares, 2014*).

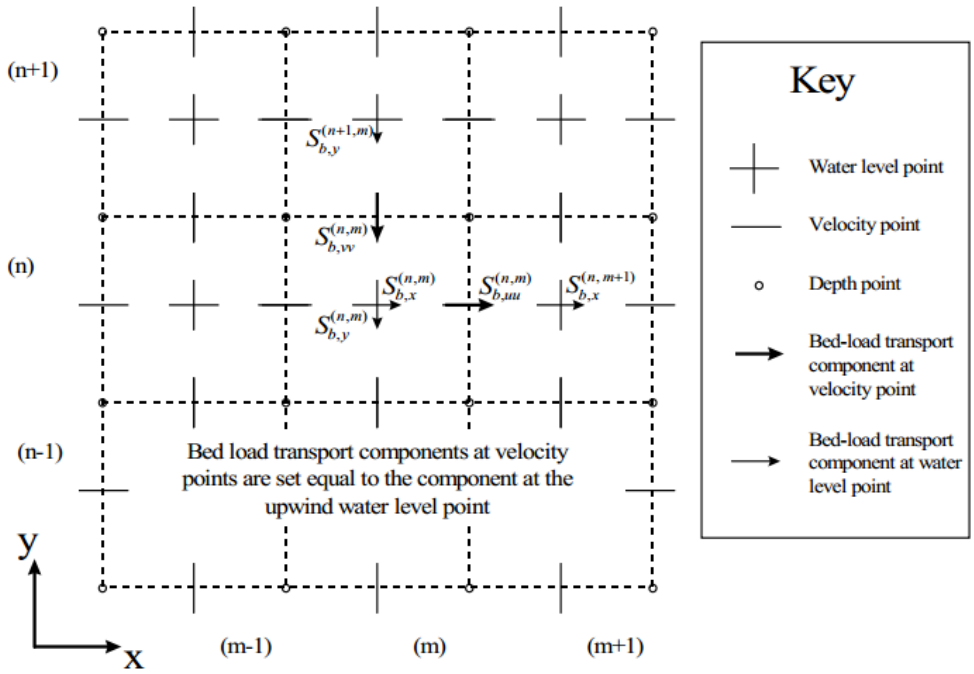

Figure 4.5: Setting of bedload transport components at velocity points (Deltares, 2014).

Some bedload transport formulae determine merely the magnitude of sediment transport. In such cases, the initial transport direction is assumed to be the same as the near-bed flow direction.

Bed level gradient has an influence on bedload transport. The effect of longitudinal bed slope (the slope in the initial direction of the transport) on the bedload transport rate is as follows:

$$\vec{S'}_b = \alpha_s \vec{S''}_b \tag{4.25}$$

Here, $\vec{S''}_b$ is the magnitude of the bedload transport vector before correction for bed slope effects, $\vec{S'}_b$ is the magnitude of the bedload transport vector after correction for bed slope effects, and α_s is the correction factor. The primary effect of transverse bed slope is to alter the direction of transport towards the downslope direction (*Deltares, 2014*).

Based on the work of Ikeda (1982), Van Rijn (1993) presented a further bedload transport vector:

$$S_{b,n} = |S'_b| \, \alpha_{bn} \left(\frac{u_{b,cr}}{|\vec{u}_b|}\right) \frac{\partial z_b}{\partial n} = |S'_b| \, \alpha_{bn} \left(\sqrt{\frac{\tau_{b,cr}}{|\vec{\tau}_b|}}\right) \frac{\partial z_b}{\partial n} \tag{4.26}$$

where $S_{b,n}$ additional bedload transport whose direction is normal to the unadjusted bedload transport vector, in the down slope direction, $|S'_b|$ is the magnitude of the unadjusted bedload transport vector $= \sqrt{\left(S'_{b,x}\right)^2 + \left(S'_{b,y}\right)^2}$, α_{bn} is a user-defined coefficient, $u_{b,cr}$ is the critical (threshold) near-bed fluid velocity, $\vec{u}_b$ is the near-bed fluid velocity vector, $\tau_{b,cr}$ is the critical bed shear stress, $\vec{\tau}_b$ is the bed shear stress due to current and waves, and $\frac{\partial z_b}{\partial n}$ is the bed slope in the direction normal to the unadjusted bedload transport (*Deltares, 2014*).

4.3.3. Morphological updating

The bed level is updated at every computational time step to provide the hydrodynamic flow calculations with updated bathymetry. The effect of sediment-transport gradient is taken into account along with sediment source-

sink terms. Change of bed level is calculated using the dry densities of different sediment fractions at the cell faces and cell centres (*Deltares, 2014*).

The change in the quantity of bottom sediments caused by the bedload transport is calculated using the expression:

$$\Delta_{SED}^{(m,n)} = \frac{\Delta t\,(f_{MORFAC})}{A^{(m,n)}} \left(S_{b,uu}^{(m-1,n)} \Delta y^{(m-1,n)} - S_{b,uu}^{(m,n)} \Delta y^{(m,n)} + S_{b,vv}^{(m,n-1)} \Delta x^{(m,n-1)} - S_{b,vv}^{(m,n)} \Delta x^{(m,n)} \right) . \quad (4.27)$$

where, $\Delta_{SED}^{(m,n)}$ is the change in quantity of bottom sediment by the bedload transport at location (m,n) [kg/m^2]; Δt is computational time step [s]; f_{MORFAC} is the user-defined morphological acceleration factor; $A^{(m,n)}$ is the area of computational cell at location (m,n) [m^2]; $S_{b,uu}^{(m,n)}$ and $S_{b,vv}^{(m,n)}$ are the computed bedload sediment transport vector components at u and v velocity points in the direction of u and v of the computational cell, respectively, at location (m,n) [kg/ms]; $\Delta x^{(m,n)}$ and $\Delta y^{(m,n)}$ are the cell dimensions (m,n) in the x and y directions, respectively [m] (figure 4.6) (*Deltares, 2014).*

Morphological developments occur at a much slower rate than typical flow changes. For example, tidal flows change in a couple of hours but morphological change in a coastline may occur over months, years, or decades. Delft-3D FLOW module offers an option to input a user-defined factor called f_{MORFAC} to accelerate bed level changes and incorporate them into the hydrodynamic calculations. This is done by simply multiplying the bed level changes by a constant factor, which results in an extension of morphological time step (*Deltares, 2014).*

$$\Delta t_{morphology} = (f_{MORFAC})\,\Delta t_{hydrodynamic} \quad (4.28)$$

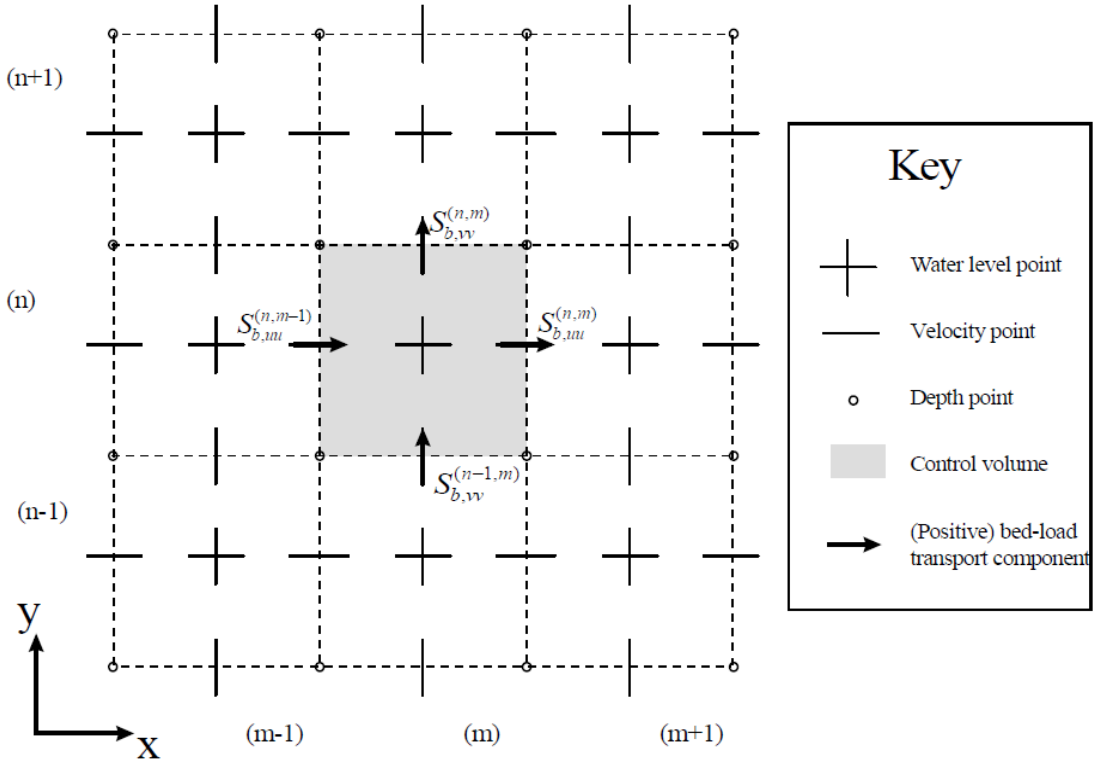

Figure 4.6: Morphological control volume and bedload transport components (Deltares, 2014)

The net sediment change due to suspended sediment transport is calculated as follows:

$$\Delta_{SUS}^{(m,n)} = (f_{MORFAC})(Sink - Source)\,\Delta t \quad . \tag{4.29}$$

where $\Delta_{SUS}^{(m,n)}$ is the sediment change due to suspended sediment, Sink and Source are the suspended-sediment sink and source terms (*Lesser et al., 2004*).

The correction for suspended sediment transported below the reference height, a, is calculated as follows:

$$\Delta_{COR}^{(m,n)} = \frac{\Delta t\,(f_{MORFAC})}{A^{(m,n)}}\left(S_{COR,uu}^{(m-1,n)}\Delta y^{(m-1,n)} - S_{COR,uu}^{(m,n)}\Delta y^{(m,n)} + S_{COR,vv}^{(m,n-1)}\Delta x^{(m,n-1)} - S_{COR,vv}^{(m,n)}\Delta x^{(m,n)}\right) \quad . \tag{4.30}$$

where, $S_{COR,uu}^{(m,n)}$ and $S_{COR,vv}^{(m,n)}$ are the suspended sediment correction vector components in the u and v directions, at the u and v velocity points of the computational cell at location (m,n). The total change in sediment is the sum of the change due to suspended load, the change due to the suspended load correction vector, and the change due to bedload. If there is more than one sediment fraction, then the calculation is repeated for all of them (*Lesser et al., 2004*).

4.4. Solution procedure

4.4.1. For hydrodynamics

DELFT3D-FLOW is a numerical model based on a finite difference spatial discretisation of the governing partial differential equations. The model domain is covered by a rectangular, curvilinear, or spherical grid. It is assumed that the grid is orthogonal and well structured. The variables are arranged in a pattern called the Arakawa C-grid (a staggered grid). In this arrangement, the water level points (pressure points) are defined at the cell centre; the velocity components are defined at cell faces in a direction perpendicular to the faces. After discretisation, the algebraic form of the continuity and momentum equations is converted into a series of equations in matrix-vector form (*Deltares, 2014).*

According to Stelling (*1984*), a robust solver for shallow water equation has to satisfy the followings:

- Robustness (unconditionally stable)
- Accuracy (at least second order consistency)
- Suitable for both time dependant and steady state problems
- Computationally efficient

An explicit time integration of the shallow water equations on a rectangular grid is subject to a time step condition based on the Courant number for wave propagation:

$$CFL_{wave} = 2\Delta t\sqrt{gH}\sqrt{\frac{1}{(\Delta x)^2}+\frac{1}{(\Delta y)^2}} < 1 \qquad (4.31)$$

Where Δt is the time step, g is the acceleration due to gravity, H is the total water depth, and Δx and Δy are the smallest grid spaces in the two directions of the physical space. In many practical cases, the time step needs to be sufficiently low to keep the CFL value within the limit. Otherwise the model will face instability which is not acceptable. An implicit method can overcome this problem. However, an implicit scheme can be uneconomic considering the storage and time needed if inversion of a large matrix is needed (*Deltares, 2014*).

An alternating direction implicit (ADI) method is used to integrate the continuity and horizontal momentum equations (*Leendertse, 1987*) forward in time. The advantage of this method is that the water levels and velocities are coupled along the grid line which leads to a system of equations of a small band width. The ADI method splits one time step into two stages and in both stages, all the terms of the equations are solved with at least second order accuracy in space. However, it is known from Benqué et al. (*1982*) and Weare (*1979*) that for flow along irregular closed boundaries, flow around islands, flow over tidal flats and flow through zigzag channels where the grid lines do not smoothly follow the geometry, the ADI method is inaccurate for Courant numbers larger than $4\sqrt{2}$.

4.4.2. For transport equation

Similar to the shallow water equation, a robust and accurate solver for scalar transport has to satisfy the following demands (*Deltares, 2014*):

- Mass conservation

- Monotony (positive solution)
- Accuracy (at least second order consistency)
- Suitable for both time-dependent and steady state problems
- Computationally efficient

An explicit time integration of the scalar advection-diffusion equation on a rectangular grid has a time step limitation based on the Courant number for advection:

$$C_{adv} = \max\left(\frac{u\Delta t}{\Delta x}, \frac{v\Delta t}{\Delta y}\right) \leq 1 \quad . \tag{4.32}$$

where Δx and Δy are the grid spaces in physical space (*Deltares, 2014*).

An explicit time integration of the vertical exchange terms on the σ co-ordinate grid leads to very severe time step limitations. To avoid this situation, a fully implicit integration method is applied, which is first order in time. The transport equation in Delft3D-FLOW is discretized with a mass conserving Finite Volume approach (*Deltares, 2014*).

4.5. Verification tests

Several verification tests were performed to confirm Delft3D's performance in simulating flooding and drying, bedload sediment transport, and suspended sediment transport. The results are compared against either an analytical solution or else results produced by another computer model.

4.5.1. Flow above parabolic bottom topography

This test was devised by Sampson et al. (*2006*) and has been used by many researchers (e.g. *Liang and Borthwick, 2009*) to verify one-dimensional wetting and drying. The bed profile is given by

$$z_b(x) = h_0\left(\frac{x}{a}\right)^2 \quad . \tag{4.33}$$

where, h_0 and a are prescribed constants, *x* is the distance in the direction of the wetting and drying motions over the parabolic bed, z_b is uniform in y-direction with zero slope. Sampson et al., (2005) presented an analytical solution for of the (*x*, *t*) nonlinear shallow water equations for flow above parabolic bottom topography where they considered linear bottom friction and neglected Coriolis force. Sampson et al.'s solution involved two parameters: the bed friction parameter, τ (which is related to bed friction coefficient, $C_f = h\tau\sqrt{u^2+v^2}$) and the hump amplitude parameter, p (here, $p = \sqrt{\frac{8gh_0}{a^2}}$). For $p > \tau$, the solution for water surface above a given horizontal datum is as follows:

$$\eta(x,t) = h_0 + \frac{a^2B^2e^{-\tau t}}{8g^2h_0}\left(-s\tau\,\sin 2st + \left(\frac{\tau^2}{4} - s^2\right)\cos 2st\right) - \frac{B^2e^{-\tau t}}{4g} - \frac{e^{-\tau t/2}}{g}\left(Bs\,\cos st + + \frac{\tau B}{2}\sin st\right)x\,, \tag{4.34}$$

where B is a constant, and $s = \sqrt{p^2-\tau^2}$. It is seen from this equation that when $t \to \infty$, then $\eta(x,t) \to h_0$, which is the still water depth. The projection of moving shorelines on the $x-y$ plane is two parallel straight lines:

$$x = \frac{a^2e^{-\tau t/2}}{2gh_0}\left(-Bs\,\cos st - \frac{\tau B}{2}\sin st\right) \pm a. \tag{4.35}$$

When $t \to \infty$, then $x \to \pm a$. So, the water moves back and forth; when $t \to \infty$ the motion dies out due to bottom friction, and the shorelines approach $x \to \pm a$.

In Delft3D, the computational model consists of a 100×10 grid covering the domain of horizontal dimensions $10{,}000$ m $\times$ 1000 m. The computational time duration is 4 hours and the time step is $0.001\ s$. Slip conditions are applied on the lateral walls. The bathymetry and the initial water level are generated using equation (4.33) and equation (4.34). The coefficients are $a = 3$ km, $h_0 = 10$ m, $B = 5$ m/s and $\tau = 0.001$ s^{-1}. Linear bed friction is assigned as an "Additional parameter" called "Filrgs" in Delft3D, which can be considered as

a rigid sheet that transmits the bed friction effect throughout the water depth causing loss of momentum.

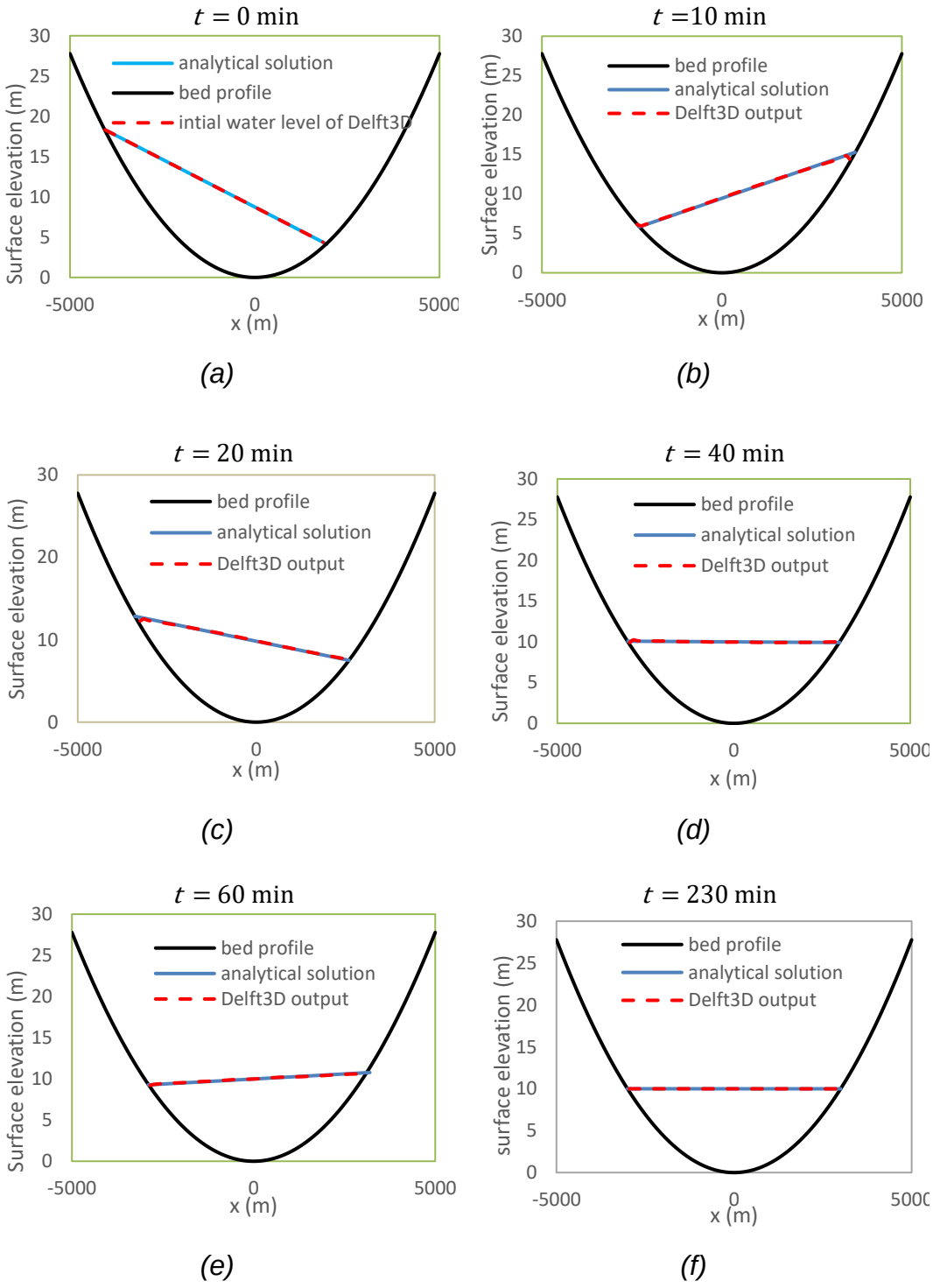

Figure 4.7: Wetting and drying in a parabolic basin: analytical and Delft3D numerically predicted water surface profiles at different times t = (a) 0 min, (b) 10 min, (c) 20 min, (d) 40 min, (e) 60 min, and (f) 230 min

Figure 4.7 shows the analytical and numerical free surface profiles at different times. It can be seen that Delft3D reproduces the moving water surface correctly, in excellent agreement with the analytical solution.

4.5.2. Dam-break wave propagating over three humps

A second case of flooding and drying is now considered. The case was initially proposed by Kawahara and Umetsu (*1986*), and has been widely utilised (see e.g. *Liang and Borthwick, 2009*). A dam-break wave propagates over a dry bed comprising of three humps. The model domain has horizontal dimensions $75\ \text{m} \times 30\ \text{m}$ which is discretised using a rectangular grid of 75×30 cells, each of 1 m x 1 m dimensions. Slip conditions are applied at the lateral walls. The bottom topography is defined as

$$z_b(x,y) = \max\left[\begin{array}{c} 0,\ 1-\frac{1}{8}\sqrt{(x-30)^2+\ (y-6)^2},\ 1-\frac{1}{8}\sqrt{(x-30)^2+\ (y-24)^2}, \\ 3-\frac{3}{10}\sqrt{(x-47.5)^2+\ (y-15)^2} \end{array}\right]. \tag{4.36}$$

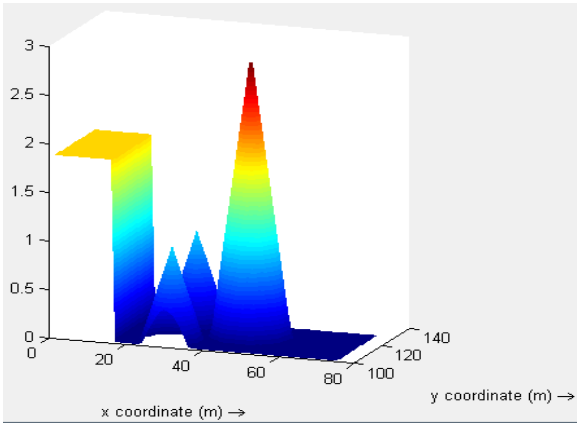

Figure 4.8: The initial condition of the model with the dam and three humps.

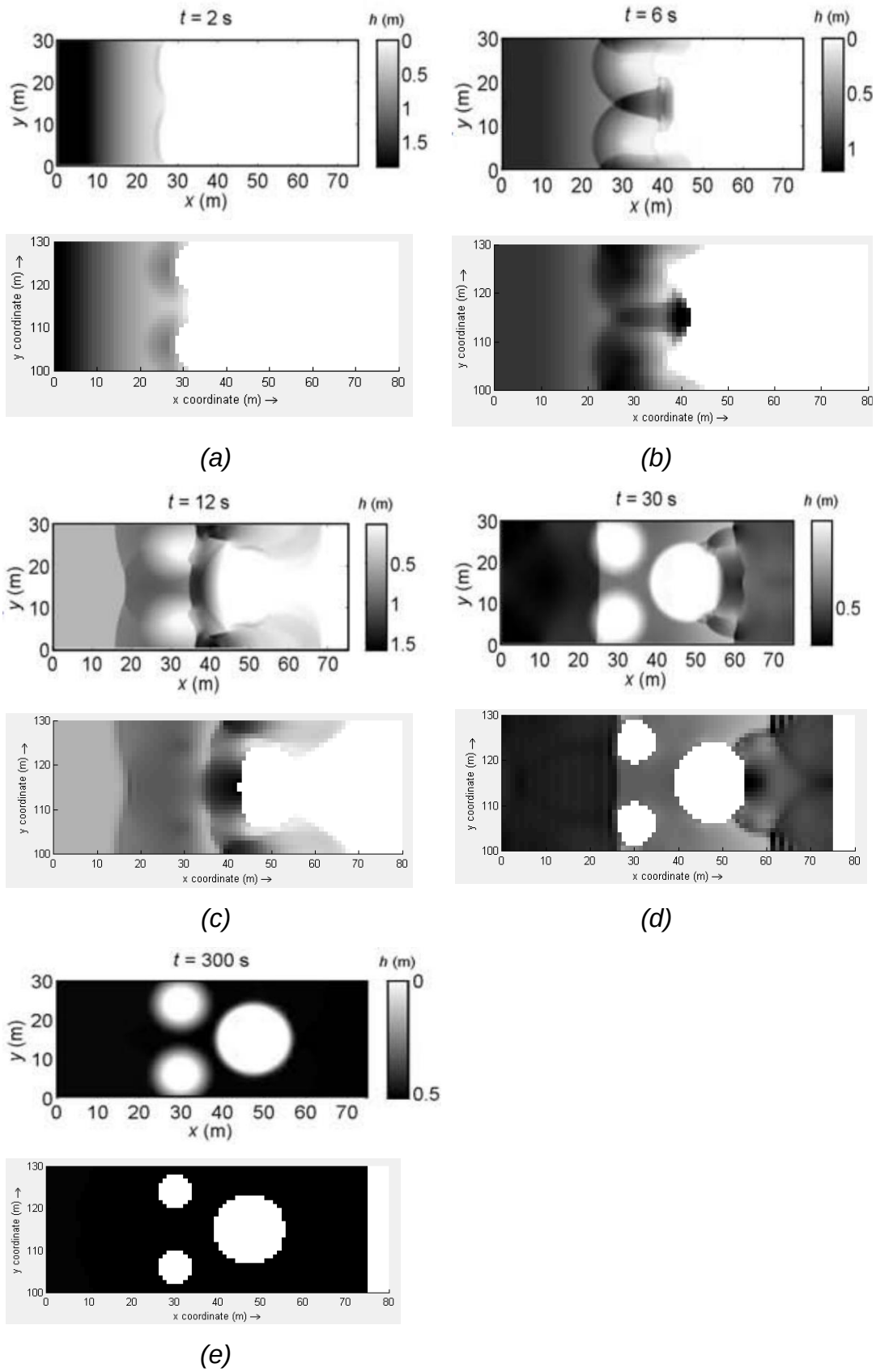

Figure 4.9: Dam-break wave propagating over the three humps.

Figure 4.8 shows the initial conditions, with a dam situated at $x = 16$ m with upstream water level retained by the dam of 1.875 m. The bed is initially dry downstream of the dam. The bed roughness is set with Manning's $n = 0.018$ s/m$^{1/3}$. The advection scheme for momentum used here in Delft3D is the "Flood" scheme which is preferable for absorbing shocks. The time step is 0.0005 s which is to be sufficiently small for stability in this scheme.

The dam collapses instantly at $t = 0$ and a flood wave starts to inundate the floodplain. At $t = 2$ s, the propagating wave begins to rise over the smaller humps; at $t = 6$ s, the wave reaches the toe of the large hump; and at $t = 12$ s, the flood water already passes the sides of that hump. Figure 4.9 shows that Delft3D generates similar results to that of Liang and Borthwick (*2009*).

4.5.3. Equilibrium condition of suspended sediment

This case was suggested by Lesser et al. (*2004*) who devised several tests for suspended sediment transport in an 8 m long straight flume. The water depth in the flume has a constant value of 5 m and the depth averaged velocity is 2 m/s. The commonly referred "Rouse" profile of suspended sediment concentration in equilibrium condition (with the assumption of constant sediment settling velocity and parabolic sediment mixing profile) is as follows:

$$\frac{c}{c_a} = \left[\frac{a(h-z)}{z(h-a)}\right]^{\lambda} \tag{4.37}$$

where λ is the suspension number $\frac{w_s}{\beta\kappa u_*}$, w_s is the settling velocity of the sediment, u_* is the bed shear velocity, κ is the von Kármán's constant (~0.4 for fluids), β is the ratio of sediment diffusion to fluid diffusion.

The model has 800 cells in the longitudinal direction and consists of 10 logarithmically spaced layers. The computational time step is 0.001 s. The duration of total computation time is 8 hours and during the first four hours, the model is run without sediment to stabilise the hydrodynamic condition. The bed slope is taken as 0.0032 with Chezy's C of 50 m$^{1/2}$/s, the dry bed

density is 2650 kg/m^3 with specific gravity 2.65, median sediment diameter D_{50} is 200 micron, and there is no sediment entering from the inflow boundary. Van Rijn's (*1993*) formula for sediment transport is used and bathymetry updating is not allowed. "Flood" advection scheme for momentum is chosen. The sediment concentration at 6 km from the upstream boundary is compared with the analytical Rouse profile. The results are shown in Figure 4.10. The computed result lies close to the analytical Rouse profile. The results from this test confirm that Delft3D correctly models equilibrium suspended sediment transport.

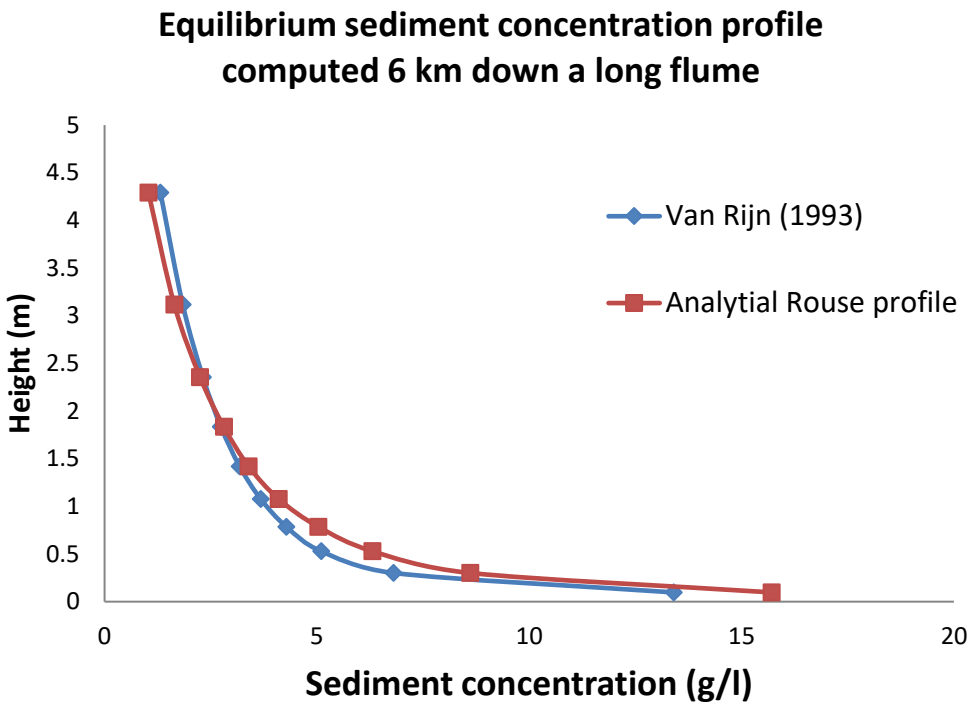

Figure 4.10: Analytical and Delft3D predicted equilibrium sediment concentration profiles computed 6 km from the inlet of a long flume.

4.5.4. 1D Bedload transport with a hump

The first case for bedload transport verification is selected from Huang et al. (*2008*). The bed of the open channel has an initial profile containing a hump of profile given by

$$h_b(x_0, 0) = \begin{cases} H \sin^2\left(\frac{\pi(x_0 - x_1)}{x_2 - x_1}\right) & if\ x_1 \le x_0 \le x_2 \\ 0 & \text{otherwise} \end{cases} . \quad (4.38)$$

This bed profile is obtained from Hudson and Sweby (*2003*) and Hudson et al., (*2005*). The movement of the hump is defined by $h_b(x,t) = h_b(x_0, 0)$, where,

$$x = x_0 + \frac{1}{t} D \begin{cases} \left[1 - \frac{H}{D} \sin^2\left(\frac{\pi(x_0 - x_1)}{x_2 - x_1}\right)\right]^{-(m+1)} \\ 1 \end{cases} . \quad (4.39)$$

Hudson and Sweby (2003) set the following parameter values: length of domain = 1000 m, $x_1 = 300$ m, $x_2 = 500$ m, $D = 10$ m, $H = 1$ m, initial discharge $q_0 = 10$ m^3/s/m, and $m = 3$. The model domain consists of 400 computational cells in the longitudinal direction. The computational time step is 0.01 s. Initial water level is set as 10 m. The specific gravity of the bed material is 2650 kg/m^3 and the median sediment diameter is 200 micron. First, the model is run for 10,800 s without sediment to get a stable hydrodynamic condition. Then the simulation is continued for a further 23,800 s with bedload sediment transport switched on and the bathymetry updated each time step. The sediment transport formula used here is given by Chesher et al. (*1993*) where the volumetric bedload sediment flux is defined as

$$q_b(x,t) = A\,[u(x,t)]^m \approx A {q_0}^m\,(D - h_b(x,t))^{-m} . \quad (4.40)$$

Figure 4.11 shows a comparison between the analytical solution and Delft3D output at the end of the simulation. There is reasonable match between these two except the underestimate of the peak elevation due to the upwind scheme in Delft3D being first order and so inherently diffusive. Neglecting the higher order terms in the equation results in acquiring lower peak of the hump from Delft3D simulation. Delft3D accepts this limitation because this represents more realistic scenarios in the estuaries and coasts. Theoretically, the peak should be conserved, but the stability of a soil hump also depends on many physical characteristics such as the rear slope of the hump, type of bed material, cohesion and internal friction, etc. This thesis focuses on the

suspended sediment and the settlement of the flocs of the cohesive sediment in particular (discusses in chapter 7), which is a different process from bedload transport. So, this thesis accepts this limitation but remains aware while analysing the results.

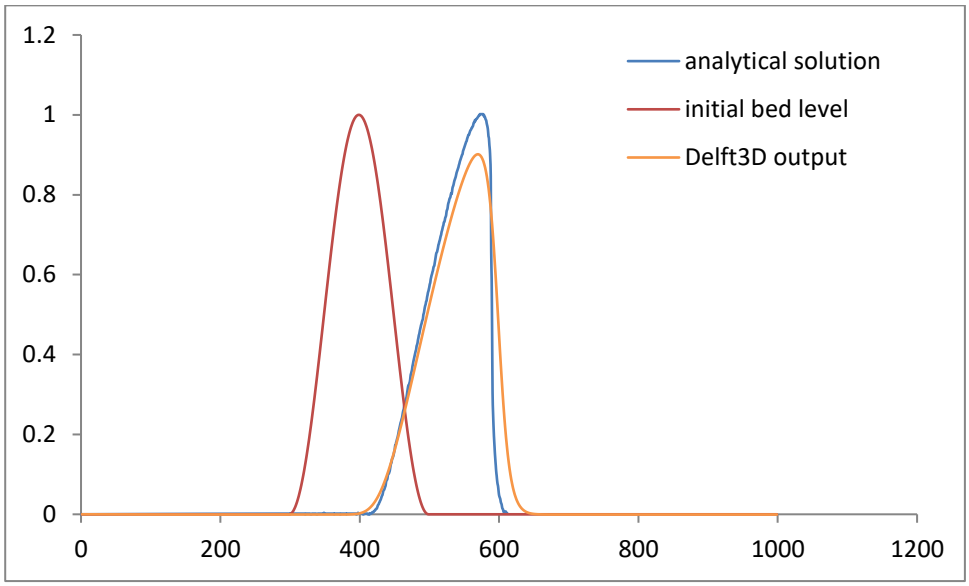

Figure 4.11: Analytical and Delft3D predicted bed profile with a hump.

4.5.5. 2D Bedload transport with a hump

This case was first proposed by de Vriend (*1987*). Later Lesser et al. (*2004*) used a very similar case as a validation test, with the initial bed profile given by (see *Huang, 2005*)

$$h_b(x,y)|_{t=0} = 5\exp\left(\frac{-(x-x_c)^2-(y-y_c)^2}{1300000}\right) . \quad (4.41)$$

where $h_b(x,y)$ is the bed surface elevation above a fixed horizontal datum, t is time, (x_c, y_c) is the location of the centre of the hump ($x_c = y_c = 5$ km), and (x,y) are the Cartesian distances measured horizontally along the channel and across the channel from the origin. The model domain consists of an east-west oriented rectangular channel which is 10 m deep, 10 km wide and 20 km long. A 200×100 horizontal computational grid is created for this domain.

The computational time step is 0.005 s. The initial water depth h is estimated as

$$h(x,y)|_{t=0} = 10 - h_b(x,y)|_{t=0} \quad . \tag{4.42}$$

The van Rijn (*1984a, 1984b*) formula is used for bedload sediment transport and suspended sediment transport. The median grain size of the sediment is 200 micron and the specific gravity of the bed material is 2650 kg/m^3. A flow of velocity of 1 m/s and an equilibrium sand concentration profile are imposed at the west boundary.

First, the model is run for 10 computational hours to obtain a stable hydrodynamic condition, then the model is run for a further 200 computational days with different morphological factors (20, 100 and 500 respectively). Figure 4.12 shows a comparison between the results obtained from Delft3D and from Huang (*2005*) who used an adaptive quadtree grid. It can be seen that the Delft3D results exhibit satisfactory agreement in that they follow the trend even with higher morphological factor; however, the Delft 3D results again underestimate the peak and predict greater spreading of the sediment than the output from Huang's quadtree grid model. This is a symptom of increased diffusivity in Delft3D due to the first-order upwinding of terms in the bed update equation (as explained in section 4.5.4).

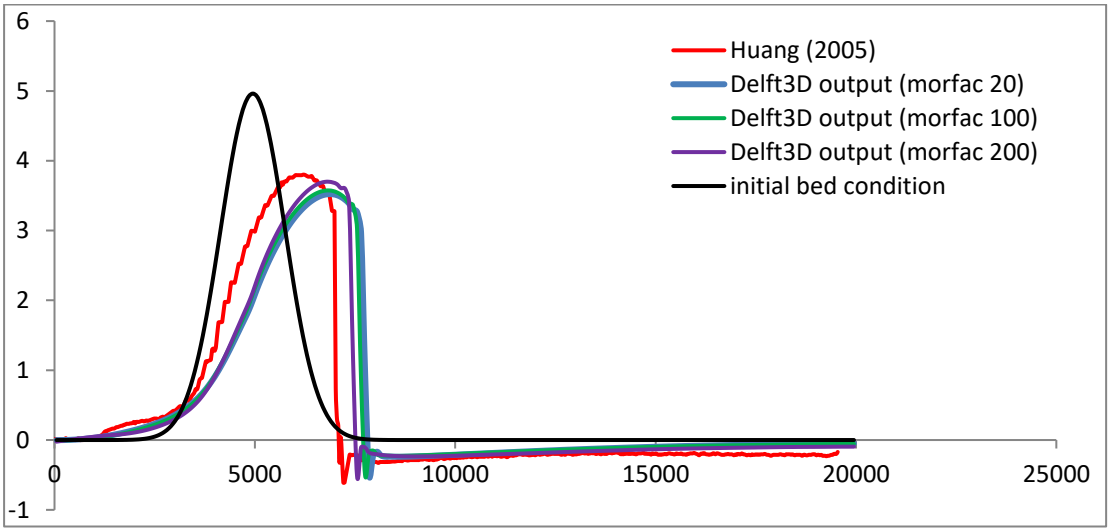

Figure 4.12: Predicted bed profile for an initial hump: Huang (2005) and Delft3D results.

4.6. Concluding Remarks

The major advantages of Delft3D simulation tool are that it is accurate, straightforward to apply, open source, and available without any monetary charge to users. Delft3D readily accommodates use of a user-defined equation, for example a sediment transport formula, through addition of sub-codes. The verification tests considered all gave satisfactory results. However, it should be noted that the the bedload transport test indicated that Delft3D produced more dissipative results than the analytical solution because of the first order differencing scheme in the bed sediment update equation in Delft3D. It was found that the morphological acceleration factor is advantageous for long term hydro-morphodynamic simulation in that it saves considerable computation resources while retaining accuracy. Evidence for this was provided by the verification test in section 3.5.5, where almost identical results were produced for both high and low values of the morphological acceleration factor. Lastly, it is worth noting that the Delft3D package contains several additional modules for waves, water quality, etc., and its availability as open source code, means that it is relatively easy to make future long-term enhancements to the model developed in this thesis.

Chapter 5

Effect of bed roughness uncertainty on estimation of maximum water levels around Meghna Estuary

5.1. Introduction

In hydraulic engineering, shallow flow solvers are widely used to predict hydrodynamics, sediment transport, and water quality in rivers, lakes, estuaries, and coastal basins. However, such models are prone to uncertainty, which can arise from inexact specification of the environment, physical and numerical model parameters, and model assumptions. One of the most important sources of uncertainty comes from assigning a value to the bed roughness (either as a non-dimensional coefficient, or in the form of the dimensional Chézy or Manning coefficients). In practice, the exact texture of the bed surface of a shallow flow domain is relatively unknown and it is very common to use the bed roughness coefficient as a tuning parameter, e.g. Western Scheldt estuary (*Dam et al., 2016*), Yangtze estuary (*Luan et al., 2017*), San Francisco bay (*Cloern et al., 2011*), etc. In flood risk assessment, the unknowns in bed roughness affect estimates of maximum water level, maximum flow speed, extent of inundation, sediment erosion and accretion, etc. This chapter examines how uncertainty, expressed as a fluctuation about a mean value, in Manning's roughness coefficient influences the expected value and higher order statistics of maximum water level.

5.2. Model set up

A two-dimensional depth averaged Delft3D model is set up for this study. The domain is shown in figure 5.1 and 5.2. The cell dimension of the curvilinear grid varies from 100 m in the estuary to 3400 m in the bay. Smaller cell size is provided where the location of interest is situated to reproduce the bathymetry and channel alignment correctly. This will minimise the errors in computation. The larger cell size is provided in the bay which is far away from the estuary and where the bathymetry is less complex.

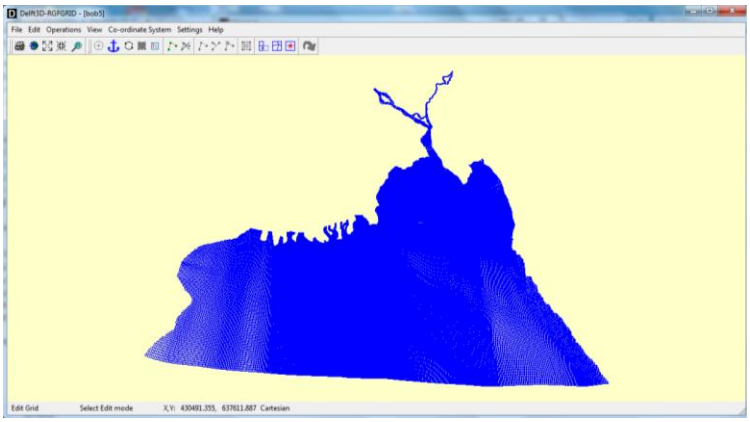

(a)

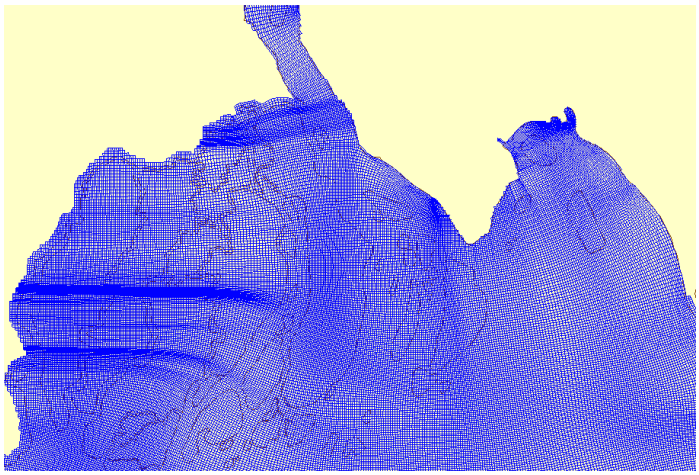

(b)

Figure 5.1: (a) The grid generated in Delft3D for model set up covering Meghna Estuary and the Bay of Bengal, (b) fractal coastal zone included in the grid.

The grid followed the riverbank and coastline as closely as possible, but for the fractal geometry along the coast comprising of multiple tributaries were extremely difficult to reproduce. At the end, the whole bay was taken under the grid, including the islands. This allows the wetting and drying of the islands and tidal flats without any constraint.

The geographical co-ordinate system followed in this thesis is Bangladesh Transverse Mercator (BTM). Bangladesh falls under two Universal Transverse Mercator (UTM) zones: 45N and 46N. Thus, the local co-ordinate system BTM is generally used by all relevant organizations in Bangladesh in order to avoid the complication of having two UTM zones. Land elevation data (SRTM data) are downloaded from Earthexplorer webpage by United States Geological Survey (USGS) *(Earthexplorer, n.d.)* and they are available in UTM co-ordinate system. The conversion of geographic co-ordinate system of these data from UTM to BTM is carried out using ArcGIS software *(Esri, n.d.)* with the parameters as specified below.

Geographic Coordinate System: GCS_WGS_1984
Angular Unit: Degree (0.0174532925199433299)
Prime Meridian: Greenwich (0.000000000000000000)
Datum: D_WGS_1984
Spheroid: WGS_1984
Semimajor Axis: 6378137.000000000000000000
Semiminor Axis: 6356752.314245179300000000

Geographic Coordinate System: Bangladesh Transverse Mercator (BTM)
Projection: Transverse_Mercator
False_Easting: 500000.000000
False_Northing: ¬2000000.000000
Central_Meridian: 90.000000
Scale_Factor: 0.999600
Latitude_Of_Origin: 0.000000
Linear Unit: Meter (1.000000)

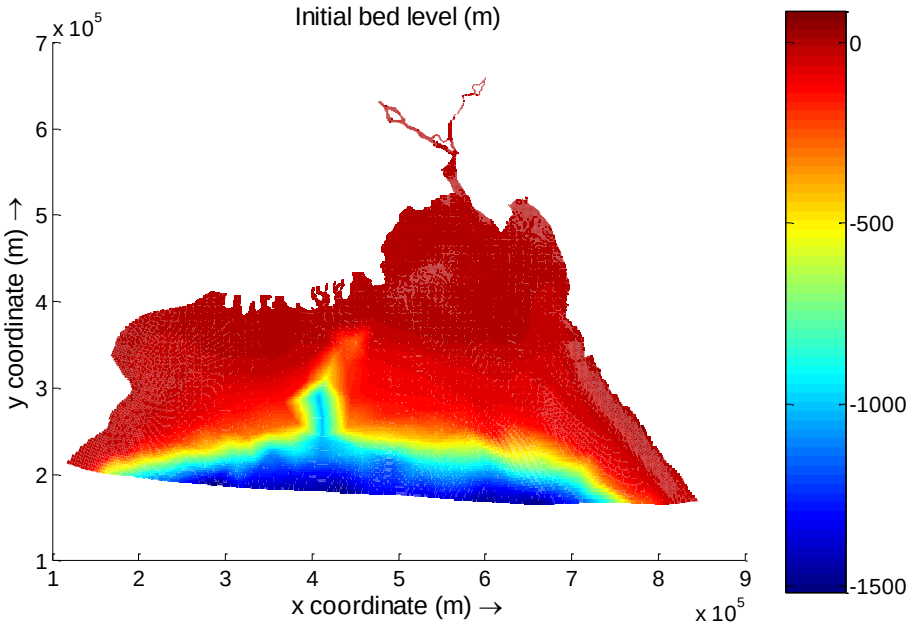

(a)

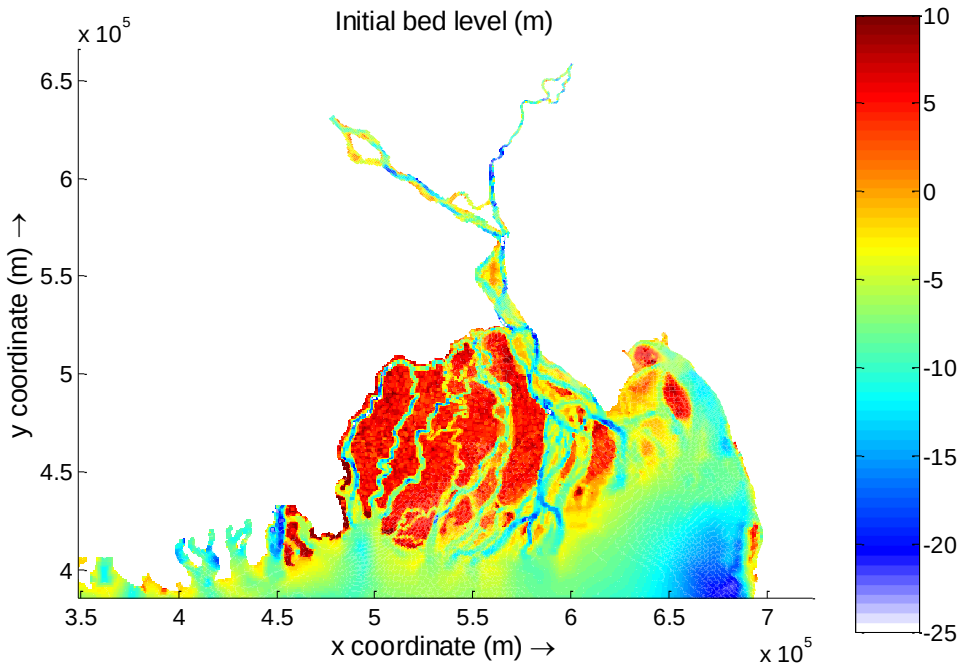

(b)

Figure 5.2: (a) Model domain with bathymetry of the Bay of Bengal and (b) Bathymetry of Meghna estuary (datum at present mean sea level). [Data: MophoFlood project, IHE Delft, The Netherlands].

The Delft3D model contained two upstream open boundaries carrying river discharge and one downstream open boundary with tidal constituents. For

simplification purposes, constant river discharge values were prescribed at both upstream boundaries. The Padma river (which is formed after Ganges and Brahmaputra met) flow input was set to 120,000 m^3/s and the Meghna river flow was set as 20,000 m^3/s. These river discharges represents the annual peak flood in the year 2007 as shown in figure 1.12. The bathymetry used in the model is from the year 2007-2008 (figure 5.2), so the river discharge of the same year is used in the model. Both the data were obtained from MorphoFlood project by IHE Delft, The Netherlands with their permission.

The downstream boundary contained M_2 and S_2 tidal components, which are dominant in the Bay of Bengal (discussed in section 1.5, and data in table 5.1). Table 5.1 provides the locations of the east and west ends of the offshore boundary. It also lists the representative amplitudes and phases, obtained from the TPXO 8.0 database using DelftDashboard tool. DelftDashboard is another tool from Deltares, The Netherlands (*Delftdashboard, n.d.*). It can be seen from Table 5.1 that among the eight major constituents, the M_2 and S_2 components have much larger amplitudes.

Table 5.1: Location of offshore open boundary and details of the tidal constituents.

East end (5.2178×10^5 E, 2.1655×10^6 N)			**West end** (-2.0422×10^5 E, 2.2103×10^6 N)		
Tidal constituents	Amplitude (m)	Phase	Tidal constituents	Amplitude (m)	Phase
M2	0.589	79.498º	M2	0.462	79.575º
S2	0.421	106.93º	S2	0.324	109.80º
N2	0.095	72.043º	N2	0.08	73.029º
K2	0.113	106.56º	K2	0.088	108.31º
K1	0.057	242.23º	K1	0.074	249.29º
O1	0.009	231.92º	O1	0.02	242.25º
P1	0.015	240.26º	P1	0.021	248.20º
Q1	0.002	251.57º	Q1	0.004	288.43º

Bed friction was incorporated as Manning's roughness parameter. In absence of field data about bed roughness, this thesis adopted the procedure described by Soulsby (*1997*) and Whitehouse (*2000*) to determine the range of Manning's *n.* The bed shear stress is

$$\tau_0 = \rho u_*^2 \quad , \tag{5.1}$$

where u_* is the friction velocity and ρ is density of water. Also, the depth-averaged velocity may be expressed using the log law as

$$\bar{u} = \frac{u_*}{\kappa}\left(\ln\frac{h}{z_0} - 1\right) \tag{5.2}$$

where h is water depth, z_0 is bed roughness length and κ is the von Kármán constant (~0.4). Values for depth-averaged velocity and water depth are obtained as simulation outputs from the hydrodynamic model. Then, z_0 in equation 6.4 can be replaced by the following equation:

$$z_0 = \frac{k_s}{30}\left[1 - \exp\left(\frac{-u_* k_s}{27\nu}\right)\right] + \frac{\nu}{9u_*} \quad , \tag{5.3}$$

where k_s is the Nikuradse roughness (= $2.5d_{50}$) and ν is kinematic viscosity of water. The friction velocity u_* is obtained by solving equations (5.2) and (5.3).

Now,

$$\tau_0 = \rho C_D \bar{u}^2 \quad , \tag{5.4}$$

which implies,

$$\rho u_*^2 = \rho C_D \bar{u}^2 \quad . \tag{5.5}$$

Hence, the drag coefficient is given by

$$C_D = \left[\frac{\kappa}{\ln\frac{h}{z_0}-1}\right]^2 \tag{5.6}$$

By definition,

$$C_D = \frac{g}{C^2} \tag{5.7}$$

where C is the Chézy coefficient. Furthermore,

$$C = \frac{R^{1/6}}{n} \tag{5.8}$$

where R is hydraulic radius and n is the Manning parameter. For very wide channels, $R \approx h$, and so,

$$n = \sqrt{C_D \frac{h^{1/3}}{g}} \quad . \tag{5.9}$$

Figure 5.3 shows the spatial map for Manning's parameter. It shows that Manning's *n* in Meghna estuary mostly falls between 0.02-0.03 s/m$^{1/3}$.

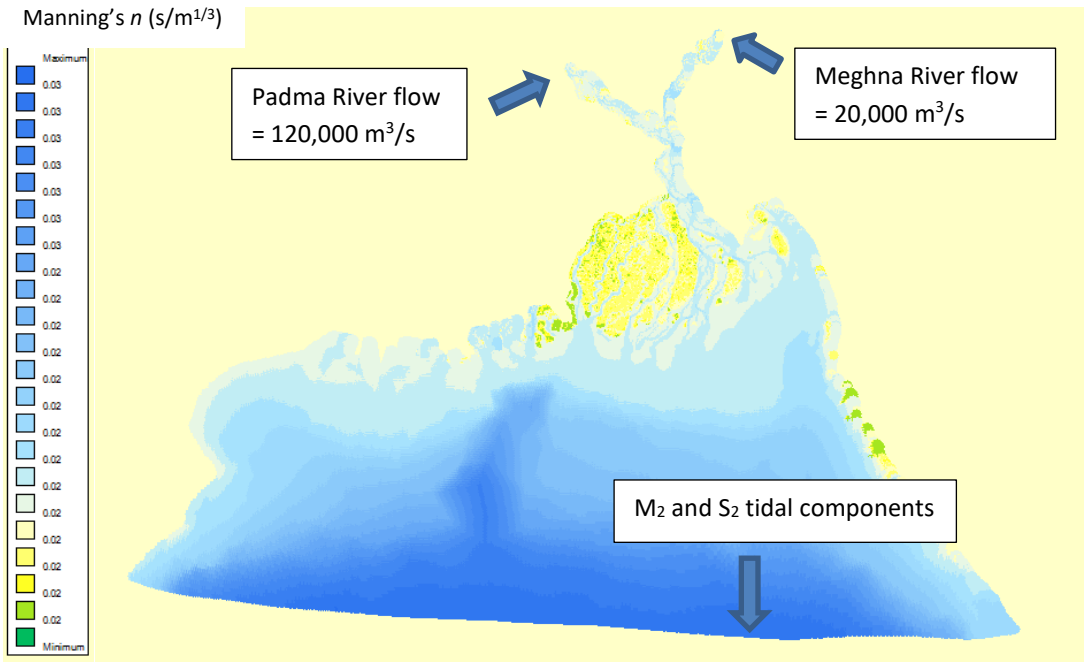

Figure 5.3: The spatial map of Manning's n calculated from Soulsby (1997) and Whitehouse et al. (2000). The arrows indicate the location of the open boundaries.

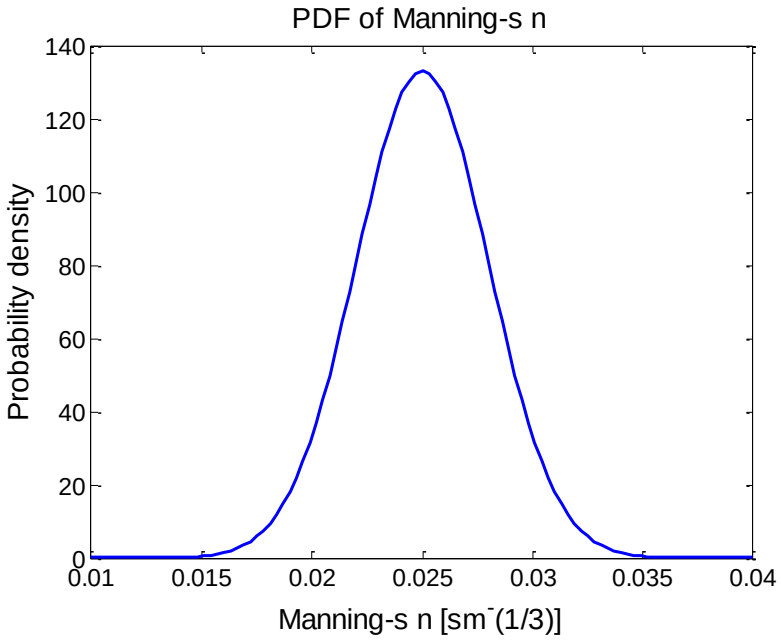

(*a*)

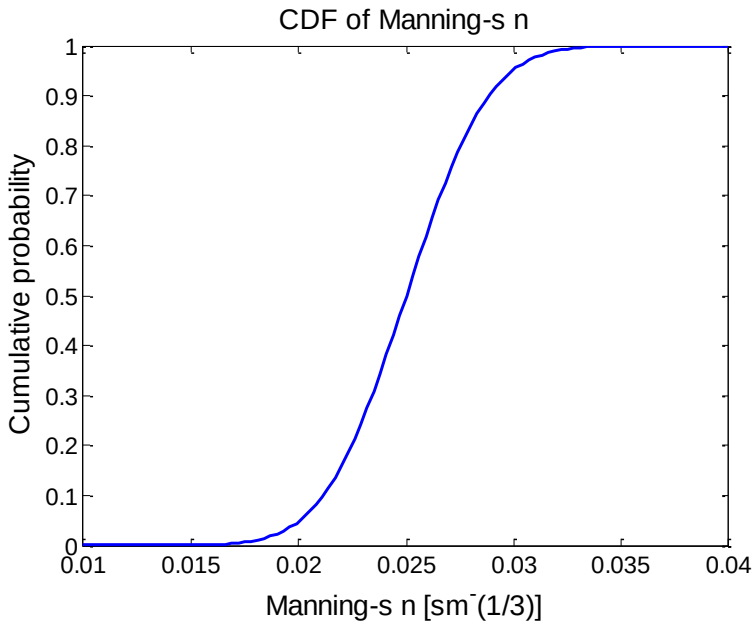

(*b*)

Figure 5.4: (a) Probability density function and (b) cumulative density function of Manning's n.

To analyse the effect of bed roughness uncertainty on the model prediction of maximum water level, the values of Manning's *n* (s/m$^{1/3}$) are prescribed to be normally distributed, with a mean (μ) of 0.025 s/m$^{1/3}$ and a standard deviation

(σ) of 0.003 s/m$^{1/3}$. Figure 5.4 shows the resulting probability density function and cumulative density function for Manning's *n*. The lower and upper tails of the probability density distribution are then cut off at 0.01 and 0.04 s/m$^{1/3}$ neglecting the near-zero values beyond these.

Then the Delft3D model was run for seven times in total, each time with a constant Manning's *n* everywhere in the domain. Seven values of Manning's *n* of equal interval were chosen for model runs; these values are 0.01, 0.015, 0.02, 0.03, 0.035 and 0.04 s/m$^{1/3}$. Each time the Delft3D model was first run for 5 days for hydrodynamic spin-up. Then the model was run for 28 days, i.e., for the duration of two spring-neap cycles. Then from each model run, the maximum water level was taken out and plotted against the Manning's *n* used for that simulation. A cubic spline was drawn to establish the relationship between maximum water level and Manning's *n*.

5.3. Uncertainty in model prediction of maximum water level

5.3.1. Convergence Test

To perform a convergence test on Manning's *n* and verify the statistical calculations, the probability density function (PDF) and cumulative density function (CDF) are first divided into a discrete number of bins and then the statistical moments determined as follows. The probability of the central value of each bin is calculated by integrating the area of each bin,

$$\Pr(n_i) = \Pr\left(n_{i-\frac{1}{2}} < n < n_{i+\frac{1}{2}}\right) = \int_{n_{i-\frac{1}{2}}}^{n_{i+\frac{1}{2}}} \text{PDF}\, dn \qquad (5.10)$$

Here, $\Pr(n_i)$ is the probability of Manning's *n* of the i-th bin. This is the CDF of the distribution between the boundary values of the bin which are denoted by $n_{i-\frac{1}{2}}$ and $n_{i+\frac{1}{2}}$.

Then the expected value $E[n]$ is calculated as

$$E[n] = \sum_i n_i \Pr(n_i) \tag{5.11}$$

and the variance σ_n is calculated by

$$\sigma_n^2 = \sum_i (n_i - E[n])^2 * \Pr(n_i) \tag{5.12}$$

The skewness may be calculated from the third-order statistical moment as:

$$Skew(n) = \sum_i (n_i - E[n])^3 * \Pr(n_i) \tag{5.13}$$

and the kurtosis from the fourth-order statistical moment as:

$$Kurt(n) = \sum_i (n_i - E[n])^4 * \Pr(n_i) \tag{5.14}$$

Finally, the non-dimensional skewness and non-dimensional kurtosis are calculated as

$$Skew_n(n) = \frac{Skew(n)}{\sigma_n^3} \tag{5.15}$$

and

$$Kurt_n(n) = \frac{Kurt(n)}{\sigma_n^4} \tag{5.16}$$

Table 5.2 shows the statistics obtained from the discretized probability density function for Manning's *n* using different numbers of bins, applied in a systematic manner. It can be seen that the distribution of Manning's *n* is not sensitive to the number of bins. The expected value is not unaffected for at least 8 significant figures and the standard deviation also remains unaffected up to 3 significant figures for all numbers of bins considered. The values of variance, non-dimensional skewness and non-dimensional kurtosis converge as the number of bins increases. For 401 bins and above, the variance converges to 4 significant figures, non-dimensional skewness up to 5 significant figures and non-dimensional kurtosis up to 7 significant figures. Moreover, the values of non-dimensional skewness and non-dimensional kurtosis of 1.4×10^{-5} and 3 respectively indicate that Manning's *n* in this case is normally distributed (truncated).

Table 5.2 Calculation of expected value and other statistical moments of Manning's *n*.

No. of bins	Expected value, $E[n]$ (s/m$^{1/3}$)	Variance, σ_n^2 (s^2/m$^{2/3}$)	Standard deviation, σ_n (s/m$^{1/3}$)	Non-dimensional skewness, $Skew_n(n)$	Non-dimensional kurtosis, $Kurt_n(n)$
21	0.024999986	9.17 x 10^{-6}	0.003028	1.38697 x 10^{-5}	2.999251
51	0.024999986	9.03 x 10^{-6}	0.003004	1.39777 x 10^{-5}	2.999660
101	0.024999986	9.007 x 10^{-6}	0.003001	1.39944 x 10^{-5}	2.999673
201	0.024999986	9.002 x 10^{-6}	0.003000	1.39987 x 10^{-5}	2.999674
401	0.024999986	9.0003 x 10^{-6}	0.003000	1.39997 x 10^{-5}	2.999674
601	0.024999986	9.00 x 10^{-6}	0.003000	1.39999 x 10^{-5}	2.999675
801	0.024999986	8.9999 x 10^{-6}	0.002999	1.40000 x 10^{-5}	2.999675

Sandwip Island is the reference case for the maximum water level convergence test. Figure 5.5 shows the location of Sandwip (645318.46 m E, 488560.77 m N) which hosts a tidal gauge station belonging to the Bangladesh Water Transport Authority. First, a series of model runs are performed, each with constant Manning's *n* set everywhere in the domain, the value ranging from 0.01 to 0.04 s/m$^{1/3}$. Figure 5.6 shows the resulting variation in maximum water level with Manning's *n* at Sandwip Island. A significant drop in maximum water level can be observed as Manning's *n* increases. If Manning's *n* increases, then flow velocity decreases. At this location, there is no upstream river inlet, only seawater enters from the downstream. Whether water level will increase or decrease depends on which of the acting forces wins in the competition (in this case, gravitational flow towards the sea due to ground slope and tidal flow towards the land). Both the flows will be hindered if Manning's parameter increases, but if water drains out quicker than the landward tidal flow, then water level at Sandwip will eventually decrease.

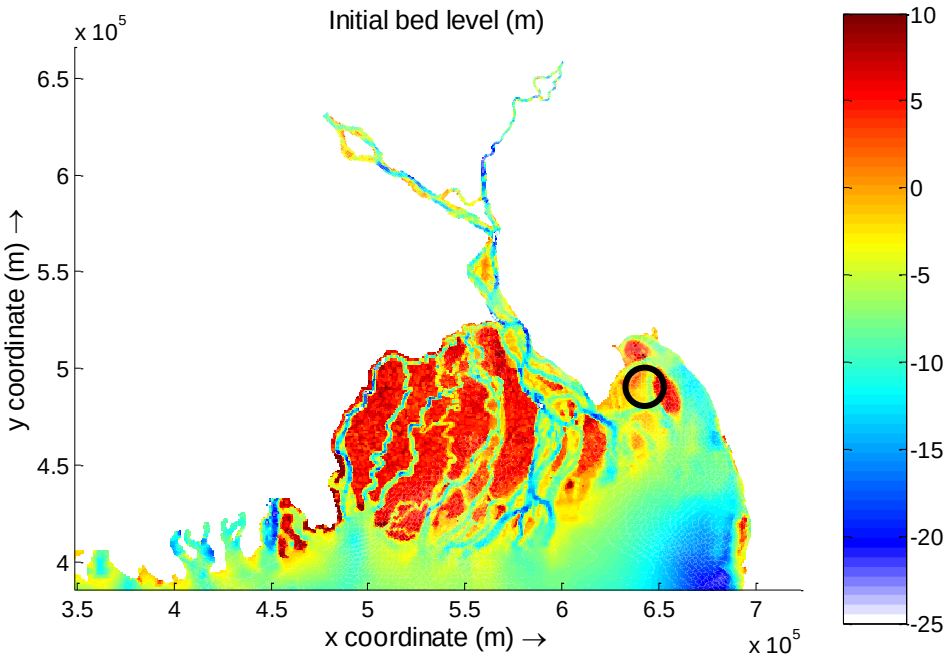

Figure 5.5: Location of Sandwip (black circle), Meghna Estuary, Bangladesh

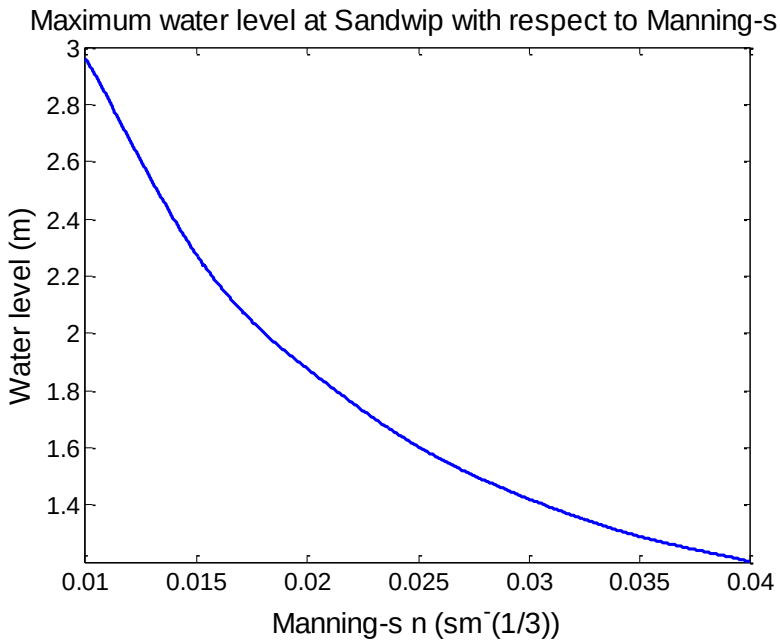

Fig 5.6: Dependence of maximum water level on Manning's n at Sandwip, Meghna Estuary, Bangladesh

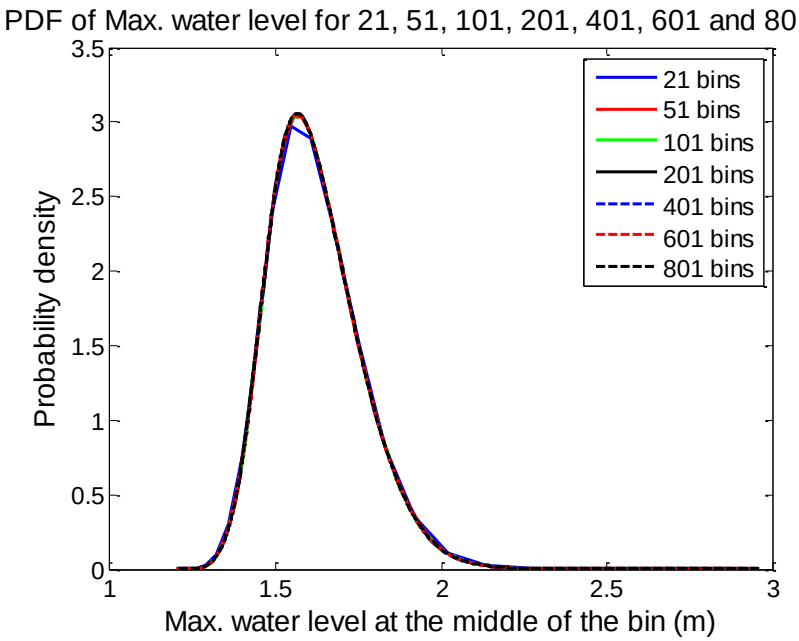

(a)

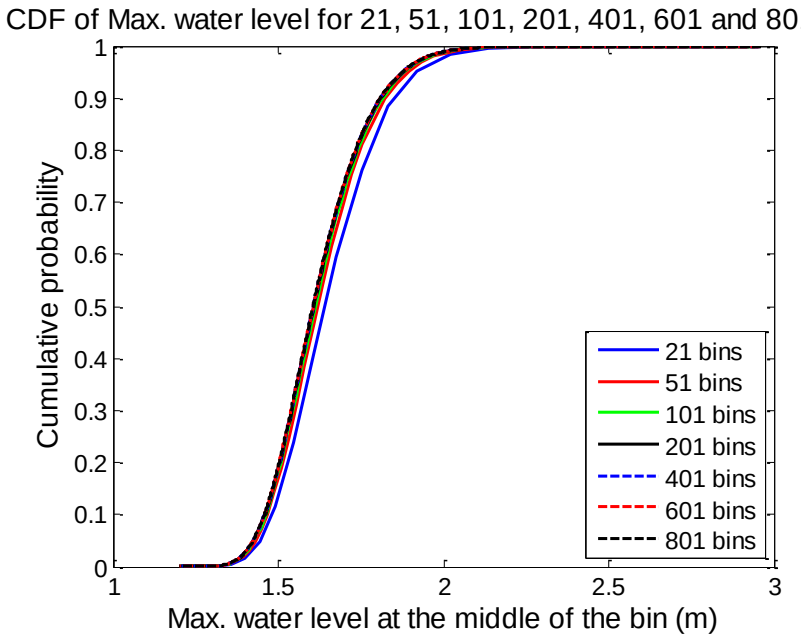

(b)

Figure 5.7: (a) Probability density function and (b) cumulative density function of maximum water level at Sandwip obtained for different numbers of bins.

Next, the statistical convergence of the maximum water level is investigated according to the number of bins used to discretize the probability density function of Manning's *n*. The derived probability distribution contains the same number of bins, but the bin width is no longer fixed; this is because of the nonlinear relationship between Manning's coefficient and maximum water level as shown in Figure 5.6. Non-linear functions do not have a constant slope (i.e., $\frac{\Delta y_i}{\Delta x_i}$ as described in section 3.3 for figure 3.1), so if Δx is kept constant then Δy will vary.

Figure 5.7 depicts the resulting probability density function and cumulative density function of maximum water level at Sandwip obtained for different numbers of bins used to discretize the probability density function of Manning's *n*.

The expected value of maximum water level (Z) is calculated as

$$E[Z] = \sum_i Z_i(n_i) * \Pr(n_i) \tag{5.17}$$

The variance in maximum water level is then determined from

$$\sigma_Z^2 = \sum_i (Z_i(n_i) - E[Z])^2 * \Pr(n_i) \tag{5.18}$$

The skewness in maximum water level is

$$Skew(Z) = \sum_i (Z_i(n_i) - E[Z])^3 * \Pr(n_i) \tag{5.19}$$

The kurtosis in maximum water level is

$$Kurt(Z) = \sum_i (Z_i(n_i) - E[Z])^4 * \Pr(n_i) \tag{5.20}$$

Finally, the non-dimensional skewness and non-dimensional kurtosis in maximum water level are calculated from

$$Skew_n(Z) = \frac{Skew(Z)}{\sigma_Z^3} \tag{5.21}$$

and

$$Kurt_n(Z) = \frac{Kurt(Z)}{\sigma_Z^4} \quad (5.22)$$

Table 5.3 provides a summary of the statistics of maximum water level at Sandwip obtained for different numbers of bins used to discretize the Manning's *n* probability density function.

Table 5.3: Expected value and other statistical moments of maximum water level at Sandwip.

No. of bins	Expected value of max. water level, $E[Z]$ (m)	Variance, σ_Z^2 (m^2)	Standard deviation, σ_Z (m)	Non-dimensional skewness, $Skew_n(Z)$	Non-dimensional kurtosis, $Kurt_n(Z)$
21	1.687	0.0242	0.1554	0.6708	3.8801
51	1.648	0.0211	0.1454	0.6701	3.8033
101	1.634	0.0202	0.1422	0.6726	3.7877
201	1.628	0.0198	0.1407	0.6743	3.7818
401	1.624	0.0196	0.1399	0.6752	3.7792
601	1.623	0.0195	0.1396	0.6755	3.7784
801	1.622	0.0195	0.1395	0.6757	3.7781

Table 5.3 indicates that the probability distribution of maximum water level is sensitive to the number of bins used to discretize the PDF of Manning's *n*. The expected value, variance, standard deviation, non-dimensional skewness, and non-dimensional kurtosis of maximum water level all converge to within 2 significant figures for 401 bins upwards. Consequently, the number of bins used in the later analysis is chosen as 401. The positive value of skewness shows that the probability distribution of maximum water level is skewed towards the right tail relative to the mean of maximum water level. Also, the positive kurtosis indicates the distribution to be leptokurtic, which

indicates a greater preponderance of extreme values of maximum water level (which affects the tailedness of the probability distribution).

5.3.2. Uncertainty in maximum water level at Location 1 (Sandwip)

After selecting the number of required bins, Sandwip is again chosen to see what happens when the mean value of Manning's coefficient is altered while keeping the standard deviation constant. Figure 5.8 shows the PDFs and CDFs of Manning's coefficient obtained for a truncated normal distribution with mean values equal to 0.02, 0.025, and 0.03 $s/m^{1/3}$ and fixed standard deviation of 0.003 $s/m^{1/3}$. The procedure described in Chapter 3 is followed to obtain the probability distribution of maximum water level.

Figure 5.9 presents the resulting PDFs and CDFs of maximum water level at Sandwip. As the mean value of Manning's *n* increases, the PDF of maximum water level reaches its peak at a lower value of maximum water level. The magnitude of the peak of the distribution of maximum water level increases progressively with the increase in mean value of Manning's *n*. However, the standard deviation of maximum water level reduces as the mean value of Manning's *n* increases. It is clear from Figure 5.9 that the distribution of maximum water level at Sandwip is highly sensitive to the mean value of Manning's coefficient.

Table 5.4 lists the expected value and higher order moments for the maximum water level obtained for the three values of mean *n*. As *n* increases from 0.02 to 0.03 $s/m^{1/3}$, the expected maximum water level drops by about 25%, the standard deviation drops by 53%, the skewness also reduces (but remains positive), and the non-dimensional kurtosis is invariably above 3 (again indicating the greater likelihood of extremes in the distribution of maximum water level). Here the probability distribution of maximum water level has an asymmetric tail extending towards higher values; the positive value of non-dimensional skewness confirms this.

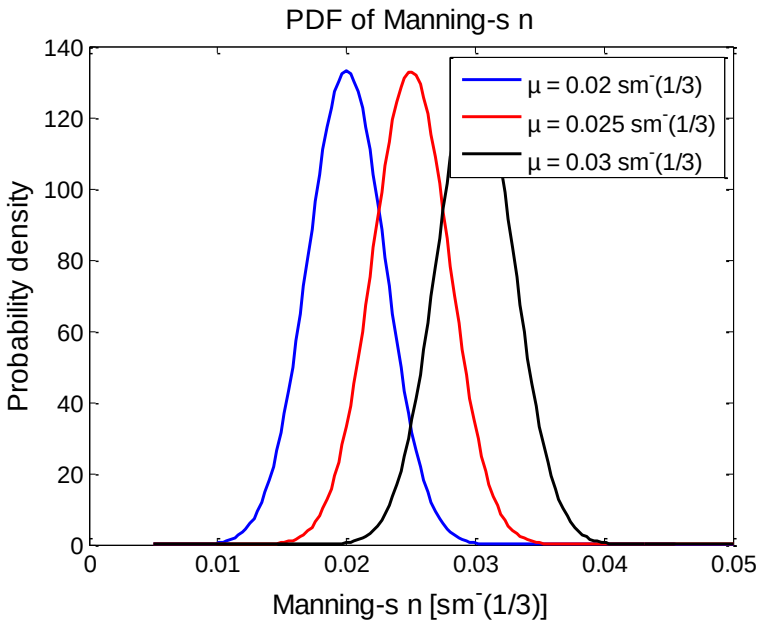

(a)

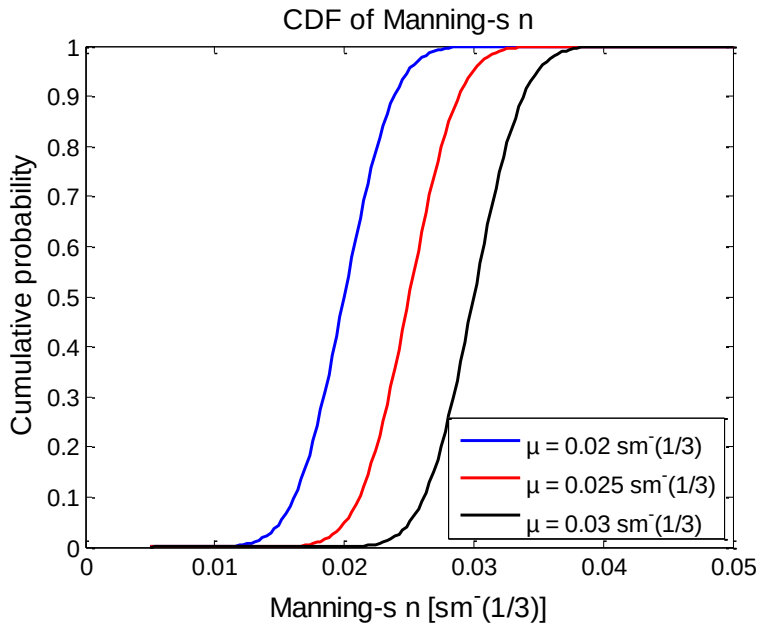

(b)

Figure 5.8: (a) Probability density function and (b) cumulative density function of Manning's coefficient for changing mean n and constant standard deviation (0.003 s/m$^{1/3}$) in n.

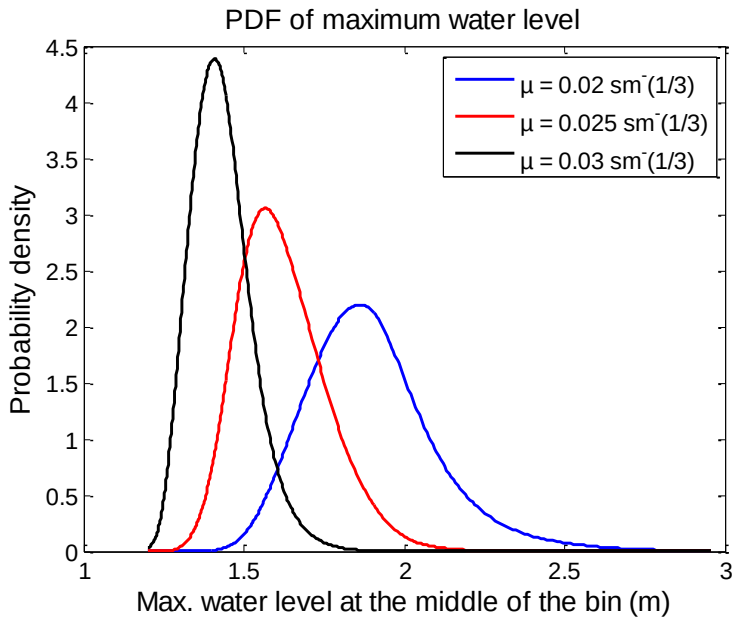

(a)

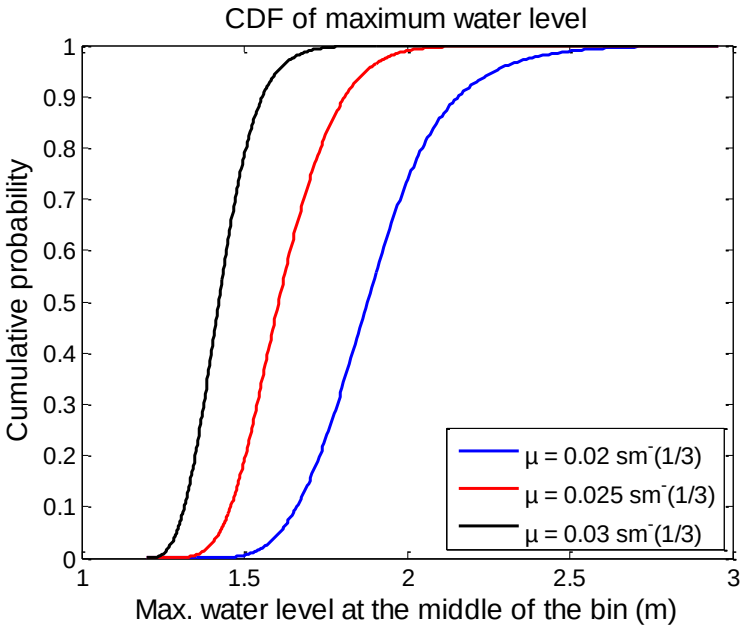

(b)

Figure 5.9: (a) Probability density function and (b) cumulative density function of maximum water level at Sandwip for different values of mean n and constant standard deviation (0.003 s/m$^{1/3}$) in n.

Table 5.4: Expected value and other statistical moments of maximum water level at Sandwip for three values of mean Manning's coefficient (with standard deviation set at 0.003 s/m$^{1/3}$).

Mean Manning's coefficient (s/m$^{1/3}$)	**Expected value of max. water level, $E[Z]$ (m)**	**Variance, σ_Z^2 (m^2)**	**Standard deviation, σ_Z (m)**	**Non-dimensional skewness, $Skew_n(Z)$**	**Non-dimensional kurtosis, $Kurt_n(Z)$**
0.02	1.8963	0.0413	0.2033	0.8557	4.4876
0.025	1.6207	0.0194	0.1391	0.6763	3.7771
0.03	1.4293	0.0091	0.0955	0.7046	3.9160

Next, the mean value of Manning's *n* is kept constant at 0.025 s/m$^{1/3}$ and the standard deviation is varied from 0.001 to 0.005 s/m$^{1/3}$ (Figure 5.10). The PDF and CDF of maximum water level at Sandwip are then obtained (Figure 5.11) for the constant *n* and three values of standard deviation in *n*. The peak of probability distribution is reached at a lower value with the increase of standard deviation of Manning roughness coefficient. Water level is highly sensitive to Manning's *n* (as seen in equation 5.9), thus incorporating more uncertainty in Manning's *n* results in more uncertainty in maximum water level. Since the total probability is 1, if the PDF becomes more dispersed (i.e, higher standard deviation), then the peak becomes lower keeping the total area of PDF equal to 1. Also, the PDF of maximum water level become more skewed to the right side of the mean value as the standard deviation of Manning's *n* increases.

Table 5.5 lists the statistical values obtained for the different standard deviations in the maximum water level for constant Manning's *n*. The expected value of the maximum water level is relatively insensitive to the standard deviation of Manning's coefficient, unlike the standard deviation. As the standard deviation of Manning's coefficient increases, the expected value of maximum water level increases slightly. But the variance and standard deviation of maximum water level increase markedly, the latter by a factor of

5.35 (almost identical to the increase in standard deviation of Manning's *n*). The non-dimensional skewness is positive in each case, and increases by a factor of 4.5 as the standard deviation in *n* increases from 0.001 to 0.005 s/m$^{1/3}$.

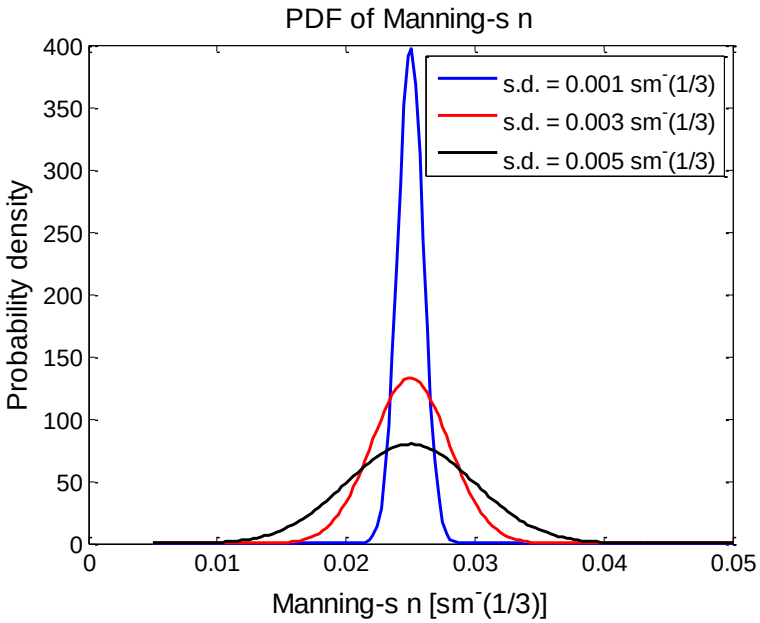

(a)

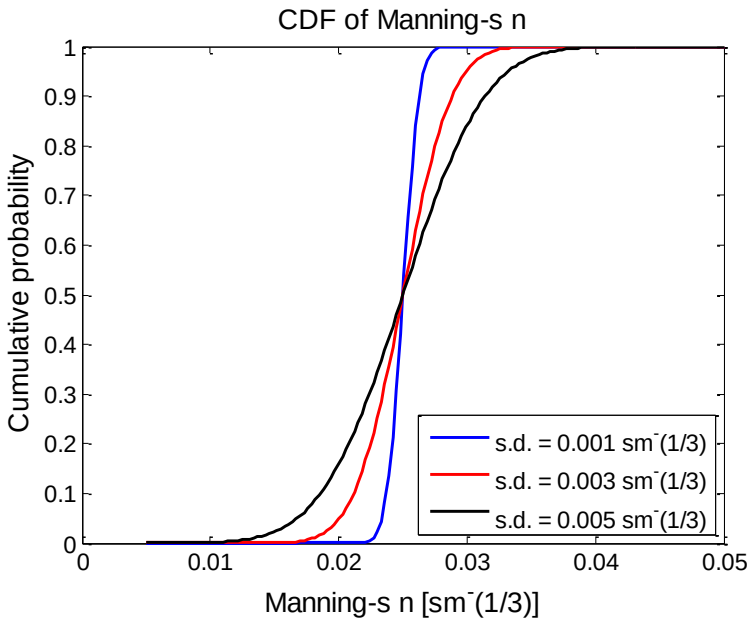

(b)

Figure 5.10: (a) Probability density functions and (b) cumulative density functions of Manning's coefficient for constant mean (0.025 s/m$^{1/3}$) and different standard deviations.

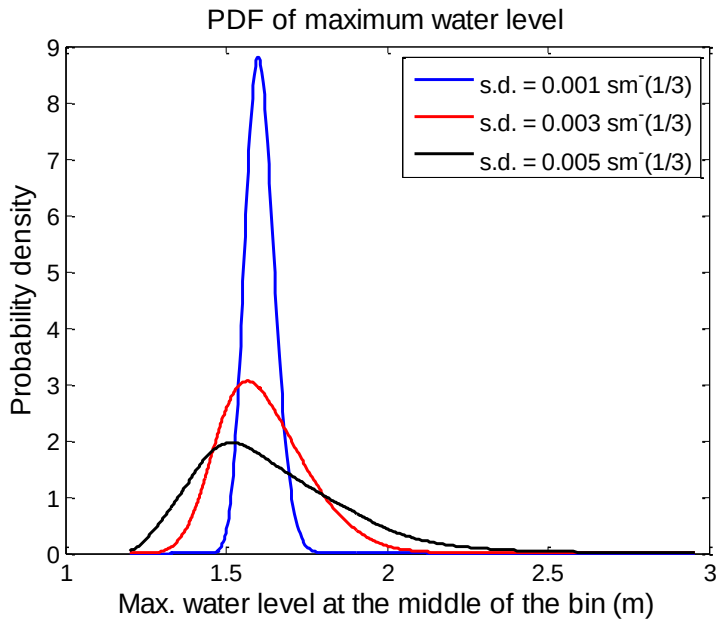

(a)

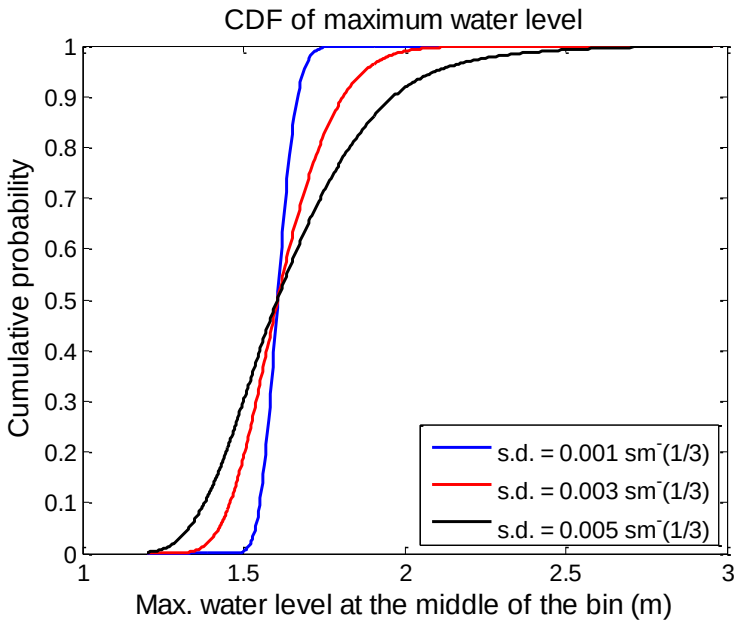

(b)

Figure 5.11: (a) Probability density function and (b) cumulative density function of maximum water level at Sandwip for constant mean (0.025 s/m$^{1/3}$) and varying standard deviation of Manning's coefficient .

For the lowest value of standard deviation in *n*, the kurtosis is about 3, indicating hardly any affect occurs to the tailedness of the distribution of maximum water level. However, the kurtosis increases to a very high value

as the standard deviation in *n* increases, partly due to truncation of the underlying probability distribution, and primarily because the probability distribution of maximum water has an asymmetric tail containing more extreme values.

Table 5.5: Expected value and other statistical moments of maximum water level at Sandwip for three values of standard deviation in Manning's coefficient (with mean set at 0.025 s/m$^{1/3}$).

Standard deviation in Manning's coefficient (s/m$^{1/3}$)	**Expected value of max. water level, $E[Z]$ (m)**	**Variance, σ_Z^2 (m^2)**	**Standard deviation, σ_Z (m)**	**Non-dimensional skewness, $Skew_n(Z)$**	**Non-dimensional kurtosis, $Kurt_n(Z)$**
0.001	1.6063	0.0021	0.0456	0.2709	3.0933
0.003	1.6207	0.0197	0.1391	0.6763	3.7771
0.005	1.6434	0.0597	0.2443	1.2178	5.2901

5.3.3. Uncertainty in maximum water level at Location 2 (Char Purulia)

The next location chosen for uncertainty estimation is Char Purulia (564321.96 m E, 546395.19 m N). Figure 5.12 shows its location. Char Purulia also hosts a gauging station owned by the Bangladesh Inland Water Transport Authority. In this case, the model output is analyzed after undertaking 7 simulations for different values of Manning's *n* ranging from 0.01 to 0.04 s/m$^{1/3}$ (that are applied throughout the whole domain). Figure 5.13 shows that the maximum water level increases with increasing Manning's *n*. Although a tidal influence from the south reaches this location, river flow from the upstream north is the dominant forcing mechanism here. An increasing Manning's roughness coefficient causes reduction in the river flow velocity and consequently the water level increases. At the lowest values of Manning's *n*

considered, the tidal signal was discernible; however, as the Manning's *n* was increased, the river flow became sufficiently strong to push the tidal effect back southwards from this location.

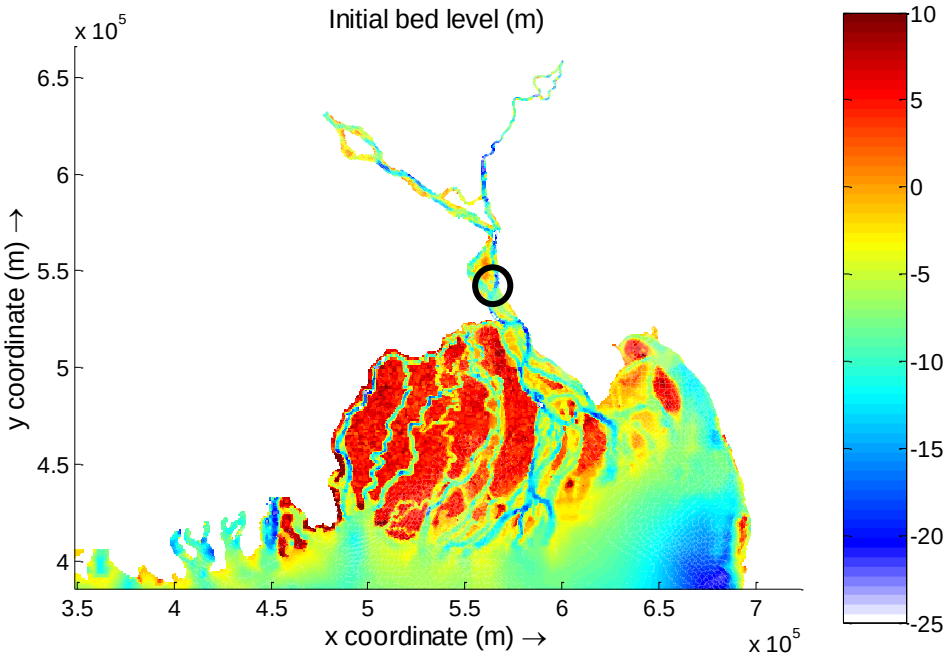

Figure 5.12: Location of Char Purulia, (black circle), Meghna Estuary, Bangladesh

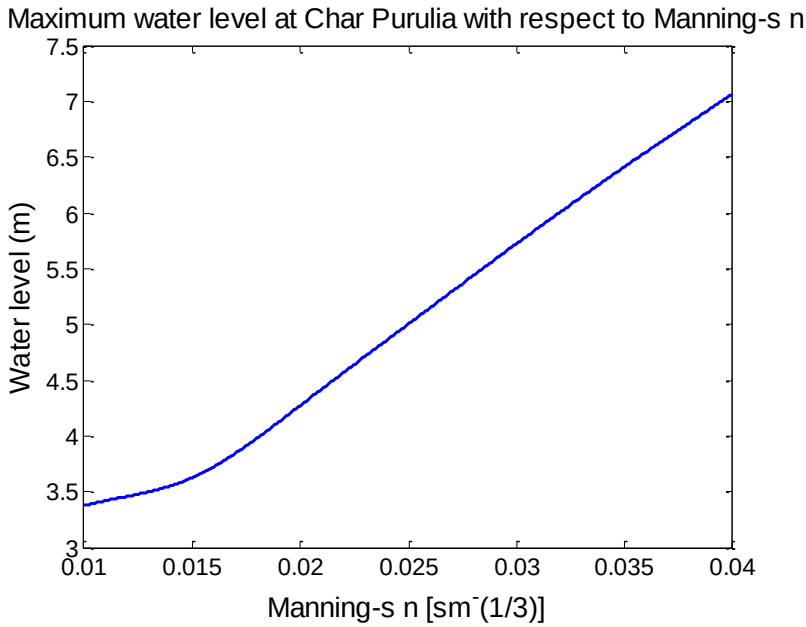

Figure 5.13: Functional relationship between maximum water level and Manning's n at Char Purulia Meghna Estuary, Bangladesh

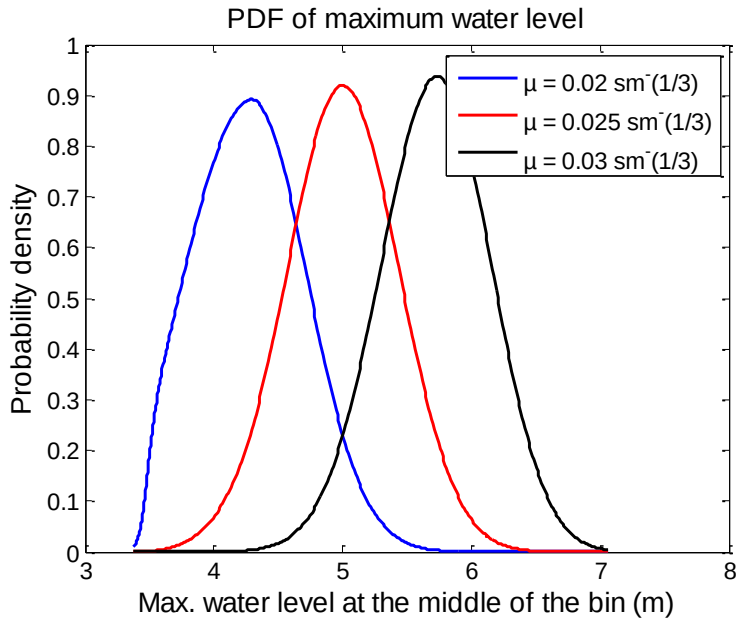

(a)

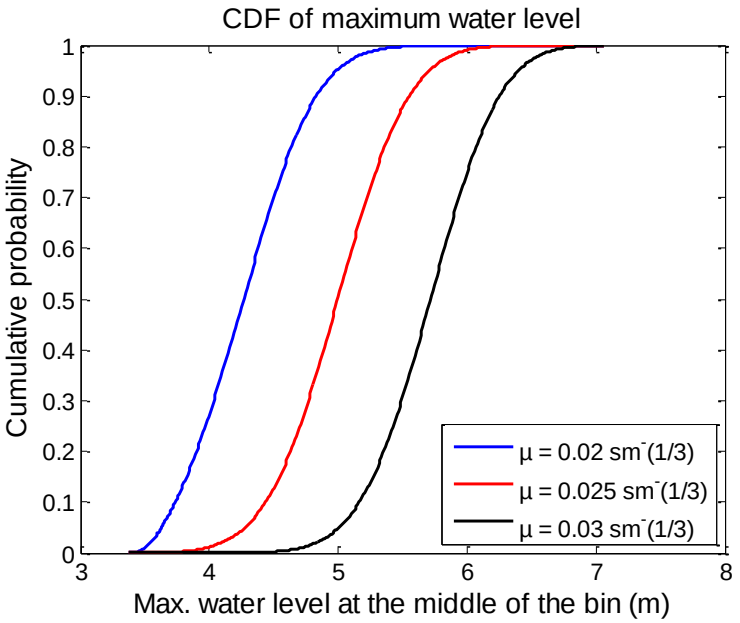

(b)

Figure 5.14: (a) Probability density function and (b) cumulative density function of maximum water level at Char Purulia for different values of mean n and constant standard deviation (0.003 s/m$^{1/3}$) in n.

The same PDF and CDF of Manning's *n* from figure 5.8 are considered in this case. Figure 5.14 shows the resulting probability distribution of maximum water level at Char Purulia. Unlike at Sandwip, the peak of the PDF of maximum water level is reached at a higher value of maximum water level. The magnitude of the peak of the PDF of maximum water level increases with increase in Manning's *n.* Table 5.6 lists the expected value of maximum water level and other statistical moments.

Table 5.6: Expected value and other statistical moments of maximum water level at Char Purulia for three values of mean Manning's coefficient (with standard deviation set at 0.003 s/m$^{1/3}$).

Mean Manning's coefficient (s/m$^{1/3}$)	**Expected value of max. water level, $E[Z]$ (m)**	**Variance, σ_Z^2 (m^2)**	**Standard deviation, σ_Z (m)**	**Non-dimensional skewness, $Skew_n(Z)$**	**Non-dimensional kurtosis, $Kurt_n(Z)$**
0.02	4.2836	0.1717	0.4144	0.2753	2.6707
0.025	5.0008	0.1881	0.4337	-0.0186	2.9509
0.03	5.7133	0.1781	0.4221	-0.0684	2.9321

The standard deviation of maximum water level does not change significantly when Manning's *n* alters from 0.02 s/m$^{1/3}$ to 0.03 s/m$^{1/3}$, but the expected value of maximum water level increases by about 33%. The non-dimensional skewness changes from positive to negative, indicating that the probability distribution of maximum water level shifts from right-skewed to left-skewed. The non-dimensional kurtosis is slightly less than 3, and so these three distributions of maximum water level are flatter than a standard normal distribution.

Now, the standard deviation of Manning's *n* is varied from 0.001 to 0.005 s/m$^{1/3}$ and the probability distribution of maximum water level is derived from the distribution of Manning's *n.* The same PDF and CDF of Manning's *n* shown in Figure 5.9 are considered. Figure 5.15 presents the PDF and CDF of

maximum water level. Table 5.7 gives the expected value of maximum water level and other statistical moments.

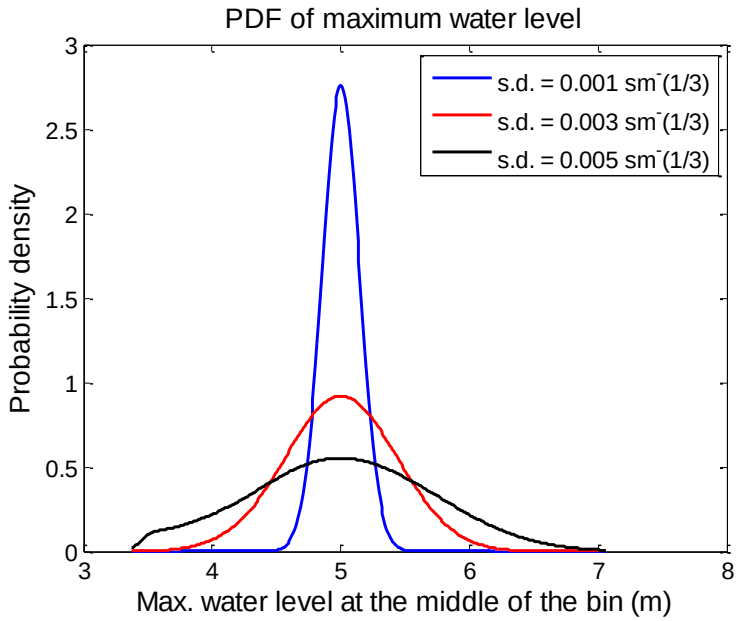

(a)

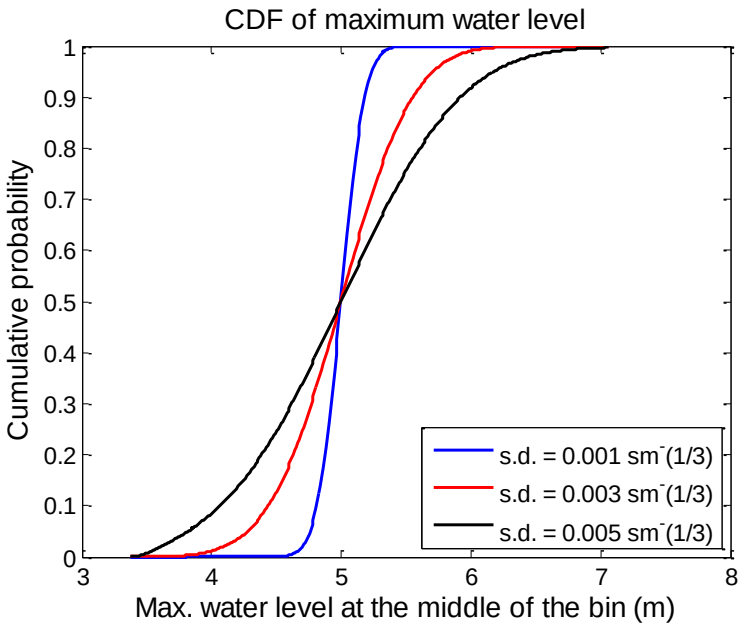

(b)

Figure 5.15: (a) Probability density function and (b) cumulative density function of maximum water level at Char Purulia for constant mean (0.025 s/m$^{1/3}$) and varying standard deviation of Manning's coefficient

Table 5.7: Expected value and other statistical moments of maximum water level at Char Purulia for three values of standard deviation in Manning's coefficient (with mean set at 0.025 s/m$^{1/3}$).

Standard deviation of Manning's coefficient (s/m$^{1/3}$)	**Expected value of max. water level, $E[Z]$ (m)**	**Variance, σ_Z^2 (m^2)**	**Standard deviation, σ_Z (m)**	**Non-dimensional skewness, $Skew_n(Z)$**	**Non-dimensional kurtosis, $Kurt_n(Z)$**
0.001	5.002	0.0209	0.1447	-9.1154×10-5	3.002
0.003	5.0008	0.1881	0.4337	-0.0186	2.9509
0.005	8.989	0.4859	0.6971	0.1111	2.6055

With the increase of standard deviation in Manning's coefficient, the standard deviation of maximum water increases remarkably, about seven-fold. The expected value of maximum water level also increases by 80%. The non-dimensional skewness rises from slightly below 0 to a positive 0.111, meaning that the PDFs change from being left-skewed to right-skewed. The non-dimensional kurtosis falls from 3 to below 3, which means the PDF becomes flatter as Manning's *n* increases. So, the expected value and standard deviation of maximum water level are again found to be sensitive to the mean and standard deviation of Manning's *n*.

5.3.4. Uncertainty in maximum water level at Location 3 (Tiger Point)

The third location chosen for uncertainty study is Tiger Point (figure 5.16), where there is also a tidal gauge station belonging to BIWTA, located at 482717.17 m E and 415387.23 m N. Applying the same procedure as for the previous two cases, the functional relationship between Manning's *n* and maximum water level is obtained from several Delft3D simulations (figure 5.17).

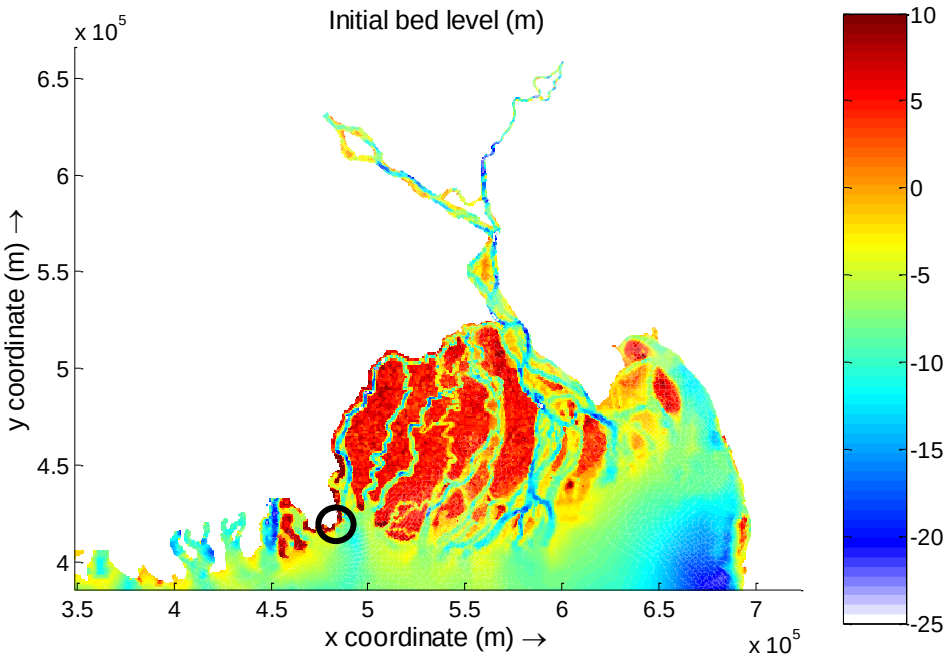

Figure 5.16: Location of Tiger Point, (black circle), Meghna Estuary, Bangladesh

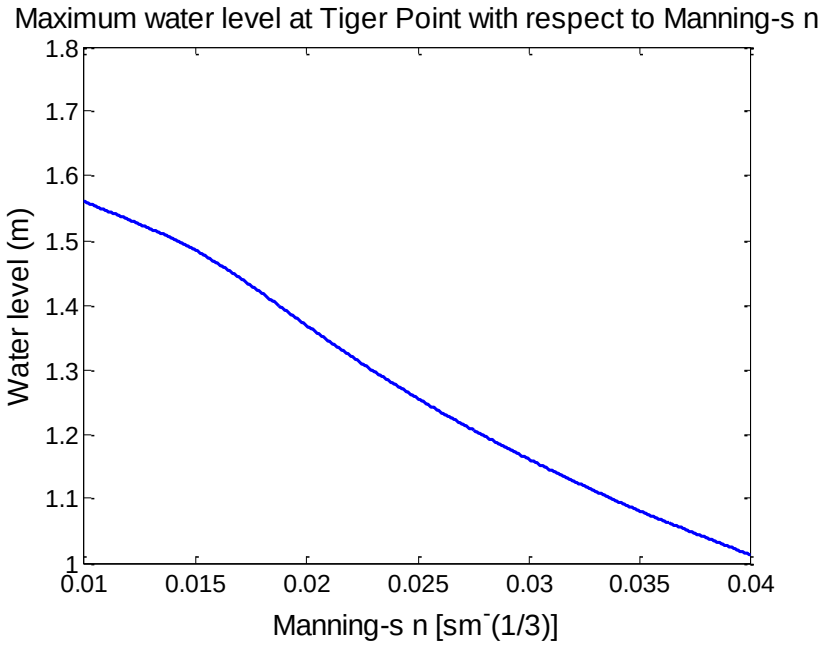

Figure 5.17: Functional relationship between maximum water level and Manning's roughness coefficient at Tiger Point.

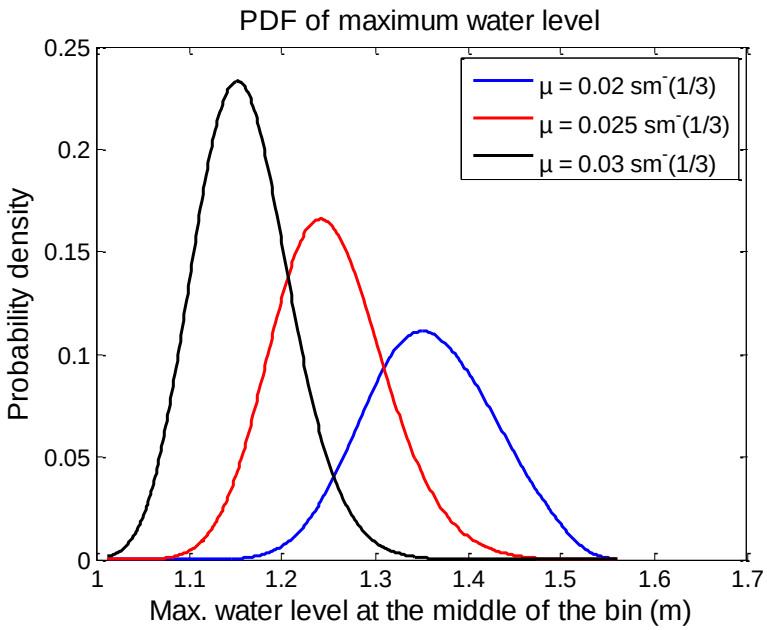

(a)

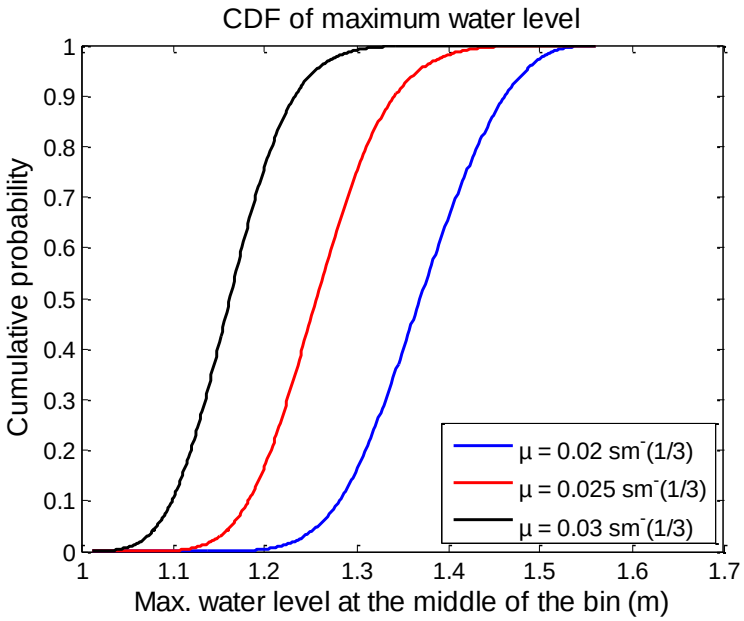

(b)

Figure 5.18: (a) Probability density function and (b) cumulative density function of maximum water level at Tiger Point for different values of mean n and constant standard deviation (0.003 s/m$^{1/3}$) in n.

Figure 5.18 shows the PDF and CDF of maximum water level at Tiger Point obtained for a constant standard deviation of 0.003 s/m$^{1/3}$ and three different

mean values of *n*. Table 5.8 lists the expected value of maximum water level and other statistical moments.

Table 5.8: Expected value and other statistical moments of maximum water level at Tiger Point for three values of mean Manning's coefficient (with standard deviation set at 0.003 s/m$^{1/3}$).

Mean Manning's coefficient (s/m$^{1/3}$)	**Expected value of max. water level, $E[Z]$ (m)**	**Variance, σ_Z^2 (m^2)**	**Standard deviation, σ_Z (m)**	**Non-dimensional skewness, $Skew_n(Z)$**	**Non-dimensional kurtosis, $Kurt_n(Z)$**
0.02	1.3687	0.0047	0.0689	0.0123	2.5759
0.025	1.2588	0.0039	0.0622	0.2978	3.0829
0.03	1.1633	0.0027	0.0524	0.3380	3.1675

As Manning's *n* increases from 0.02 to 0.03 s/m$^{1/3}$, the expected value of maximum water level decreases by 15% and standard deviation decreases by 24%. The non-dimensional skewness is close to 0 and remains positive in each case indicating that the probability density distribution is very slightly skewed to the right sight side of the mean value. The non-dimensional kurtosis increases from slightly below 3 to slightly above 3 with increasing mean value of *n*; this means that the probability density distribution is close to a truncated normal distribution in every case.

Figure 5.19 shows the PDF of CDF of maximum water level when the standard deviation varies from 0.001 to 0.003 s/m$^{1/3}$ keeping the mean constant at 0.025 s/m$^{1/3}$. Table 5.9 lists the statistical moments.

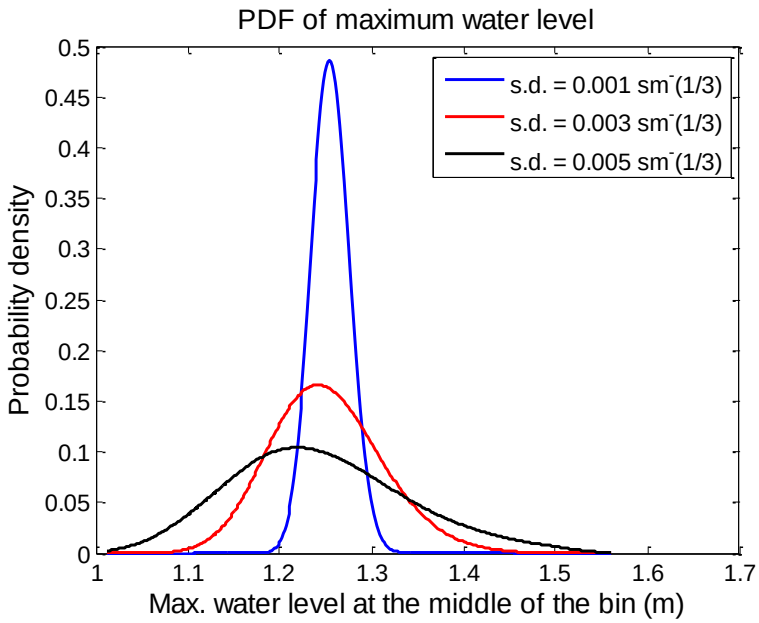

(a)

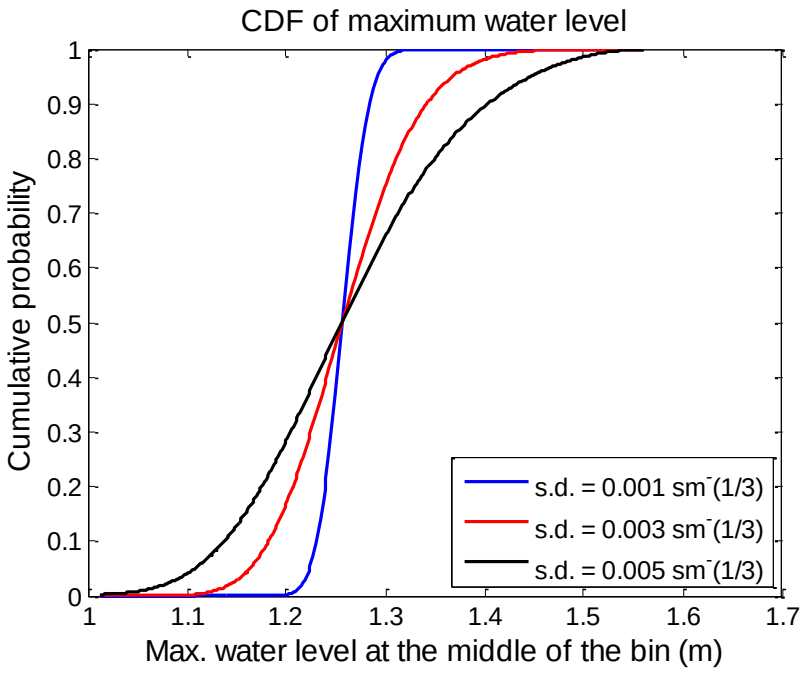

(b)

Figure 5.19: (a) Probability density function and (b) cumulative density function of maximum water level at Tiger Point for constant mean (0.025 s/m$^{1/3}$) and varying standard deviation of Manning's coefficient

Table 5.9: Expected value and other statistical moments of maximum water level at Tiger Point for three values of standard deviation in Manning's coefficient (with mean set at 0.025 s/m$^{1/3}$).

Standard deviation of Manning's coefficient (s/m$^{1/3}$)	**Expected value of max. water level, $E[Z]$ (m)**	**Variance, σ_Z^2 (m^2)**	**Standard deviation, σ_Z (m)**	**Non-dimensional skewness, $Skew_n(Z)$**	**Non-dimensional kurtosis, $Kurt_n(Z)$**
0.001	1.2558	0.00042	0.0206	0.1162	3.0327
0.003	1.2588	0.0039	0.0622	0.2978	3.0829
0.005	1.2598	0.0102	0.1008	0.4145	2.7630

As the standard deviation in Manning's *n* increases from 0.001 to 0.005 s/m$^{1/3}$, the expected value of maximum water level does not change but the standard deviation increases by 4.9 times. The non-dimensional skewness of the probability density distribution of maximum water level is close to 0 and remains positive in each case. In other words, the probability distribution is very slightly skewed to the right hand side of the mean value. Again, the non-dimensional skewness varies from slightly below 3 to slightly higher than 3, again meaning that the probability density distribution of maximum water level is close to a truncated normal distribution in each case.

The maximum water level at this Tiger Point is less sensitive to uncertainty in the Manning's coefficient than at the previous two stations considered.

5.3.5. Uncertainty in maximum water level at Location 4 (Hatia)

At Hatia (614683.65 m E, 479910.7 m N) the maximum water level is not either monotonically increasing or decreasing function of Manning's *n*. Instead, the maximum water level first decreases, reaches a minimum, and then starts increasing as the value of Manning's *n* is raised (figure 5.21). Hatia is situated

just at the mouth of the estuary where tide and river flow are competing dominant forcing processes (figure 5.20).

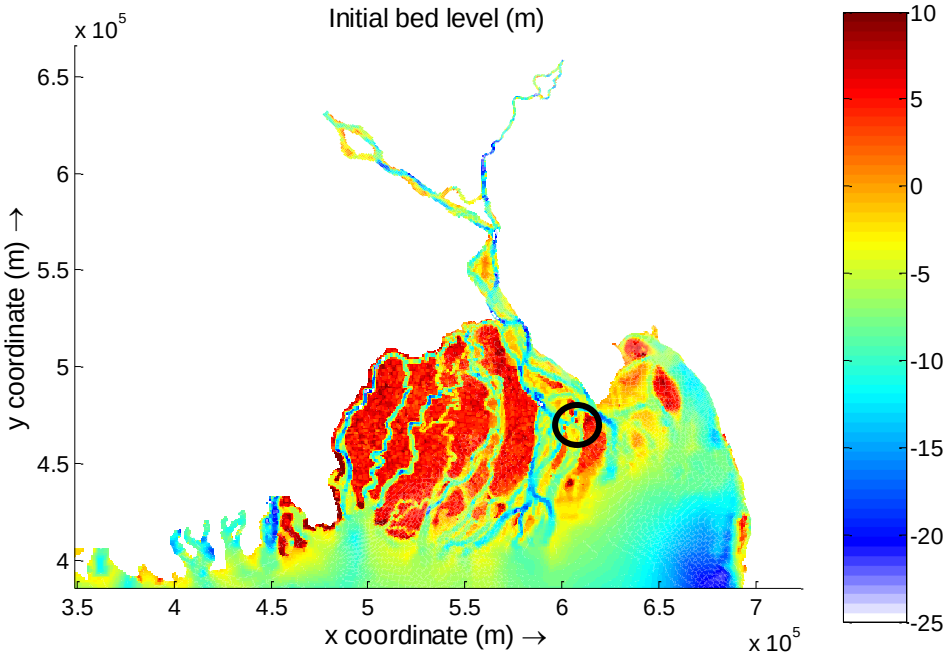

Figure 5.20: Location of Hatia (black circle), Meghna Estuary, Bangladesh

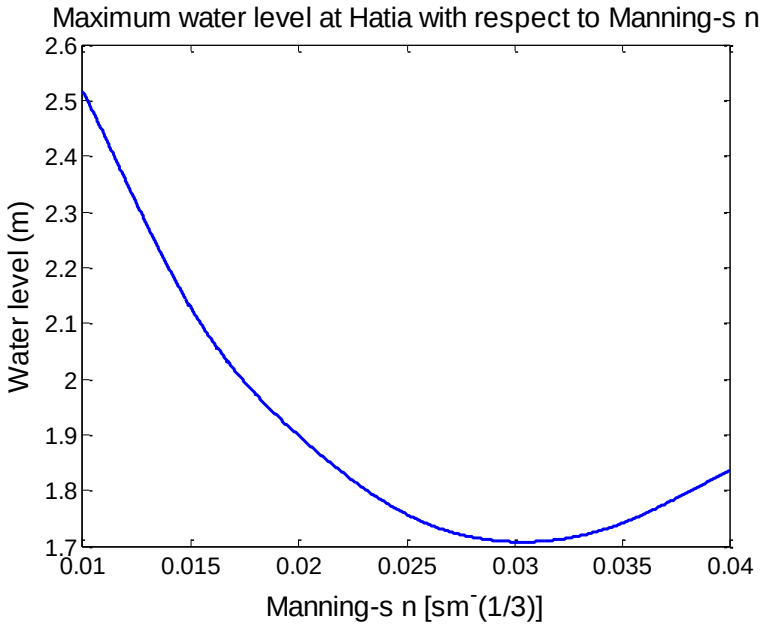

Figure 5.21: Functional relationship between maximum water level and Manning's roughness coefficient at Hatia

At low values of Manning's coefficient, the river flow gains high velocity, the landward tidal flow also increases; and at the end, tide wins the competition raising water level. On the other hand, at higher values of *n*, the velocity of the upstream river flow becomes more hindered, so the water level in the river increases, and the tidal flow towards land decreases. This estuary has extremely complex bathymetry which plays a vital role in the spatial variation of water level and velocity. For all these reasons, the functional relationship between Manning's *n* and maximum water level at Hatia turns out to be non-monotonic.

The derived distribution approach (Chapter 3) assumes that the response function (connecting the input and output variables of interest) should be either monotonically increasing or decreasing so that the response function is single-valued with a unique inverse function. In applying this method to the maximum water level at Haita, three distinct problems are encountered. First, when the maximum water level reaches its lowest value of 1.705 m, there are several bins with values close to this minimum where the difference between maximum water level at the beginning and end of the bin is zero or very close to zero. Thus $|\mathrm{d}y|$ in the equation 3.14 approaches zero, making it impossible to determine the probability distribution of maximum water level as $f_Y(y)$ becomes singular. Second, because the function is neither monotonically increasing nor decreasing in this case, Manning's *n* becomes double-valued for a single value of maximum water level. This makes the probability distribution very complicated to generate, because the numerical derived distribution approach requires the probability of Manning's *n* in each bin to be conserved in order to determine the probability of the consecutive bin of maximum water level. Third, for a monotonically increasing function, the derived cumulative probability distribution is determined using $F_Y(y) = F_X(x)$ from equation 3.1. However, for a monotonically decreasing function, then equation 3.12 applies where $F_Y(y) = 1 - F_X(x)$. A test was carried out to examine whether it was possible to use the derived distribution approach to determine the cumulative probability distribution from both sides of the response function approach assuming monotonic functions either side of the

minimum. Preliminary results indicate that this heuristic approach did not generate a sensible cumulative probability distribution in maximum water level at Hatia. Thus, it is concluded that the present version of the numerical derived distribution approach is not applicable for cases like Haita, where the response function is not wholly monotonic.

5.3.6. Concluding remarks

Overall, the expected value and standard deviation of maximum water level at selected sites (Sandwip, Char Purulia, and Tiger Point) around the Meghna estuary and Bay of Bengal are very sensitive to the mean and standard deviation of Manning's *n*. This indicates that uncertainty in Manning's roughness coefficient as an input (possibly tuning) parameter in a standard shallow flow model, has a severe impact on uncertainty in the estimated value of maximum water level (which is used in practice as an indicator of potential flood inundation of the nearby coastal region). The results demonstrate that it is of utmost importance to upgrade present modelling practices in Bangladesh so that observed field data on bed roughness is incorporated in any computational model of the Meghna estuary and Bay of Bengal. Obviously, many important hydrodynamic and morphodynamic parameters are very dependent on the estimate of bed roughness in any shallow flow model. Given the present lack of information on the bed roughness of the Meghna estuary and Bay of Bengal, it is recommended that a field campaign be conducted in the Meghna estuary and the Bay of Bengal to collect high quality data on bed roughness (in particular its spatial distribution and local uncertainty). Armed with this information, modellers would have much greater confidence in coastal flood prediction for Bangladesh using suitably calibrated hydro-morphodynamic models.

It should be noted that the numerical derived distribution approach used herein is presently limited to cases where there is a single-valued monotonic functional relationship between single input and single output variables of interest. This was confirmed by the case concerning maximum water level

uncertainty at Hatia. Further investigation into the derived distribution approach is recommended in order to seek a more general technique that can apply to non-monotonic, multi-valued response functions between input and output variables.

Chapter 6

Effect of sea level rise uncertainty on estimation of maximum water level around Meghna estuary

6.1. Introduction

The Ganges-Brahmaputra-Meghna delta is under threat of sea level rise from global warming, putting its coastal community under huge flood risk. In the 5th Assessment Report by IPCC (*Church et al., 2013*) the local sea level rise in the northern Bay of Bengal is predicted to range from 0.1 to 0.3 m by 2050 and from 0.3 to 0.6 m by 2100. The relative sea level rise is location-specific, and depends on the bed topography, local coastline, and water depth, which are influencing factors for land subsidence and tidal amplification or dampening. This chapter discusses how uncertainty in sea level rise affects uncertainty in local maximum water level, an indicator of potential future flooding. IPCC model predictions of global sea level rise obtained for different combinations of contributing factors are incorporated in the Delft3D hydrodynamic model of the Meghna Estuary and Bay of Bengal. Model results from the same locations as considered in chapter 4 are examined to investigate uncertainty propagation from sea level rise to maximum water level.

6.2. Model set up

The two-dimensional-depth averaged hydrodynamic Delft3D model, established in chapter 5, was used for the sea level uncertainty study, with a few adjustments. The domain and the bathymetry were the same as shown in figure. 5.1, with the bathymetry altered throughout to simulate a given level of sea level rise. The model contained two upstream open boundaries carrying river discharges and one downstream open tidal boundary. The upstream boundary conditions were set the same as in Chapter 5, i.e., constant river discharges representing a peak flood situation. The downstream tide boundary was adjusted to the prescribed rise in sea level. Figure 1.10 in Chapter 1 shows the prediction of global sea level rise by IPCC with 95% confidence limits. Considering the data for year 2100, four expected (mean) values and four standard deviations of sea level rise were calculated for four different scenarios, RCP2.6, RCP4.5, RCP6.0, and RCP8.5 (*Church et al., 2013*). The values are listed in table 6.1. The RCP scenarios are described in chapter 1 under section 1.4.2. Then, a normal distribution was fitted to each scenario according to its respective mean and standard deviation in predicted sea level rise (figure 6.1). RCP4.5 and RCP6.0 have almost the same mean and standard deviation, thus only one distribution needed to be fitted to represent these two scenarios. A series of simulations was then run, with the sea level increased incrementally from 0.1 to 1.20 m at the downstream boundary. Another input parameter is Manning's *n*. The spatial distribution of Manning's *n* shown in figure 5.3 in chapter 5 was used for all the cases in this chapter. Once the model outputs of maximum water level against sea level rise had been determined, a cubic spline was fitted using MATLAB to interpolate the relationship between maximum water level and sea level rise at each location considered in Chapter 5. Then, using the method described in Chapter 3, the PDF and CDF of maximum water level were obtained.

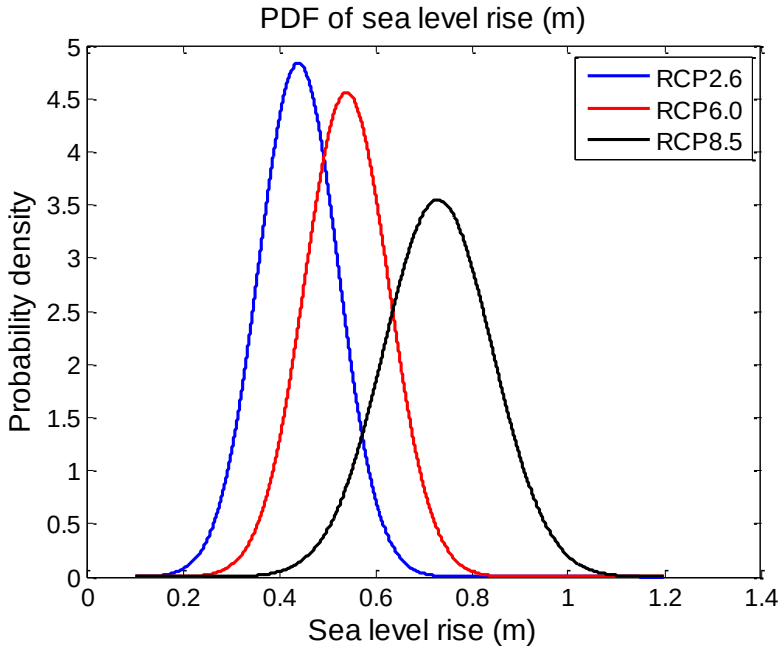

(a)

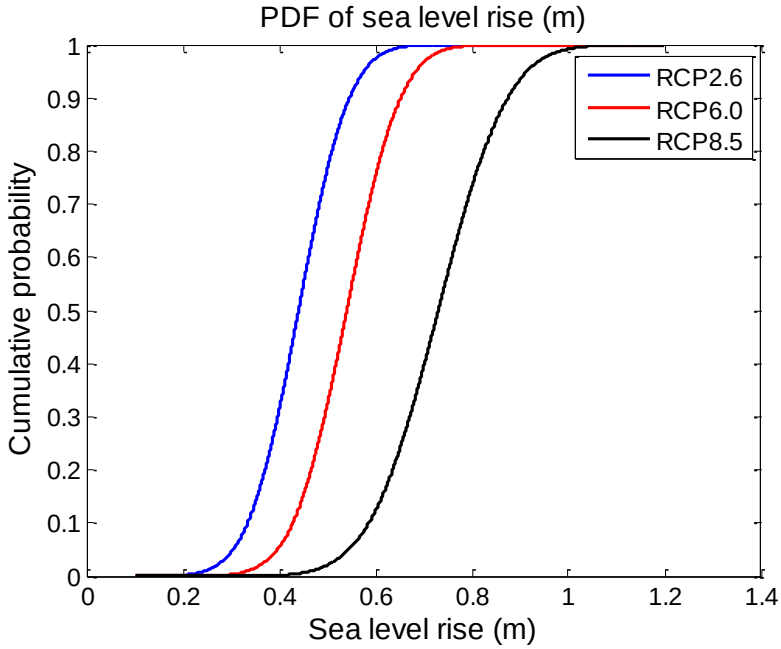

(b)

Figure 6.1: (a) PDF and (b) CDF of global sea level rise fitted to IPCC scenarios RCP2.6, RCP6.0, and RCP8.5.

Table 6.1: Expected value and standard deviation of sea level rise by 2100 predicted by different IPCC scenarios from Church et al. *(2013*)

IPCC scenario	Expected value (mean) sea level rise (m)	Standard deviation in sea level rise (m)
RCP2.6	0.44	0.0825
RCP4.5	0.53	0.0875
RCP6.0	0.54	0.0875
RCP8.5	0.73	0.1125

6.3. Uncertainty in model prediction of maximum water level when including the effect of sea level rise

6.3.1. Convergence Test

A series of model runs was performed for specific values of mean sea level rise with respect to a datum ranging from 0.1 to 1.2 m. Figure 6.2 shows the model output where the maximum water level increases almost linearly with increasing mean sea level rise. Figure 6.3 shows the PDF and CDF of sea level rise corresponding to a normal distribution with an expected value of 0.54 m and standard deviation of 0.0875 m, chosen for the convergence test. As in chapter 5, a maximum water level convergence test is then carried out, with Sandwip Island chosen as the reference location.

In order to perform the convergence test on the maximum water level, and thus verify the statistical calculations, the derived PDF and CDF distributions were divided into a discrete number of bins and then the statistical moments determined. Figure 6.4 depicts the resulting probability density functions and cumulative density functions of maximum water level at Sandwip obtained for different numbers of bins used to discretize the probability density function of sea level rise. The expected value of maximum water level (Z), the variance,

the non-dimensional skewness, and the non-dimensional kurtosis are calculated using equations 5.11, 5.12, 5.15, and 5.16 respectively.

Table 6.2 provides a summary of the resulting statistics of maximum water level at Sandwip. Table 6.2 indicates that the probability distribution of maximum water level is sensitive to the number of bins used to discretize the PDF of sea level rise. The expected value, variance, standard deviation and non-dimensional skewness of maximum water level converge to within 3 significant figures and the non-dimensional kurtosis converges to within 2 significant figures for 601 bins upwards. Consequently, the number of bins used in the later analysis is chosen as 601. The non-dimensional skewness is positive-valued with magnitude close to zero; this indicates that the probability distribution of maximum water level at Sandwip is almost symmetric and very similar to a truncated normal distribution. The non-dimensional kurtosis has a value of 3, confirming that the distribution is close to normal (truncated).

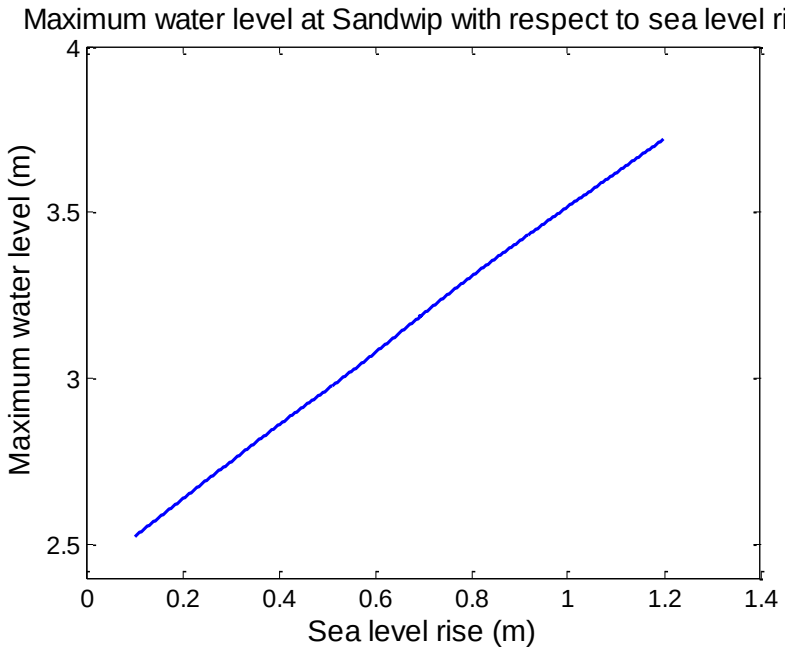

Figure 6.2: Functional relationship between maximum water level and sea level rise at Sandwip.

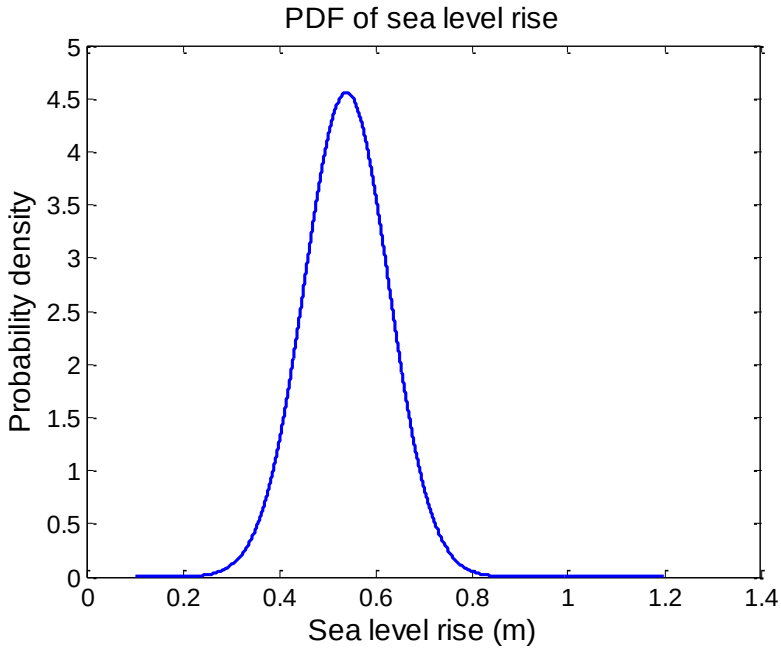

(a)

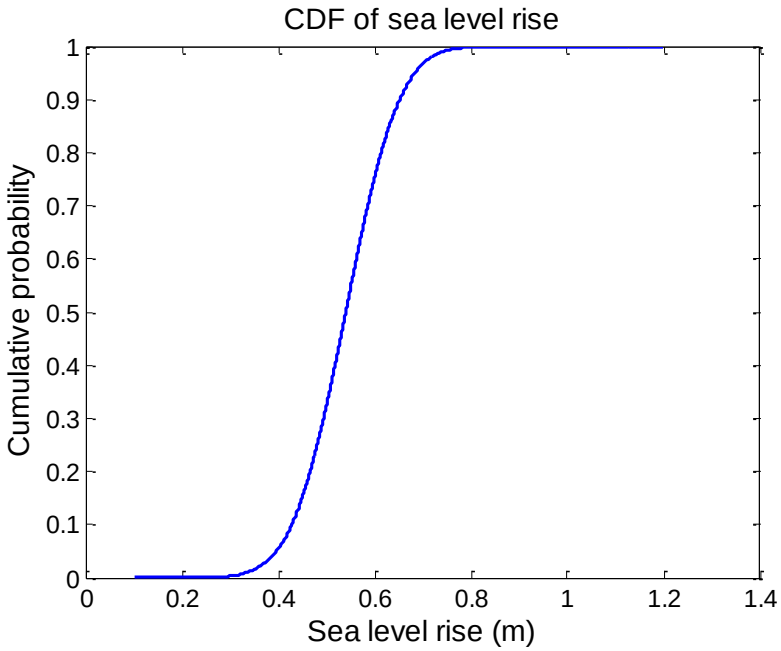

(b)

Figure 6.3: (a) Probability density function and (b) cumulative density function of maximum water level at Sandwip for a normal distribution of sea level rise with mean value of 0.54 m and standard deviation of 0.0875 m.

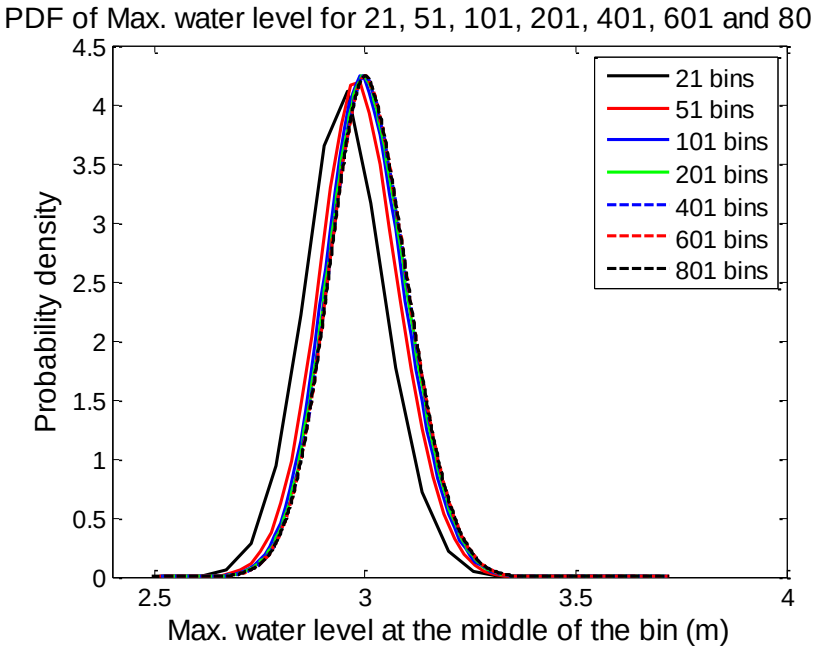

(a)

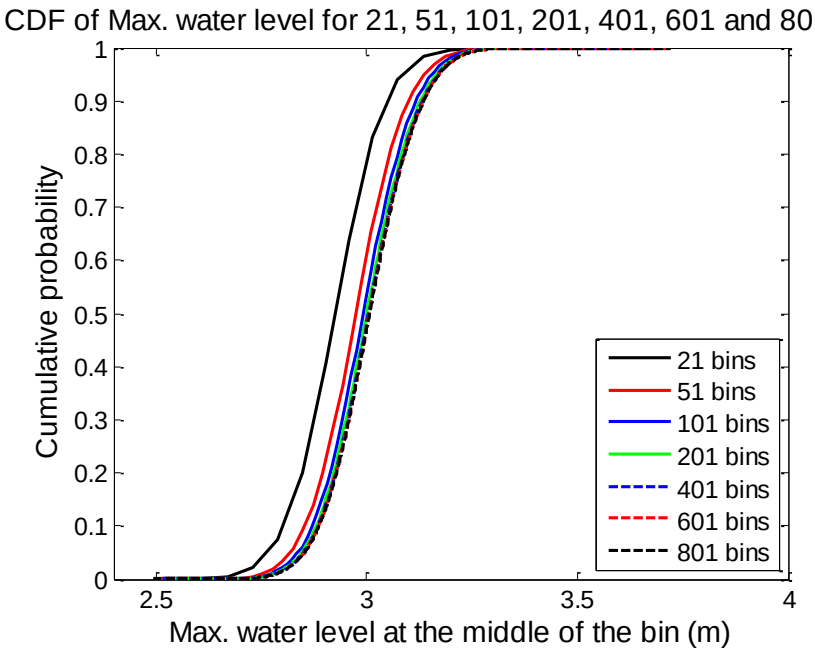

(b)

Figure 6.4: (a) PDF and (b) CDF of maximum water level at Sandwip plotted for different numbers of bins for a normal distribution of sea level rise with mean value of 0.54 m and standard deviation of 0.0875 m.

Table 6.2: Convergence of statistical moments of maximum water level at Sandwip.

No. of bins	Expected value of max. water level, $E[Z]$ (m)	Variance, σ_Z^2 (m^2)	Standard deviation, σ_Z (m)	Non-dimensional skewness, $Skew_n(Z)$	Non-dimensional kurtosis, $Kurt_n(Z)$
21	2.9535	0.00943	0.0971	0.0515	3.1528
51	2.9876	0.00936	0.0967	0.0699	3.1037
101	2.9994	0.00938	0.0969	0.0756	3.0843
201	3.0054	0.00940	0.0970	0.0783	3.0741
401	3.0084	0.00942	0.0970	0.0796	3.0689
601	3.0094	0.00942	0.0971	0.0800	3.0671
801	3.0099	0.00942	0.0971	0.0803	3.0663

6.3.2. Uncertainty in maximum water level at Sandwip

After selecting the number of required bins, the PDFs and CDFs of maximum water level for the RCP2.6, RCP6.0, and RCP8.5 scenarios considered by IPCC are obtained from the corresponding input PDF distributions in sea level rise (figure 6.5), following the numerical derived distribution procedure described in Chapter 3. As the expected value of sea level rise increases, the peak value in the PDF of maximum water level progressively moves to higher values of sea level rise. But the magnitude of the peak of the distribution of maximum water level decreases as the expected value of sea level rise increases. Maximum water level at Sandwip is proportional to sea level rise (figure 6.2), so the PDF with higher mean of sea level rise will result in the PDF with higher mean of maximum water level. Now, when uncertainty in sea level rise increases according to table 6.1, this uncertainty is propagated to maximum water level causing the PDF with higher uncertainty as well. Since the total probability should be 1, the PDF having larger standard deviation obviously reaches lower peak than the PDF having smaller standard

deviation. Conversely, the standard deviation of maximum water level increases as the expected value of sea level rise increases.

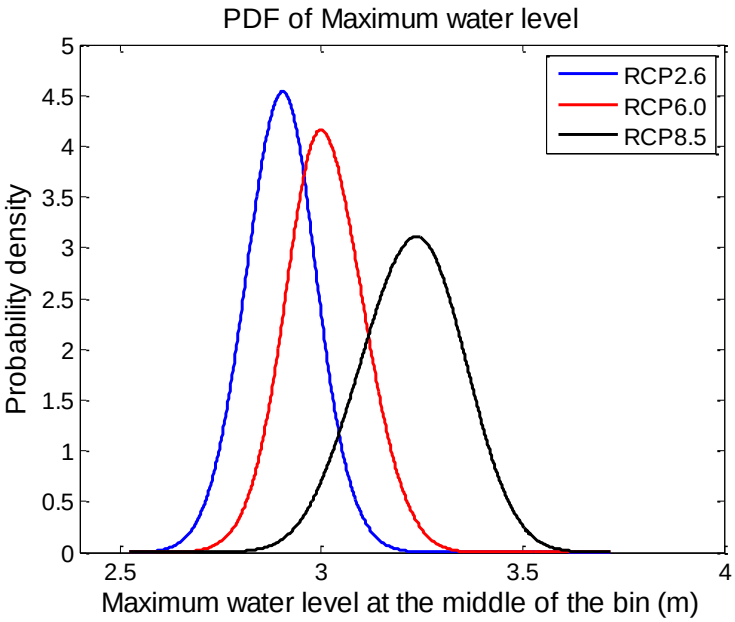

(a)

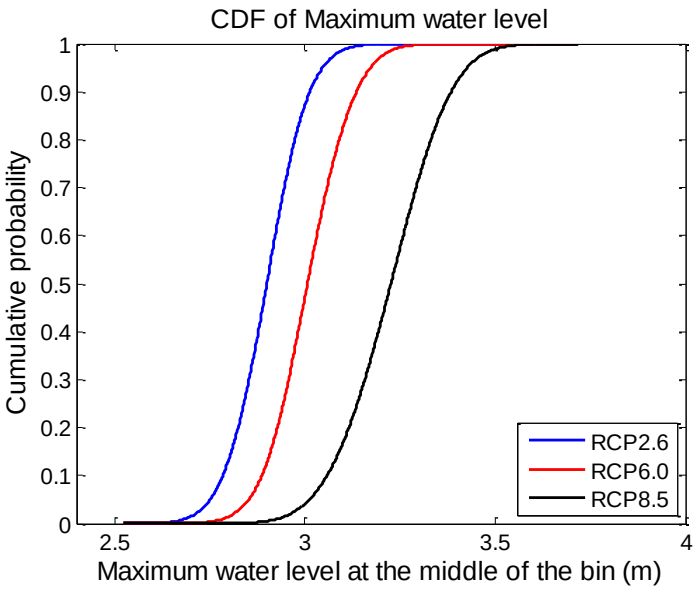

(b)

Figure 6.5: (a) Probability density function and (b) cumulative density function of maximum water level at Sandwip for three normal distributions of sea level rise representing IPCC scenarios: RCP2.6, RCP6.0, and RCP8.5.

Table 6.3 lists the expected value and higher order moments for the maximum water level obtained for the three scenarios of sea level rise. As the sea level rise increases from 0.44 m to 0.73 m, the expected maximum water level increases by about 11%, and the standard deviation increases by 40%. The non-dimensional skewness remains about zero indicating a truncated normal distribution in maximum water level. Also, the non-dimensional skewness is very close to 3 in each case, which again indicates a normal distribution (truncated).

Table 6.3: Expected value and other statistical moments of maximum water level at Sandwip for three different sea level rise scenarios by IPCC

IPCC scenario	Mean sea level rise (m)	Standard deviation in sea level rise (m)	Expected value of max. water level, $E[Z]$ (m)	Standard deviation, σ_Z (m)	Non-dimensional skewness, $Skew_n(Z)$	Non-dimensional kurtosis, $Kurt_n(Z)$
RCP2.6	0.44	0.0825	2.90	0.0901	-0.0094	3.0882
RCP6.0	0.54	0.0875	3.01	0.0971	0.0803	3.0663
RCP8.5	0.73	0.1125	3.22	0.1264	-0.07	2.8609

Next, the amount of rise in sea level is subtracted from the model output of maximum water level; this enables assessment as to how uncertainty in sea level rise affects the uncertainty in maximum water level when the linear effect of sea level rise is removed. Figure 6.6 shows the cubic spline relationship between the maximum water level after deduction of sea level rise. In this case, the relationship is no longer predominantly linear, though the curve is monotonically increasing. Following the same procedure as described in chapter 3, the PDF and CDF distributions of maximum water level minus sea level rise are derived (figure 6.7). It can be seen from figure 6.7(a) that the PDF changes from an almost symmetric shape for RCP2.6 to left-skewed for RCP6.0, and then becomes right-skewed for RCP8.5 scenario. With

increasing values of maximum water level minus sea level rise, the PDF becomes flatter.

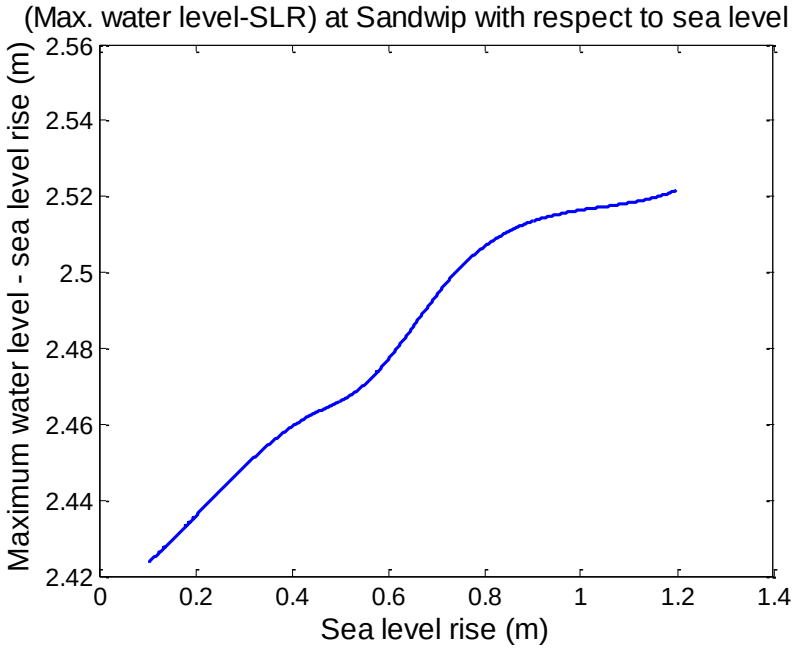

Figure 6.6: Functional relationship between maximum water level (after deducting sea level rise) with sea level rise at Sandwip

Table 6.4 summarizes the expected values and statistical moments and the expected values of maximum water level minus sea level rise at Sandwip. As the rise in sea level increases from 0.44 m to 0.73 m, the expected maximum water level increases by only 1.3%, but the standard deviation increases by 80%. The non-dimensional skewness confirms that the distribution related to RCP2.6 sea level rise is a truncated normal distribution (non-dimensional skewness for RCP2.6 is around zero). The probability density distribution becomes skewed to the right side of the mean for the RCP6.0 scenario (positive non-dimensional skewness). And the PDF becomes skewed to the left side of the mean of the distribution for the RCP8.5 scenario (negative non-dimensional skewness). The non-dimensional kurtosis for RCP2.6 is above 3, which indicates that the distribution is narrower than the standard normal distribution, whereas for RCP6.0 the distribution is slightly above 3 indicating than the probability distribution is close to a normal distribution (truncated).

For RCP8.5 the non-dimensional skewness is below 3 suggesting that the distribution is flatter than a standard normal distribution.

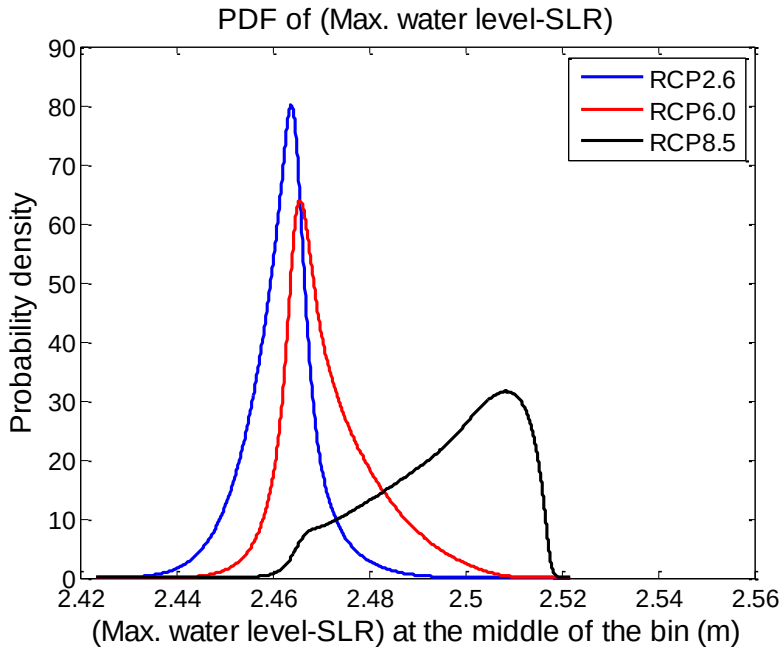

(a)

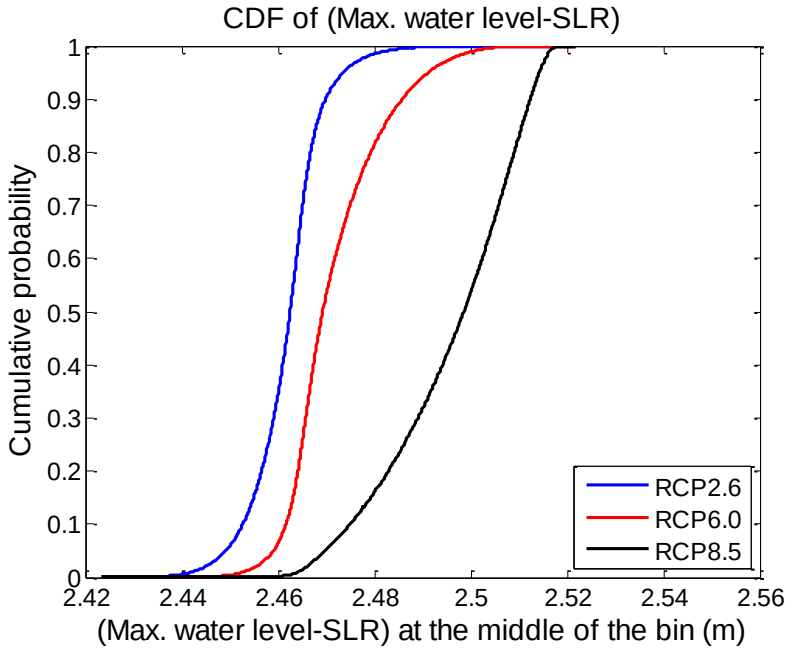

(b)

Figure 6.7: (a) PDF and (b) CDF of maximum water level after deducting sea level rise at Sandwip for three normal distributions of sea level rise representing IPCC scenarios: RCP2.6, RCP6.0, and RCP8.5.

Table 6.4: Expected value and other statistical moments of maximum water level without the linear effect of sea level rise at Sandwip for three different sea level rise scenarios by IPCC

IPCC scenario	Mean sea level rise (m)	Standard deviation in sea level rise (m)	Expected value of (Max. water level-sea level rise), $E[Z]$ (m)	Standard deviation, σ_Z (m)	Non-dimensional skewness, $Skew_n(Z)$	Non-dimensional kurtosis, $Kurt_n(Z)$
RCP2.6	0.44	0.0825	2.4616	0.0074	-0.0013	4.89
RCP6.0	0.54	0.0875	2.4714	0.0099	0.8529	3.81
RCP8.5	0.73	0.1125	2.4957	0.0138	-0.5472	2.367

To investigate in more detail the influence of choice of mean sea level rise on the PDF and CDF maximum water levels after subtracting sea level rise, Figure 6.8 shows the PDFs and CDFs of maximum water level minus sea level rise obtained for sea level rise with a constant standard deviation of 0.0875 m and the mean varied in 0.05 m increments from 0.4 m to 0.8 m. For the lowest value of mean sea level rise, the PDF is right-skewed. As the mean sea level rise is increased to 0.5 m, the PDF becomes taller and narrower, and more symmetric. As mean sea level rise changes from 0.5 to 0.65 m, the peak PDF value drops considerably and the PDF becomes fatter, first left skewed and then more symmetric. For higher values of mean sea level rise, the PDF becomes progressively taller, and right-skewed. There is obviously a substantial change in the water level physics at Sandwip as the mean sea level rises. Table 6.5 gives the expected value and statistical moments obtained for the foregoing cases.

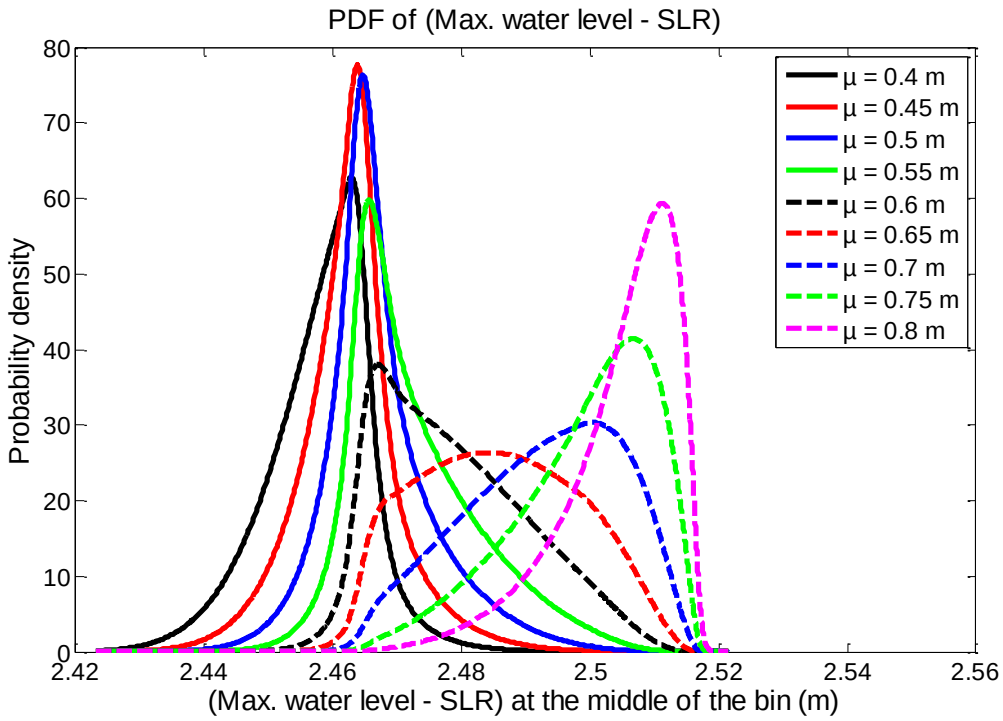

(a)

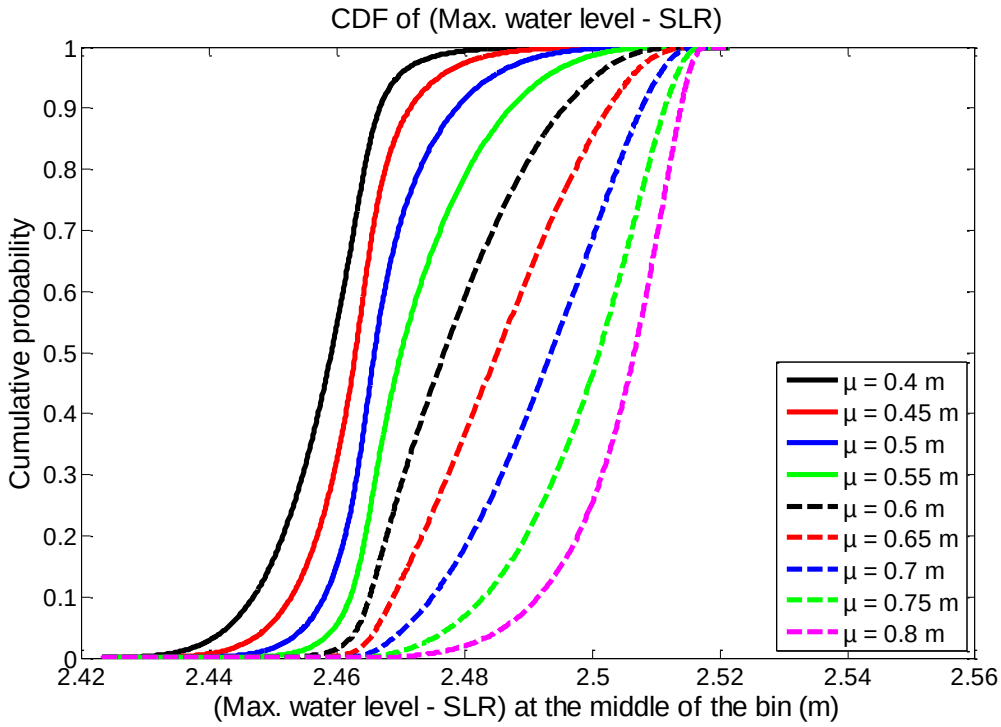

(b)

Figure 6.8: (a) PDF and (b) CDF of maximum water level after deducting sea level rise at Sandwip for nine normal distributions of sea level rise with different mean values ranging from 0.4 to 0.8 m and constant standard deviation of 0.0875 m.

Table 6.5: Expected value and other statistical moments of maximum water level after the linear effect of sea level rise has been removed, for nine different mean of sea level rise scenarios, at Sandwip.

Mean of sea level rise (m)	Standard deviation in sea level rise (m)	Expected value of (Max. water level- sea level rise), $E[Z]$ (m)	Standard deviation, σ_Z (m))	Non-dimensional skewness, $Skew_n(Z)$	Non-dimensional kurtosis, $Kurt_n(Z)$
0.40	0.0875	2.4572	0.0083	-0.01293	2.9717
0.45	0.0875	2.4625	0.0080	0.2014	3.8935
0.50	0.0875	2.4672	0.0088	0.7839	5.0144
0.55	0.0875	2.4725	0.0102	0.8195	4.7870
0.60	0.0875	2.4786	0.0188	0.5014	3.5519
0.65	0.0875	2.4855	0.0124	0.0925	2.5356
0.70	0.0875	2.4925	0.0121	-0.3276	2.1198
0.75	0.0875	2.4990	0.0109	-0.7478	2.2725
0.80	0.0875	2.5044	0.0090	-1.1660	4.2588

It is seen from table 6.5 that for a 100% increase in the mean of sea level rise, the mean of the maximum water level without the sea level rise increases by only about 2%. Although the standard deviation (which is a measure of uncertainty) is generally quite small, its value is relatively more sensitive to mean sea level rise. The standard deviation increases from about 0.0083 m to 0.0124 m as the mean sea level rise increases from 0.4 to 0.65 m, after which the standard deviation starts to reduce, falling to 0.0090 m when the mean sea level rise is 0.8 m. The values of skewness and kurtosis confirm the shape of the PDFs. For increasing values of mean sea level rise, the PDF of maximum water level without sea level rise becomes first increasingly left-skewed (negative value for non-dimensional skewness) reaching a maximum non-dimensional skewness when the sea level rise is 0.55 m, and then alters to become progressively right-skewed as the mean sea level rise exceeds 0.7

m. The non-dimensional kurtosis commences from about 3 at the lowest value of mean sea level rise, corresponding to a normal distribution (truncated), then exceeds 3 until mean sea level rise is about 0.6 m, indicating the distribution is steeper than the standard normal distribution. For mean sea level rise between 0.65 m and 0.75 m, the non-dimensional kurtosis is below 3, and the PDFs are flatter than the standard normal distribution. The PDF distribution becomes narrower again at 0.8 m mean sea level rise as the non-dimensional kurtosis again rises above 3.

A similar study is now conducted for sea level rise of constant mean 0.5 m and standard deviation varying from 0.06 m to 0.14 m. Figure 6.9 shows the derived PDFs and CDFs of maximum water level minus sea level rise. As the standard deviation in sea level rise increases, the peak in the PDF of maximum water level minus sea level rise occurs at slightly lower values of maximum water level minus sea level rise, and the tail of the distribution extends more. Table 6.6 lists the expected value and other statistical moments for the distributions shown in Figure 6.9. The mean values of all these PDFs are the same up to two significant figures. But with 133% increase of standard deviation in sea level rise, the standard deviation in maximum water level after deduction of sea level rise increases by about 206%. All values of non-dimensional skewness are positive, indicating that all the probability distributions are skewed to the right side of the mean value. Also, all the values of non-dimensional kurtosis are above 3, which indicates that a standard normal distribution would be fatter than all these PDFs.

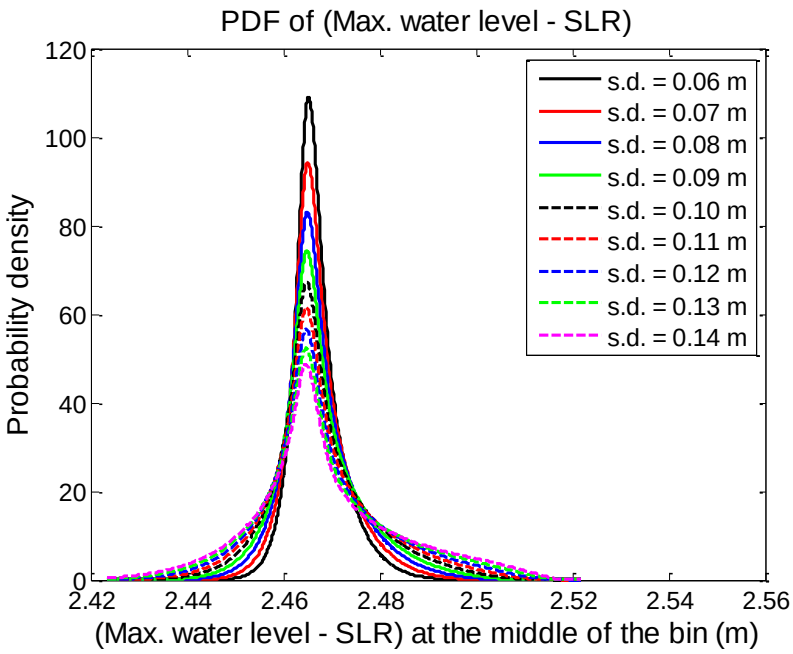

(a)

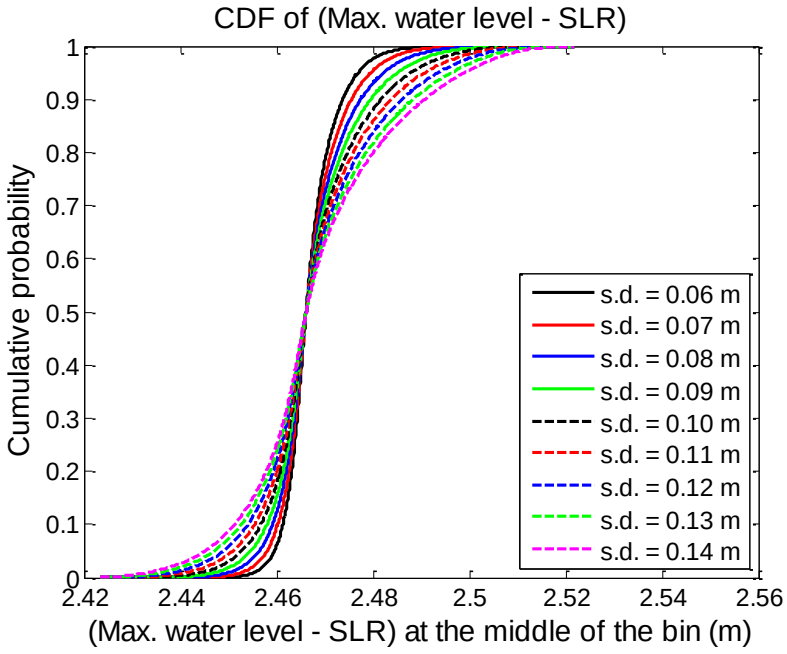

(b)

Figure 6.9: (a) PDF and (b) CDF of maximum water level after deducting sea level rise at Sandwip for 9 normal distributions of sea level rise with constant mean value of 0.5 m and different standard deviations ranging from 0.06 to 0.14 m

The relationship between maximum water level (after deducting SLR) and SLR is non-linear (figure 6.6). The functional relationship between these two is still monotonic, but the slope changes its direction multiple times. Being monotonically increasing function, PDF of SLR with higher mean results in PDF of maximum water level (without SLR) with higher mean as well. But the skewness and kurtosis vary dramatically. The reason is their non-linear relationship with varying slope direction. When different values of mean of SLR are chosen to create PDFs, the shape of derived PDFs (which is expressed through skewness and kurtosis) of maximum water level after deducting SLR also changes accordingly as shown in figure 6.8(a). However, with different standard deviations of SLR, no such thing occurs with the PDFs of maximum water level after deducting SLR as seen in figure 6.9(a). This is because the mean is kept constant and so the PDFs do not get influenced by the fluctuating functional relationship.

Table 6.6: Expected value and other statistical moments of maximum water level after the linear effect of sea level rise has been removed, for nine different standard deviation in sea level rise scenarios, at Sandwip.

Mean sea level rise (m)	Standard deviation in sea level rise (m)	Expected value of (max. water level- sea level rise), $E[Z]$ (m)	Standard deviation, σ_Z (m))	Non-dimensional skewness, $Skew_n(Z)$	Non-dimensional kurtosis, $Kurt_n(Z)$
0.50	0.06	2.4666	0.0053	0.8936	4.0234
0.50	0.07	2.4668	0.0065	0.8723	5.2870
0.50	0.08	2.4671	0.0078	0.8269	5.1744
0.50	0.09	2.4673	0.0091	0.7693	4.9699
0.50	0.10	2.4674	0.0104	0.7203	4.7240
0.50	0.11	2.4674	0.0117	0.7170	4.4778
0.50	0.12	2.4668	0.0130	0.8066	4.2682
0.50	0.13	2.4655	0.0144	1.0177	4.1197
0.50	0.14	2.4630	0.0162	1.3073	3.9048

Next, in order to examine the effect of mean sea level rise on excess maximum water level at Sandwip, further analysis is carried out concerning the statistical relationship between excess maximum water level and sea level rise. Here, the excess maximum water level is defined as the maximum water level minus both the mean sea level rise and the reference maximum water level obtained for no sea level rise. Figure 6.10 shows the cubic spline fit to data on excess maximum water level at Sandwip plotted against sea level rise. The relationship is nonlinear, even though there is a progressive increase in excess maximum water level from about 0.02 m to 0.12 m for a sea level rise from 0.1 to 1.2 m.

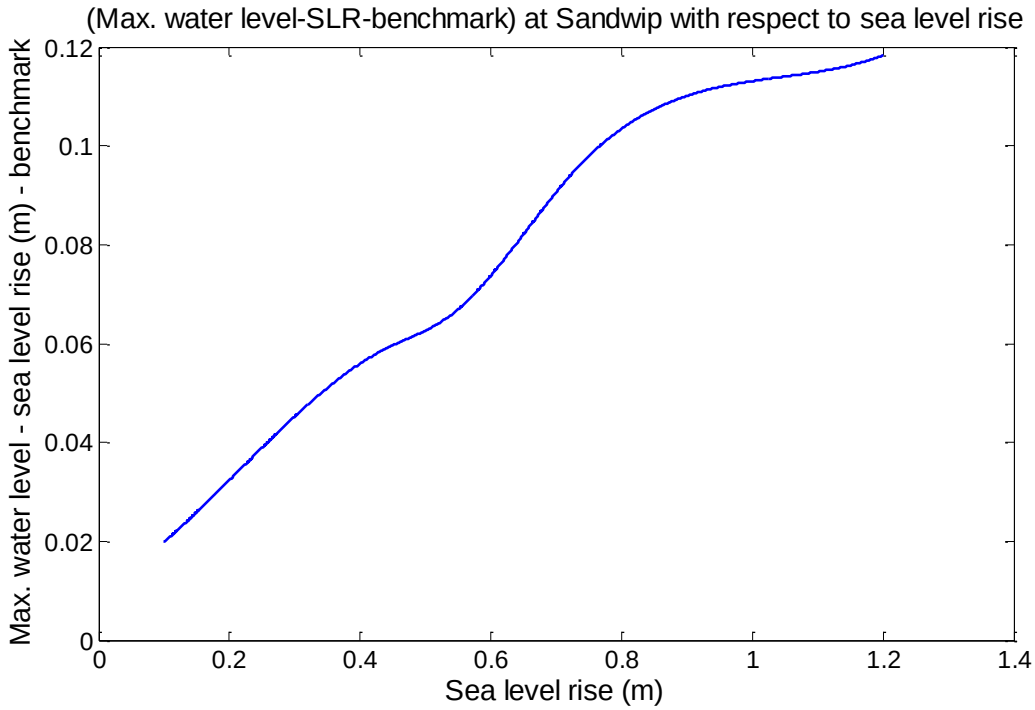

Figure 6.10: Functional relationship between excess maximum water level (maximum water level minus both sea level rise and the benchmark maximum sea level obtained for no sea level rise) and sea level rise at Sandwip.

Figure 6.11 shows the PDF and CDF distributions of excess maximum water level obtained at Sandwip for the normal distributions in mean sea level corresponding to the RCP2.6, RCP6.0, and RCP8.5 scenarios.

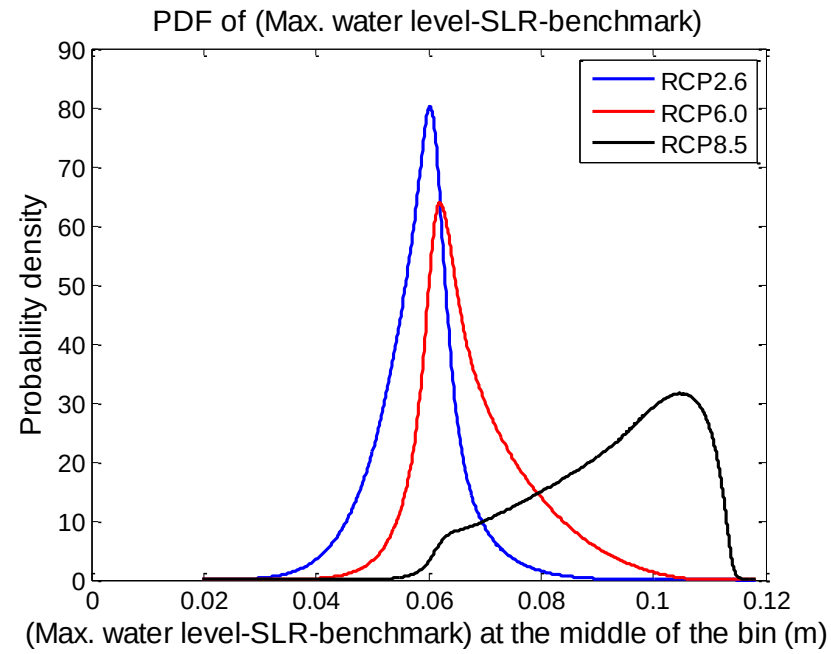

(a)

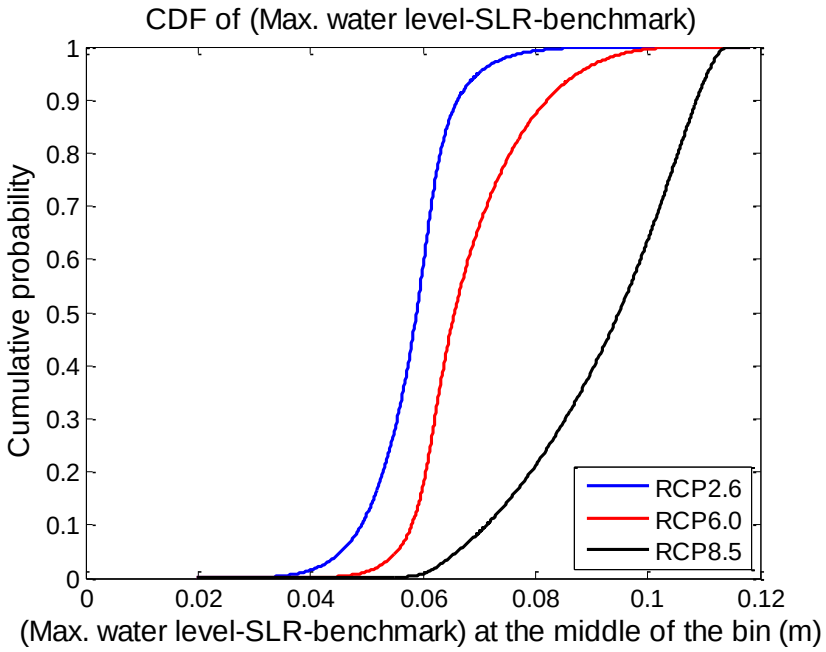

(b)

Figure 6.11: (a) PDF and (b) CDF of excess maximum water level (maximum water level minus both sea level rise and the benchmark maximum water level for no sea level rise) at Sandwip for three normal distributions of sea level rise representing IPCC scenarios: RCP2.6, RCP6.0, and RCP8.5.

The PDF is slightly right-skewed and quite tall for RCP2.6. It then alters to be left-skewed with a lower peak and long right-hand tail for RCP6.0. And the PDF is more complicated, with a further reduced peak, right-skewed and fatter for RCP8.5. This is a similar trend like the PDFs of maximum water level minus sea level rise (figure 6.7). Table 6.7 gives the expected value of excess maximum water level and other statistical moments.

Table 6.7: Expected value and other statistical moments of excess maximum water level at Sandwip for three different sea level rise scenarios fitted to RCP2.6, RCP6.0, and RCP8.5

IPCC scenario	Mean sea level rise (m)	Standard deviation in sea level rise (m)	Expected value of (Max. water level-sea level rise), $E[Z]$ (m)	Standard deviation, σ_Z (m)	Non-dimensional skewness, $Skew_n(Z)$	Non-dimensional kurtosis, $Kurt_n(Z)$
RCP2.6	0.44	0.0825	0.0583	0.0074	-0.0219	4.8890
RCP6.0	0.54	0.0875	0.0681	0.0099	0.8531	3.8142
RCP8.5	0.73	0.1125	0.0924	0.0139	-0.5536	2.3709

When the mean of the sea level rise increases by about 66%, then the mean of the excess maximum water level increases by about 58.5%. With about 36% increase in the standard deviation in sea level rise, the standard deviation in excess maximum water level increases about 88%. The non-dimensional skewness indicates that for RCP2.6, the PDF of excess maximum water level is mildly skewed to the left side of the mean of the distribution (negative value of non-dimensional skewness but magnitude close to zero). The PDF for RCP6.0 becomes skewed to the right of the mean value of the distribution (positive non-dimensional skewness) with increasing excess maximum water level. Meanwhile, the PDF for RCP8.5 becomes skewed to the left again (confirmed by the negative value of non-dimensional skewness). The PDFs

for RCP2.6 and RCP6.0 are narrower than for a standard normal distribution, whereas the PDF for RCP8.5 is fatter than for a standard normal distribution.

6.3.3. Uncertainty in maximum water level at Char Purulia

The next location considered is Char Purulia. In this case, Delft3D model outputs are analyzed after undertaking 5 simulations for different values of sea level rise ranging from 0.1 m to 1.20 m. Figure 6.12 shows that the maximum water level increases with increasing sea level rise and the relationship is again almost linear.

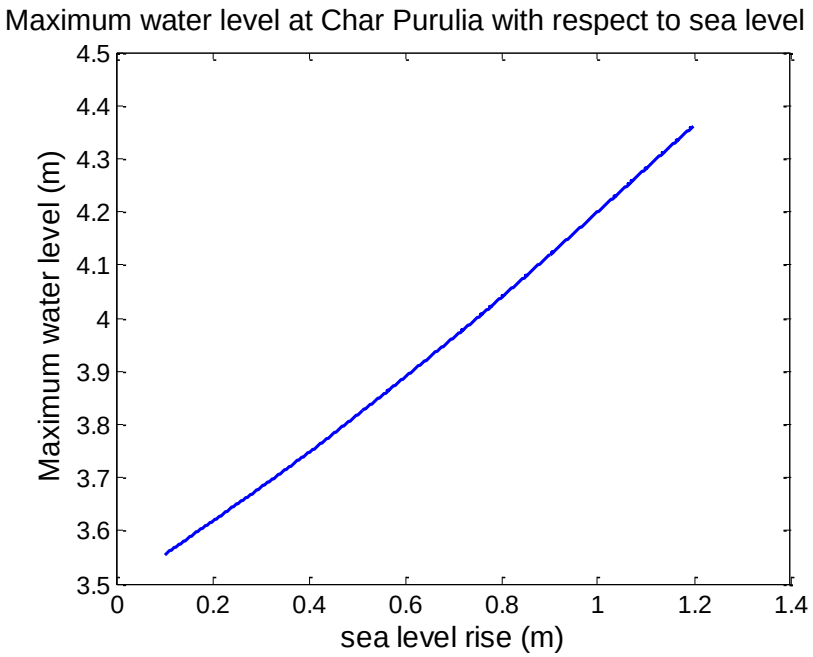

Figure 6.12: Functional relationship between maximum water level and sea level rise at Char Purulia.

At Char Purulia, both the river discharge and tide are dominant forcing parameters. An increasing sea level rise causes a corresponding increase in water level.

Figure 6.1 shows the PDF and CDF of sea level rise. Figure 6.13 shows the resulting probability distributions of maximum water level at Char Purulia obtained for the normal distributions fitted to the IPCC RCP2.6, RCP6.0, and RCP8.5 scenarios.

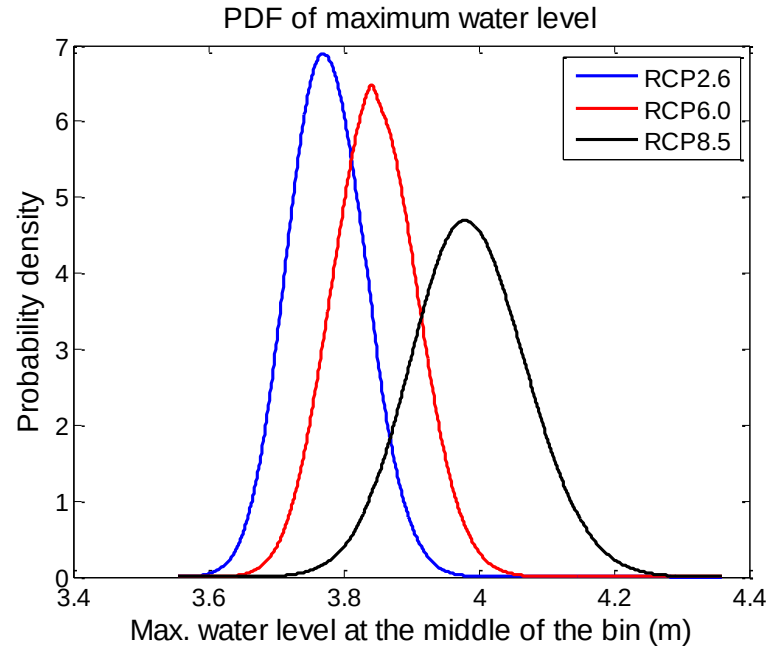

(a)

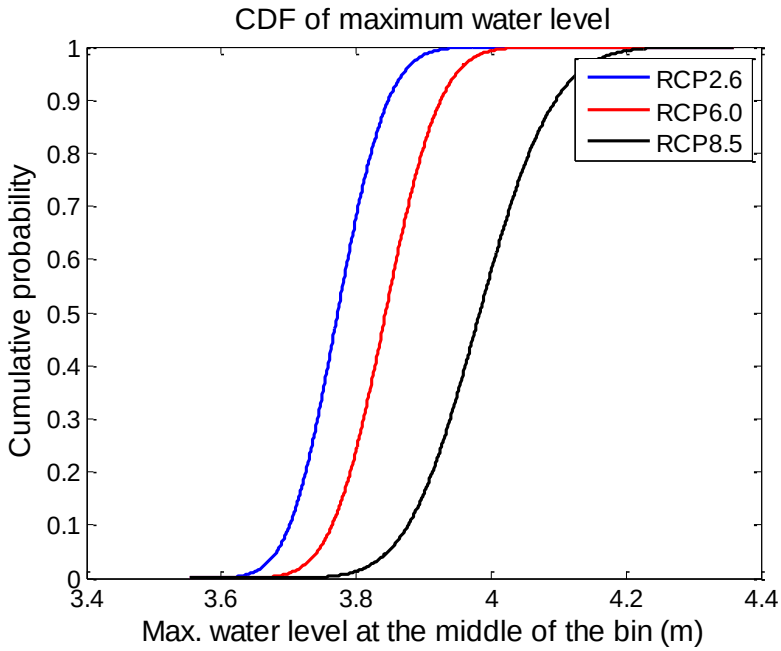

(b)

Figure 6.13: (a) Probability density function and (b) cumulative density function of maximum water level at Char Purulia for three normal distributions of sea level rise representing IPCC scenarios: RCP2.6, RCP6.0, and RCP8.5.

As at Sandwip, the peak in the PDF of maximum water level is reached at progressively higher values of maximum water level as the sea level rise increases. Again, the magnitude of the peak of the PDF of maximum water

level decreases with increasing sea level rise. Table 6.8 lists the expected value and other statistical moments of maximum water level at Char Purulia. The expected value of maximum water level increases about 5.5% when the mean sea level rise alters from 0.44 m to 0.73 m (66% increase), whereas the standard deviation in maximum water level increases by about 49.5% as the standard deviation of sea level rise increases by 36%. The non-dimensional skewness is slightly higher than zero and is positive-valued, indicating that the probability distribution of maximum water level is slightly skewed to the right of the mean value. The non-dimensional kurtosis is about 3, indicating that these three distributions of maximum water level are almost truncated normal distributions.

Table 6.8: Expected value and other statistical moments of maximum water level at Char Purulia for three different IPCC sea level rise scenarios

IPCC scenario	Mean sea level rise (m)	Standard deviation in sea level rise (m)	Expected value of max. water level, $E[Z]$ (m)	Standard deviation, σ_Z (m)	Non-dimensional skewness, $Skew_n(Z)$	Non-dimensional kurtosis, $Kurt_n(Z)$
RCP2.6	0.44	0.0825	3.7739	0.0571	0.1144	2.9691
RCP6.0	0.54	0.0875	3.8446	0.0628	0.0738	2.9828
RCP8.5	0.73	0.1125	3.9851	0.0854	0.1128	3.0220

To investigate the sharp peak of the derived PDF for RCP6.0 scenario (figure 6.13), a series of PDFs for maximum water level has been derived, keeping the standard deviation constant at 0.0875 m and changing the mean value of sea level rise from 0.4 m to 0.8 m (figure 6.14). Table 6.9 gives a summary of the statistical moments these probability distributions.

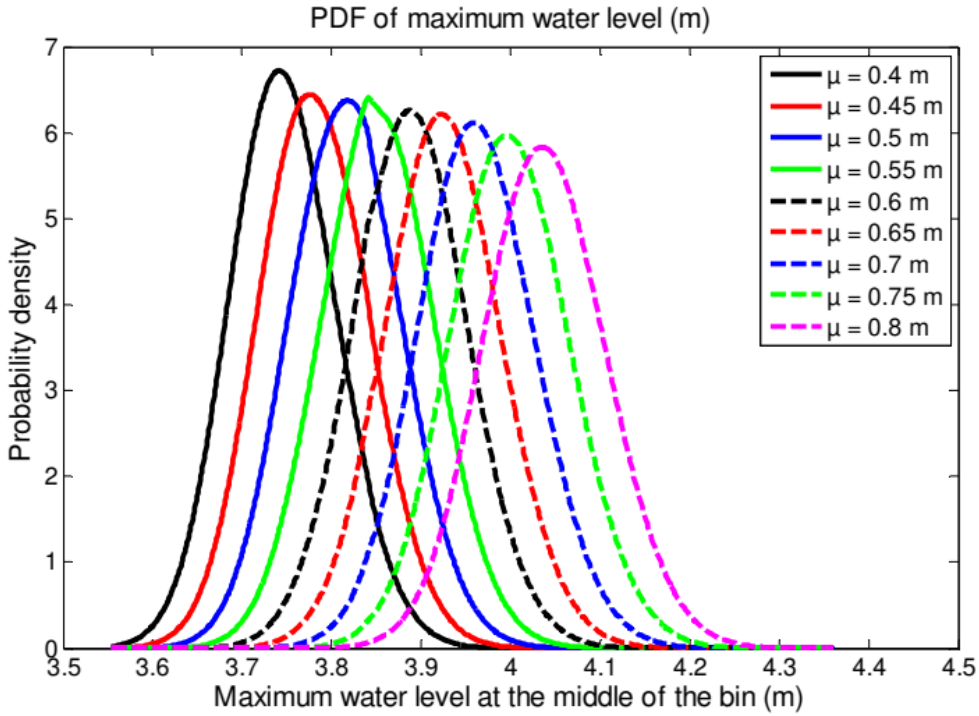

(a)

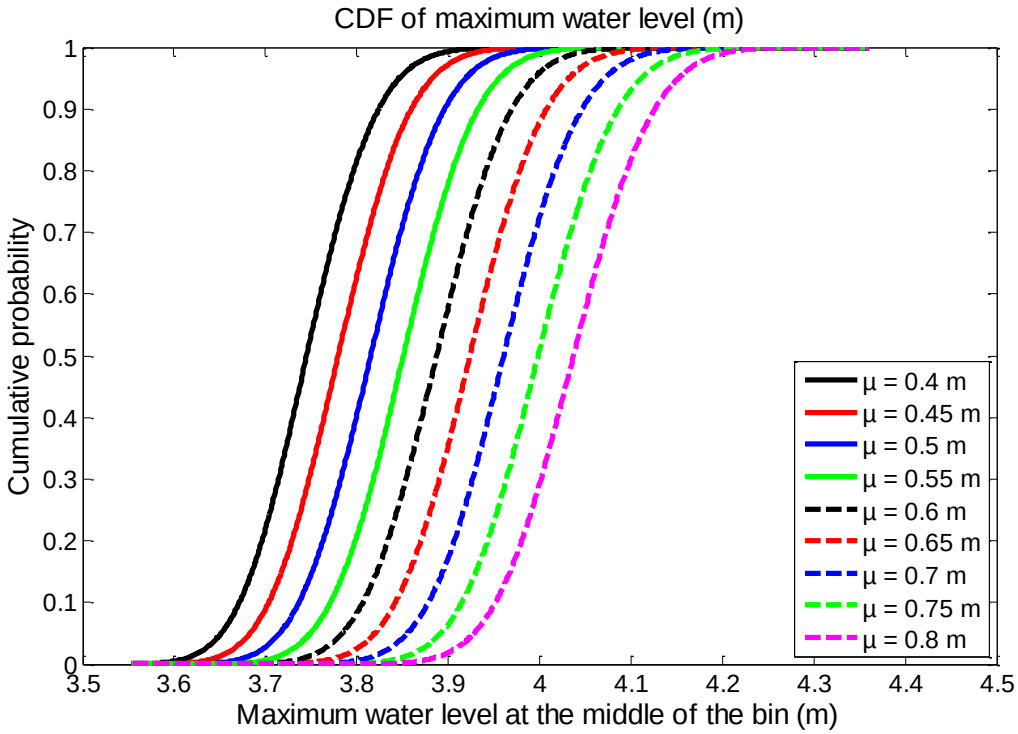

(b)

Figure 6.14: (a) PDF and (b) CDF of maximum water level at Char Purulia for normal distributions of sea level rise with 9 different mean values and constant standard deviation of 0.0875 m.

The peak value of the PDF of maximum water level decreases monotonically increasing mean value of sea level rise (figure 6.14), except when the mean value of sea level rise is 0.55 m and a small secondary peak can be seen the transferred probability distribution. However, the mean and standard deviation in maximum water level do fit a monotonically rising trend, without exception. All the probability distributions have positive non-dimensional skewness with magnitude slightly above 0, which means these are mildly right-skewed distributions. All PDFs have non-dimensional kurtosis about 3, establishing that the derived PDFs are very close to a truncated normal distribution. Finally, the total probability invariably reaches unity (figure 6.14b).

Table 6.9: Expected value and other statistical moments of maximum water level for nine sea level rise scenarios with constant standard deviation but varying mean value at Char Purulia.

Mean sea level rise (m)	Standard deviation in sea level rise (m)	Expected value of (max. water level-sea level rise), $E[Z]$ (m)	Standard deviation, σ_Z (m))	Non-dimensional skewness, $Skew_n(Z)$	Non-dimensional kurtosis, $Kurt_n(Z)$
0.40	0.0875	3.7459	0.0594	0.1937	3.0181
0.45	0.0875	3.7812	0.0608	0.1172	2.9949
0.50	0.0875	3.8164	0.0620	0.0875	2.9651
0.55	0.0875	3.8521	0.0629	0.0716	2.9650
0.60	0.0875	3.8883	0.0638	0.0693	2.9889
0.65	0.0875	3.9250	0.0647	0.0777	3.0183
0.70	0.0875	3.9622	0.0657	0.0894	3.0380
0.75	0.0875	4.0001	0.0669	0.0955	3.0378
0.80	0.0875	4.0386	0.0681	0.0913	2.9909

Now, consider the statistics of maximum water level minus sea level rise at Char Purulia. Figure 6.15 shows the response surface between maximum water level minus sea level rise and sea level rise obtained after cubic spline

interpolation. As the sea level rise increases, the deducted maximum water level decreases. The derived probability distributions for maximum water level minus sea level rise at Char Purulia are shown in Figure 6.16, where it can be seen that the tallest peak in the PDF occurs for RCP6.0. All PDFs and CDFSs are similar across the scenarios in that they all exhibit almost normal distributions, with RCP8.5, RCP 6.0, and RCP 2.6 having peak values at increasing values of maximum water level minus sea level rise.

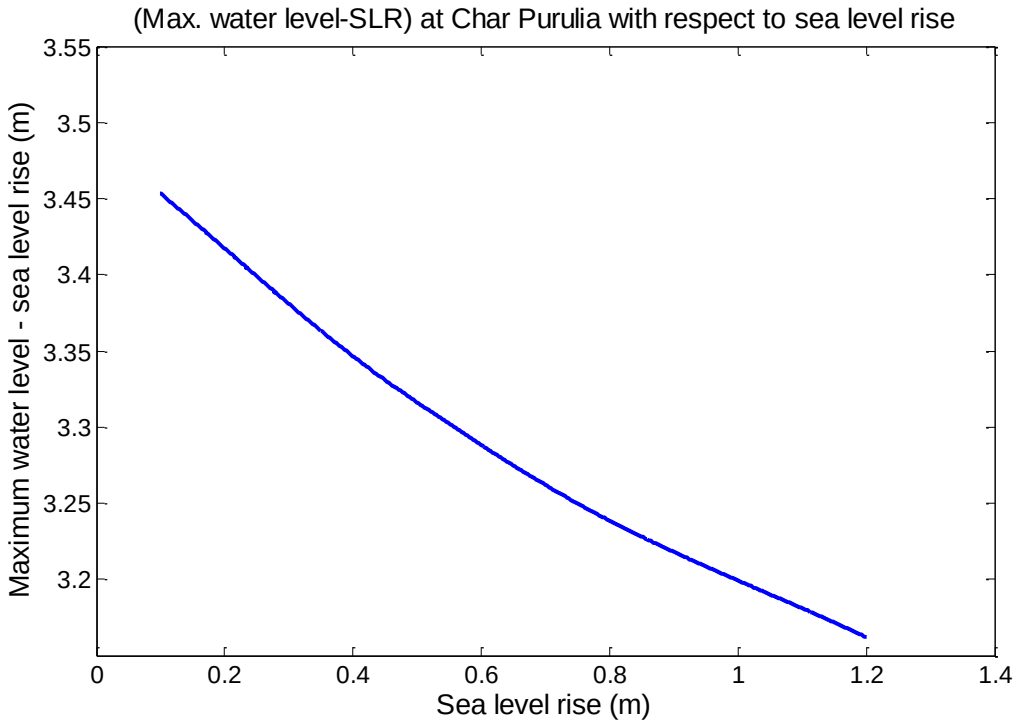

Figure 6.15: Functional relationship between maximum water level (after deducting sea level rise) with sea level rise at Char Purulia

Table 6.10 lists the expected values and other statistical parameters. The non-dimensional skewness shows that the three probability distributions are slightly skewed to right of the mean of the distribution (positive value) and the non-dimensional kurtosis (all are above 3.0) suggests that all the derived PDFs are a little steeper than a standard normal distribution. When the mean sea level rise increases by 66%, the mean of the maximum water level minus sea level rise decreases by about 2% only. An increase of 36% in standard deviation in sea level rise leads to a small (about 6%) increase in standard deviation in maximum sea level rise minus sea level rise.

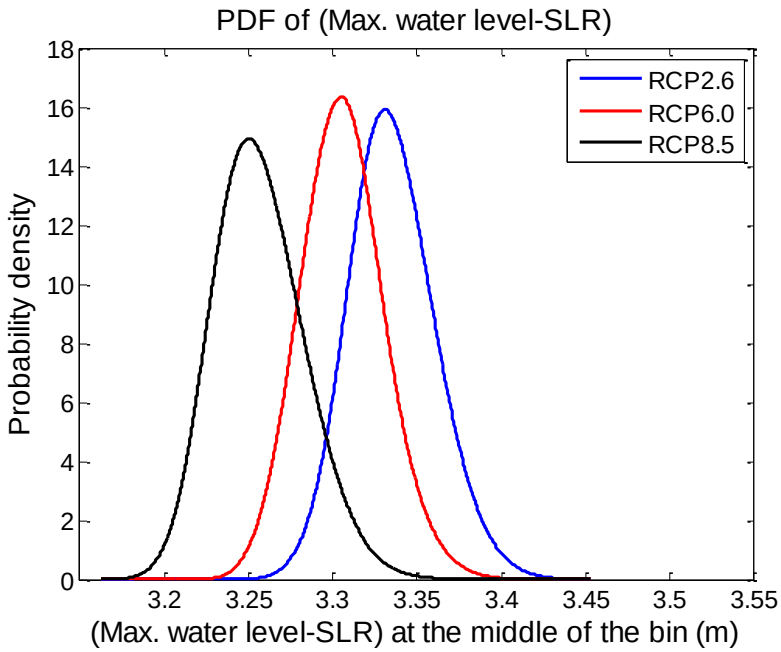

(a)

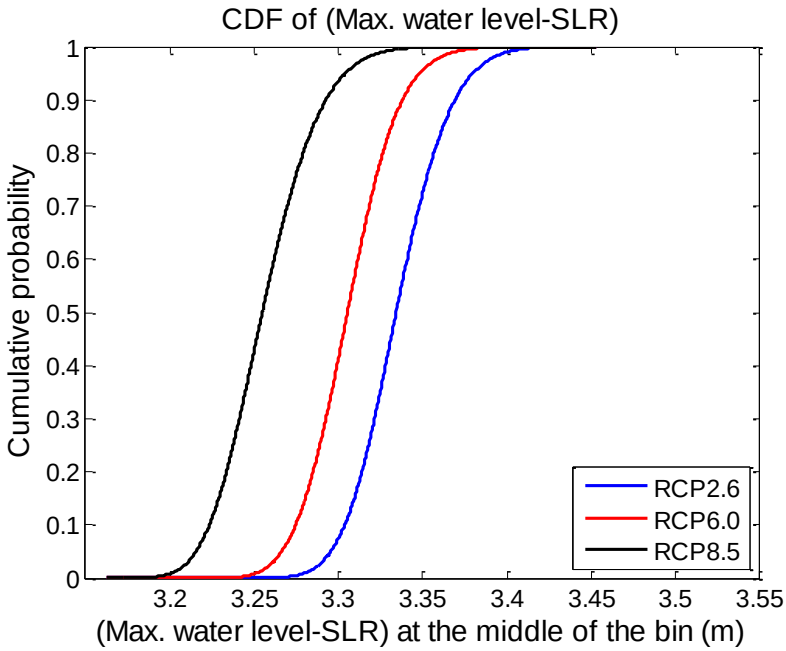

(b)

Figure 6.16: (a) PDF and (b) CDF of maximum water level after deducting sea level rise at Char Purulia for three normal distributions of sea level rise representing IPCC scenarios: RCP2.6, RCP6.0, and RCP8.5.

Table 6.10: Expected value and other statistical moments of maximum water level without linear effect of sea level rise at Char Purulia for three different IPCC sea level rise scenarios

IPCC scenario	Mean sea level rise (m)	Standard deviation in sea level rise (m)	Expected value of (max. water level-sea level rise), $E[Z]$ (m)	Standard deviation, σ_Z (m)	Non-dimensional skewness, $Skew_n(Z)$	Non-dimensional kurtosis, $Kurt_n(Z)$
RCP2.6	0.44	0.0825	3.3352	0.0256	0.2599	3.1147
RCP6.0	0.54	0.0875	3.3058	0.0248	0.2099	3.1479
RCP8.5	0.73	0.1125	3.2564	0.0270	0.3583	3.1353

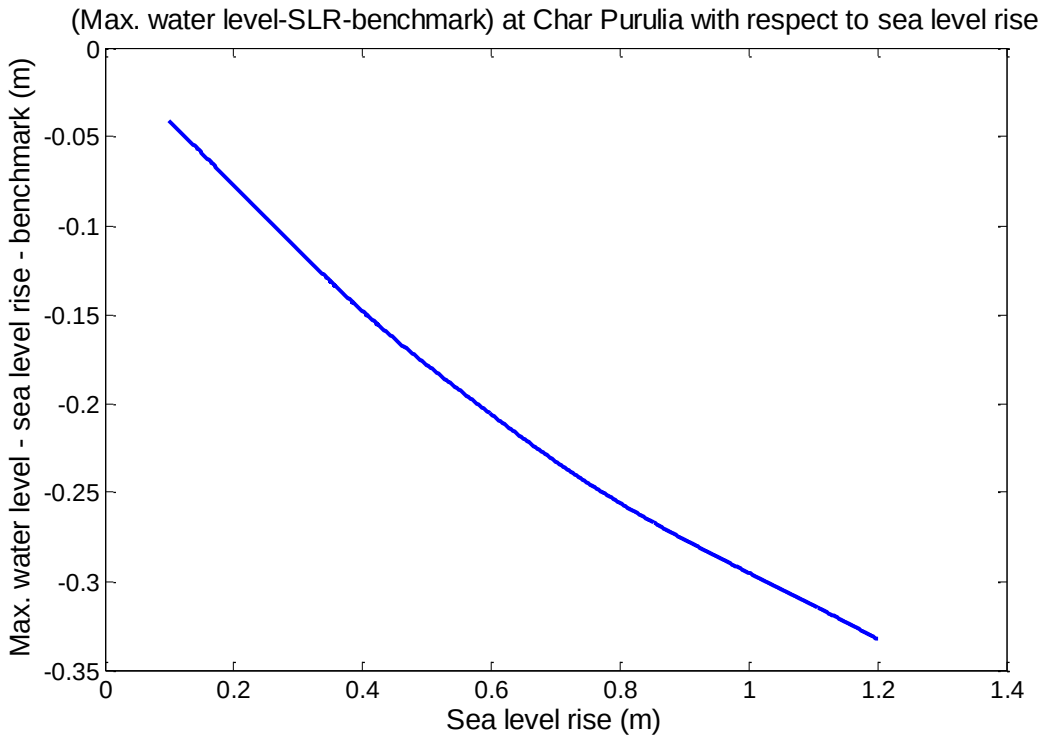

Figure 6.17: Functional relationship between excess maximum water level (maximum water level minus both sea level rise and the benchmark maximum water level obtained for no sea level rise) and sea level rise at Char Purulia

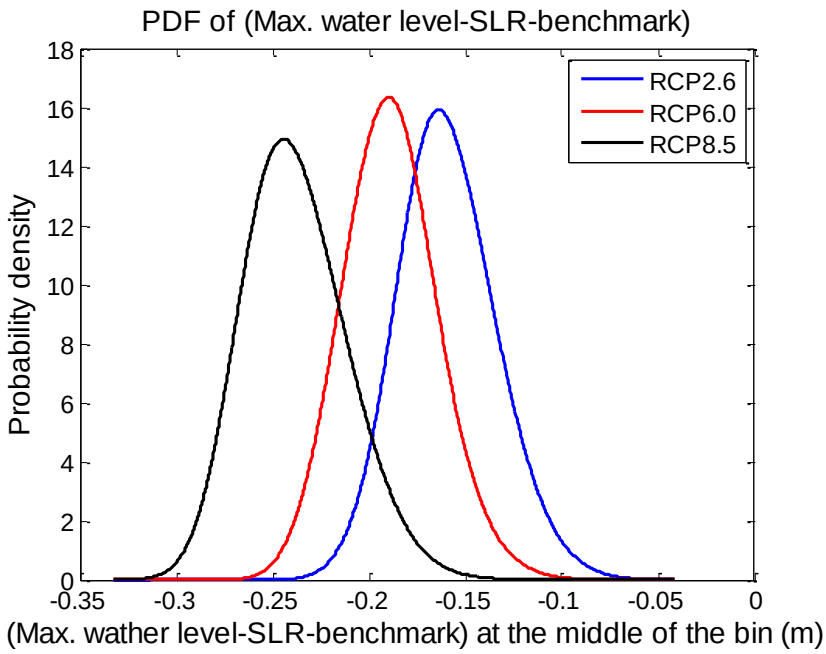

(a)

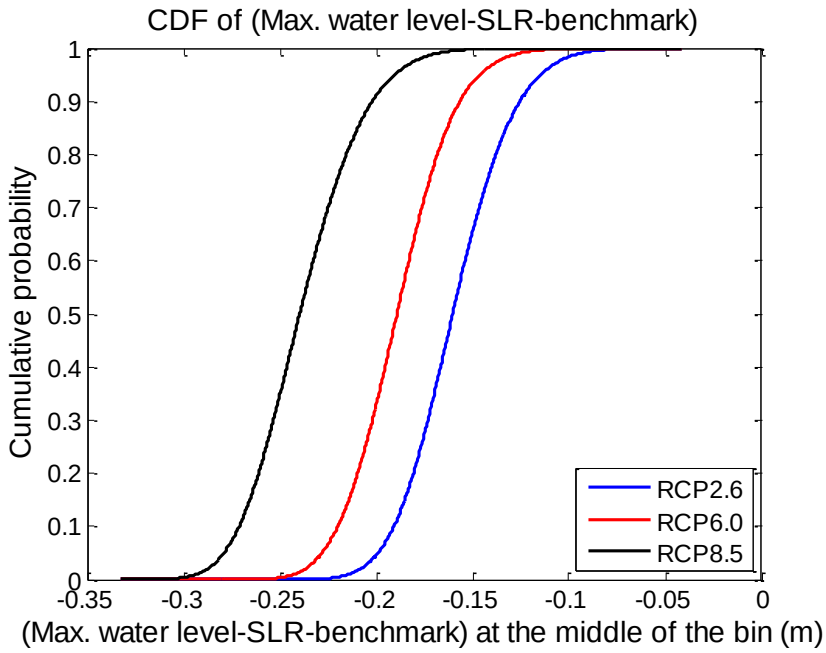

(b)

Figure 6.18: (a) PDF and (b) CDF of excess maximum water level (maximum water level minus both sea level rise and the benchmark maximum water level for no sea level rise) at Char Purulia for three normal distributions of sea level rise representing IPCC scenarios: RCP2.6, RCP6.0, and RCP8.5.

Next, consider the excess maximum water level (defined as maximum water level minus both sea level rise and the benchmark maximum water level obtained for no sea level rise) at Char Purulia. Figure 6.17 shows the cubic spline fit between the excess water level and sea level rise at Char Purulia. Figure 6.18 shows the PDFs and CDFs of excess maximum water level at Char Purulia for the three IPCC scenarios. The PDFs and CDFs exhibit similar trend as for the maximum water level minus sea level rise at Char Purulia. Table 6.11 lists the statistical moments of these PDFs. For RCP2.6 the excess maximum water level reduces about 49.5% and the standard deviation increases about 5.5%.

Table 6.11: Expected value and other statistical moments of excess maximum water level at Char Purulia for three different IPCC sea level rise scenarios.

IPCC scenario	Mean sea level rise (m)	Standard deviation in sea level rise (m)	Expected value of (max. water level-sea level rise), $E[Z]$ (m)	Standard deviation, σ_Z (m)	Non-dimensional skewness, $Skew_n(Z)$	Non-dimensional kurtosis, $Kurt_n(Z)$
RCP2.6	0.44	0.0825	-0.1593	0.0256	0.2522	3.1121
RCP6.0	0.54	0.0875	-0.1888	0.0248	0.2098	3.1478
RCP8.5	0.73	0.1125	-0.2381	0.0270	0.3526	3.1326

6.3.4. Uncertainty in maximum water level at Tiger Point

The final location at which the propagation of uncertainty from sea level rise to maximum water level is considered is at Tiger Point. Applying the same procedure as in the previous two cases, the functional relationship between sea level rise and maximum water level is obtained from several Delft3D

simulations (figure 6.19). Figure 6.20 shows the PDF and CDF of maximum water level at Tiger Point obtained for the three different IPCC scenarios of sea level rise. Table 6.13 lists the expected value and other statistical moments of maximum water level at Tiger Point.

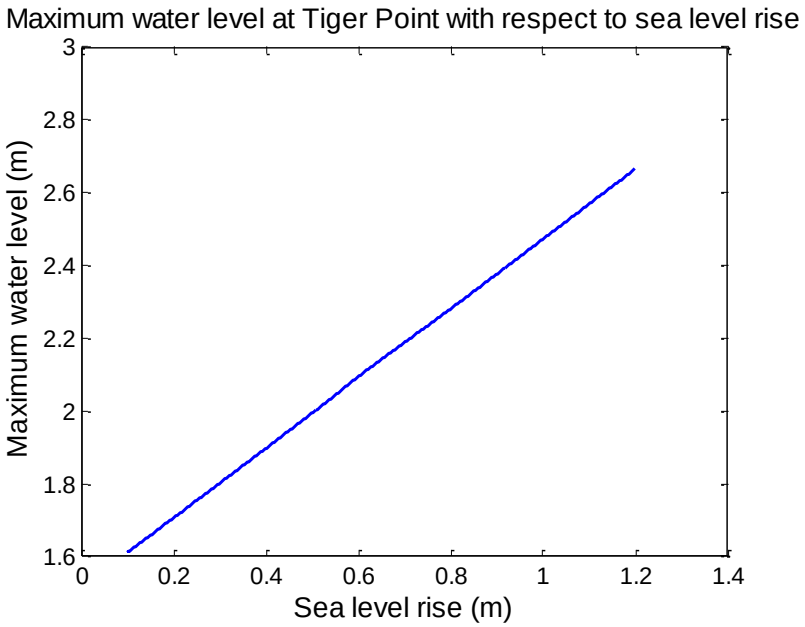

Figure 6.19: Functional relationship between maximum water level and sea level rise at Tiger Point.

It can be seen in table 6.12 that the expected value of maximum water level increases by about 14.5% with a 66% increase in mean of the sea level rise. The standard deviation in maximum water level increases by about 33% for a 36% increase in the standard deviation in sea level rise. The magnitude of non-dimensional skewness for all the PDFs is invariably very small indicating that the probability density function of maximum water level is close to a normal distribution. The non-dimensional kurtosis has values near 3 which again indicates the PDF is very well represented by a normal distribution. Just as in the case of Char Purulia, the PDF for RCP6.0 again shows a small irregularity at the peak, unlike the other two distributions. This implies that there is either some complicated flow physics at Tiger Point or some computational error or both. Even so, this secondary effect does not prevent the total cumulative probability from reaching 1. The statistical parameters for RCP6.0 are found to be consistent with RCP2.0 and RCP8.5.

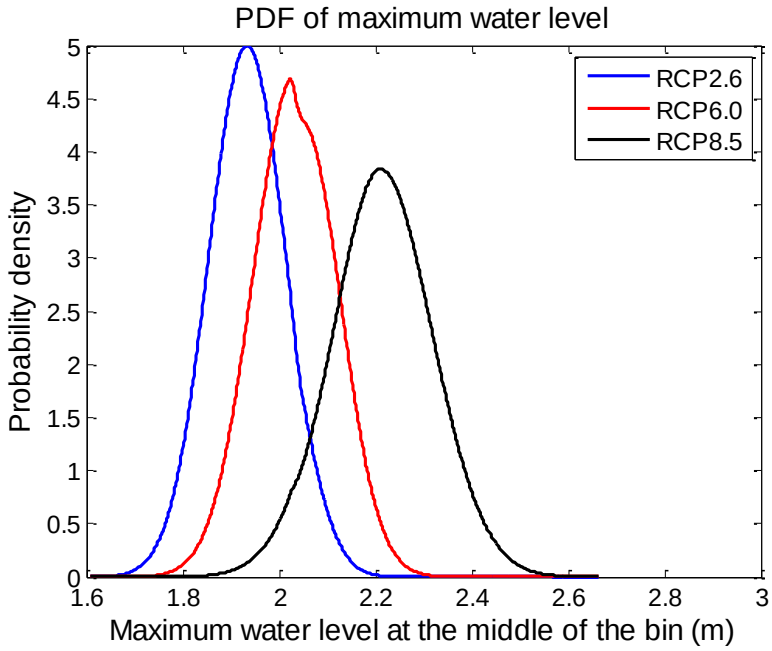

(a)

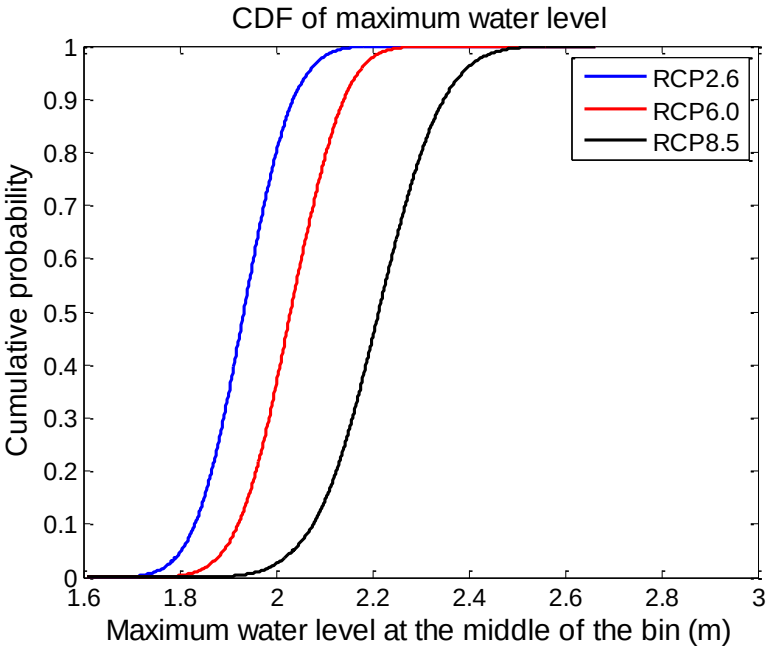

(b)

Figure 6.20: (a) Probability density function and (b) cumulative density function of maximum water level at Tiger Point for three normal distributions of sea level rise representing IPCC scenarios: RCP2.6, RCP6.0, and RCP8.5

Table 6.12: Expected value and other statistical moments of maximum water level at Tiger Point for three different IPCC sea level rise scenarios

Mean sea level rise (m)	Standard deviation in sea level rise (m)	Expected value of max. water level, $E[Z]$ (m)	Variance, σ_Z^2 (m^2)	Standard deviation, σ_Z (m)	Non-dimensional skewness, $Skew_n(Z)$	Non-dimensional kurtosis, $Kurt_n(Z)$
0.44	0.0825	1.9339	0.0064	0.0799	0.034	2.9983
0.54	0.0875	2.0314	0.0073	0.0853	-0.0122	2.9081
0.73	0.1125	2.2132	0.0113	0.1065	-0.0233	3.0856

Figure 6.21 displays the cubic spline fit of maximum water level minus sea level rise against sea level rise at Tiger Point. As the sea level rise increases, there is a monotonic decreasing trend in maximum water level minus sea level rise.

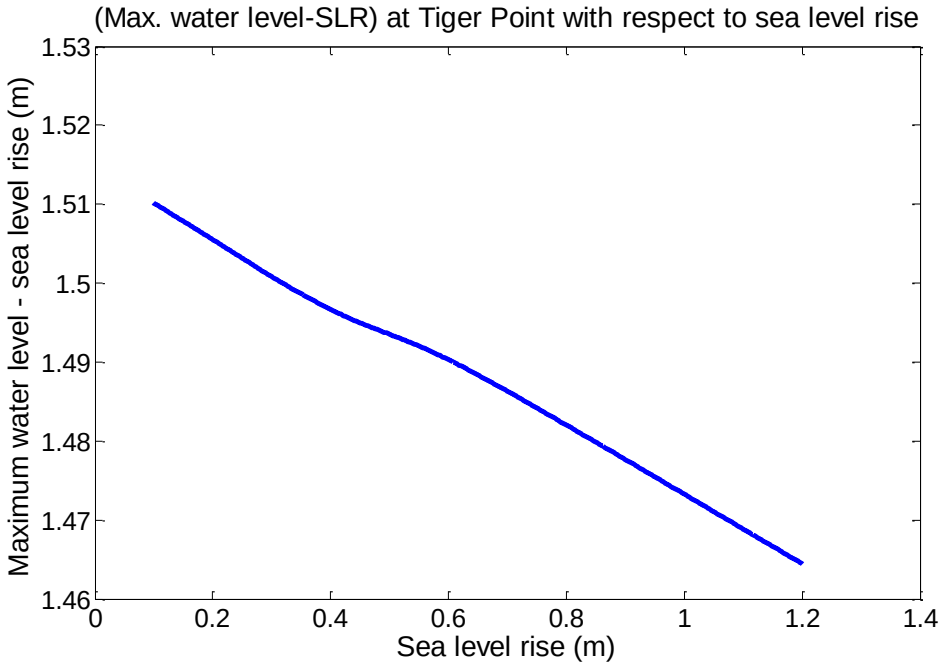

Figure 6.21: Functional relationship between maximum water level (after deducting sea level rise) with sea level rise at Tiger Point.

Figure 6.22 shows the PDFs and CDFs for maximum water level minus sea level rise.

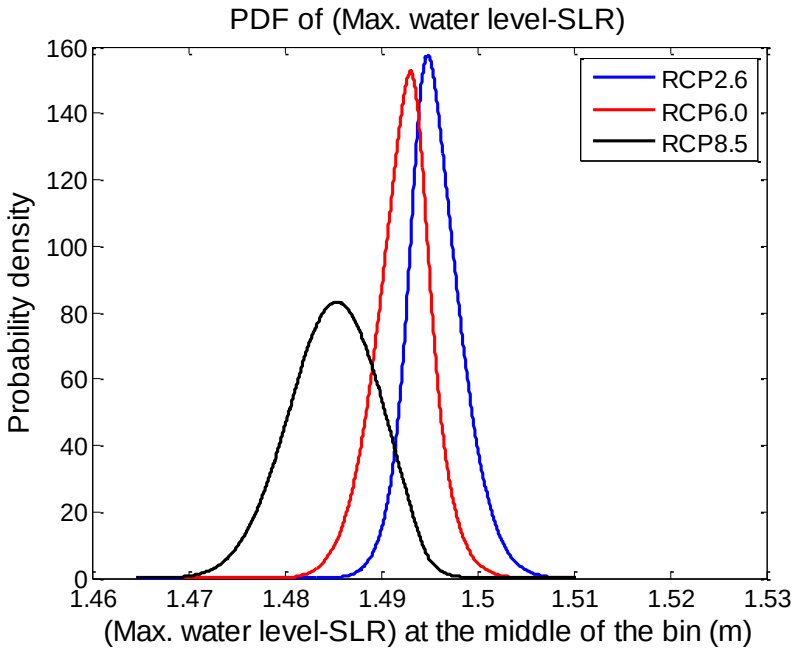

(a)

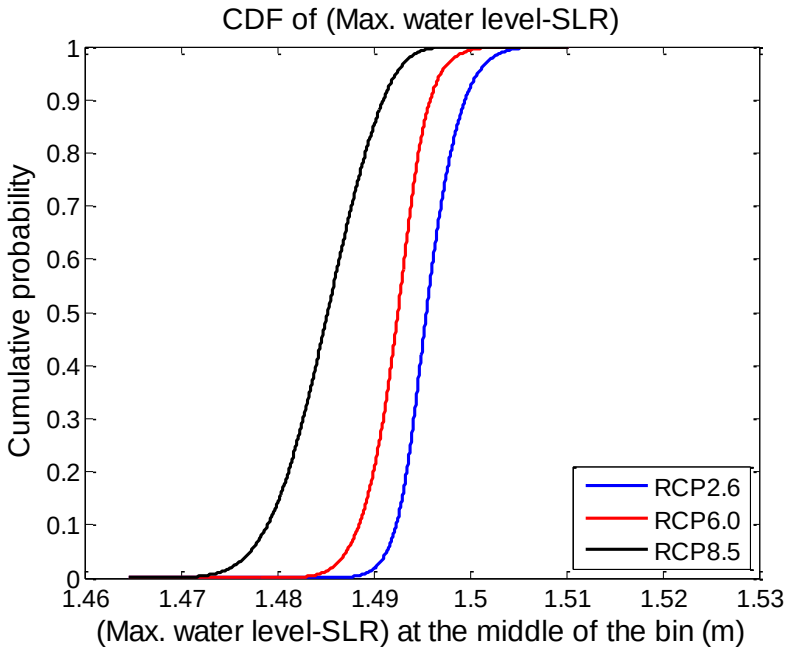

(b)

Figure 6.22: (a) PDF and (b) CDF of maximum water level after deducting sea level rise at Tiger Point for three normal distributions of sea level rise representing IPCC scenarios: RCP2.6, RCP6.0, and RCP8.5

Table 6.13 lists the corresponding statistical parameters. The maximum water level minus sea level rise PDFs obtained for the RCP2.6 and RCP6.0 scenarios have non-dimensional kurtosis higher than 3, which indicates that these PDFs are narrower than the standard normal distribution. On the other hand, the PDF for RCP8.5 is flatter than a normal distribution (non-dimensional kurtosis is less than 3). The mean of the maximum water level excluding sea level rise hardly varies (0.7%) reduction indicating it is almost insensitive to sea level rise. But the standard deviation increases by about 59%, indicating that there is a much higher propagation of uncertainty.

Table 6.13: Expected value and other statistical moments of maximum water level without the linear effect of sea level rise at Tiger Point for three different sea level rise scenarios by IPCC

IPCC scenario	Mean of sea level rise (m)	Standard deviation in sea level rise (m)	Expected value of (Max. water level-sea level rise), $E[Z]$ (m)	Standard deviation, σ_Z (m)	Non-dimensional skewness, $Skew_n(Z)$	Non-dimensional kurtosis, $Kurt_n(Z)$
RCP2.6	0.44	0.0825	1.4955	0.0029	0.3913	3.6294
RCP6.0	0.54	0.0875	1.4922	0.0230	-0.2023	3.6236
RCP8.5	0.73	0.1125	1.4849	0.0046	-0.1930	2.8531

Lastly, the excess maximum water level (obtained by subtracting the sea level rise and the maximum water level for no sea level rise from the maximum water level) is investigated at Tiger Point. Figure 6.23 displays the functional relationship between excess maximum water level and sea level rise. Figure 6.24 shows the resulting probability distributions obtained using the numerical derived distribution approach.

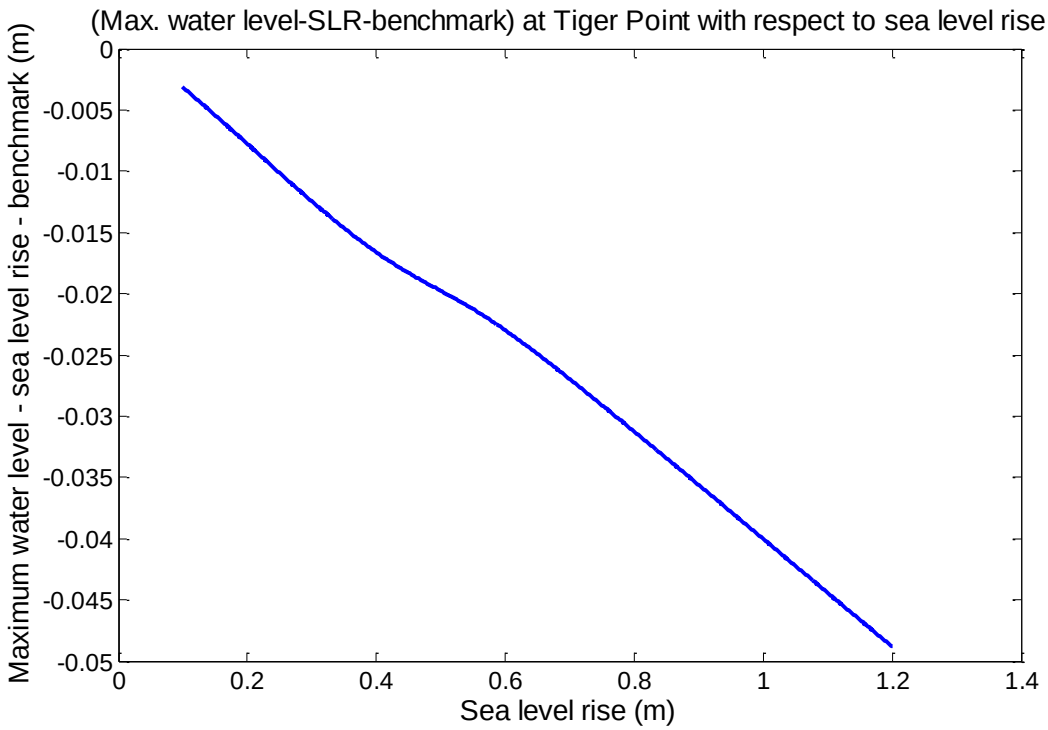

Figure 6.23: Functional relationship between excess maximum water level (maximum water level minus both sea level rise and the benchmark maximum water level obtained for no sea level rise) and sea level rise at Tiger Point.

The response surface (i.e. cubic spline curve) and probability distributions present similar behavior to the corresponding profiles for the reference case of maximum water level without sea level rise. Table 6.14 lists the statistical moments for the PDF of excess maximum water level at Tiger Point. The non-dimensional kurtosis and the standard deviation are the same as found for the maximum water level minus sea level rise. This indicates that the hydrodynamic response to sea level rise does not appear to contain higher order effects at Tiger Point, and is essentially linearly proportional to the sea level rise itself. The mean reduces by about 60% for a 66% increase in the mean value of sea level rise.

Table 6.14: Expected value and other statistical moments of excess maximum water level at Tiger Point for three different IPCC sea level rise scenarios.

IPCC scenario	Mean sea level rise (m)	Standard deviation in sea level rise (m)	Expected value of (max. water level-sea level rise), $E[Z]$ (m)	Standard deviation, σ_Z (m)	Non-dimensional skewness, $Skew_n(Z)$	Non-dimensional kurtosis, $Kurt_n(Z)$
RCP2.6	0.44	0.0825	-0.0177	0.0029	0.3617	3.6152
RCP6.0	0.54	0.0875	-0.0211	0.0230	-0.2027	3.6237
RCP8.5	0.73	0.1125	-0.0284	0.0046	-0.2075	2.8571

6.4. Concluding Remarks

This chapter investigated the effect of sea level rise on maximum water level at three locations in the Bay of Bengal, based on fits of IPCC scenario forecasts of sea level rise by 2100 to a normal probability density distribution. The results show that the local maximum water level is closely linked to the sea level rise, being almost linearly proportional. There is little evidence of higher order (nonlinear) effects in the local hydrodynamics patterns causing secondary super-elevation increases (or decreases) in maximum water level at the locations of interest. Even so the standard deviation of maximum water level (with and without the linear effect of sea level rise) presents more obvious changes with the variation in standard deviation in sea level rise. This indicates that uncertainty in sea level rise directly translates into uncertainty in maximum water level for sites in the Bay of Bengal. The numerical derived distribution method worked satisfactorily for the three locations considered because, in each case, the response curve linking sea level rise to maximum water level was either progressively increasing or progressively decreasing. The numerical derived distribution approach therefore shows promise as a

tool for general sea level risk analysis by oceanographers, coastal scientists, and coastal engineers.

Many underlying factors affect the derived probability distribution of maximum water level, and there are also possibilities of performance optimization. For example, the choice of probability distribution of sea level rise or the functional relationship between maximum water level and sea level rise (whether a cubic spline fit or a fitted average) has a huge impact on the probability distribution of maximum water level. In this chapter, the model distribution was selected to be a truncated normal distribution. In further studies, it is recommended that other distributions be considered, with the objective of identifying ones that best fit the sea level rise. Obviously, the numerical derived distribution approach could also work with raw data on the probability distribution for sea level rise, and not be so limited by a fit to a smooth distribution (so long as the requirement for progressive increase or decrease in the response curve is not violated).

In the Bay of Bengal, the water level is highly sensitive to the bathymetry and bed roughness. As yet, such physical data tend to be of coarse resolution or incomplete or simply missing. It is therefore recommended that field campaigns be conducted to improve the availability of good quality data, from which more refined estimates can be made of tide- and river-driven water levels, etc. It should also be noted that the results are sensitive to the choice of simulation engine, wetting and drying algorithms, empiricism, three or two dimensionality, and so on.

It is recommended that the present work be extended to consider local land subsidence in the Bay of Bengal, given recent evidence of such subsidence (discussed in chapter 1). It would also be interesting to investigate how the uncertainty in sea level rise affects other hydro-morphodynamic parameters, such as uncertainty in sediment transport and/or sedimentation.

Chapter 7

Effect of uncertainty in floc size on sedimentation rate at sites in Meghna Estuary

7.1. Introduction

Mud is a common type of cohesive sediment found in the estuarine environment, and is composed of silt and clay particles, typically < 63 μm in size (*Whitehouse et al., 2000*). Suspended sediment in the Meghna estuary consists of fine to medium silt near the water surface, silty sand at increasing depth, and sandy silt close to the bottom (*Borromeo et al., 2019*). The behavior of fine sediment in a complex environment with multiple drivers (river discharge, tide, etc.) is comparatively little understood; this is mainly because the deposition and erosion processes of fine sediment depend on many chemical, biological, and physical factors. This chapter discusses the formulation of a fine-sediment hydro-morphodynamic model for the Bay of Bengal and Meghna estuary, and the propagation of uncertainty from input floc size to output sedimentation rate in that region using Delft3D. Given that this chapter is primarily concerned with uncertainty analysis, it is assumed for simplification purposes that sediment particles and flocs are both single-sized throughout the model domain.

7.2. Model set up

To establish the morphodynamic model for the Bay of Bengal and coast of Bangladesh, the hydrodynamic Delft3D model in Chapter 5 is extended to include sediment transport, entrainment, bed deposition and erosion.

The model domain has two upstream open boundaries and one downstream open boundary, as indicated in figure 6.1. Similar to the hydrodynamic cases, the Ganges-Brahmaputra and Meghna river flow inputs are set to constant values of 120,000 m^3/s and 20,000 m^3/s, respectively. These river discharges represent the annual peak flood. The spatial distribution of Manning's *n* shown in figure 5.2 in chapter 5 is used for all the cases in this chapter.

Following the tidal component input reduction method suggested by Latteux (*1995*), the downstream offshore boundary is tidal, comprising a single M_2 component multiplied by 1.20. This method utilizes a single representative tidal component rather than the whole set of tidal components in order to produce the same morphological changes in the long term. When validating the method, Latteux studied several locations in the vicinity of the English Channel, and represented the tidal behavior there using an equivalent single tide, finding that the representative tidal range was about 7 to 20% higher than the mean tidal range. However, the increase is case specific, and depends on various parameters such as velocity, bathymetry, etc. In practice, a detailed investigation would be desirable to determine a value for the single representative tidal component for the Bay of Bengal, but in the absence of such information, for the present hypothetical scenarios, it is simply assumed that the representative tidal component is 20% higher than the actual M_2 component. The amplitude and phase are obtained from the TPXO 8.0 database using the DelftDashboard tool *(Delftdashboard, n.d.*).

In addition to water discharge, the open boundary of the Ganges-Brahmaputra river accommodates an extreme flood inflow of suspended sediment of concentration 0.799 kg/m^3. This value is based on the highest measured concentration of fine sediment at the open boundary location, obtained on

random days in 2007, 2008, and 2009 by the Bangladesh Water Development Board. Sediment concentrations at the Meghna river boundary and the offshore boundary are assumed to be zero. The Meghna river has negligible morphological activity, and the Bangladesh Water Development Board has no data on suspended sediment concentration at this location. Turning to the offshore boundary, it is assumed that no sediment enters the estuary from the deep ocean and all sediment reaching the bay from the river is deposited before reaching the offshore boundary.

Particle settling velocity is one of the most important parameters that influences the sedimentation rate. Winterwerp and van Kesteren (*2004*) provide the following empirical expression for the settling velocity of fine sediment,

$$w_s = \frac{\alpha g}{18\beta\mu} \frac{\rho_s - \rho_w}{1+.15R_{ef}^{0.687}} d_p^{3-n_f} d_f^{n_f-1} \quad , \tag{7.1}$$

where d_p is particle diameter, d_f is floc diameter, R_{ef} is floc Reynolds number (given by $\frac{w_s d_f}{\nu}$, in which ν is kinematic viscosity of water), ρ_s is density of solid sediment, ρ_w is density of water, g is acceleration due to gravity, μ is dynamic viscosity of fluid, α is a shape factor for gravitational force (which is equal to 1 for a spherical particle), β is a shape factor for drag force (which is equal to 1 for a spherical particle), and n_f = 3 for a Euclidean particle in the Stokes' regime where $R_e \ll 1$.

The size of bed material particles near the mouth of the Meghna estuary ranges from 16 to 250 µm (*Ministry of Water Resources of Bangladesh, 2001)*. Borromeo et al. (*2019*) collected silt from the Bengal Shelf and found that at certain locations, particles of size < 5 µm occupied from 65 to 80% of the total sediment by weight. In the present research, the particle size of the fine sediment is taken as 5µm.

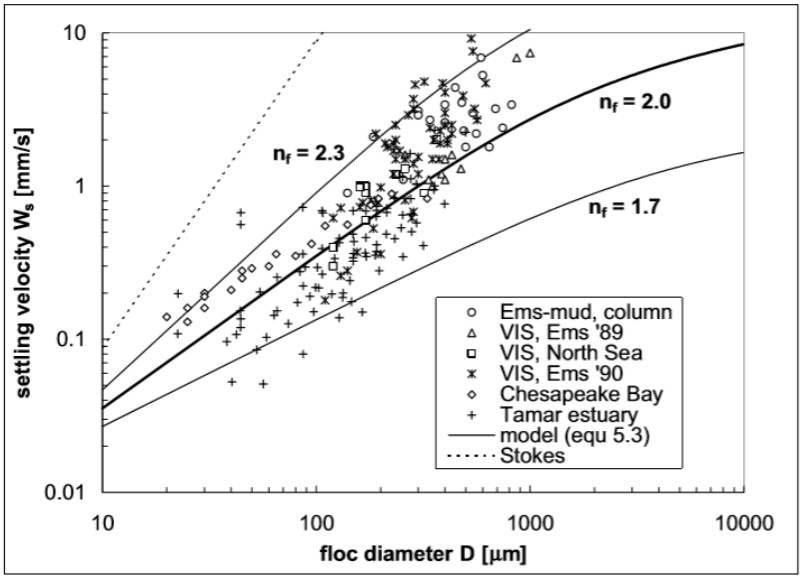

Figure 7.1: Relation between floc diameter and settling velocity (Winterwerp and van Kesteren, 2004).

Figure 7.1 presents the relation between floc size and settling velocity of the sediment obtained by Winterwerp and Kesteren (*2004*). From field observations, the floc diameter falls in the range of 20 µm – 1000 µm. The present thesis assumes the same range of floc diameter for uncertainty analysis because of the unavailability of such data for the study location.

The critical bed shear stress for erosion in the case of fine sediment can be expressed as follows (*Thorn and Parsons, 1980; Whitehouse et al., 2000*):

$$\tau_e = E_1 C_M^{E_2} \quad , \tag{7.2}$$

where τ_e is critical shear stress for erosion, C_M is dry density, and E_1 and E_2 are site-specific dimensional coefficients. E_1 is 5.42 × 10^{-6} for water-sediment samples of dry density between 30-200 kg/m^3 (*Thorn and Parsons, 1980*) and 0.0012 for water-sediment samples of dry density 30-400 kg/m^3 (*Delo and Ockenden, 1992*). Also, E_2 is 2.28 for water-sediment samples of dry density between 30-200 kg/m^3 (*Thorn and Parsons, 1980*) and 1.2 for water-sediment samples of dry density 30-400 kg/m^3 (*Delo and Ockenden, 1992*).

Critical bed shear stress for deposition typically is half the value of the critical shear stress for erosion (τ_e). Laboratory tests have shown the critical bed shear stress for deposition to be about 0.06-0.10 N/m^2 (*Whitehouse et al., 2000*).

The Delft3D model was first run solely for hydrodynamics in the Meghna Bay driven by tidal flow and river water discharge inputs. The simulation commenced from a cold start comprising an initial water level set at 3 m vertically above mean sea level. After 7 days of hydrodynamic simulation, when the velocity and water level in the domain became stable, the output map file was used as the initial condition for the morphodynamic run. The time step of the model was 0.5 minutes.

For the morphodynamic computations, one day of simulation time was set as the spin-up period, during which sediment transport calculations were undertaken without implementing bathymetry update. After spin-up, the duration of the morphodynamic change simulation was set to 14 cycles of the representative M_2 constituent tide, i.e. 7 days 5 hours and 50 minutes. In Delft3D, a morphological acceleration factor (Morfac) equal to 12 was used to optimize the model simulations of overall duration 3 months. It was important to run complete cycles of the tidal component while using Morfac because the hydrodynamic run-time was multiplied by Morfac to calculate morphological changes in Delft3D, and so it was necessary to simulate complete tidal cycles in order to obtain the best possible output with less error. The time step for the morphodynamic change computations was 0.25 minutes.

7.3. Uncertainty in model prediction of sediment deposition rate

Before carrying out the computations, it was necessary to determine a suitable statistical distribution of floc sizes that might apply to the Meghna Estuary. In the absence of field data, specific to the estuary, it was decided to use an extensive set of floc size data compiled by Winterwerpen and van Kesteren (*2004*) from sites in the North Atlantic and North Sea, and plotted in Figure

7.1. After digitization, the floc size data were found to have a mean value of 227.21 µm and standard deviation of 170.74 µm. Several candidate probability distributions were then fitted to this data, and the chi-square (χ^2) goodness of fit test used to determine the best fit distribution.

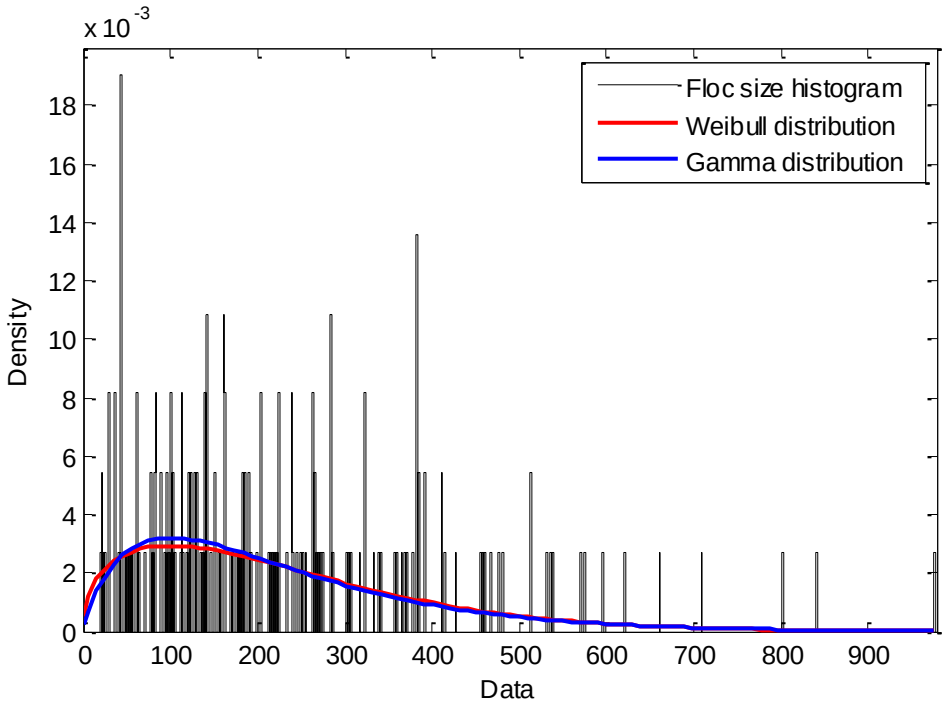

Figure 7.2: Floc size data from Winterwerpen and Kesteren (2004) classified in 480 bins with fitted Gamma and Weibull distribution superimposed.

Weibull and Gamma distributions were the closest among other well-known distributions (figure 6.2). From the frequency distribution of floc size, χ^2 values $[\sum \frac{(Expected\ value - Observed\ value)^2}{Observed\ value}]$ were calculated for both Weibull and Gamma distributions. The χ^2 values for the Gamma and Weibull distributions were 696.2 and 719.1, respectively. Considering the significance level, α = 1%, the p-value for the Gamma distribution was 3.61×10^{-10} and for the Weibull distribution, the p-value was 1.30×10^{-17}. It should be noted that the p-value or the right-tail probability is the value of the cumulative probability at $(1 - \chi^2)$ in the associated χ^2-distribution. If an assumed distribution has a p-value below the significance level, then the assumed distribution is acceptable. Hence, both Weibull and Gamma distributions proved to be suitable statistical representations of the floc size data. Given that the Gamma distribution had

the smaller χ^2-value, the Gamma distribution is therefore selected as the best-fitted distribution for this case. This Gamma distribution has a mean of 227.21 µm, standard deviation of 169.33 µm (figure 7.2), and coefficient of variation of 169.33/227.21 = 0.745.

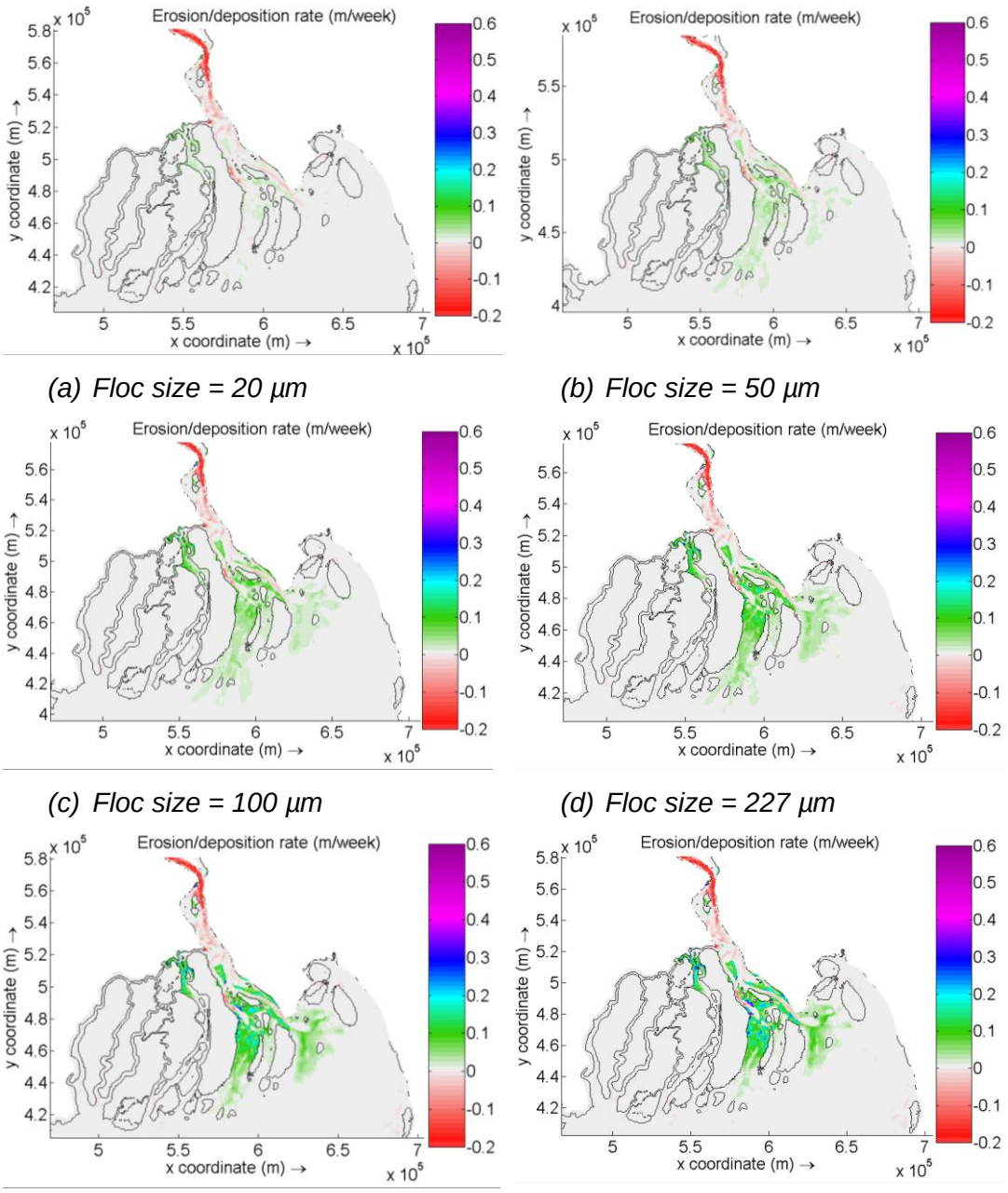

(a) Floc size = 20 µm

(b) Floc size = 50 µm

(c) Floc size = 100 µm

(d) Floc size = 227 µm

(e) Floc size = 500 µm

(f) Floc size = 1000 µm

Figure 7.3: Spatial distribution of suspended cohesive sediment deposition rate (m/week) in the Meghna estuary after 14 cycles of the 1.2 M_2 constituent tide for different floc sizes.

Delft3D morphodynamic computations were then undertaken for the following six representative floc sizes: 20, 50, 100, 227, 500, and 1000 μm. Figure 7.3 presents the sedimentation rate distribution in the Meghna estuary for flocs of different sizes, obtained from the simulation output. Smaller-sized flocs have lower settling velocities and hence exhibit lower deposition rates. The pattern of deposition of sediment indicates that deposition phenomena in the Meghna estuary are closely linked to the complicated bathymetry, with erosion prevalent in the deeper reaches of rivers, and sedimentation evident in shallower areas. It is worth recalling here that the sediment deposition rate is driven by the combined effects of rivers and tidal current.

Three locations, where the deposition rate is substantial, were selected for uncertainty analysis. Figure 7.4 indicates the locations, which surround Bhola, the largest island of Bangladesh. Location 1 is in the West Shahbazpur channel at the north of Char Gazaria, Location 2 is a tidal flat in West Shahbazpur channel west to the Manpura island and Location 3 is at the north of Bhola Kheyaghat in Tetulia channel.

Figure 7.4 shows that the erosion-deposition pattern along the main estuary mouth is broadly similar to the historical map given by Brammer (*2014*). Both the map and model output indicate that the selected locations are prone to deposition. However, the model failed to generate erosion in the historically erosion-prone areas around Hatia and Sandwip islands. Furthermore, the model did not reproduce the accretion along the whole Tetulia channel illustrated in Brammer's map. There are several possible reasons for this. First, the model was not calibrated and validated against field observations for the sediment transport and bed morphodynamics calculations. Second, the present morphodynamic model study assumed a constant single size of cohesive sediment particle and a constant single floc size applied throughout the domain in each simulation. In fact, the Meghna estuary contains particles and flocs that both have size distributions and are not single-valued. However, in the absence of field data on sediment particle and floc size distributions in the Meghna Estuary, and for model simplification purposes,

the assumption was made on the basis that the aim of this thesis is purely to look at uncertainty propagation. Even so, it must be emphasized that without proper information concerning the spatial variations in size distribution of particles in the Meghna estuary, the model outputs must be treated as purely hypothetical. Third, the model was run for a steady peak flood event lasting three months. This is a hypothetical event, which represents a highly idealised extreme flood situation. Historical records show that such a prolonged extreme situation has not lasted for more than a week in the Meghna estuary. Fourth, it would have been computationally very expensive to simulate the morphodynamics over an entire monsoon season lasting 5-6 months, and so a simplified approach was taken using the morphological acceleration factor in Delft3D simulation tool. Fifth, noting that the amount of erosion-accretion would be rather small during a short-duration peak flood event, a simulation time of 3 months was selected in order to drive obvious morphological change in Bay of Bengal and around Meghna estuary. Of course, if the model input comprised more accurate time series of river flow, sediment size, and suspended sediment concentration covering the whole year including consecutive dry and monsoon seasons, then it would be expected that the model would produce output closer to the historic evidence. Sixth, all the properties of the cohesive sediment were either assumed or calculated from theoretical formulae. The lack of field data about the bed material, sediment size, unit weight, etc. are of course major sources of uncertainty. For reasons of brevity, this thesis focuses on uncertainty arising from a single parameter, the floc size, and how it translates to uncertainty in sediment deposition/erosion rate. This is discussed in the context of the Meghna Estuary in the following sections.

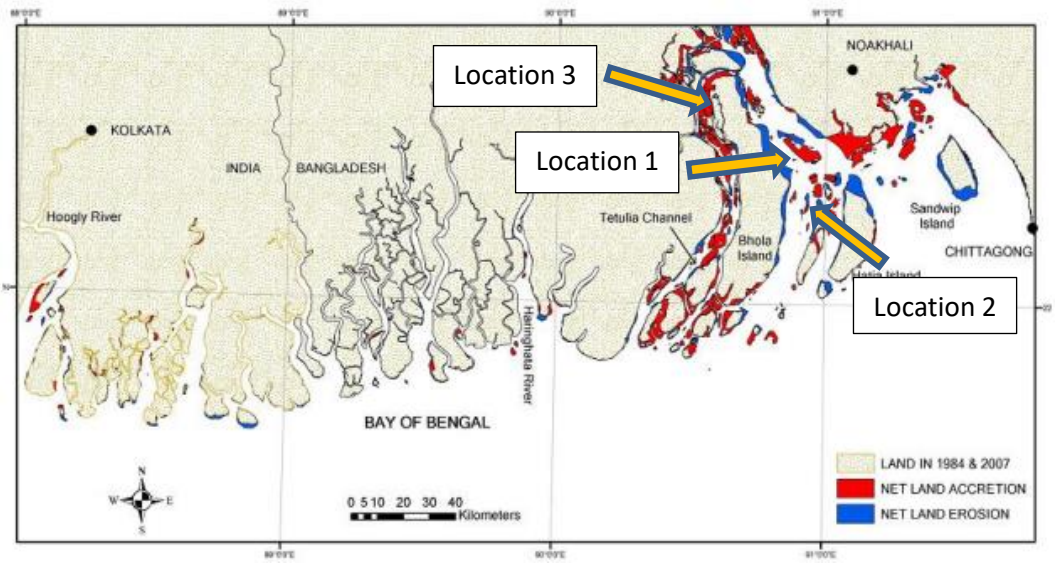

(a)

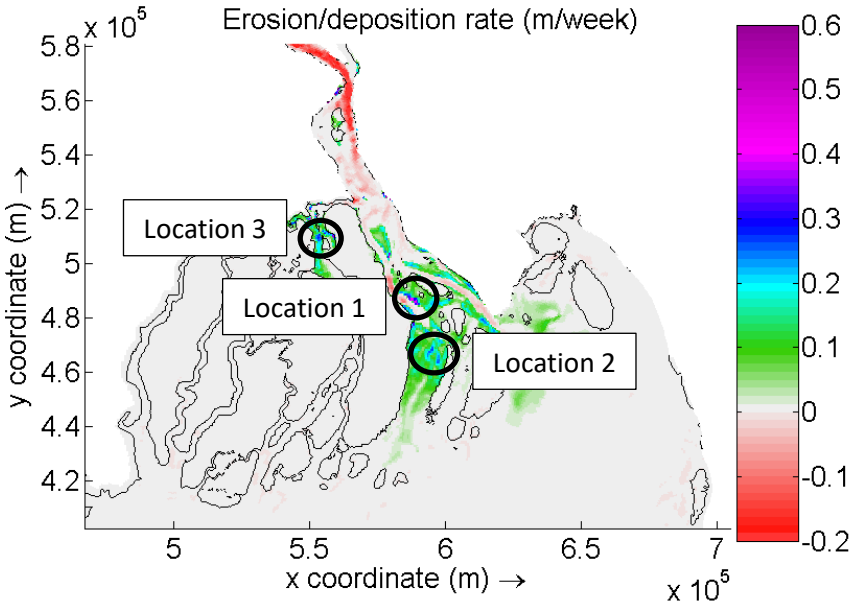

(b)

Figure 7.4: Locations considered in the sediment rate uncertainty study: (a) historical map of land erosion and accretion by Brammer (2014); (b) simulation output from Delft3D model.

7.3.1. Convergence test

As before, the numerical uncertainty propagation method used herein, required a response surface to be derived connecting values of the input parameter to the output response. Here, the morphodynamic version of

Delft3D was used to predict output values of sediment deposition/erosion rate for a series of given input values of sediment floc size covering the majority of the range of floc sizes within the truncated probability distribution. Delft 3D was first run for floc sizes of 20, 50, 200, 500, 1000 microns, and the output sediment deposition/erosion rates in m/week extracted from the results, at the locations of interest. To refine the parameter relationship between the input floc size data and the output sedimentation/erosion rate, a cubic spline was then fitted (using Matlab). Once, this distribution was obtained, the uncertainty propagation method involved discretizing the probability density distribution for floc size into a number of bins, and then using the numerical derived distribution approach to determine the probability density distribution for sedimentation/erosion rate. As before, it was important to conduct a convergence test to check that the probability density distribution had been divided into a sufficient number of bins.

Location 1, West Shahbazpur channel, was selected as a suitable candidate site for the convergence test. Figure 7.5 shows the cubic spline that interpolates the functional relationship between (output) sedimentation rate and (input) floc size. As can be seen, this functional relationship is monotonically increasing.

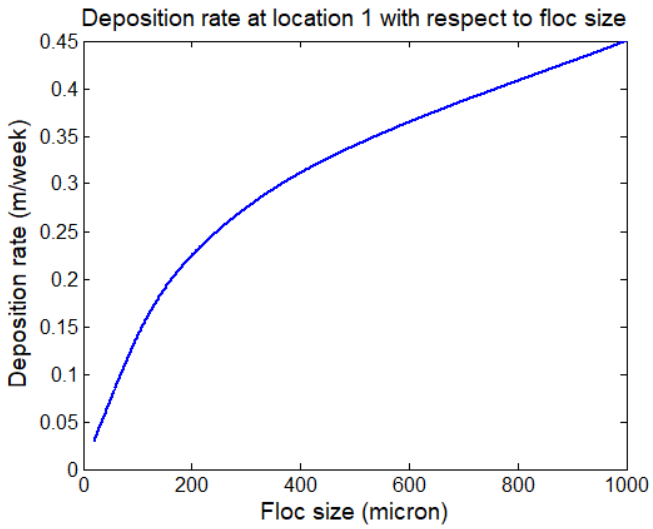

Figure 7.5: Cubic spline relation between sedimentation rate and floc size at Location 1 (West Shahbazpur channel) in the Meghna estuary, obtained by considering 14 cycles of the 1.2 M_2 constituent tide.

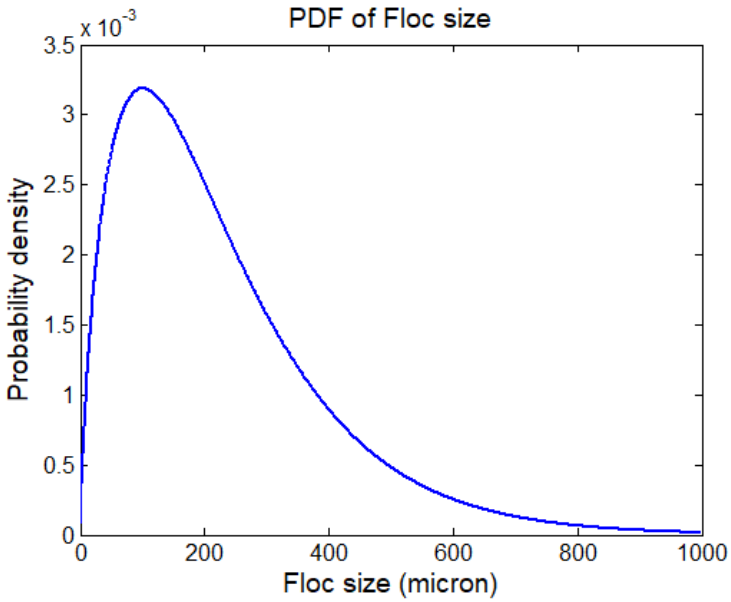

Figure 7.6: Probability density function of floc size of cohesive sediment at Location 1 (West Shahbazpur channel) in the Meghna Bay, obtained from the data given by Winterwerpen and Kesteren (2004).

Figure 7.6 shows the probability density distribution in floc size. It can be seen that the PDF exhibits strong asymmetry, with the peak occurring at about 120 micron, and a long tail to 1000 micron.

Next, the statistical convergence of deposition rate is investigated according to the number of bins used to discretize the probability density function of floc size. Given that the deposition rate is a function of floc size and that probability is conserved, the cumulative probability of a floc size is equal to the cumulative probability of the corresponding sedimentation rate. The transferred probability distribution contains the same number of bins, but the bin width is no longer fixed; this is because of the nonlinear relationship between floc size and deposition rate (as obvious in Figure 7.5). The numerical PDF transfer method described in Chapter 3 is used to obtain the probability density of deposition rate and the statistical moments. Figure 7.7 depicts the resulting probability density function and cumulative density function of deposition rate at Location 1 obtained for different numbers of bins used to discretize the probability density function of floc size. Table 7.1 summarizes the expected value and other statistical moments of sediment deposition rate at Location 1.

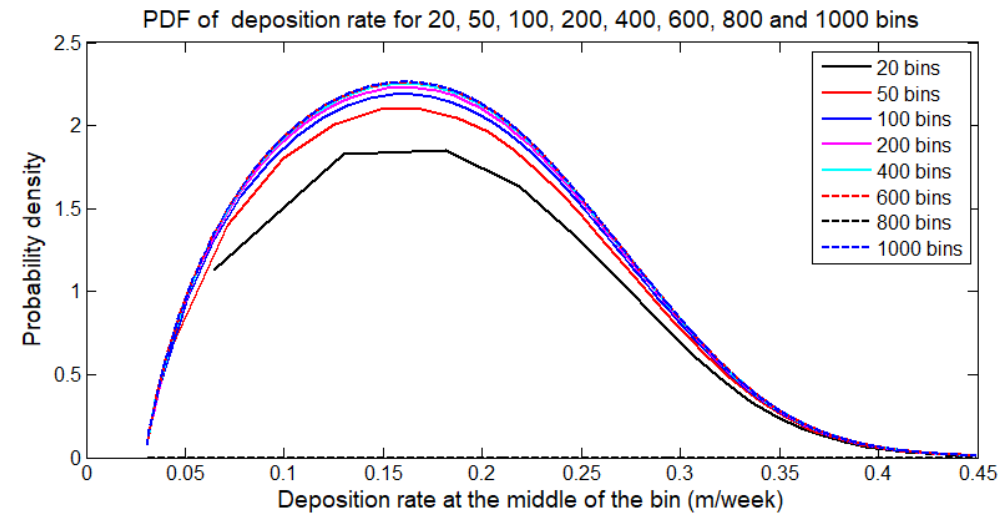

(a)

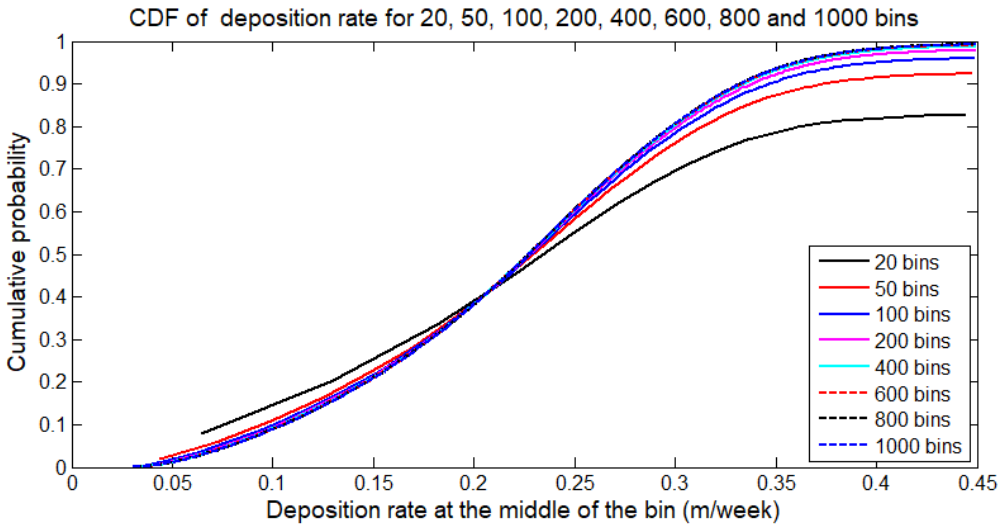

(b)

Figure 7.7: PDF (a) and CDF (b) of sedimentation rate at Location 1 (West Shahbazpur channel) in Meghna Bay plotted for different numbers of bins, obtained by considering 14 cycles of the 1.2 M_2 constituent tide

Table 7.1 indicates that the probability distribution of deposition rate is sensitive to the number of bins used to discretize the PDF of floc size. The expected value, variance, standard deviation and non-dimensional kurtosis of deposition rate converge to within 2 significant figures when the number of bins ≥ 400. Non-dimensional skewness converges to within 1 significant figure to a value close to zero. Consequently, the number of bins used in the later analysis is chosen as 400.

Table 7.1: Expected value and other statistical moments of sedimentation rate at Location 1 (West Shahbazpur channel, Meghna Bay).

No. of bins	Expected value of deposition rate, $E[D]$ (m/week)	Variance, σ_D^2 ($m^2/week^2$)	Standard deviation, σ_D (m/week)	Non-dimensional skewness, $Skew_n(D)$	Non-dimensional kurtosis, $Kurt_n(D)$
20	0.1818	0.0072	0.0848	1.1318	2.9149
50	0.2052	0.0067	0.0821	0.5257	2.6053
100	0.2135	0.0068	0.0822	0.2453	2.5079
200	0.2178	0.0068	0.0826	0.0992	2.4654
400	0.2200	0.0069	0.0828	0.0219	2.4463
600	0.2207	0.0069	0.0830	-0.0041	2.4403
800	0.2211	0.0069	0.0830	-0.0172	2.4374

7.3.2. Uncertainty in deposition rate at Location 1 (Northwest of Char Gazaria, West Shahbazpur channel, Meghna estuary)

Location 1 is located in a shallow area of West Shahbazpur channel at the northwest of Char Gazaria, where the mean depth is about 6 m (relative to mean sea level), at 5.89×10^5 m East and 4.86×10^5 m North. Figure 7.8 shows the initial bathymetry, which corresponds to a complicated pattern of islands and shoals, created in the delta region as river branches meet the sea. Figure 7.9 shows the velocity field at two-hourly intervals. West Shahbazpur channel around this location is erosion prone, as confirmed by both the historical map and the Delft3D results. The depth-averaged velocity during high water is about 2.75 m/s and the current is invariably directed southward during the whole tidal cycle.

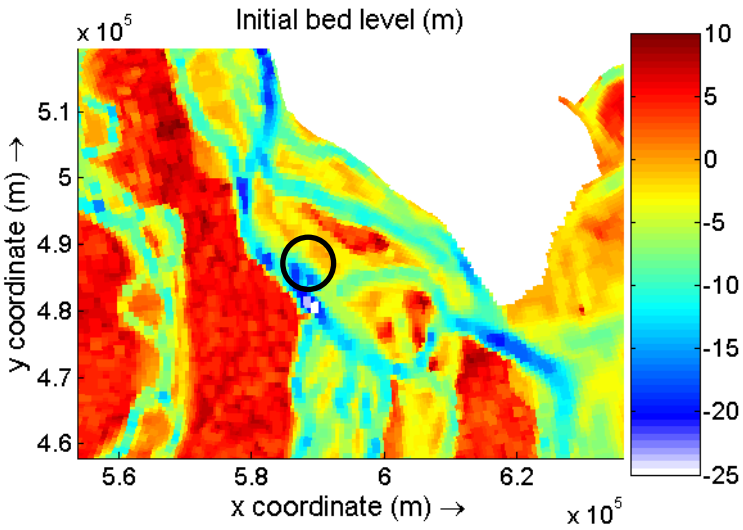

Figure 7.8: Initial bed level in the vicinity of Location 1 in Meghna estuary (black circle).

At Location 1, the river flow slows down as it interacts with the tide. Figure 7.9 depicts two-hourly depth averaged velocity vector and magnitude fields at this location. Figure 7.9(a) represents the high water condition (at elapsed time t_e = 0 h), when the flow velocity is almost zero and some reverse circulation can be discerned. Two hours later (at elapsed time t_e = 2 h), in figure 7.9(b), the channel flow has begun to speed up, and the southward direction of the all arrows indicates that the bulk of the flow is now directed downstream in the vicinity of Location1. From Figure 7.9(c) at t_e = 4 h as the tidal low water condition is reached, it is evident that the deeper channels contain high-velocity flow. Later at t_e = 6 h and 8 h, (figures 7.9(d) and 7.9(e)), the velocity in the channels further intensifies. As would be expected, such locations where the water speed is high are particularly erosion-prone (figure 7.10). From figure 7.9(f), it can be seen that at t_e = 10 h, the high-water tide level is returning, and the flow velocity has already reduced in shallow areas surrounding location 1. At t_e = 12 h, the flow velocity is even lower everywhere, including deep channels (figure 7.9(g)).

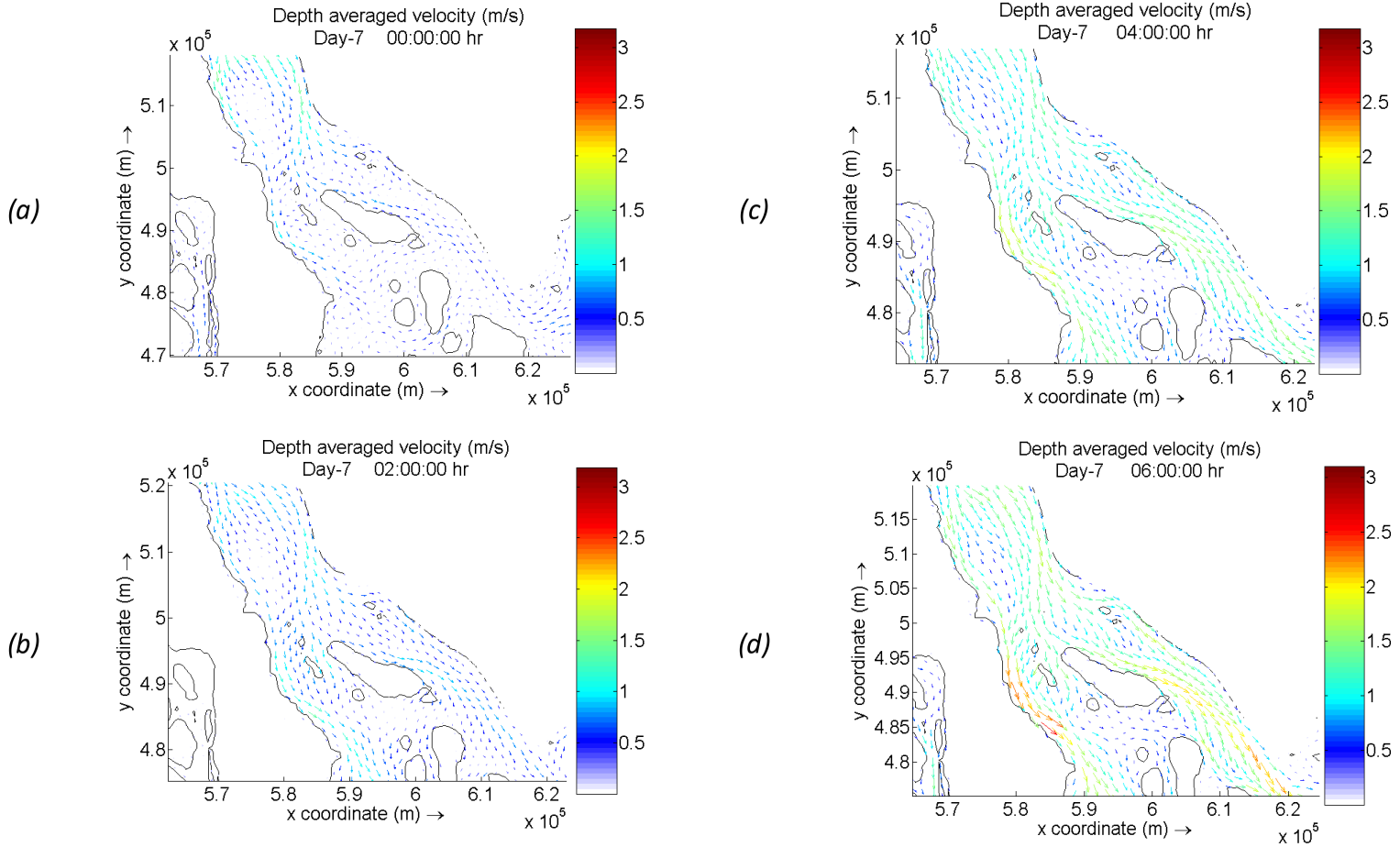

Figure 7.9: Depth-averaged velocity fields at two hourly intervals in the vicinity of Location 1 (West Shahbazpur channel) in Meghna estuary

(e)

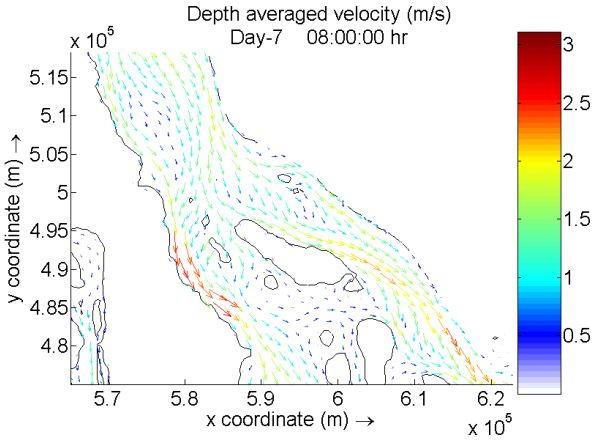

(g)

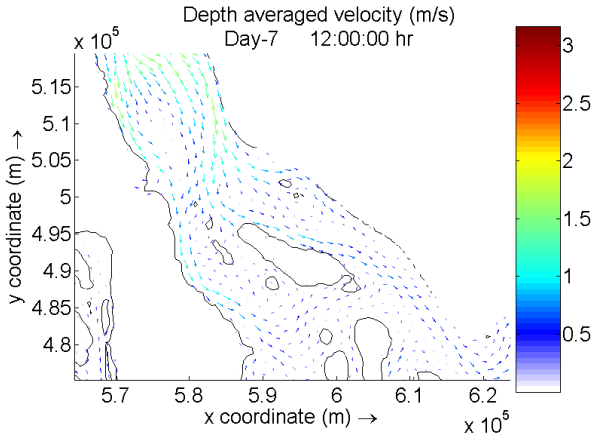

(f)

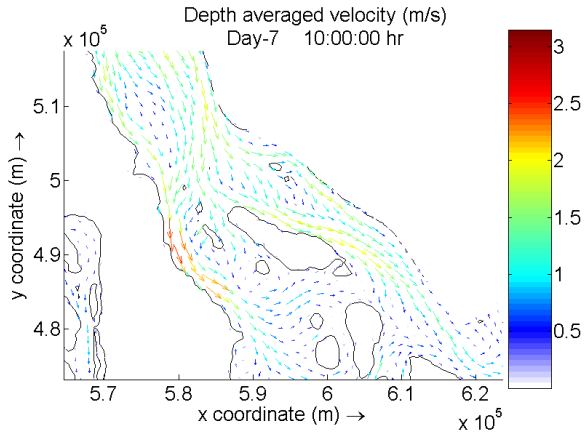

Figure 7.9 contd.: Depth-averaged velocity fields at two hourly intervals in the vicinity of Location 1 (West Shahbazpur channel) in Meghna estuary

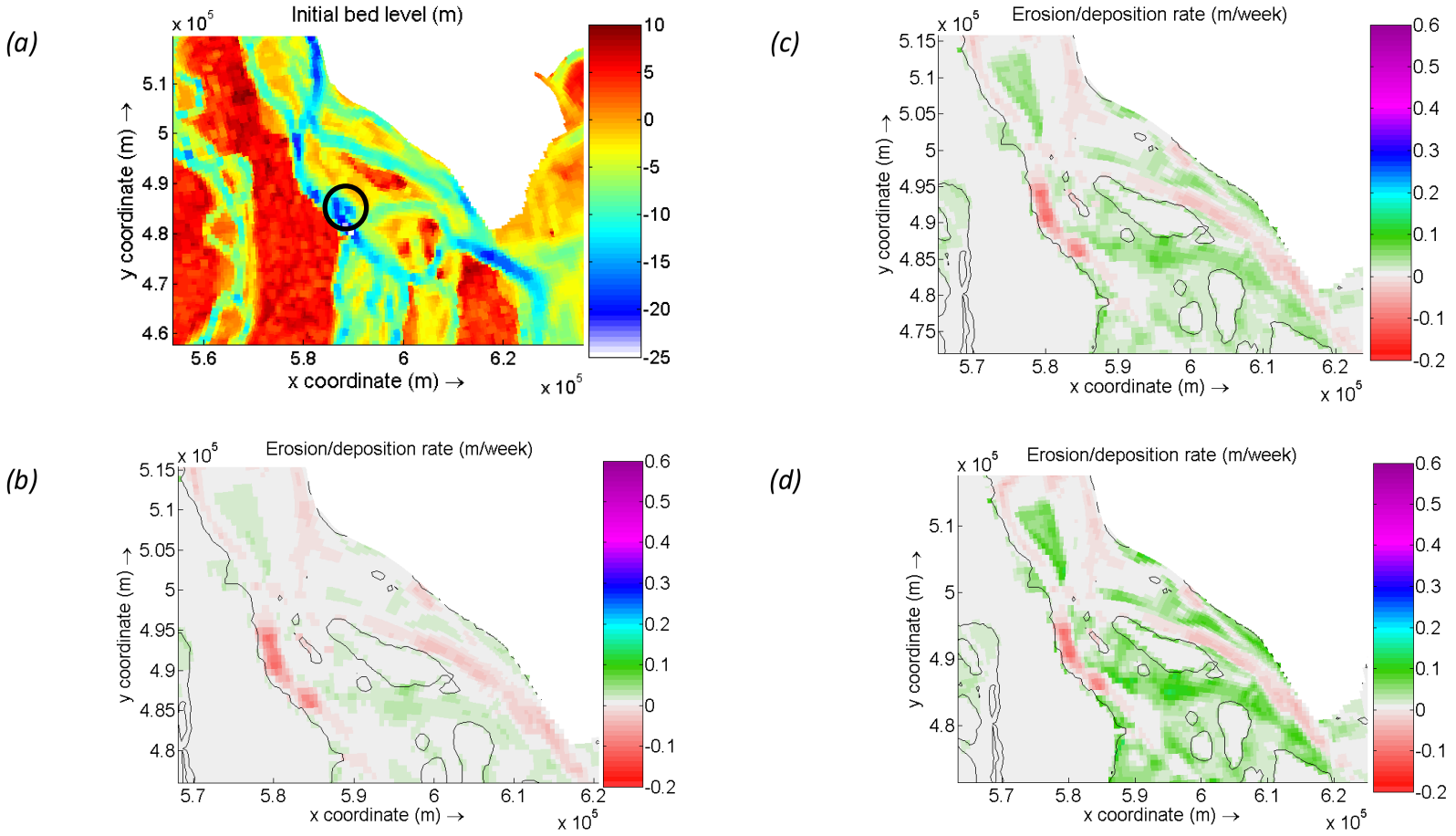

Figure 7.10: (a) Initial bed level in the vicinity of Location 1 (black circle) in Meghna estuary. Erosion and accretion obtained by considering 14 cycles of the 1.2 M_2 constituent tide for different floc sizes: (b) 20 µm, (c) 50 µm, (d) 100 µm, (e) 227.21 µm, (f) 500 µm, (g) 1000 µm

(e)

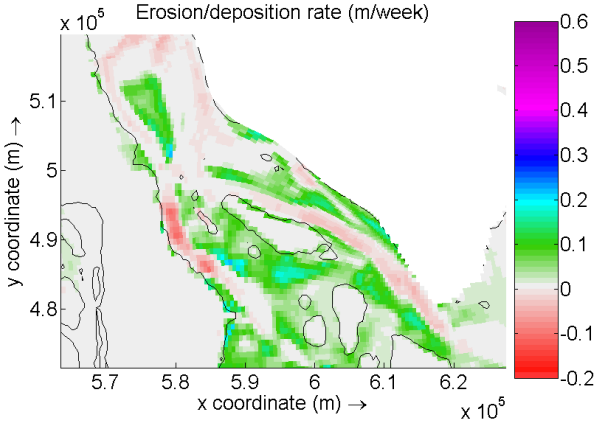

(g)

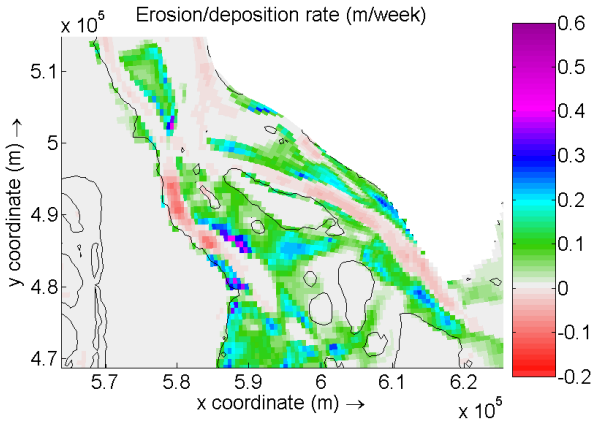

(f)

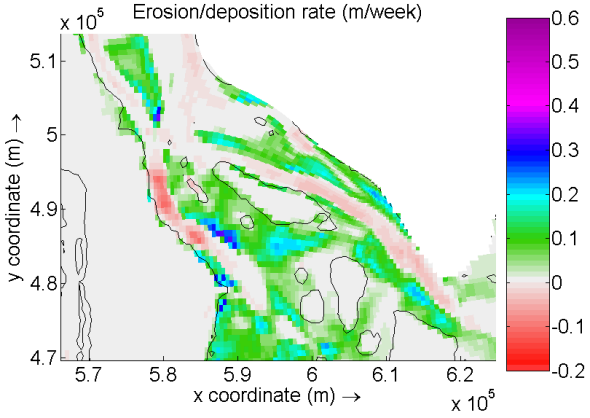

Figure 7.10 contd. : (a) Initial bed level in the vicinity of Location 1 (black circle) in Meghna estuary. Erosion and accretion obtained by considering 14 cycles of the 1.2 M_2 constituent tide for different floc sizes: (b) 20 µm, (c) 50 µm, (d) 100 µm, (e) 227.21 µm, (f) 500 µm, (g) 1000 µm

Accumulation of sediment occurs when and where flocs settle as the flow velocity slows. The flow direction reverses around the shallow tidal flats and islands during tidal high water, triggering the localized movement of sediment. Figure 7.10 repeats the local bathymetry (Figure 7.10(a)) and the changes in sediment deposition/erosion per week averaged over 14 tidal cycles for increasing floc size (Figures 7.10(b)-(g)). Figure 7.10 indicates that the deposition-prone locations occur where the depth is predominantly shallow. It may also be seen that as the floc size increases, the deposition rate also increases. This is because, the settling velocity increases progressively with floc size leading to more deposition of sediment.

Figure 7.11 displays the PDF and CDF of sedimentation rate at Location 1. The peak of the derived probability distribution occurs at 0.16 m/week. The right-hand tail of the distribution appears elongated, a reflection of its asymmetry. The CDF approaches 1, but does not quite reach unity. This slight mismatch would be expected to reduce if a higher number of bins were to be used for discretisation and a larger portion of the stretched right-hand tail of the PDF were to be taken into consideration. Table 7.2 lists the expected value, coefficient of variation, and other statistical moments of sediment deposition rate at Location 1.

From Table 7.2, the expected value of the sedimentation rate at Location 1 is 0.22 m and the standard deviation is 0.0828 m. The coefficient of variation is smaller than unity, implying that this is a low-variant dataset. The non-dimensional skewness is ≈ 0, which indicates that the probability density distribution of sedimentation rate at Location 1 is almost symmetric around its mean. The kurtosis is a little below 3, which indicates that the probability density distribution of sedimentation at Location 1 is slightly flatter than a standard normal distribution.

The propagation of uncertainty in floc size (74.5% of the mean value) caused the standard deviation of deposition rate to be 37.6% of the mean value. The coefficient of variation of deposition rate at Location 1 is smaller than that of

the input floc size, implying the dispersion of the distribution of deposition rate is less than that of floc size. This indicates that uncertainty in deposition rate of suspended cohesive sediment is not so sensitive to uncertainty in the floc size at Location 1.

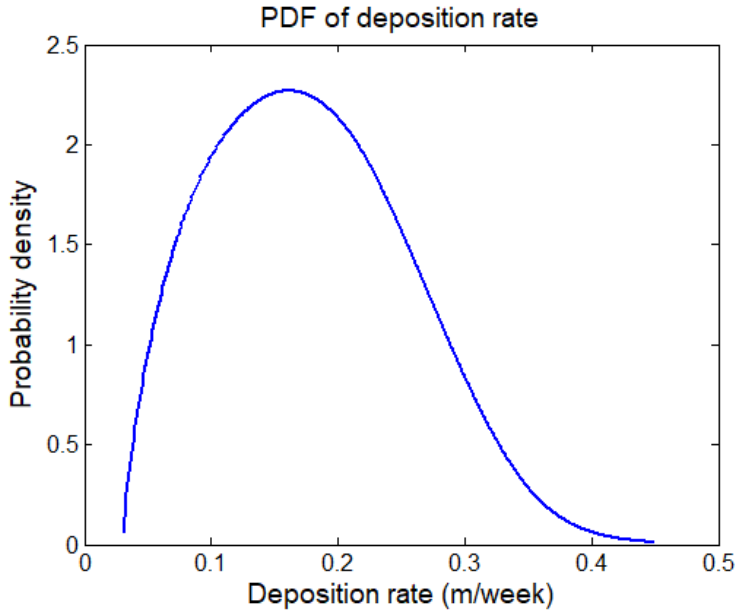

(a)

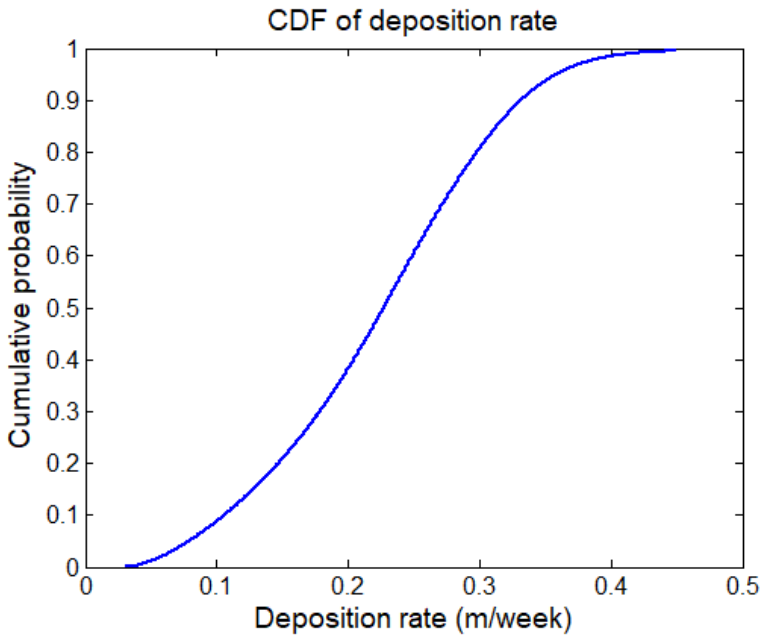

(b)

Figure 7.11: PDF (a) and CDF (b) of the deposition rate at Location 1 (Northwest of Char Gzaria, West Shahbazpur channel) in Meghna estuary, obtained by considering 14 cycles of the 1.2 M_2 constituent tide.

Table 7.2: Expected value and other statistical moments of deposition rate at Location 1 (West Shahbazpur channel, Meghna Bay).

Mean floc size (μm)	Expected value of deposition rate, $E[D]$ (m/week)	Standard deviation, σ_D (m/week)	Coefficient of variation, $\frac{\sigma_D}{E[D]}$	Non-dimensional skewness, $Skew_n(D)$	Non-dimensional kurtosis, $Kurt_n(D)$
227.21	0.22	0.0828	0.376	0.0219	2.4463

7.3.3. Uncertainty in deposition rate at Location 2 (West of Manpura, West Shahbazpur channel, Meghna Estuary)

The second location chosen for uncertainty analysis is Location 2 at a tidal flat where the local bathymetry is extremely irregular, varying from 5 to 12 m below mean sea level, at about 5.95×10^5 m East and 4.66×10^5 m North. Figure 7.12 depicts the local bathymetry near Location 2, which is again characterized by islands and shoals. The deepest channels are located to the northeast and southeast of Bhola island, and just to the north of Hatia island. Figure 7.13 shows the velocity field at two-hourly intervals, covering a representative tidal cycle, at Location 2. At tidal high water, when t_e = 0 h, the river flow passing through West Shahbazpur channel bifurcates, and slackens losing intensity. Further downstream, the flow velocity speeds up again, as it enters the deeper channel. During low water at elapsed times t_e = 2 h, 4 h, 6 h, and 10 h, the flow in the whole estuary is directed southwards towards the Bay [see figure 7.13(b), 7.13(c), 7.13(d), and 7.13(e)]. During high water, considerable residual circulation occurs in the shallow areas [figure 7.13(f) and 7.13(g)]. Some of these shallow areas, including Location 2, even dry out at low water [figure 7.13(a)].

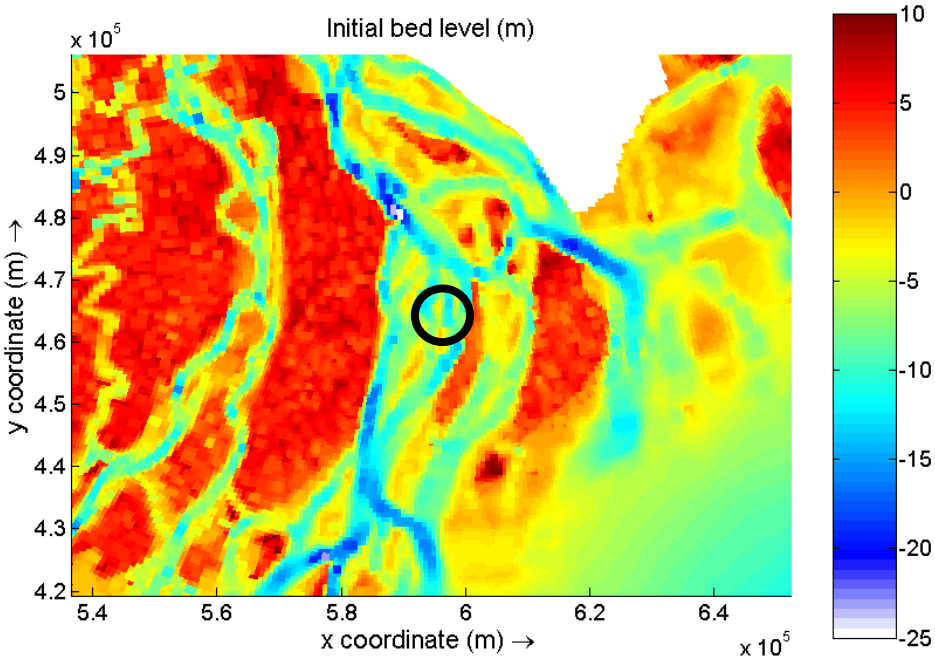

Figure 7.12: Initial bed level in the vicinity of Location 2 in Meghna estuary (black circle).

Figure 7.14 depicts the initial bed condition and deposition after 14 cycles of M_2 tide (about a week). As also for Location 1, deposition increases progressively with the increase in floc size. This figure again shows that deposition is most prevalent in shallow areas where the flow velocity drops to zero or near-zero. The residual circulation adds to the deposition process by inducing further localized movement of sediment.

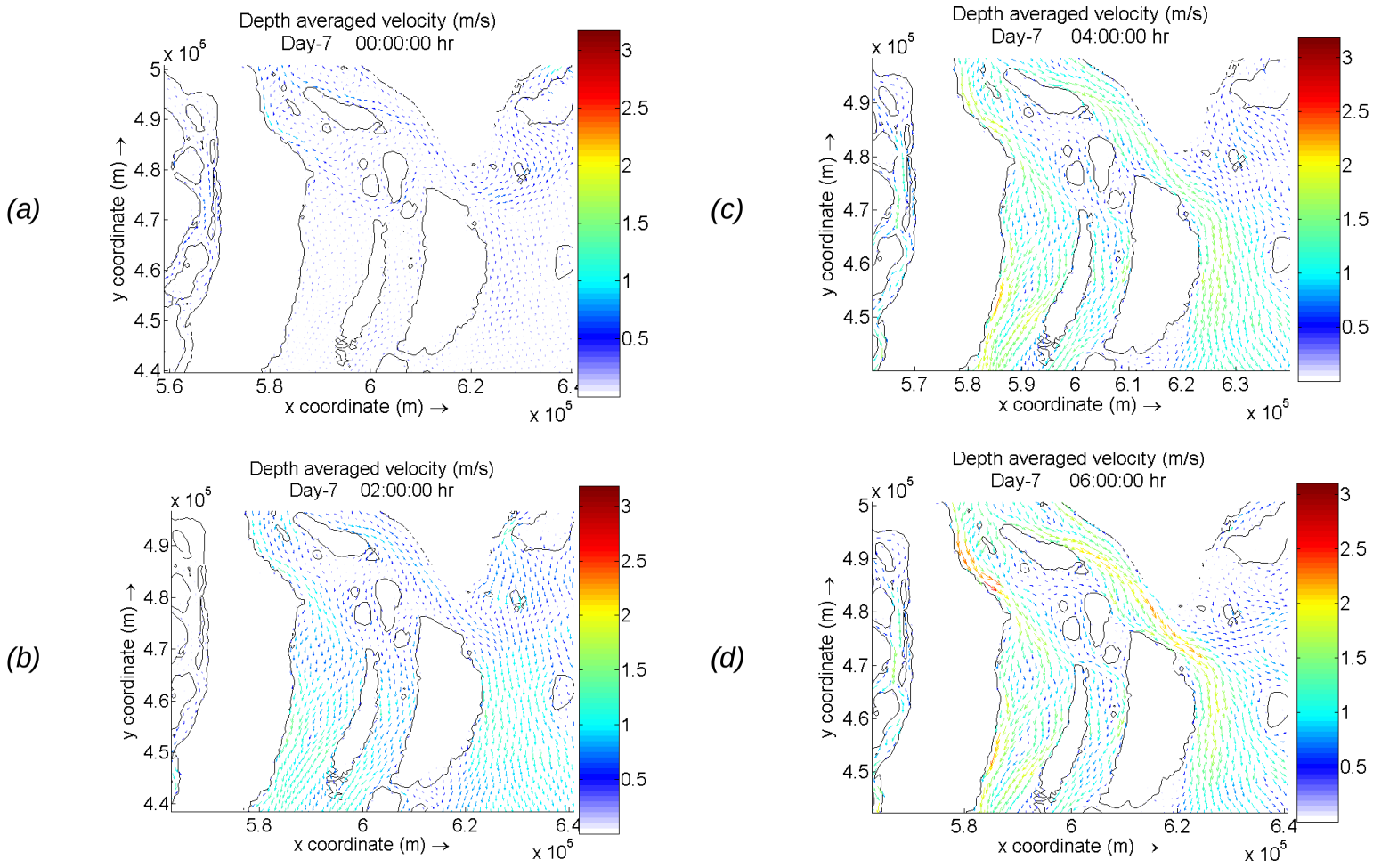

Figure 7.13: Depth-averaged velocity fields at two hourly intervals in the vicinity of Location 2 in Meghna estuary

(e)

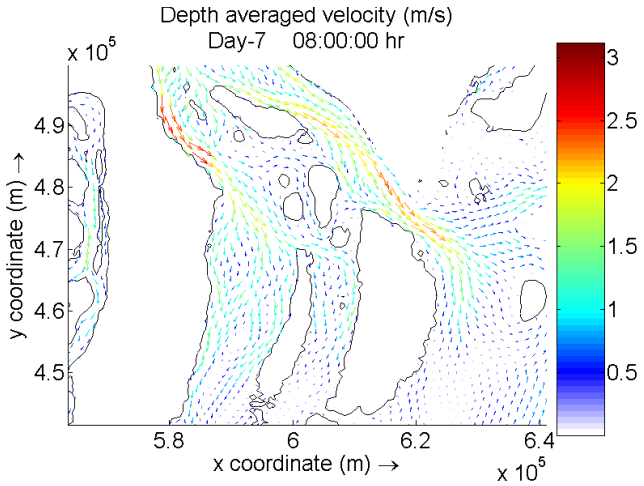

(g)

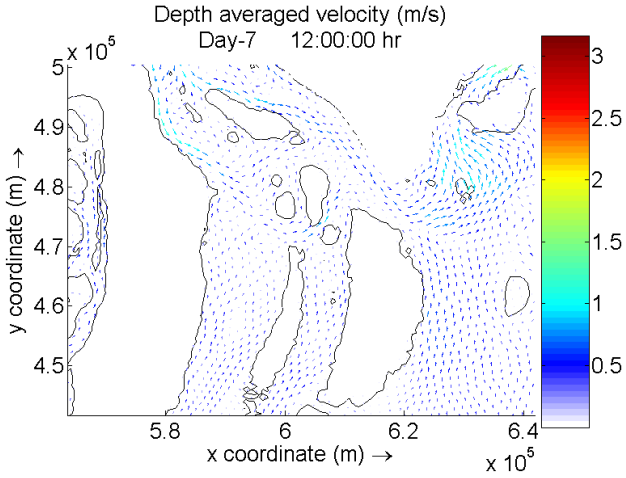

(f)

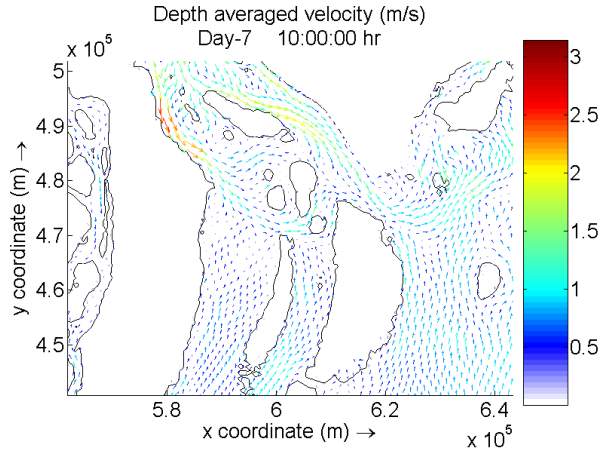

Figure 7.13 contd.: Depth-averaged velocity fields at two hourly intervals in the vicinity of Location 2 in Meghna estuary

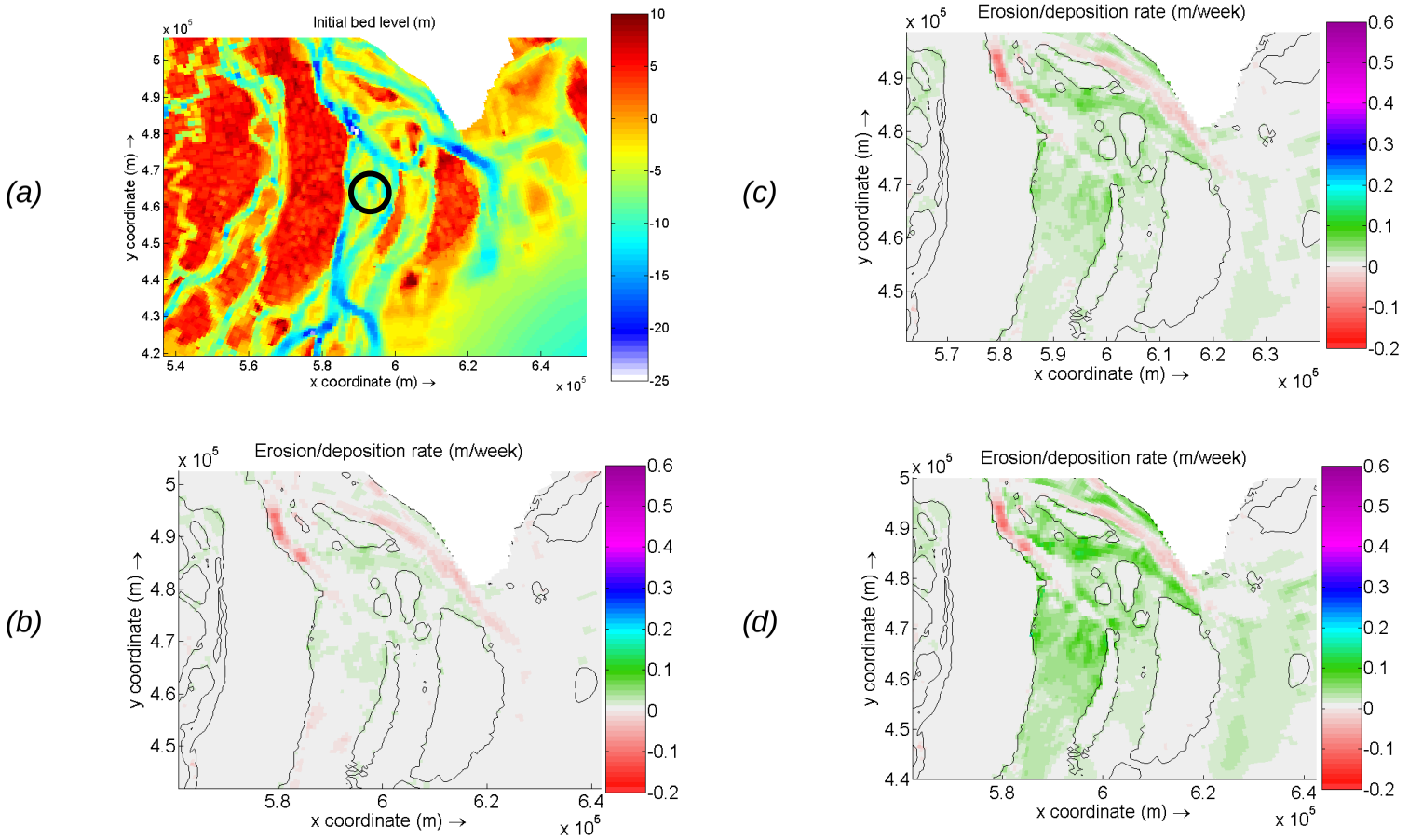

Figure 7.14: (a) Initial bed level in the vicinity of Location 2 in Meghna estuary. Erosion and accretion obtained by considering 14 cycles of the 1.2 M_2 constituent tide for different floc sizes: (b) 20 µm, (c) 50 µm, (d) 100 µm, (e) 227.21 µm, (f) 500 µm, (g) 1000 µm

(e)

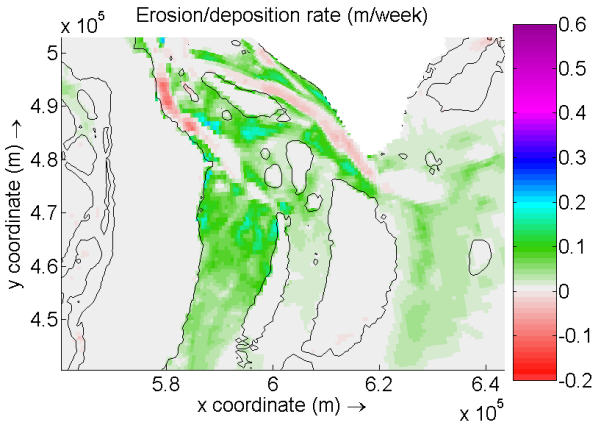

(g)

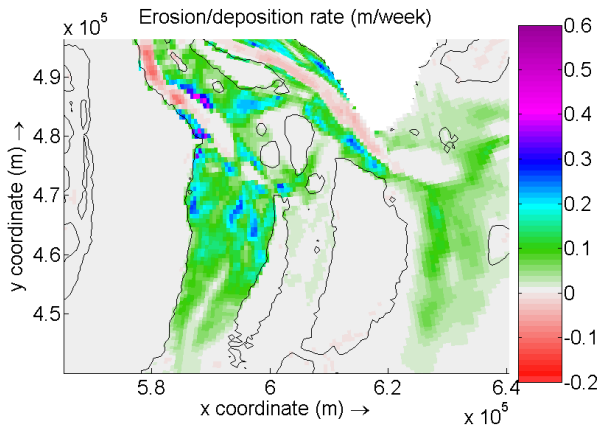

(f)

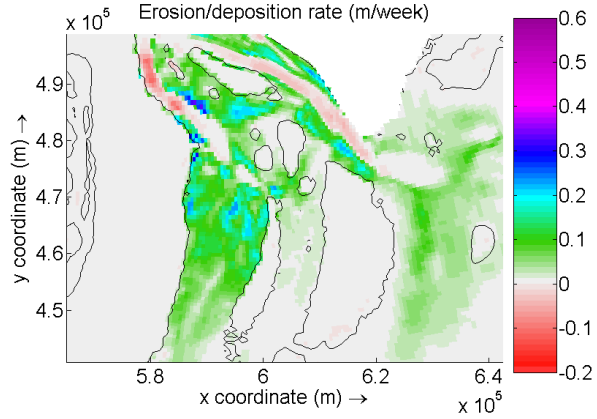

Figure 7.14 contd.: (a) Initial bed level in the vicinity of Location 2 in Meghna estuary. Erosion and accretion obtained by considering 14 cycles of the 1.2 M_2 constituent tide for different floc sizes: (b) 20 µm, (c) 50 µm, (d) 100 µm, (e) 227.21 µm, (f) 500 µm, (g) 1000 µm

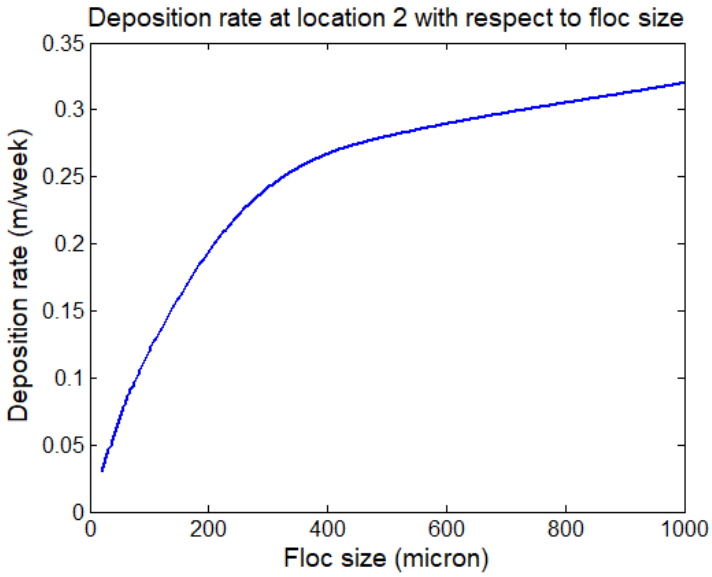

Figure 7.15: Cubic spline relation between sedimentation rate and floc size at Location 2 (West of Manpura, West Shahbazpur channel) in the Meghna estuary, obtained by considering 14 cycles of the 1.2 M_2 constituent tide.

Figure 7.16 shows the PDF and CDF of deposition rate at Location 2. The peak of the derived probability distribution occurs for a deposition rate of 0.13 m/week. This PDF appears flatter than that of location 1. Table 7.3 summarizes the expected value and other statistical moments of sediment deposition rate at Location 2.

Similar to Location 1, numerical data on the total deposition of sediment (in m) is obtained from the Delft3D results at Location 2, and the rate of deposition (in m/week) then calculated. Then a cubic spline is drawn connecting the resulting data on the rate of deposition of cohesive sediment (figure 7.15). The same input probability density distribution of floc size (figure 7.6) as for Location 1 is used here.

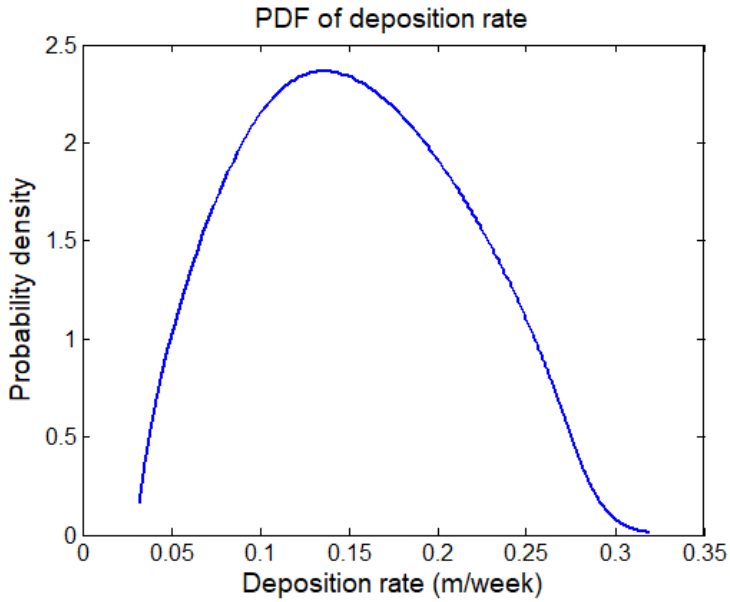

(a)

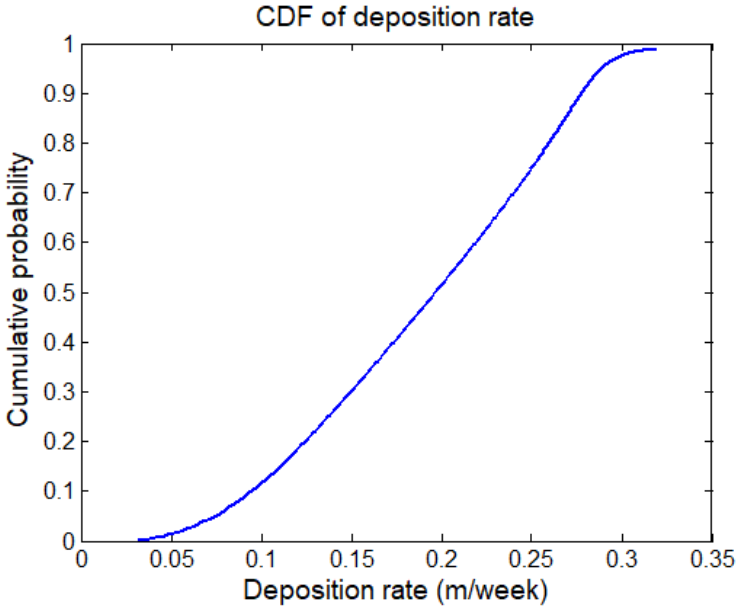

(b)

Figure 7.16: PDF (a) and CDF (b) of the sedimentation rate at Location 2 (West of Manpura, West Shahbazpur channel) in Meghna estuary, obtained by considering 14 cycles of the 1.2 M_2 constituent tide .

Table 7.3: Expected value and other statistical moments of deposition rate at Location 2 (West of Manpura, West Shahbazpur channel).

Mean floc size (μm)	Expected value of deposition rate, $E[D]$ (m/week)	Standard deviation, σ_D (m/week)	Coefficient of variation, $\frac{\sigma_D}{E[D]}$	Non-dimensional skewness, $Skew_n(D)$	Non-dimensional kurtosis, $Kurt_n(D)$
227.21	0.1883	0.0669	0.355	-0.1567	2.0362

From Table 7.3, the expected value of the sedimentation rate at Location 2 is 0.1883 m and the standard deviation is 0.0669 m. The coefficient of variation is less than 1, and so this is again a low-variant dataset. The non-dimensional skewness is negative, which indicates that the tail of the probability density distribution is asymmetric; most of the values lean towards the left side of the mean value of deposition rate. The non-dimensional kurtosis is less than that at Location 1, and so this probability density distribution is flatter than the probability density of deposition rate at Location 1. The coefficient of variation of floc size is 74.5%, which is more than twice the coefficient of variation of deposition rate. The standard deviation, which indicates the uncertainty incorporated in a parameter, is 35.5 % of the mean value of the deposition rate at Location 2. The derived probability distribution is less dispersed than the primary distribution, which means that the deposition rate is again not very sensitive to floc size.

7.3.4. Uncertainty in deposition rate at Location 3 (North of Bhola Kheyaghat, Tetulia channel)

Location 3 is at the Northwest of Bhola island in Tetulia channel, about 5.59 × 10^5 m East and 5.1 × 10^5 m North. Figure 7.17 presents the initial bathymetry in the region of Location 3. Figure 7.18 shows the velocity field (at two hourly intervals through a representative tidal cycle in the vicinity of Location 3. The mean depth is about 3-5 m.

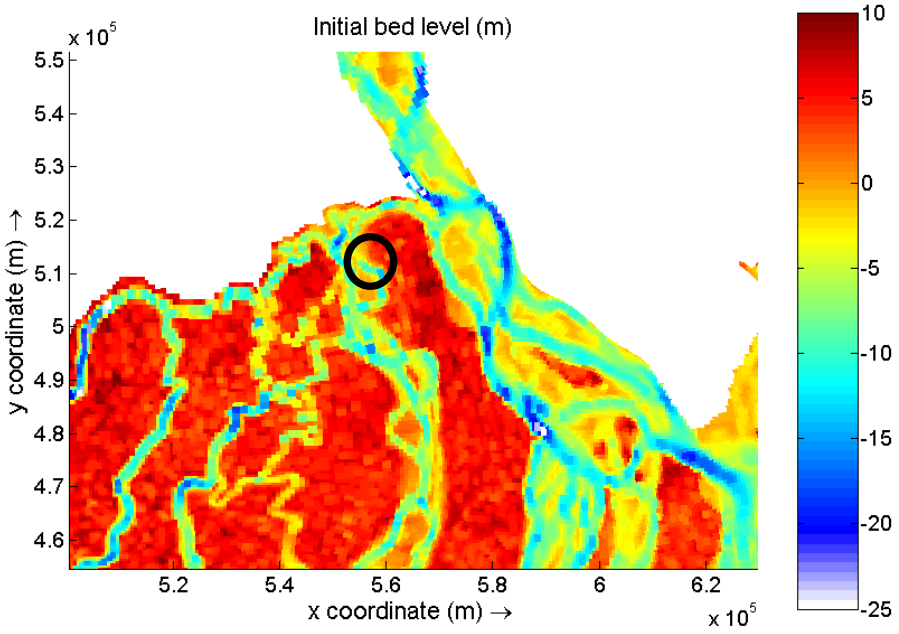

Figure 7.17: Initial bed level in the vicinity of Location 3 in Meghna estuary (black circle).

Historically, the whole Tetulia channel has been deposition-prone. During high water, the shallow area near Location 3 experiences very low flow velocity. It can be seen from figure 7.18 that a part of river flow from the large Meghna river diverts to the Tetulia channel. The tidal reach extends northwards, a little beyond the mouth of the Tetulia channel in Meghna river. Figure 7.18(a) and 7.18(b) present the velocity condition at high tidal water, when t_e = 0 h. River water coming from the upper Meghna river mixes with saline water on entry to the estuary. During low water, the river flow is sufficiently strong to push the sea water southwards towards the Bay of Bengal, and the flow velocity intensifies in both the Meghna river and Tetulia channel [figure 7.18(c), 7.18(d), 7.18(e) and 7.18(f)]. In figure 7.18(g), high water conditions have again returned, with the flow speed decreasing throughout the whole Tetulia channel, including Location 3. Seawater has entered the Meghna estuary, but is yet to reach the mouth of the Tetulia channel.

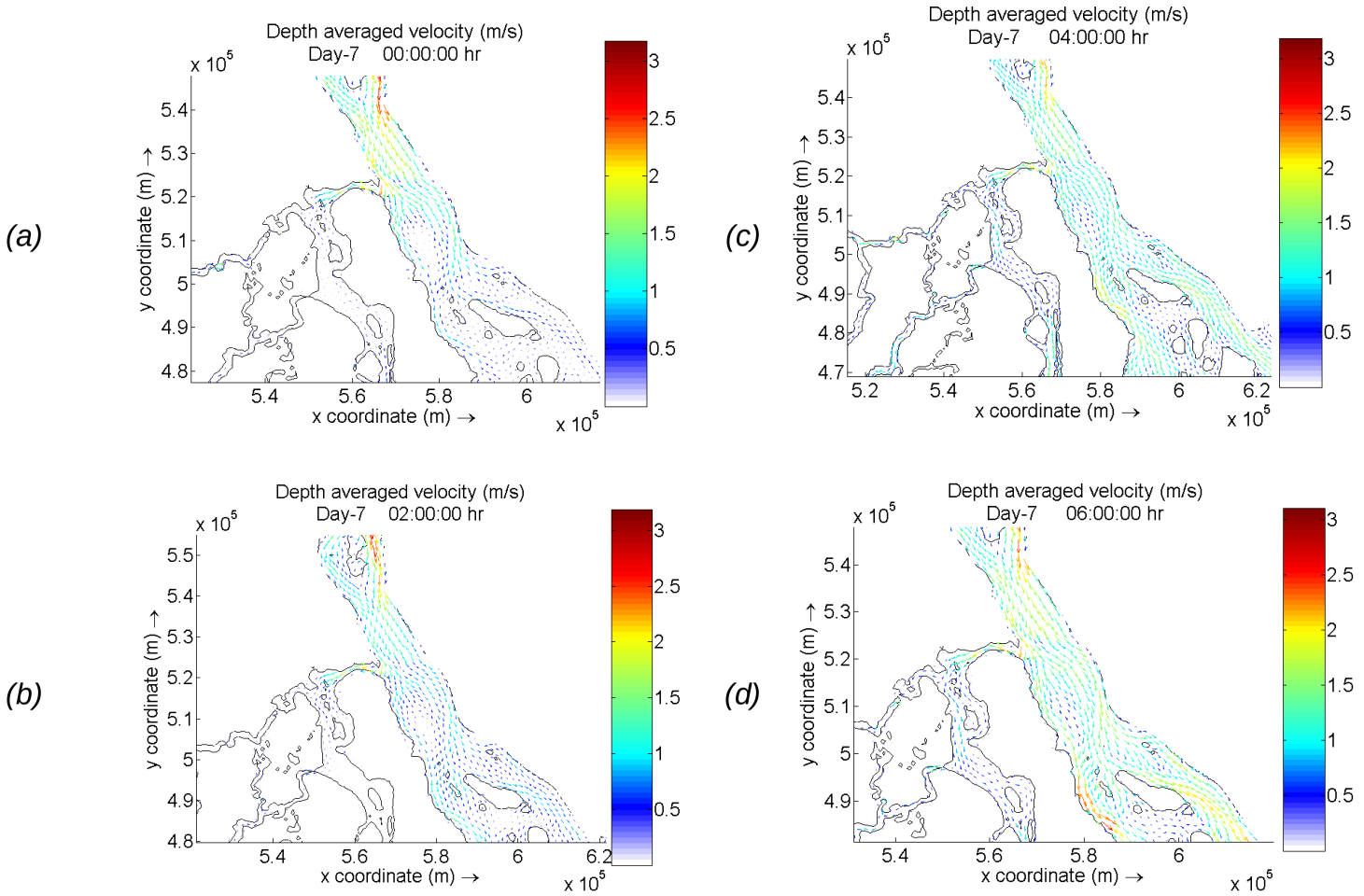

Figure 7.18: Depth-averaged velocity fields at two hourly intervals in the vicinity of Location 3 in Meghna estuary

(e)

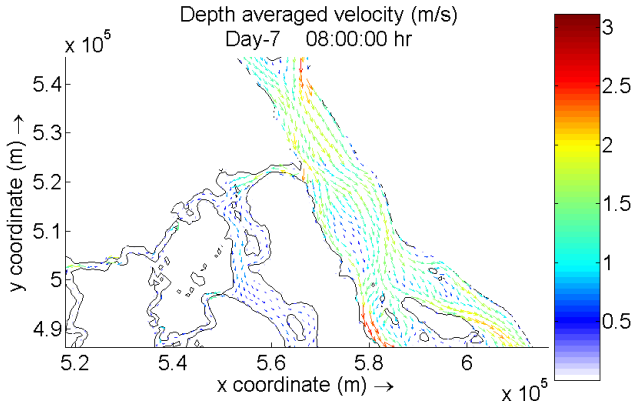

(g)

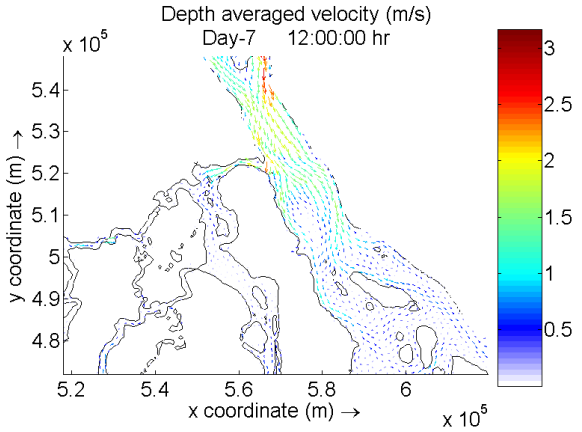

(f)

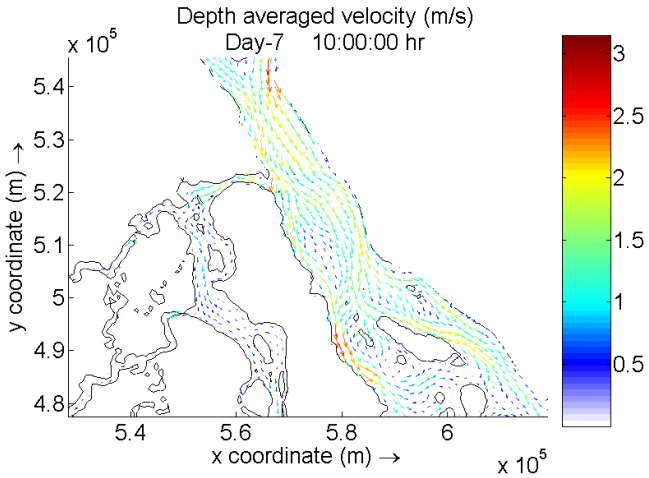

Figure 7.18 contd.: Depth-averaged velocity fields at two hourly intervals in the vicinity of Location 3 in Meghna estuary

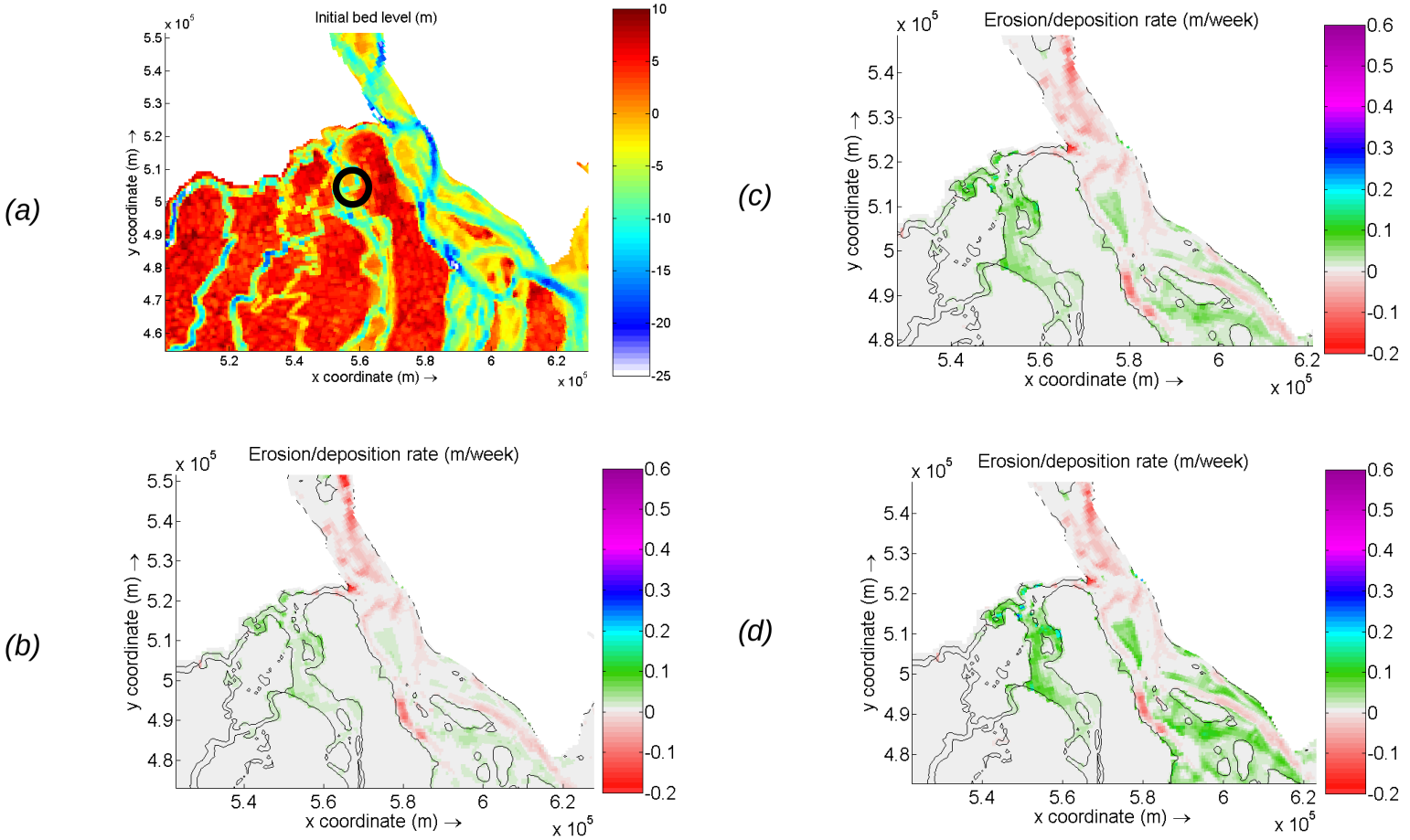

Figure 7.19: (a) Initial bed level in the vicinity of Location 3 in Meghna estuary. Erosion and accretion obtained by considering 14 cycles of the 1.2 M_2 constituent tide for different floc sizes: (b) 20 µm, (c) 50 µm, (d) 100 µm, (e) 227.21 µm, (f) 500 µm, (g) 1000 µm

(e)

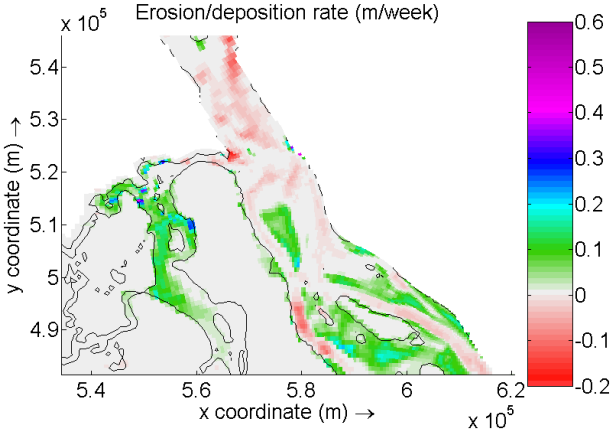

(g)

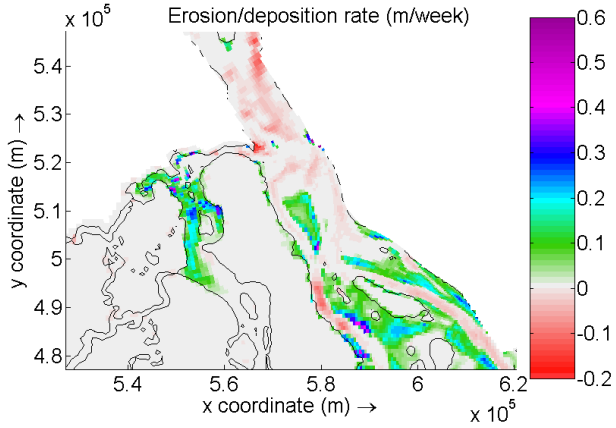

(f)

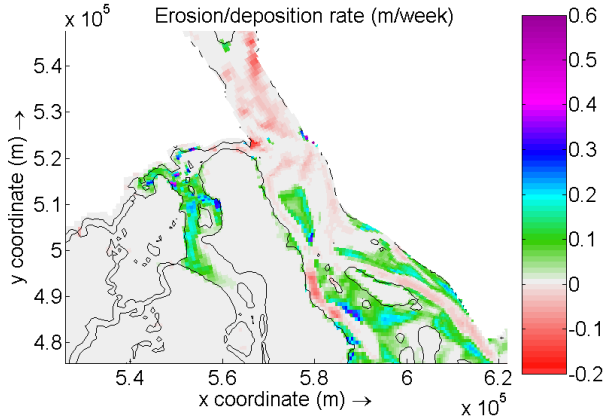

Figure 7.19 contd.: (a) Initial bed level in the vicinity of Location 3 in Meghna estuary. Erosion and accretion obtained by considering 14 cycles of the 1.2 M_2 constituent tide for different floc sizes: (b) 20 µm, (c) 50 µm, (d) 100 µm, (e) 227.21 µm, (f) 500 µm, (g) 1000 µm

Figure 7.19 shows the initial bed condition and the bed morphology changes in the region of Location 3. Due to near-zero flow velocity during high water period, the Tetulia channel is deposition-prone. The river flow in Meghna follows the bathymetry in that the velocity is larger in the deeper channels. This results in erosion. Shallower areas display a depositional trend because of the low magnitude of flow velocity. Similar to previous cases, deposition increases as floc size increases because the settling velocity is proportional to floc size, but the rate of increase becomes extremely low at the higher values of floc size (figure 7.20).

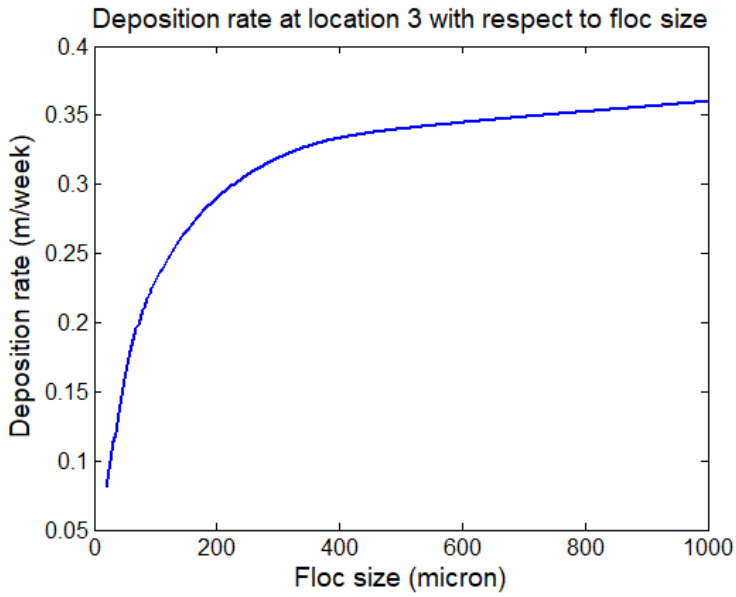

Figure 7.20: Cubic spline relation between sedimentation rate and floc size at Location 3 (North of Bhola Kheyaghat, Tetulia Channel) in the Meghna estuary, obtained by considering 14 cycles of the 1.2 M_2 constituent tide.

The PDF and CDF of deposition rate per week are shown in figure 7.20. They are derived from the PDF of floc size (figure 7.8) and the cubic spline drawn between deposition rate and floc size (figure 7.20). The probability distribution reaches its peak for a deposition rate of 0.25 m/week. The left tail of this PDF is more elongated than the right tail. The CDF approaches close to 1.

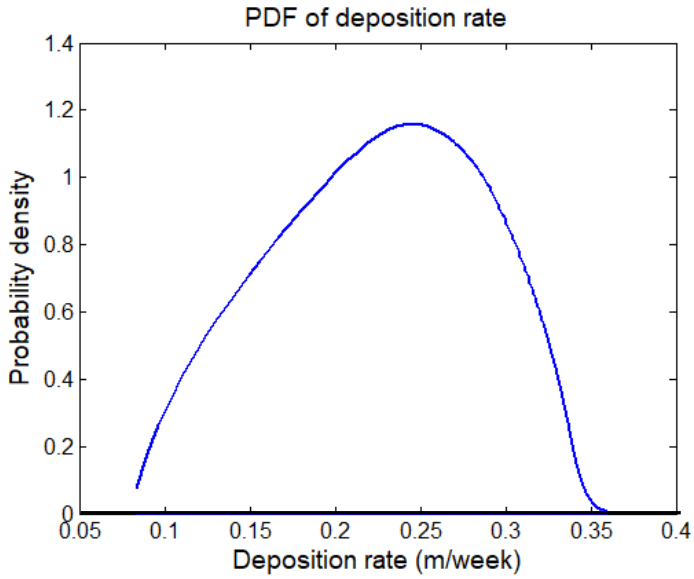

(a)

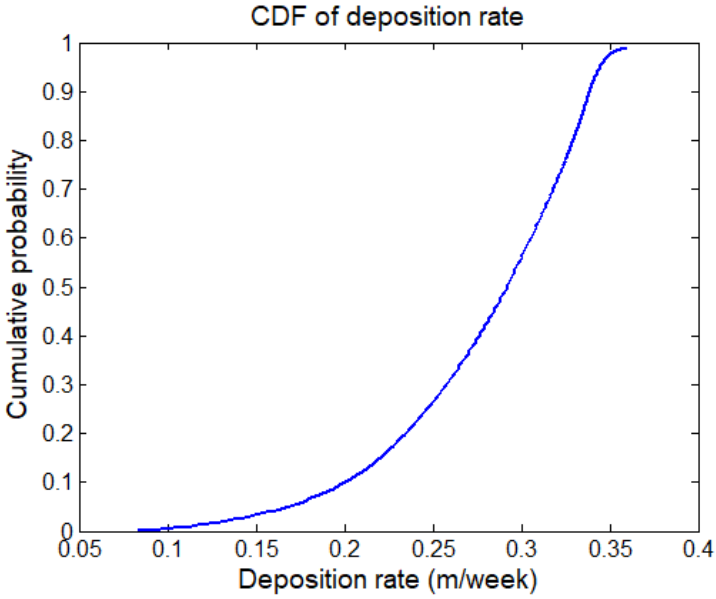

(b)

Figure 7.21: PDF (a) and CDF (b) of the sedimentation rate at Location 3 (North of Bhola Kheyaghat, Tetulia Channel) in Meghna estuary, obtained by considering 14 cycles of the 1.2 M_2 constituent tide.

Table 7.4: Expected value and other statistical moments of deposition rate at Location 3 (North of Bhola Kheyaghat, Tetulia Channel).

Mean floc size (μm)	Expected value of deposition rate, $E[D]$ (m/week)	Standard deviation, σ_D (m/week)	Coefficient of variation, $\frac{\sigma_D}{E[D]}$	Non-dimensional skewness, $Skew_n(D)$	Non-dimensional kurtosis, $Kurt_n(D)$
227.21	0.2756	0.0545	0.198	-0.7917	3.3127

From Table 7.4, the expected value of sedimentation rate is 0.2756 m and its standard deviation is 0.0545 m, at Location 3. The coefficient of variation is 0.198, the lowest value among all three locations. The non-dimensional skewness is negative, which means the tail of the probability density distribution is asymmetric and the tail extends towards the left side of the mean value of the sedimentation rate. Kurtosis is slightly higher than 3, which indicates that the probability density distribution of sedimentation rate at Location 3 is not as flat as a standard normal distribution. The probability density distribution here is even more low-variant than at the other locations; the input uncertainty in the floc size propagates to cause an uncertainty of 19.8% of the mean value of the deposition rate.

7.4. Concluding remarks

This chapter has investigated the effect of input uncertainty in a sediment parameter on the output uncertainty in sedimentation rate at three locations of interest in the Meghna Bay. The uncertainty in deposition rate emerged to be less sensitive to uncertainty in floc size, with the values of normalized variance being lower for deposition rate than floc size. At all three locations, flow coming from the Meghna river appears to depend closely on local bathymetry, whereas the sediment erosion/deposition is closely linked to the local flow speed. In the regions of the Meghna estuary considered herein, shallow areas are deposition-prone whereas the deeper parts of the channels are erosion-prone. Flocs deposit in areas where the current speed, arising

from the combined effect of river flow and tide, approaches close to zero. This is to be expected, because as the water approaches stagnation, the particle settling velocity becomes an increasingly important driving parameter in the sediment transport process.

The standard deviation being close to mean indicates that irrespective of different size of floc formation, 5 micron particles are expected to cause deposition in the study locations of a value around the mean. Whereas land erosion is a threat to valuable land of a densely populated country, the deposition near the islands and narrow channels increases flood risk in the long term.

It should be noted that this study did not include the effect of tropical cyclones and Coriolis force. And it is also necessary to investigate the deposition with different type and size of sediment in this region. Field data about the bed material and suspended sediment is vitally important as a prerequisite for the model predictions to become closer to reality. This study opens a way by which to conduct further extensive study on the morphological behavior of Meghna estuary (considering several other important input parameters) and can help decision makers to plan flood mitigation measures and land protection works, or even land reclamation activities.

Chapter 8
Discussion

8.1. Discussion

One of the objectives of the thesis was to find and use an appropriate method for uncertainty propagation by assessing the statistics of hydro-morphodynamic properties obtained from a regional scale model for uncertain input parameters. The thesis utilized the numerical analogy of the derived distribution approach originally used by Kreitmair et al. (*2019*) to compute uncertainty propagation arising from bed roughness through a shallow flow model to estimates of maximum hydro-power. To the best of the present author's knowledge, the numerical derived distribution approach is used herein for the first time in uncertainty quantification for the Meghna Estuary of Bangladesh. Chapters 4, 5, and 6 demonstrate its successful application to uncertainty propagation from a bed roughness parameter (Manning's *n*) to the maximum water level, from sea level rise to the maximum water level, and from floc size to the deposition of fine sediment. The output parameters were obtained from the well-established Delft3D model that solved the shallow water equations for the complicated flow geometry comprising the Meghna estuary and Bay of Bengal. The numerical derived distribution approach proved to be a suitable risk assessment tool in cases where the input uncertainty propagates to output uncertainty in selected hydro-morphodynamic characteristics, and was highly efficient in that it required very few simulations. However it is important to note that the numerical derived distribution method was limited to cases where the input and output

parameters have a monotonically increasing or decreasing relationship with each other. Further research is needed to overcome this limitation.

The model of Meghna estuary and Bay of Bengal was created using Delft3D FLOW which includes the option of sediment transport. The difficulty of generating a curvilinear grid with appropriate resolution was tackled by using small cell sizes in the area of interest (i.e., within the estuary) and larger cell sizes offshore. Use of a morphological acceleration factor with Delft3D proved to be an excellent option when modelling sediment transport, resulting in a huge saving in simulation time. The model was not calibrated against field data, because of its unavailability; instead, the thesis focused on a hypothetical parameter study. In future, when adequate field observation data become available, the present model can be readily extended to examine more realistic scenarios after calibration and validation.

Three different locations, namely Sandwip, Char Purulia and Tiger Point, were chosen to investigate uncertainty propagation from the Manning's roughness parameter to the maximum water level. Sandwip island is situated at the eastern side of Meghna estuary. Tiger Point is on the western side. Char Purulia is inside the mouth of the estuary. For a 5-fold increase in standard deviation of Manning's n at Sandwip, the standard deviation of maximum water level exhibited a 5.35-fold increase. For the same 5-fold increase in standard deviation of Manning's n at Char Purulia and Tiger Point, the standard deviation of the maximum water level increased remarkably by 7 times at Char Purulia, and about 5 times at Tiger Point. Char Purulia is shallower than the other two locations, and is close to where the Meghna river enters the bay. So, Char Purulia is more sensitive to bed roughness and hence uncertainty in Manning's n translates to increased uncertainty in maximum water level (reflected by the higher standard deviation obtained at Char Purulia than at the other two locations). Overall, uncertainty in bed roughness has a substantial effect on uncertainty in maximum water level at each of the locations considered in the Meghna estuary.

Bed roughness is commonly used as a calibration parameter in hydro-morphodynamic models for different locations around the world, e.g. Western Scheldt estuary (*Dam et al., 2016*), Yangtze estuary (*Luan et al., 2017*), San Francisco bay (*Cloern et al., 2011*), etc. Such models are usually validated against field data at certain locations, while neglecting the spatial variation in roughness over the whole domain. The present thesis has shown how a remarkable level of uncertainty can arise in estimates of the maximum water level around Meghna estuary from bed roughness parameter uncertainty. By neglecting the spatial distribution in bed roughness parameter, significant error can result in output parameters from shallow flow models. Thus, it is of utmost importance to conduct thorough field investigations on the bed roughness conditions in the Meghna estuary and alter the present modelling practice of simply treating bed roughness as a spatially uniform tuning parameter to one of inputing bed roughness according to a spatially detailed dataset.

For the three different IPCC scenarios considered, the standard deviation in maximum water level including sea level rise increased by between 33% at Tiger Point and 49.5% at Char Purulia for a 36% increase in standard deviation of mean sea level rise in the Bay of Bengal. By excluding the linear effect of sea level rise, the increase in standard deviation in maximum water level was found to vary remarkably from 6% (at Char Purulia) to 80% (at Sandwip) for the 36% increase in standard deviation of sea level rise. From the website of the Bangladesh Water Development Board (*BWDB, n.d.*), extensive embankment construction has been undertaken along the coastline, including the three locations of interest. These embankments have been designed to protect people and properties in nearby cities and villages from flood inundation and land erosion. Given an accurate estimate of the uncertainty in maximum water level arising from uncertainty in sea level rise, then the resulting effect on risk can be assessed properly, and the safety factor modified if deemed necessary during the design phase of such embankments. Furthermore, both flood mitigation planning measures and warning system

operations can be efficiently executed if such uncertainty is taken into consideration.

After deriving the PDF of deposition rate from the PDF in floc size of the suspended cohesive sediment, the coefficient of variation was found to range from 19.8% to 37.6% across Sandwip, Char Purulia, and Tiger Point, in the Meghna estuary. In general, shallower areas were found to be more prone to sediment deposition, implying higher flood risk. Deeper areas were more erosion-prone. Given that the cohesive sediment fraction was solely considered, the erosion-accretion pattern only partially matched historical evidence given by Brammer (*2014*). Further investigation involving multiple sediment fractions will be necessary to generate more realistic scenarios. By computing the uncertainty in rate of deposition rate, it is then possible to evaluate the effect on elevated bed level and hence the flood risk. Such analysis can also provide useful information regarding different land reclamation options, enabling the government to make a systematic choice between such options thus aiding the coastal planning process. For example, the Estuary Development Plan (*2007*) produced by the Ministry of Water Resources of Bangladesh identified several deposition-prone areas; in this case, uncertainty quantification could be highly beneficial. For areas where significant erosion occurs in the model domain, then the uncertainty in erosion can also be calculated when assessing the risk of land erosion. Similar to its flood risk counterpart, erosion risk assessment will help local authorities plan long-term protective measures. Of particular relevance is the ongoing Bangladesh Delta Plan 2014 which is adopting a holistic approach for which uncertainty quantification of key parameters related to relevant natural disasters would be extremely advantageous, particularly for government agencies charges with coastal management and protection.

Lastly, although only three locations were chosen for quantification of output uncertainty arising from a few input parameters, the analysis in this thesis indicates that it would be straightforward to apply the same procedure to estimate output uncertainty at multiple locations of interest for uncertainty in

multiple input parameters along the coastline of Bangladesh. Such an approach would provide a holistic picture of uncertainty propagation throughout the whole coastal region of Bangladesh. Given that the basic hydro-morphodynamic model has been established, the approach can be applied to risk assessments related to flood inundation, sea level rise, land erosion and accretion, salinity intrusion, cyclonic surges and ocean wave propagation, etc., contributing to the planning and management for coastal zone of Bangladesh for many years to come.

Chapter 9

Conclusions and Recommendations

9.1. Preamble

With a land mass of 148,460 square km and a population of more than 162 million, Bangladesh is one of the most densely populated countries in the world. The coastal zone of Bangladesh along the Bay of Bengal is particularly vulnerable to natural disasters, including flood inundation, land erosion, sea level rise, cyclones, etc. This thesis has examined use of a fast numerical method for estimating the propagation of uncertainty in selected input hydro-morphodynamic parameters relevant to flooding and land erosion. Uncertainty can arise from many sources including incomplete information on physical parameters arising from insufficient or inaccurate field data on bathymetry, bed roughness, sediment characteristics, etc., as well as choice of numerical model, numerical error, and model limitations. The thesis studies the propagation of uncertainty in bed roughness, sea level rise, and floc size of suspended cohesive sediment through a standard shallow water-sediment code, Delft3D, to output statistics in maximum water levels, sediment transport, and deposition and erosion processes at certain sites in the Bay of Bengal. Uncertainty quantification is potentially very helpful for risk analysis. It is likely that policy makers will benefit from understanding how uncertainty propagates in standard numerical simulations of hydrodynamic and sediment processes, particularly in a flood-prone, data-scarce region like Bangladesh.

This chapter discusses the findings from this thesis and its significance. Some recommendations for future work are given at the end of this chapter.

9.2. Conclusions

This thesis aimed to identify an appropriate uncertainty analysis method to use for outputs from a limited number of model simulations, to establish a fundamental hydro-morphodynamic model for Meghna estuary and Bay of Bengal, to calculate uncertainty in maximum water level at different locations of Meghna estuary due to input uncertainty in bed roughness and sea level rise, and to estimate the uncertainty in the deposition rate of suspended cohesive sediment propagated from uncertainty in floc size.

The probability transfer mechanism applied in the thesis is a numerical analogy of an existing analytical approach called the derived distribution approach that was previously established by hydrologists for flood prediction, peak flood estimation, etc. (as discussed in chapter 2). The derived distribution approach enables rapid assessment of the probability distribution of a dependent variable (in this case, the output parameter of a numerical shallow water-sediment model) from the known or assumed probability distribution of an independent variable (i.e., an input parameter of the model). Whereas Monte Carlo simulation requires thousands or tens of thousands of model runs, the numerical derived distribution approach is able to efficiently produce the derived probability distribution from a very small number of model simulations. This approach can be used for any set of input and output parameters from state-of-the art, robust models for any location to estimate uncertainty, provided the relationship between the input and output parameters are monotonic.

From the results, it was found that a five-fold increase in standard deviation of Manning's *n*, led to a five- to seven-fold increase in standard deviation in maximum water level at the locations. Also, a 50% increase in the mean value of Manning's *n* caused the increase from 24% to 80% in the mean value of maximum water level. These results confirm the great importance of the bed

roughness parameter in predicting flooding scenarios using a standard numerical model. The underlying uncertainty in the Manning's *n* strongly affects the uncertainty in maximum water level. The present findings are hypothetical in that they are limited to spatially constant distributions of Manning's *n*, which is not the case in the Bay of Bengal where bed sediment can vary from fine clay to coarse sand particles. To include spatial variation in bed roughness parameter, though highly desirable, would require a much more involved analysis, and is beyond the scope of this thesis. It should also be emphasized that the widespread practice whereby a spatially constant bed roughness parameter is used merely as a tuning parameter in a hydro-morphodynamic model may permit overall calibration and validation tests to be undertaken apparently successfully, but incur local inaccuracy due to the spatial variation in bed roughness. In the case of the Meghna estuary, which has a highly complicated bathymetry and coastal hydrodynamics that are very sensitive to local bed roughness, it is obviously preferable that bed roughness not be used merely as a calibration parameter; instead extensive field campaigns are needed to provide in-situ data on the bed conditions throughout the Bay of Bengal.

A study was also made of the effect of uncertainty in sea level rise on the statistics of maximum water level. Truncated normal distributions of sea level rise were fitted to year 2100 data for IPCC global scenarios RCP2.6, RCP6.0, and RCP8.5. At all the locations considered, increased uncertainty in sea level rise translated to increased uncertainty in maximum water level. This implies significant additional flood risk due to sea level rise, particularly outside the mouth of the estuary. This uncertainty analysis is beneficial for the scientists, engineers, local authorities and policy makers who will assess the risk of flooding and will make flood control and mitigation planning, including the construction of embankments and operation of flood warning system. Again, it should be noted that the numerical probability distribution transfer method proved very effective at estimating the output uncertainty using results from very few model simulations.

In the third part of the study, the Delft3D model was set up for cohesive sediment transport, and the effect of uncertainty in floc size examined on the output sediment transport statistics at the three sites of interest. After deriving the PDF of suspended cohesive sediment, the coefficient of variation was found to range from 19.8% to 37.6% across the three locations, Sandwip, Char Purulia, and Tiger Point, around the Meghna estuary. This is a substantial uncertainty to be considered for planning in the coastal zone, noting the increased risk of flooding in deposition-prone areas as they become shallower. Land reclamation and erosion control planning will also benefit from this study because planners will be able to estimate better the amount of uncertainty to be considered. Floc settlement in the estuary is dominated by the local magnitude of bulk flow speed and the deposition mechanism is very sensitive to the local bathymetry. In general, this thesis has shown that shallower areas are likely to be more prone to sediment deposition, implying higher flood risk. Deeper areas are more erosion prone.

Lastly, the Delft3D model used for this study shows huge potential for future development. It is possible to add wave climate, cyclone tracks, multiple sediment fractions (both cohesive and non-cohesive), Coriolis force, salinity concentration, etc. in the existing model. With the availability of sufficient data, this model can be improved to simulate numerous scenario analysis with multiple parameters representing troublesome natural disasters.

In a nutshell, this thesis contributed to the knowledge base as follows:

i) A numerical analogy of existing analytical derived distribution approach has been successfully used in this thesis, which is a new approach for hydro-morphodynamic modelers. It has been shown that results generated from a very limited number of simulations can be used for PDF generation and hence uncertainty estimation.

ii) Uncertainty propagated through Manning's roughness parameter to maximum water level has been estimated for three different locations in Meghna estuary. This analysis establishes the

importance of detailed investigation of the effect of spatially varying bed roughness, a parameter which is commonly used as a calibration parameter by numerical modellers in different regions around the world.

iii) Uncertainty propagated through sea level rise to maximum water level has been estimated for different locations in the Meghna estuary. In the absence of sufficient high-quality data, the analysis provides information useful in flood risk assessment for coastal zone management and flood control planning.

iv) Uncertainty in the deposition rate of suspended cohesive sediment around the Meghna estuary due to the underlying uncertainty in the floc size has been calculated. Again, without proper field observation data, this study also provides important information on a risk assessment methodology concerning flood inundation, siltation and land erosion for use by policy makers, scientists and local authorities.

v) A fundamental Deltf3D model has been established which can be extended further in the geographical domain, and has the potential to be advanced to a full 3D model. This would allow consideration of the effect of a wider range of key parameters representing more realistic conditions.

9.3 Recommendations

Based on the work carried out for this thesis, the following future research directions are suggested:

i) The numerical probability transfer method as it presently stands is suitable only for application to monotonically increasing or decreasing functions linking an input variable to an output variable. In practice, such monotonic relationships do not always exist between the two parameters. Thus, it is recommended that further research be undertaken to derive a more general form of the

numerical derived distribution approach so that it can be applied to cases where the relationship between input and output is more complicated.

ii) Even though the maximum water level is an indicator of potential flood phenomena, it is recommended that uncertainty analysis be carried out to examine the effect of uncertainty in bed roughness, sea level rise, and sediment particle/floc size on other hazard parameters, such as flow speed, flood extent, sediment flux, water quality, biodiversity, etc.

iii) The model would benefit from further development to incorporate more physical information so that it would generate more holistic scenarios. For example, Coriolis forces, salinity, and seasonal cyclones have an important influence on morphological change, but were not included in the thesis. Their inclusion would be expected to improve the quality of the results, particularly in comparison against historical records.

iv) A single particle size of 5 μm was chosen for sediment deposition in this thesis. It is recommended that future studies consider other the effect of particle size on uncertainty propagation. Moreover, it would be greatly beneficial if both cohesive and non-cohesive sediment fractions be included together in order to improve the practical relevance of the model simulations.

v) Land subsidence is evident in the Bay of Bengal, and is location specific. It is recommended that future work include local land subsidence along with sea level rise in order to gain a better understanding of these effects on flooding parameters at different locations along the coast of the Bay of Bengal.

vi) The probability distribution of floc size was derived from field investigations undertaken in estuaries and coastal waters in other continents, far from the Bay of Bengal. It is recommended therefore that field campaigns be carried out to collect high quality data on suspended sediment in the Bay of Bengal, so that such data can be incorporated in hydro-morphodynamic models.

vii) Field campaigns are also necessary to determine the bed sediment conditions throughout the Bay of Bengal. Such campaigns would need to be repeated at regular intervals in order to monitor short- to long-term changes in local sedimentation and sediment properties (size, texture, etc.). Such information about the bed sediment conditions would be very useful in refining the probability distribution of bed roughness parameter (especially by extending it to cover its spatial variation) and bedload transport. The availability of more refined data would obviously improve the usefulness of the model.

viii) The present model utilizes simplified open boundary conditions for the river inputs to enhance computational efficiency. However, the river discharges are set to constant peak flood discharges which do not represent the seasonal fluctuations throughout the year. In practice, a flood event does not occur with a constant discharge lasting over 3 months. To improve the realism of the numerical model, it is recommended that actual river flow data be used; this would of course lengthen the simulation time, but provide a more realistic scenario. Similarly, the offshore boundary tidal condition could be prescribed with have more tidal constituents than merely M_2 and S_2 components; this would again increase the computational cost, though with the benefit of greater realism.

ix) Morphological change is a slow process. This thesis simulated extreme river flow conditions over a period of 3 months. To obtain a better long-term picture of the estuary morphodynamics, it is

recommended that much longer simulations be carried out using hydrographs that cover consecutive dry and monsoon seasons.

x) It is recommended that similar studies be carried out using other hydro-morphodynamic modelling tool in order to investigate the effect of choice of model on uncertainty propagation in shallow flows. And it would be very interesting, should the computational power be available, to compare the present findings with those from other uncertainty propagation methods described in chapter 2.

References

Ahmed, M., 1989. Flood in Bangladesh, Dhaka: Community Development Library.

Allison, M. A., 1998. Historical changes in the Ganges-Brahmaputra delta. Journal of Coastal Research, 14(4), 1269-1275.

Akter, J., Sarker, M.H., Popescu, I., and Roelvink, D., 2016. Evolution of the Bengal Delta and its prevailing processes. Journal of Coastal Research, 32(5), 1212–1226.

Akter, R., Asik, T. Z., Sakib, M., Akter, M., Sakib, M. N., Azad, A. S. M. A., Maruf, M., Haque, A., and Rahman, M. M., 2019. The dominant climate change event for salinity intrusion in the GBM delta. Climate, 7(5), 69.

Ang, A. H-S and Tang, W. H, 1975. Probability concepts in engineering planning and design v.1: Basic principles. John Wiley and Sons, Inc., The USA.

Aronica, G., Hankin, B., and Beven K., 1998. Uncertainty and equifinality in calibrating distributed roughness coefficients in a flood propagation model with limited data. Advances in Water Resources, 22 (4), 349-365.

Bahauddin, K. M., Rahman, N. and Hasnine, T. M., 2016. Environmental reviews and case studies: Public perception, knowledge and participation in climate change adaptation governance in the coastal region of Bangladesh using social ecological inventory (SET) tool. Environmental Practice 18(1). 32-43.

Bangladesh Planning Commission, 2018. Bangladesh Delta Plan 2100 Baseline Studies: Volume 1 - Water Resource Management. Bangladesh Delta Plan (BDP) 2100 Formulation Project, General economic Division,

Bangladesh Planning Commission, Government of People's Republic of Bangladeh, Dhaka, Bangladesh.

Barua, K. D., 1990. Suspended sediment movement in the estuary of Meghna river system. Marine Geololgy, 91, 243–253.

Barua, K. D., 1997. The active delta of the Ganges-Brahmaputra rivers: Dynamics of its present formations. Marine Geodesy, 20(1), 1-12.

Bates, P.D., Horritt, M.S., Aronica, G. and Beven K., 2004. Bayesian updating of flood inundation likelihoods conditioned on flood extent data. Hydrological Processes, 18, 3347–3370.

Benjamin, J.R., and Cornell, C.A.,1970. Probability, Statistics, and Decision for Civil Engineers, McGraw-Hill.

Benqué, J. P., Cunge, J. A., Feuillet, J., Hauguel A. and Holly, F. M., 1982. New method for tidal current computation. Journal of the Waterway, Port, Coastal and Ocean Division, ASCE 108, 396–417.

Borromeo, L., Ando, S., France-Lanord, C., Coletti, G., Hahn, A. and Garzanti, E., 2019. Provenance of Bengal Shelf sediments: 1. Minerology and Geochemistry of silt. Minerals, MDPI, 9(10), 640.

Brammer, H., 2014. Bangladesh's dynamic coastal regions and sea-level rise. Climate Risk Management, 1, 51–62.

Brammer, H., Asaduzzaman, M., and Sultana, P., 1993. Effects of climate and sea level changes on the natural resources of Bangladesh. Briefing Document No. 3. Bangladesh Unnayan Parishad, Dhaka.

Bricheno, L. M., Wolf, J. and Islam, S., 2016. Tidal intrusion with a mega delta: An unstructured grid modelling approach. Estuarine, Coastal and Shelf Science, 182, 12-26.

Brocchiola, D., and Rosso, R., 2009. Use of a derived distribution approach for flood prediction in poorly gauged basins: A case study in Italy, Advances

in Water Resources, 32(8), 1284-1296.

BWDB, 1991a. Annual flood report 1991. Surface Water Hydrology-2. UNDP/WMO-BGD/88/013. Dhaka, Bangladesh.

BWDB, n.d., Bangladesh Water Water Development Board, accessed in February 2021. <https://www.bwdb.gov.bd/project>

Chen, J., and Adams, B. J., 2007a. Development of analytical models for estimation of urban stormwater runoff, Journal of Hydrology, 336(3–4), 458-469.

Chen, J. and Adams, B. J., 2007b. A derived probability distribution approach to stormwater quality modelling. Advances in Water Resources, 30(1), 80-100.

Chertock A. Jin S. and Kurganov A., 2015a. An operator splitting based stochastic Galerkin method for the one-dimensional compressible Euler equations with uncertainty. <http://www.math.wisc.edu/~jin/research.html>

Chertock A., Jin S. and Kurganov A., 2015b. A well-balanced operator splitting based stochastic Galerkin method for the one-dimensional Saint-Venant system with uncertainty.
<http://www.math.wisc.edu/~jin/research.html>

Chesher, T.J., Wallace, H.M., Meadowcroft, I.C., Southgate, H.N. (1993).

Church, J. A., Clark, P. U., Cazenave, A., Gregory, J. M., Jevrejeva, S., Levermann, A., Merrifield, M. A., Milne, G. A., Nerem, R. S., Nunn, P. D., Payne, A. J., Pfeffer, W. T., Stammer, D. and Unnikrishnan, A. S., 2013. Sea level Change. In: Climate Change 2013: The physical science basis. Contribution of working group I to the Fifth Assessment Report of the Intergovernmental Panel on Climate Change [Stocker, T. F., Qin, D., Plattner, G. -K., Tignor, M., Allen, S. K., Boschung, J., Nauels, A., Xia, Y., Bex, V. and Midgley, P. M. (eds.)]. Cambridge University Press, Cambridge, United Kingdom and New York, NY, USA.

Cloern, J. E., Knowles, N., Brown, L. R., Cayan, D., Dettinger, M. D., Morgan, T. L., Schoellhammer, D.H., Stacey, M.T., van der Wegen, M., Wagner, W., and Jassby, A.D., 2011. Projected Evolution of California's San Francisco Bay-Delta-River System in a Century of Climate Change, PLoS ONE, 6(9), e24465.

Cox, D. C., and Baybutt, P., 1981. Methods for Uncertainty Analysis: A Comparative Survey, Risk Analysis, 1(4), 251-258.

Dam, G., van der Wegen, M., Labeur, R.J., and Roelvink, D., 2016. Modeling centuries of estuarine morphodynamics in the Western Scheldt estuary, Geophysical Research Letters, 43(8), 3839-3847.

Dasgupta, S., Kamal, F. A., Khan, Z. H., Chourdhury, S., and Nishat, A., 2014. River Salinity and Climate Change: Evidence from Coastal Bangladesh, vol. 6817. World Bank Policy Research Working Paper.

Delo, E. A. and and Ockenden, M. C., 1992. Estuarine muds manual. HR Walingford Report SR 309.

Delftdashboard, n.d., last accessed in November 2019, < https://publicwiki.deltares.nl/display/DDB/Delft+Dashboard>

Deltares, 2014. Delft3D-FLOW User Manual version 3.15.34158. Deltares, The Netherlands. <https://oss.deltares.nl/documents/183920/185723/Delft3D-FLOW_User_Manual.pdf>

Després B., Poëtte G. and Lucor D., 2013. Robust uncertainty propagation in systems of conservation laws with the entropy closure method. In: Bijl H., Lucor D., Mishra S., Schwab C. (Eds.), Uncertainty Quantification in Computational Fluid Dynamics, Springer, Berlin.

De Vriend, H. J., 1987. 2DH mathematical modelling of morphological evolutions in shallow water. Coastal Engineering, 11, 1-27.

Díaz-Granados, M.A., Valdes, J.B., and Bras, R.L., 1984. A physically based flood frequency distribution, *Water Resources Research*, 20(7), 995-1002.

Di Baldassarre, G., Yan, K., Ferdous, M. R., and Brandimarte, L., 2014. The interplay between human population dynamics and flooding in Bangladesh: a spatial analysis. Evolving water resources systems: understanding, predicting and managing water-society interactions. Proceedings of ICWRS2014, Bologna, Italy.

Eagleson, P.S., 1972. Dynamics of flood frequency, *Water Resources Research*, 8(4), 878-898.

Eagleson, P.S.,1978. Climate, soil, and vegetation 7. A derived distribution of annual water yield. Water Resources Research, 14(5), 765–776.

Earthexplorer, n.d., United States Geological Survey, accesses in November, 2017. < https://earthexplorer.usgs.gov/>

Eckart, C., 1958. Properties of water, Part II. The equation of state of water and sea water at low temperatures and pressures. American Journal of Science 256, 225–240.

Elman H.C., Miller C.W., Phipps E.T. and Tuminaro R.S., 2011. Assessment of collocation and Galerkin approaches to linear diffusion equations with random data, International Journal for Uncertainty Quantification, 1(1), 19-33.

Esri, n.d., access in November 2017. < https://www.esri.com/en-us/arcgis/products/arcgis-pro/overview>

Fiorini, C., Despres, B., and Puscas, M. A., 2021. Sensitivity equation method for the Navier-Stokes equationsapplied to uncertainty propagation, International Journal for Numerical Methods in Fluids, 93, 71-92.

Fischer, H. B., List, E. J., Koh, R. C. Y., Imberger, J. & Brooks, N. A., 1979. Mixing in Inland and Coastal Waters. Academic Press Inc., New York.

Flandoli, F., and Pappalettera, U., 2020. Stochastic modelling of small-scale perturbation, Water, 12(10), 1-17.

Ge, L., Cheung K.F. and Kobayashi M.H., 2008. Stochastic solution for uncertainty propagation in nonlinear shallow-water equations, J. Hydraul. Eng. 134 (12), 1732–1743.

Ghanem, R.G., and Spanos, P.D., 2003. Stochastic finite elements: a spectral approach, Springer, New York.

Gholami, H., Jafari TakhtiNajad, E., Collins, A.L., and Fathabadi, A., 2019. Monte Carlo fingerprinting of the terrestrial sources of different particle size fractions of coastal sediment deposits using geochemical tracers: some lessons for the user community. Environmental Science and Pollution Research, 26, 13560–13579.

Goodbred, S. L. and Kuehl, S. A., 2000. Enormous Ganges-Brahmaputra sediment discharge during strengthened early Holocene monsoon. Geology, 28(12), 1083–1086.

Gottschalk, L., and Weingartner, R., 1998. Distribution of peak flow derived from a distribution of rainfall volume and runoff coefficient, and a unit hydrograph, Journal of Hydrology,208(3–4), 148-162.

Haque, A. and Nicholls, R. J., 2018. Floods and the Ganges-Brahmaputra-Meghna Delta. In: Nicholls. R., Hutton, C., Adger, W., Hanson, S., Rahman, M., Salehin, M. (eds.). Ecosystem services for well-being in deltas. Palgrave Macmillan, Cham.

Hebson, C., and Wood, E.F., 1982. A derived flood frequency distribution using Horton Order Ratios, Water Resources Research, 18(5), 1509-1518.

Hofer, E., 2018. The uncertainty analysis of model results, Springer, Cham.

Hofer, T. and Messerli, B., 2006. Floods in Bangladesh: History, dynamics and rethinking the role of the Himalayas. United Nations University Press. United Nations University Press, Tokyo, Japan.

Horritt, M.S., (2002). Stochastic Modelling of 1-D Shallow Water Flows over Uncertain Topography. Journal of Computational Physics, 180(1): 327-338.

Horritt, M.S., (2006). A linearized approach to flow resistance uncertainty in a 2-D finite volume model of flood flow. Journal of Hydrology, 316: 13–27.

Hossain, M., Islam, A. T. M. A., and Saha, S. K., 1987. Floods in Bangladesh: Recurrent disaster and people's survival. Universities Research Centre, Dhaka.

Hu J. and Jin S., 2016. A stochastic Galerkin method for the Boltzmann equation with uncertainty, Journal of Computational Physics. 315, 150-168.

Hu J., Jin S. and Xiu D., 2015. A Stochastic Galerkin Method for Hamilton--Jacobi Equations with Uncertainty, SIAM Journal on Scientific Computing, 37(5), A2246-A2269.

Huang, J., 2005. Simulation of shallow fluvial morphodynamics. D.Phil.Thesis, University of Oxford.

Huang, J., Borthwick, A .G. L., and Soulsby, A. L., 2008. One-dimensional modelling of fluvial bed morphodynamics. Journal of Hydraulic Research, 46(5), 636-647.

Hudson, J. and Sweby, P. K., 2003. Formulations for numerically approximating hyperbolic systems governing sediment transport. Journal of Scientific Computing, 19, 225-252.

Hudson, J., Damgaard, J., Dodd, N., Chesher, T., and Cooper, A., 2005. Numerical approaches for 1D morphodynamic modelling. Coastal Engineering, 52(8), 691– 707.

Hughes, R., Adnan, S., and Dalal-Clayton, B., 1994. Floodplainsorfloodplans? A review of approaches to water management in Bangladesh. International Institute for Environment and Development, London.

Hull, J.C., 2018. Options, Futures, and Other Derivatives, Pearson, London.

Hussain, S. G., 2017. Identification and Modeling of Suitable Cropping Systems and Patterns for Saline, Drought and Flood Prone Areas of Bangladesh. Christian Commission for Development in Bangladesh (CCDB). Dhaka 1216, Bangladesh.

Islam, M. R., Begum, S. F., Yamaguchi, Y. and Ogawa, K., 2002. Distribution of suspended sediment in the coastal area off the Ganges-Brahmaputra River mouth: observation from TM data. Journal of Maritime Systems, 32, 307-321.

Jahan, M., Chowdhury, M. M. A., Shampa, Rahman, M. M., and Hossain, M. A., 2015. Spatial variation of sediment and some nutrient elements in GBM delta estuaries: a preliminary assessment. In: International Conference on Recent Innovation in Civil Engineering for Sustainable Development (IICSD-2015), vol. 6.

Jakobsen, F., Azam, M. H., and Kabir, M., 2002. Residual flow in the Meghna estuary on the coastline of Bangladesh. Estuarine, Coastal and Shelf Science, 55, 587–597.

Jiang, S., 1998. Application of stochastic differential equations in risk assessment for flood releases. Hydrological Sciences, 43(3), 349-360.

Jin S. and Shu R., .2017. A stochastic asymptotic-preserving scheme for a kinetic-fluid model for disperse two-phase flows with uncertainty, Journal of Computational Physics, 335, 905-924.

Kamruzzaman, M., Jang, M-W., Cho, J. and Hwang, S., 2019. Future changes in precipitation and drought characteristics over Bangladesh under CMIP5 climatological projections. Water, 11, 2219.

Karim, M. and Mimura, N., 2008. Impacts of climate change and sea-level rise on cyclonic storm surge floods in Bangladesh. Global Environmental Change, 18(3), 490-500.

Kawahara, M. and Umetsu, T., 1986. Finite element method for moving boundary problems in river flow. International Journal for Numerical Methods in Fluids, 6, 365-386.

Kay, S., Caesar, J., Wolf, J., Bricheno, L., Nicholls, R. J., Islam, A. K. M. S., Haque, A., Pardaens, A. and Lowe, J. A., 2015. Modelling the increases frequency of extreme sea levels in the Ganges-Brahmaputra-Meghna delta due to sea level rise and other effects of climate change. Environmental Science: Processes and Impacts, 17, 1311-1322.

Kreitmair, M. J., Draper, S., Borthwick, A. G. L. and van den Bremer, T. S., 2019. The effect of uncertain bottom friction on estimates of tidal current power. Royal Society Open Science, 6, 180941.

Kreitmair, M. J., 2019. Uncertainty quantification in tidal energy resource assessment. Ph.D. thesis, The University of Edinburgh, UK.

Kreitmair, M.J., Adcock, T.A.A., Borthwick, A.G.L., Draper, S. and van den Bremer T.S., 2020. The effect of bed roughness uncertainty on power estimates for the Pentland Firth. Royal Society Open Science, 7(1), 191127.

Kuehl, S. A., Hariu, T. M. and Moore, W. S., 1989. Shelf sedimentation off the Ganges–Brahmaputra river system: Evidence for sediment bypassing to the Bengal fan. Geology, 17, 1132–1135.

Kurothe, R.S., Goel, N.K., and Mathur, B.S., 1997. Derived flood frequency distribution for negatively correlated rainfall intensity and duration, Water Resources Research, 33(9), 2103-2107.

Kusche, J., Uebbing, B., Rietbroek, R., Shum, C. K. and Khan, Z. H., 2016. Sea level budget in the Bay of Bengal (2002-2014) from GRACE and altimetry. Journal of Geophysical Research: Oceans, 121, 1194-1217.

Lacor C., Savin É., 2019. General Introduction to Polynomial Chaos and Collocation Methods. In: Hirsch C., Wunsch D., Szumbarski J., Łaniewski-Wołłk Ł., Pons-Prats J. (eds) Uncertainty Management for Robust Industrial Design in Aeronautics. Notes on Numerical Fluid Mechanics and Multidisciplinary Design, vol 140. Springer, Cham.

Latteux, B., 1995. Techniques for long-term morphological simulation under tidal action. Marine Geology, 126, 129-141.

Lesser, G. R., Roelvink, van Kester, J. A., J. A. T. M. and Stelling, G. S., 2004. Development and validation of a three-dimensional morphological model. Coastal Engineering, 51, 883–915.

Leendertse, J.J., 1987. A three-dimensional alternating direction implicit model with iterative fourth order dissipative nonlinear advection terms. WD-333-NETH, The Netherlands Rijkswaterstaat.

Li, L., Sandu, C., Lee, J., and Liu, B., 2009. Stochastic modeling of tire–snow interaction using a polynomial chaos approach, Journal of Terramechanics, 46(4), 165-188.

Li, X., Zhang, Z., Wade, T. L., Knap, A. H., and Zhang, C. L., 2017. Sources and compositional distribution of organic carbon in surface sediments from the lower Pearl River to the coastal South China Sea, Journal of Geophysical Research: Biogeosciences, 122, 2104– 2117.

Liang, Q., and Borthwick, A. G. L., 2009. Adaptive quadtree simulation of shallow flows with wet-dry fronts over complex topography. Computers & Fluids, 38(2), 221-234.

Lin, G., Wan, X., Su, C., and Karniadakis, G. E., 2007. Stochastic computational fluid mechanics, Computing in Science & Engineering, 9 (2), 21-29

Lin, N., and Shullman, E., 2017. Dealing with hurricane surge flooding in a changing environment: part I. Risk assessment considering storm climatology

change, sea level rise, and coastal development. Stochastic Environmental Research and Risk Assessment, 31, 2379–2400.

Loukas, A., 2002. Flood frequency estimation by a derived distribution procedure. Journal of Hydrology, 255(1-4), 69-89.

Lovelock, C., Cahoon, D., Friess, D. *et al*., 2015. Vulnerability of Indo-Pacific mangrove forests to sea-level rise. Nature, 526, 559-563.

Luan, H. L., Ding, P. X., Wang, Z. B., and Ge, J. Z., 2017. Process-based morphodynamic modeling of the Yangtze Estuary at a decadal timescale: Controls on estuarine evolution and future trends, Geomorphology, 290, 347-364

Mahmood, R., Ahmed, N., Zhang, L. and Li, G., 2020. Coastal vulnerability assessment of Meghna estuary of Bangladesh using integrated geospatial techniques. International Journal of Risk Reduction, 42, 1-14.

Mazhdrakov M., Benov D. and Valkanov N., 2018. The Monte Carlo Method. Engineering Applications. ACMO Academic Press.

Meier, C. I., Moraga, J. S., Pranzini, G., and Molnar, P., 2016. Describing the interannual variability of precipitation with the derived distribution approach: effects of record length and resolution, Hydrology and Earth System Sciences, 20, 4177-4190.

Miah, M. M., 1988. Flood in Bangladesh: A hydromorphological study of the 1987 flood. Academic Publishers, Dhaka.

Mikhailov, V. N., and Dotsenko, M. A., 2007. Processes of delta formation in the mouth area of the Ganges and Brahmaputra rivers. Water Resources, 34, 385–400.

Milliman, J.D. and Meade, R.H., 1983. World-wide delivery of river sediments to the oceans. Journal of Geology, 91, 1-22.

Ministry of Water Resources, 1999. Meghna Estuary Study, Draft master plan. Rep. Prepared by DHV Consultants, v. 1, Bangladesh Water Development Board, Bangladesh.

Ministry of Water Resources, 2001. Meghna Estuary Study-II. Hydro-morphological dynamics of the Meghna Estuary, Meghna Estuary Study, prepared by DHV Consultants BV and associates, Bangladesh Water Development Board, Bangladesh.

Ministry of Water Resources, 2007. Estuary Development Plan, Technical Note EDP -1. Rep. Prepared by DHV Consultants, Bangladesh Water Development Board, Bangladesh.

Mishra S., Schwab C. and Sukys J., 2012. Multilevel Monte Carlo finite volume methods for shallow water equations with uncertain topography in multi-dimension, SIAM Journal on Scientific Computing, 34(6), B761-B784.

Mukherjee, A., Fryar, A.E. and Thomas, W. A., 2009. Geologic, geomorphic and hydrologic framework and evolution of the Bengal basin, India and Bangladesh. Journal of Asian Earth Sciences, 34, 227-244.

Ni, J. R., Borthwick, A. G. L., and Qin, H. P., 2002. ‘‘Integrated approach to determining postreclamation coastlines.’’ Journal of Environmental Engineering, 128(6), 543–551.

Patra, A. and Bhaskaran, P. K., 2016. Trends in wind-wave climate over the head Bay of Bengal region. International Journal of Climatology, 36, 4222-4240.

Perona, P., Durrenmatt, D.J., and Characklis, G.W., 2013. Obtaining natural-like flow releases in diverted river reaches. Journal of Environmental Management, 118, 161-169.

Pettersson P., Iaccarino G. and Nordström J., 2014. A stochastic Galerkin method for the Euler equations with Roe variable transformation, Journal of Computational Physics, 257, 481-500.

Philip, S., Sparrow, S., Kew, S. F., Van der Wiel, K., Wanders, N., Singh, R., Hassan, A., Mohammed, K., Javid, H., Haustein, K., Otto, F. E. L., Hirpa, F., Ruksana H. Rimi, R. H., Islam, A. K. M. S., Wallom, D. C. H., and Van Oldenborgh, G. J., 2019. Attributing the 2017 Bangladesh floods from meteorological and hydrological perspectives. Hydrology and earth sciences, 23, 1409-1429.

Poëtte G., Després B. and Lucor D., 2009. Uncertainty quantification for systems of conservation laws, J. Comput. Phys. 228(7), 2443-2467.

Qin, H.P., Ni. J.R., and Borthwick, A.G.L. (2002) Harmonized optimal postreclamation coastline for Deep Bay, China. ASCE Journal of Environmental Engineering, 128(6): 552-561.

Ramírez, J. A., and Senarath, S., 2000. A statistical-dynamical parameterization of canopy interception and land surface-atmosphere interactions, Journal of Climate, 13, 4050–4063.

Roelvink, J. A. and Walstra, D. J. R., 2004. Keeping it simple by using complex models. In Proceedings of the 6th International Conference on Hydro-Science and Engineering. Advances in Hydro-Science and Engineering, Brisbane, Australia, 6, 12.

Romanowicz, R., and Beven, K., 1998. Dynamic real-time prediction of flood inundation probabilities. Hydrological Sciences Journal, 43(2), 181-196.

Russo, F., 2006. Stochastic Differential Equations, In: Encyclopedia of Mathematical Physics, Elsevier Academic Press.

Salsburg, D., 2002, The lady tasting tea: How statistics revolutionized science in the twentieth century. Henry Holt and Company, New York.

Sampson, J., Easton, A. and Singh, M., 2006. Moving boundary shallow water flow above parabolic bottom topography. ANZIAM J. 47 (EMAC2005), C373–C387.

Sarker, M.H., Choudhury, G.A., Akter, J., and Hore, S.K., 2012. Bengal Delta Is Not Sinking at a Very High Rate as Indicated by Recent Research: A Pragmatic Assessment Based on Archaeological Monuments. http://www.thedailystar.net/news-detail-262153.

Schaeffer, M., Hare, W., Rahmstorf, S. and Vermeer, M., 2012. Long-term sea-level rise implied by 1.5 ºC and 2 ºC warming levels. Nature Climate Change, 2, 867-870.

Siddique-E-Akbar, A. H. M., Hossain, F., Lee, H. and Shum, C. K., 2011. Inter-comparison study of water level estimates derived from hydrodynamic–hydrologic model and satellite altimetry for a complex deltaic environment. Remote Sensing of Environment, 115(6), 1522-1531.

Shaw J. and Kesserwani G., 2020. Stochastic Galerkin finite volume shallow flow model: well-balanced treatment over uncertain topography, Journal of Hydraulic Engineering, 146(3), 04020005.

Shu R., Hu J. and Jin S., 2017. A stochastic Galerkin method for the Boltzmann equation with multi-dimensional random inputs using sparse wavelet bases, Numerical Mathematics: Theory, Methods and Application, 10(02), 465-488.

Singler, J.R., 2005. Sensitivity analysis of partial differential equations with applications to fluid flow, PhD thesis, Virginia Polytechnic Institute and State University, The USA.

Soar, P.J., and Thorne, C., 2001. *Channel Restoration Design for Meandering Rivers*. ERDC/CHL Report CR-01-1. US Army Corps of Engineers, Vicksburg MS, USA.

Soulsby, R., 1997. Dynamics of marine sands: A manual for practical applications. Thomas Telford Publications, London.

Stelling, G. S., 1984. On the construction of computational methods for shallow water flow problems. Technical Report 35, Rijkswaterstaat.

Syvitski, J.P.M., Kettner, A.J., Overeem, I., Hutton, E.W.H., Hannon, M.T., Brakenridge, G.R., Day, J., Vorosmarty, C., Saito, Y., Giosan, L., and Nicholls, R.J., 2009. Sinking deltas due to human activities. Nature Geoscience, 2, 681–686.

Thorn, M. F. C. and Parsons, J. G., 1980. Erosion of cohesive sediments in estuaries: an engineering guide. 3rd International Symposium of Dredging Technology, Bordeaux, 349-358. BHRA, Cranfield.

Umitsu, M., 1993. Late Quaternary sedimentary environments and land forms in the Ganges Delta. Sedimentary Geology, 83, 177–186.

van Kampen, N.G., 2007. Chapter XVI – Stochastic Differential Equations, In: Stochastic Processes in Physics and Chemistry (Third Edition), North-Holland Personal Library, 396-421.

van Rijn, L. C., 1984a. Sediment transport, Part I: bed load transport. Journal of Hydraulic Engineering, 110 (10), 1431–1456.

van Rijn, L. C., 1984b. Sediment transport, Part II: suspended load transport. Journal of Hydraulic Engineering, 110 (11), 1613–1640.

van Rijn, L. C., 1993. Principles of Sediment Transport in Rivers, Estuaries and Coastal Seas. Aqua Publications, The Netherlands.

Wang, S., and Wang, Y., 2019. Improving probabilistic hydroclimatic projections through high-resolution convection-permitting climate modeling and Markov chain Monte Carlo simulations. Climate Dynamics, 53, 1613–1636.

Weare, T. J., 1979. Errors arising from irregular boundaries in ADI solutions of the shallow water equations. International Journal Numerical Methods Engineering, 14, 921–931.

Whitehouse, R., Soulsby, R., Roberts, W. and Mitchener, H., 2000. Dynamics of estuarine muds: A manual for practical applications. Thomas Telford Publications, London.

Winsemius, H. C., et al. (2013) A framework for global river flood risk assessments. Hydrology and Earth System Sciences, 17, 1871–1892.

Winterwerp, J. C. and van Kesteren, W. G. M., 2004. Introduction to the physics of cohesive sediment in the marine environment. Development in Sedimentology 56, Elsevier, Amsterdam.

Xiu, D., 2009. Fast numerical methods for stochastic computations: a review, Communication in Computational Physics, 5(2-4) (2009) 242-272.

Xiu D., 2010. *Numerical methods for stochastic computations*, Princeton University Press, Princeton, USA, 2010.

Xiu, D., and Hesthaven, J.S., 2005. High-order collocation methods for differential equations with random inputs, SIAM Journal on Scientific Computing, 27(3), 1118-1139.

Xiu D. and Shen J., 2009. Efficient stochastic Galerkin methods for random diffusion equations, Journal of Computational Physics, 228(2), 266-281.

Xu, S., Huang, W., Zhang, G., Gao, F., and Li, X., 2014. Integrating Monte Carlo and hydrodynamic models for estimating extreme water levels by storm surge in Colombo, Sri Lanka. Natural Hazards, 71, 703–721.

Yang, S., Xiong, F., and Wang, F., 2017. Polynomial Chaos Expansion for Probabilistic Uncertainty Propagation, In: Uncertainty Quantification and Model Calibration, edited by Hessling, J. P., IntechOpen.